

**STRUCTURAL AND PHYSICAL PROPERTIES OF TORSIONAL CARBON  
NANOTUBE DEVICES BY ELECTRON DIFFRACTION AND MICROSCOPY**

Taoran Cui

A dissertation submitted to the faculty of the University of North Carolina at Chapel Hill in  
partial fulfillment of the requirements for the degree of Doctor of Philosophy in the  
Department of Physics and Astronomy.

Chapel Hill  
2013

Approved by:

Sean Washburn

Lu-Chang Qin

Jianping Lu

Charles Evans

Adam Hall

James Cahoon

©2013  
TAORAN CUI  
ALL RIGHTS RESERVED

## ABSTRACT

TAORAN CUI: Structural and Physical Properties of Torsional Carbon Nanotube Devices by Electron  
Diffraction and Microscopy  
(Under the direction of Sean Washburn and Lu-Chang Qin)

This dissertation first probes into the detailed development process of a nanoelectromechanical system based on one-dimensional carbon nanotubes. Various types of carbon nanotubes with a sparse spatial distribution are grown with corresponding chemical vapor deposition recipes. The synthesis is followed by the microelectronic fabrication to pattern a circuit with a suspended carbon nanotube, which allowed the *in situ* observation and manipulation of this nano-electromechanical system in a transmission electron microscope.

The theoretical deduction and the experimental result prove the sophistication of *in situ* nanobeam electron diffraction with transmission electron microscopy to determine the chiral structure of a carbon nanotube, especially each individual inner shell of a multiwalled carbon nanotube, while the electron transport behavior of the carbon nanotube is measured. Based on the experimental results of large numbers of carbon nanotubes, a model is established to correlate the transport property with the atomic structure of a carbon nanotube. Given the unambiguous chirality and therefore the explicit band structure, it is concluded that both the thermal excitation and the multiple conducting subbands significantly contribute to the ballistic transport in a carbon nanotube at room temperature.

External torsional strains are applied on a carbon nanotube via a nano-pendulum system fabricated with the similar techniques. The corresponding deformations are determined with nanobeam electron diffraction analysis, and the calculated shear moduli agree with the theoretical predictions and other experimental results. This nano-pendulum with a multiwalled carbon nanotube provides a perfect platform to study friction. The interlayer interactions and the frictions are investigated by monitoring the relative motions between the neighboring shells when the carbon nanotube undergoing a torsional strain. Furthermore, The resistance variations of a carbon nanotube responding to strains are also measured *in situ* at room temperature, and the transport behavior of a deformed carbon nanotube is successfully explained by our established model.

## ACKNOWLEDGMENTS

There are lots of people I would like to thank for a huge variety of reasons.

Firstly, I would like to thank my advisors, Prof. Sean Washburn and Prof. Lu-Chang Qin, without whose common-sense, knowledge and perceptiveness I would have never finished, I can't overstate the importance of their involvements in my graduate career. I thank both of them for their enthusiasms, kindnesses and encouragements which always supported me, and their timely comments and profound experiences were invaluable throughout.

I am particularly indebted to Dr. Letian Lin, former group member who introduced me into the project and with whom I spent most of my time during PhD, for his patient guidance and precious suggestions, as well as his profound knowledge of ancient Chinese literature for amusements during the tedious late night experiments.

I am grateful to all my colleagues, Dr. Lamar Mair, Dr. Haijing Wang, Dr. Zheng Ren, Nadira Williams, Robert Zhang, and Jerome Carpenter. I will always miss the enlightening discussions with you and the generous help you provided. I would like to express my appreciation to Prof. Jie Tang for the internship opportunity at NIMS and the heart-warming hospitality. I also want to acknowledge Yingwen Chen from Dr. Jie Liu's group at Duke University for the help in nanotube growth and catalyst synthesis. My sincere regards go to all CHANL personnel, especially Dr. Amar Kumbhar, for the fabrication apparatus support and maintenance.

I owe a debt of gratitude to all my committee members, especially Prof. Jianping Lu, without whose fundamental theoretical work and detailed explanations, all my project would have been unrealistic; and Prof. Adam Hall, thank you for the help and suggestions in experiment design, and your PhD dissertation has been the Bible to me throughout the project.

Finally, to my parents and my wife, for everything.



## TABLE OF CONTENTS

|   |     |
|---|-----|
| LIST OF TABLES .....  | x   |
| LIST OF FIGURES .....   | xi  |
| LIST OF ABBREVIATIONS .....   | xiv |
| 1 Introduction to Carbon Nanotubes .....                                      | 1   |
| 1.1 History .....   | 1   |
| 1.2 From Graphene to Carbon Nanotube .....                                    | 2   |
| 1.3 Structure of Single-Walled Carbon Nanotubes .....                         | 3   |
| 1.4 Energy Dispersion of Single-Walled Carbon Nanotubes .....                 | 6   |
| 1.5 Multi-Walled Carbon Nanotubes .....                                       | 9   |
| 1.6 Mechanical Properties of Carbon Nanotubes .....                           | 12  |
| BIBLIOGRAPHY .....  | 14  |
| 2 Characterization of Carbon Nanotubes .....                                  | 16  |
| 2.1 Scanning Tunneling Microscopy and Other Techniques .....                  | 16  |
| 2.2 Transmission Electron Microscopy and Nano-Beam Electron Diffraction ..... | 17  |
| 2.2.1 Mechanism of Transmission Electron Microscopy .....                     | 18  |
| 2.2.2 Imaging of Carbon Nanotubes in the Real Space with TEM .....            | 20  |
| 2.2.3 Theory of Electron Diffraction of Carbon Nanotubes .....                | 20  |
| 2.2.4 Determination of Chiral Structure of a Carbon Nanotube .....            | 25  |
| BIBLIOGRAPHY .....  | 33  |
| 3 Synthesis of Carbon Nanotubes .....   | 35  |
| 3.1 Introduction .....  | 35  |
| 3.2 Fundamentals of Chemical Vapor Deposition(CVD) .....                      | 35  |
| 3.2.1 Carbon Precursor .....  | 37  |

|       |   |    |
|-------|---|----|
| 3.2.2 | Temperature .....   | 38 |
| 3.2.3 | Catalytic Nanoparticles .....                                   | 38 |
| 3.2.4 | Gas Flow Rates .....  | 40 |
| 3.3   | CNT Synthesis Experiment .....                                  | 40 |
| 3.3.1 | Motivation and Objective .....                                  | 40 |
| 3.3.2 | Experimental Process .....                                      | 42 |
| 3.3.3 | Synthesis Results .....   | 45 |
|       | BIBLIOGRAPHY .....  | 48 |
| 4     | Nano-Electromechanical Device Based on a Suspended CNT .....    | 50 |
| 4.1   | Introduction .....  | 50 |
| 4.2   | Device Fabrication .....  | 51 |
| 4.2.1 | Basic Configuration .....                                       | 51 |
| 4.2.2 | Back Etching .....  | 54 |
| 4.2.3 | Fabrication of Circuit and Paddle .....                         | 54 |
| 4.2.4 | Suspending Nanotube .....                                       | 58 |
| 4.3   | Customized NEMS Specimen Holder for <i>in situ</i> TEM .....    | 61 |
|       | BIBLIOGRAPHY .....  | 66 |
| 5     | Electron Transport in Carbon Nanotubes of Known Chirality ..... | 68 |
| 5.1   | Introduction .....  | 68 |
| 5.2   | Experimental Results .....                                      | 70 |
| 5.2.1 | Determination of Chirality .....                                | 72 |
| 5.2.2 | Transport Measurement .....                                     | 82 |
| 5.2.3 | Bandgaps of CNTs .....  | 85 |
|       | BIBLIOGRAPHY .....  | 89 |
| 6     | Nano-Tribology in MWNT NEMS Devices .....                       | 92 |
| 6.1   | Introduction to the Torsional Experiment on CNTs .....          | 92 |
| 6.2   | Electric Responses of Twisted CNTs .....                        | 95 |
| 6.3   | Chiral Structures of Inner Tubes in a MWNT .....                | 97 |
| 6.4   | Experimental Results .....                                      | 98 |

|     |  |     |
|-----|--|-----|
| 6.5 | Results and Discussion .....                                     | 106 |
|     | BIBLIOGRAPHY .....   | 114 |
| 7   | Summary .....  | 117 |
|     | Appendix A CNTs syntheses with Chemical Vapor Deposition .....   | 119 |
|     | A.1 SWNT synthesis .....   | 119 |
|     | A.2 DWNT synthesis .....   | 119 |
|     | A.3 FWNT synthesis .....   | 120 |
|     | A.4 Aligned SWNT synthesis on quartz wafer .....                 | 120 |
|     | A.5 CNT transferring .....                                       | 121 |
|     | Appendix B Instruction of Suspended CNT Device Fabrication ..... | 122 |
|     | B.1 Backside Etching I .....                                     | 122 |
|     | B.1.1 Wafer preparation .....                                    | 122 |
|     | B.1.2 Photolithography .....                                     | 123 |
|     | B.1.2.1 Standard solvent clean .....                             | 123 |
|     | B.1.2.2 Coating of photoresist .....                             | 123 |
|     | B.1.2.3 Alignment, exposure and development .....                | 123 |
|     | B.1.3 Removal of Si substrate with wet etching .....             | 123 |
|     | B.1.4 Plasma Enhanced Vapor Deposition .....                     | 124 |
|     | B.2 Circuit Deposition .....                                     | 124 |
|     | B.2.1 Photolithography for large electrodes .....                | 124 |
|     | B.2.1.1 Standard solvent clean .....                             | 124 |
|     | B.2.1.2 Coating of photoresist .....                             | 126 |
|     | B.2.1.3 Alignment, exposure and development .....                | 126 |
|     | B.2.1.4 Metallization .....                                      | 126 |
|     | B.2.2 E-beam Lithography of fiducials .....                      | 127 |
|     | B.2.2.1 Bi-layer Resist Coating .....                            | 127 |
|     | B.2.2.2 CAD .....  | 128 |
|     | B.2.2.3 Run File Set up .....                                    | 129 |
|     | B.2.2.4 Exposure .....   | 129 |

|         |  |     |
|---------|--|-----|
| B.2.2.5 | Development .....                                  | 130 |
| B.2.3   | E-beam Lithography of channels .....               | 130 |
| B.2.3.1 | Bi-layer Resist Coating .....                      | 130 |
| B.2.3.2 | CAD .....  | 130 |
| B.2.3.3 | Run File Set up .....                              | 131 |
| B.2.3.4 | Exposure .....                                     | 132 |
| B.2.3.5 | Development .....                                  | 132 |
| B.2.3.6 | Metallization .....                                | 132 |
| B.3     | Backside Etching II .....                          | 133 |
| B.4     | FIB Etching.....                                   | 133 |
| B.4.1   | Front Etching .....                                | 133 |
| B.4.2   | Back Etching .....                                 | 134 |
| B.4.3   | E-beam Lithography of windows .....                | 134 |
| B.4.3.1 | Bi-layer Resist Coating .....                      | 134 |
| B.4.3.2 | CAD .....  | 135 |
| B.4.3.3 | Run File Set up .....                              | 135 |
| B.4.3.4 | Exposure .....                                     | 136 |
| B.4.3.5 | Development .....                                  | 136 |
| B.4.4   | Buffered hydrofluoric acid etching.....            | 137 |
| B.4.5   | Critical Point Dry .....                           | 137 |
| B.5     | Before Starting.....                               | 138 |
| B.6     | Alignment .....                                    | 138 |
| B.6.1   | Condenser Aperture Alignment .....                 | 139 |
| B.6.1.1 | Condenser Aperture Centering .....                 | 139 |
| B.6.1.2 | Condenser Lens Astigmatism .....                   | 139 |
| B.6.2   | Gun Shift .....                                    | 139 |
| B.6.3   | Gun Tilt.....                                      | 139 |
| B.6.4   | Condenser Deflector Tilt/Pivot Point Balance ..... | 140 |
| B.6.5   | Beam Tilt/Voltage Center .....                     | 140 |
| B.6.6   | Intermediate Lens Astigmatism/Caustic Point .....  | 140 |

|       |                                  |     |
|-------|----------------------------------|-----|
| B.6.7 | Condenser Deflector Shift.....   | 141 |
| B.6.8 | Objective Lens Astigmatism ..... | 141 |
| B.7   | Nanobeam Diffraction .....       | 141 |
| B.8   | Finishing TEM Session.....       | 142 |

## LIST OF TABLES

|     |   |     |
|-----|---|-----|
| 1.1 | Values of Young's and shear moduli calculated by various groups with different methods. ....  | 13  |
| 2.1 | Characteristic ratio $P_2/P_1$ , $P_1/\Delta_{12}$ for Bessel function of orders from 0 to 50. ....                                       | 28  |
| 5.1 | Summary of physical properties of CNTs. ....  | 73  |
| 5.2 | NBED pattern calculations for SWNT (38, 21) ....  | 73  |
| 5.3 | Possible combinations from the NBED result of the chiral indices $(u, v)$ in SWNT (38, 21). ..  | 74  |
| 5.4 | Determination of the chiral index ratios $\frac{v}{u}$ using the interlayer line spacings $D_1$ and $D_2$ of each shell in the QWNT. .... | 78  |
| 5.5 | Possible values of $v/u$ of two shells in a QWNT (I) ....   | 79  |
| 5.6 | Possible values of $v/u$ of two shells in a QWNT (II) ....  | 80  |
| 6.1 | NBED pattern analysis of the twisted DWNT (56, 2)@(37, 18) with diameters of 4.467 nm and 3.805 nm. ....                                  | 101 |
| 6.2 | NBED pattern analysis of the twisted DWNT (5, 65)@(24, 44) with diameters of 4.467 nm and 3.805 nm. ....                                  | 101 |
| 6.3 | NBED pattern analysis of the twisted DWNT (49, 18)@(38, 16) with diameters of 4.705 nm and 3.500 nm. ....                                 | 104 |
| 6.4 | NBED pattern analysis of the twisted TWNT (7, 53)@(8, 42)@(11, 28) with diameters of 4.45 nm, 3.64nm and 2.70 nm ....                     | 104 |
| 6.5 | Summary of the calculated shear moduli and frictions in two DWNT devices. ....  | 109 |

## LIST OF FIGURES

|      |  |    |
|------|--|----|
| 1.1  | 3D Energy Dispersion Relation of a Graphene Sheet .....  | 3  |
| 1.2  | 1D Energy Dispersion Relation of a Graphene Sheet .....  | 4  |
| 1.3  | Formation of carbon nanotubes on a graphene plane .....  | 4  |
| 1.4  | Band Structure of Single-walled Carbon Nanotubes with Determined Chiralities .....   | 7  |
| 1.5  | Correlation between the band gap of carbon nanotubes and the radii .....   | 10 |
| 1.6  | Differences of band structure of a commensurate DWNT (5, 5)@(10, 10) induced<br>by symmetry and interlayer interaction .....                   | 11 |
| 2.1  | Atomically resolved STM image of an individual SWNT .....  | 16 |
| 2.2  | TEM images of CNTs .....   | 20 |
| 2.3  | Simulated high resolution image of a (4, 4) SWNT. ....   | 21 |
| 2.4  | Schematic of periodicities of a CNT in both the real and the reciprocal space .....  | 22 |
| 2.5  | Diffraction pattern simulation of an individual SWNT .....   | 27 |
| 2.6  | Intensity distribution on a principal line and fitted Bessel function .....  | 31 |
| 2.7  | Simulated diffraction patterns of SWNTs of different sizes.....  | 32 |
| 3.1  | Hypothesis for mechanisms of CNTs synthesis in CVD.....  | 36 |
| 3.2  | Schematic diagram of a CVD setup in its simplest form.....   | 37 |
| 3.3  | Different synthesized CNTs with different growth temperatures. ....  | 39 |
| 3.4  | Schematic illustration shows the use of different diameter iron nanocluster catalysts<br>for the controlled synthesis of carbon nanotubes..... | 40 |
| 3.5  | Different synthesized CNTs with different gas flow rate. ....  | 41 |
| 3.6  | High density of long and aligned CNTs grown on a quartz wafer. ....  | 43 |
| 3.7  | Synthesis of DWNTs with different sizes of FeSi <sub>2</sub> nanoparticles .....   | 44 |
| 3.8  | SEM image of a substrate with proper density of SWNTs. ....  | 45 |
| 3.9  | Synthesis of CNTs on pre-etched Si/SiO <sub>2</sub> substrates .....   | 46 |
| 3.10 | TEM images of a SWNT grown on a pre-etched substrate. ....   | 47 |
| 4.1  | Experiment geometry for applying strain and gate voltage with an AFM tip, and<br>measuring conductance with contacts. ....                     | 51 |
| 4.2  | Schematic illustration of the fabrication processes of suspended CNT NEMS. ....  | 52 |

|      |   |    |
|------|---|----|
| 4.3  | Schematic of the suspended CNT NEMS device ready for <i>in situ</i> TEM imaging.....  | 53 |
| 4.4  | Schematic of back etching processes of device fabrication. ....   | 55 |
| 4.5  | Schematic of the macroscopic electrodes deposited onto a wafer by photolithography. ....  | 55 |
| 4.6  | Schematic of the alignment of electrodes to the window on the back.....   | 56 |
| 4.7  | Comparison of a CNT connecting two electrodes before and after burn out. ....   | 56 |
| 4.8  | Schematic of EBL liftoff process using double-layer PMMA ....   | 57 |
| 4.9  | Comparison of two EBL processes with different sequences of fiducials and patterns.....   | 59 |
| 4.10 | Comparison of a schematic of EBL pattern and the actual result. ....  | 60 |
| 4.11 | A SEM image of a device after Si and Si <sub>3</sub> N <sub>4</sub> windows beneath the paddles were removed with FIB. ....         | 61 |
| 4.12 | SEM images of a sample after CNTs are suspended from the substrate. ....  | 62 |
| 4.13 | Schematic of the final structure of the NEMS device. ....   | 63 |
| 4.14 | A TEM image of the NEMS device.....   | 64 |
| 4.15 | Schematic of the TEM specimen holder for <i>in situ</i> NEMS experiment. ....   | 65 |
| 5.1  | Three dimensional schematic of a 4-probe CNT device ready for HRTEM imaging and NBED. ....  | 71 |
| 5.2  | Illustration of the diffraction analysis of a SWNT.....   | 74 |
| 5.3  | Comparison between the simulated diffraction pattern and the NBED result of SWNT (38, 21) . ....                                    | 75 |
| 5.4  | HRTEM image and NBED pattern of a QWNT.....   | 76 |
| 5.5  | NBED pattern of a QWNT with fitted hexagons. ....   | 77 |
| 5.6  | Comparison between the simulated diffraction pattern and the NBED result of the QWNT (61, 7)@(40, 28)@(35, 22)@(21, 21).....        | 81 |
| 5.7  | The source/drain current $I_{SD}$ versus voltage $V_{SD}$ for different SWNT devices. ....  | 83 |
| 5.8  | Low bias resistance $R = \frac{dV}{dI}$ near zero bias as a function of conducting length $L$ . ....                                | 84 |
| 5.9  | Schematic representation of the main phonon contributions to backscattering. ....   | 84 |
| 5.10 | Depiction of the energy dispersion of the metallic SWNTs in the first Brillouin zone and in the vicinity of the Fermi surface. .... | 86 |
| 5.11 | Depiction of the energy dispersion of the semiconducting SWNTs in the vicinity of the Fermi surface. ....                           | 87 |
| 5.12 | The dependence of the measured resistance $R$ on the band gap $E_g$ in the ballistic limit at room temperature $T = 300K$ . ....    | 88 |



|      |   |     |
|------|---|-----|
| 6.1  | Schematic and TEM images of a telescoping MWNT. ....  | 93  |
| 6.2  | SEM images of the twisted CNT device. ....  | 94  |
| 6.3  | Band gap change of SWNTs under uniaxial and torsional strains. Notice the linear variation of band gap with the strain and its dependence of the chiral indices. .... | 96  |
| 6.4  | Schematic of the lattice deformation of a twisted CNT. ....   | 97  |
| 6.5  | Schematic of the simulated diffraction pattern of a twisted SWNT (22,2). ....   | 99  |
| 6.6  | Schematic of the device which is ready for electrical actuation and <i>in situ</i> electron imaging and electron diffraction analysis. ....                           | 99  |
| 6.7  | Schematic of the device subject to the uniaxial strain. ....  | 100 |
| 6.8  | TEM images and electron diffraction patterns of the suspended DWNT (56, 2)@(37, 18). The diffraction patterns are false-colored and marked by arrows. ....            | 102 |
| 6.9  | TEM images and electron diffraction patterns of the suspended DWNT (65, 5)@(24, 44). The diffraction patterns are false-colored and marked by arrows. ....            | 103 |
| 6.10 | TEM images and NBED patterns of the suspended DWNT (49, 18)@(38, 16). The diffraction patterns are false-colored and marked by arrows. ....                           | 103 |
| 6.11 | Comparison between the NBED pattern of a TWNT before and after the twist. ....  | 105 |
| 6.12 | The inner shells' torsional responses to the twist of the outer shell of the four MWNT devices measured. ....   | 107 |
| 6.13 | The plot of the ratio of the twist angles in the outer and inner shells $\frac{\theta_o}{\theta_i}$ v.s. the corresponding interlayer spacing $\Delta d$ . ....       | 107 |
| 6.14 | Schematic illustration of the suspended CNT with a paddle attached device. ....   | 108 |
| 6.15 | The schematic device model and the voltage distribution in FE analysis. ....  | 109 |
| 6.16 | Simulated results of the interlayer energy DWNT (10, 10)@(5, 5) in two models. ....   | 111 |
| 6.17 | Simulated results of the interlayer energy DWNT (11, 10)@(6, 5) in two models. ....   | 111 |
| 6.18 | Characterization of DWNT (49, 18)@(38, 16) and TWNT (7, 53)@(8, 42)@(11, 28) transport properties under torsional strain. ....  | 113 |
| B.1  | Device Fabrication: Backside etching with photolithography ....   | 125 |
| B.2  | Device Fabrication: Additional Si <sub>3</sub> N <sub>4</sub> and SiO <sub>2</sub> films deposited with PECVD ....  | 125 |
| B.3  | The playground of the chip after the deposition of large electrodes under SEM ....  | 128 |

## LIST OF ABBREVIATIONS

|      |                                  |
|------|----------------------------------|
| AFM  | Atomic Force Microscope          |
| BHF  | Buffered Hydrofluoric Acid       |
| CPD  | Critical Point Drying            |
| CNT  | Carbon Nanotube                  |
| CVD  | Chemical Vapor Deposition        |
| DWNT | Double-Walled Carbon Nanotube    |
| DRIE | Deep Reactive Ion Etching        |
| EBL  | Electron Beam Lithography        |
| FE   | Finite Element                   |
| FIB  | Focused Ion Beam                 |
| FWNT | Few-Walled Carbon Nanotube       |
| MEMS | Micro-Electromechanical System   |
| MWNT | Multi-Walled Carbon Nanotube     |
| NBD  | Nano-Beam Diffraction            |
| NEMS | Nano-Electromechanical System    |
| PMMA | Polymethyl Methacrylate          |
| RIE  | Reactive Ion Etching             |
| SEM  | Scanning Electron Microscope     |
| STM  | Scanning Tunneling Microscope    |
| SWNT | Single-Walled Carbon Nanotube    |
| TEM  | Transmission Electron Microscope |
| TWNT | Triple-Walled Carbon Nanotube    |

# CHAPTER 1

## Introduction to Carbon Nanotubes

### 1.1 History

Carbon is one of the most recognized and widely used chemical elements in human history. As the sixth element in the periodic table, a free carbon atom has six electrons which occupy  $1s^2$ ,  $2s^2$  and  $2p^2$  atomic orbitals. Due to the small energy level difference between the  $2p$  and  $2s$  orbitals, the probabilities that four electrons fall into  $2s$ ,  $2p_x$ ,  $2p_y$  or  $2p_z$  orbitals could be even and such mixture of  $2s$  and  $2p$  orbitals is called hybridization. Carbon atom can hybridize in  $sp$ ,  $sp^2$  or  $sp^3$ , which can be found in acetylene, polyacetylene or methane, respectively. The property of hybridization distinguishes carbon from other chemical elements, even from group IV elements such as silicon and germanium, because of the absence of  $sp$  and  $sp^2$  hybridizations.

Hybridization is the reason that the physical properties of carbon vary significantly with different allotropic forms, such as graphite, diamond and amorphous carbon, which all have been well known even since antiquity. Although predicted in 1970, it is not until the late twentieth century that another allotrope of carbon was found by Kroto and Smalley as  $C_{60}$  [1]. Such a hollow sphere also known as buckyball, stimulated research in the related area. Iijima *et al.* [2, 3] first discovered carbon nanotubes in 1991. Shortly after, the variety of intriguing properties of carbon nanotubes attracted tremendous amount of research interest in fundamental science [4, 5, 6, 7, 8].

Since carbon atoms in carbon nanotubes are  $sp^2$  hybridized, carbon nanotubes can be considered as wrapped hexagonal carbon sheets, namely graphene, which have been well understood as the basic layer component of graphite. It is interesting that,  $sp^2$  hybridization not only forms a planar structure in two-dimensional graphene, but also in the zero-dimensional closed polyhedra of fullerene and in the one-dimensional cylinders of carbon nanotubes. After more than a decade of investigations on carbon nanotubes, in 2004 the first individual graphene plane was isolated by Andre Geim and Konstantin Novoselov [9]. The special physical properties, mostly due to the massless Dirac fermions, immediately led to an explosive interest in graphene [10, 11, 12].

In this context of dissertation, our research interest will mainly focus on carbon nanotubes. Because carbon nanotubes derive most of the physical properties from graphene, it is reasonable and useful to scrutinize its properties first.

## 1.2 From Graphene to Carbon Nanotube

Graphene is a one-atom-thick planar sheet of  $sp^2$ -bonded carbon atoms in a honeycomb crystal lattice. Bulk graphite is formed by stacking graphene layers over each other. The weak van der Waals interaction between layers makes it easy to slip one layer from another, therefore making the extraction of graphene from a graphite crystal through mechanical/chemical exfoliation possible.

The 2-D graphene lattice can be described by unit vectors  $\mathbf{a}_1$  and  $\mathbf{a}_2$ , which can be written as:

$$\mathbf{a}_1 = (a, 0), \quad (1.1)$$

$$\mathbf{a}_2 = \left( \frac{a}{2}, \frac{\sqrt{3}a}{2} \right), \quad (1.2)$$

where  $a$  is the lattice constant given by  $a = \sqrt{3}a_{c-c}$ , and  $a_{c-c}$  is the carbon-carbon bond length of 1.44 Å. Correspondingly, basic vectors of the reciprocal lattice  $\mathbf{b}_1$  and  $\mathbf{b}_2$  can be expressed as:

$$\mathbf{b}_1 = \left( \frac{2\pi}{a}, -\frac{2\pi}{\sqrt{3}a} \right), \quad (1.3)$$

$$\mathbf{b}_2 = \left( 0, \frac{4\pi}{2\sqrt{3}a} \right). \quad (1.4)$$

Due to the existence of one  $\pi$ -electron in each  $sp^2$  hybridized carbon atom, there are two  $\pi$ -energy bands called bonding and anti-bonding  $\pi$ -bands in the Brillouin zone of graphene [13, 14]. With the tight binding method, the approximate energy dispersion relation can be derived as:

$$E_{\text{graphene}}(k_x, k_y) = \pm t_0 \sqrt{1 + 4 \cos\left(\frac{\sqrt{3}k_x a}{2}\right) \cos\left(\frac{k_y a}{2}\right) + 4 \cos^2\left(\frac{k_y a}{2}\right)}, \quad (1.5)$$

where  $t_0$  is the nearest-neighbor overlap transfer integral in the tight binding calculation for  $\pi$  orbitals.

The dispersion relation is illustrated in Figure 1.1 and Figure 1.2. The upper and lower halves of the energy dispersion describe the  $\pi^*$ -energy anti-bonding band and  $\pi$ -energy bonding band, respectively, and only the lower  $\pi$  band is occupied by two electrons in one unit cell. Note that  $\pi$  and  $\pi^*$  bands are degenerate

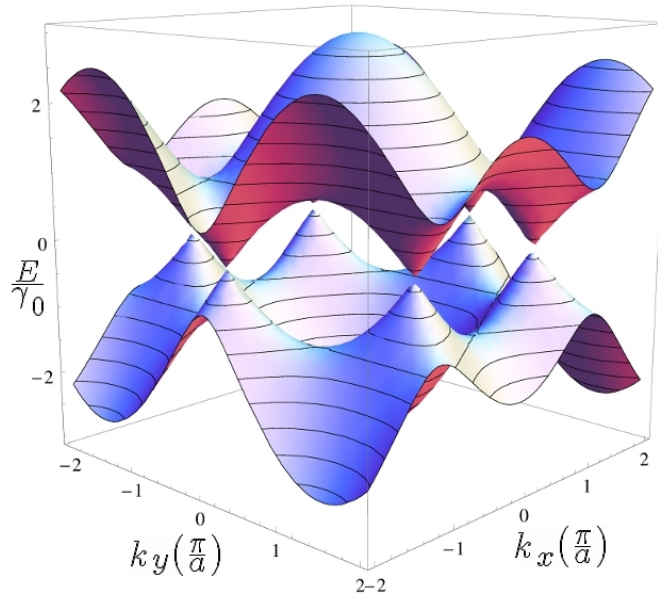


Figure 1.1: 3D energy dispersion relation of a graphene sheet with  $\pi$  orbital tight binding structure. The Fermi surface consists of six points at the corners of the first Brillouin zone.

at the  $K$  points through which the Fermi level passes, where the  $K$  points are the corners of the first Brillouin zone and can be described as  $\left(\pm \frac{4\pi}{3\sqrt{3}a}, 0\right)$  and  $\left(\pm \frac{2\pi}{3\sqrt{3}a}, \pm \frac{2\pi}{3a}\right)$ , implying that the density of states at the Fermi level is zero. As imposed by the symmetry, the band gaps of graphene at the  $K$  points are zero, which makes graphene a zero band gap semiconductor, or semi-metal. Also, in the vicinity of the  $K$  points, according to Equation (1.5), the energy dispersion becomes linear at low energies which leads to massless electrons.

### 1.3 Structure of Single-Walled Carbon Nanotubes

A single-walled carbon nanotube (SWNT) can be defined as a graphene sheet rolled into a seamless cylindrical shape with helical symmetry, and different ways to wrap up graphene sheets result in SWNTs with different structures. When several tubes with different diameters share the same axis, the structure is named a multi-walled carbon nanotube (MWNT). The smallest diameter of a carbon nanotube was discovered as 0.4 nm [15], while the length of a SWNT goes up to centimeters. This remarkable length-diameter ratio of  $10^7$  makes a carbon nanotube a perfect physics model of one-dimensional material.

The atomic structure of a SWNT is uniquely characterized by the chiral vector  $\mathbf{C}_h = u\mathbf{a}_1 + v\mathbf{a}_2 \equiv (u, v)$  that crystallographically connects the equivalent sites on a graphene sheet, where  $u$  and  $v$  are integers and

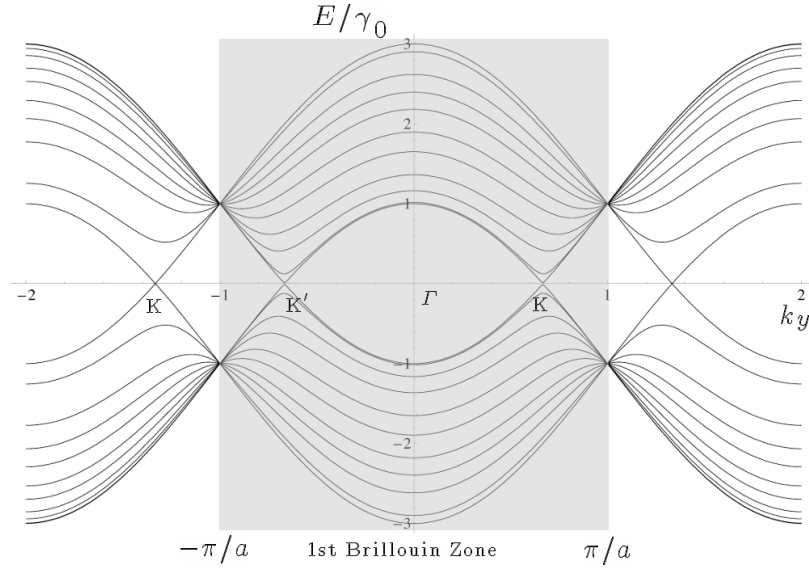


Figure 1.2: 1D energy dispersion relation of a graphene sheet. The energy dispersion along the high symmetry directions of the triangle  $\Gamma MK$ .

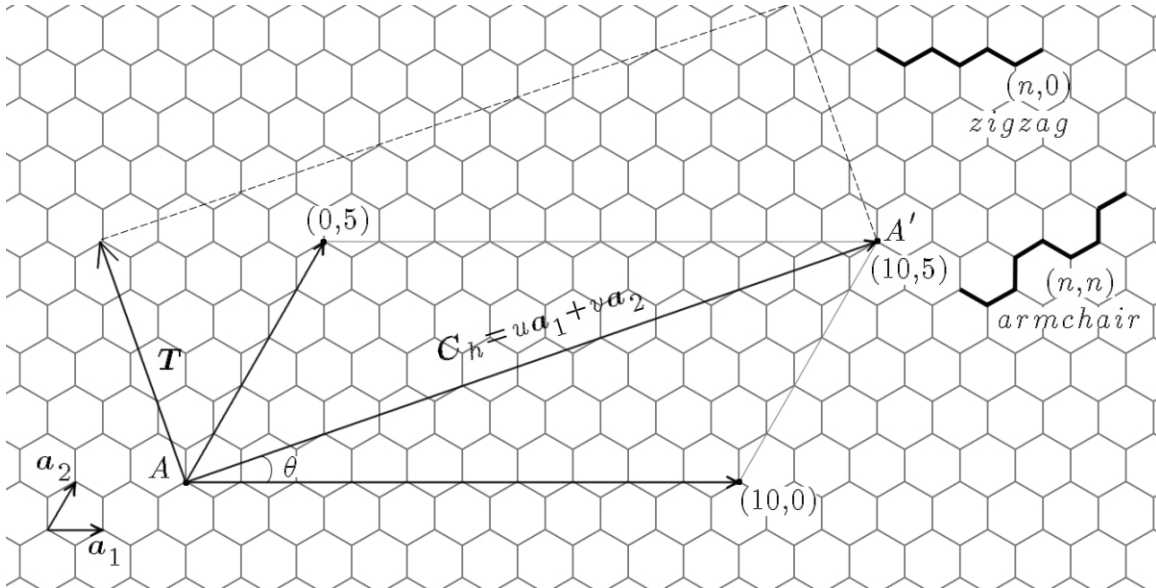


Figure 1.3: Formation of carbon nanotubes on a graphene plane. The chiral vector  $\mathbf{C}_h = u\mathbf{a}_1 + v\mathbf{a}_2$  of nanotube (10,5) is shown with the translational vector  $\mathbf{T}$ , where  $\mathbf{a}_1$  and  $\mathbf{a}_2$  are the basis vectors.

called chiral indices, as shown in Figure 1.3. Therefore, when rolling up a graphene sheet as a carbon nanotube, the perimeter is determined by the magnitude of the chiral vector, which is:

$$|\mathbf{C}_h| = a\sqrt{u^2 + v^2 + uv}, \quad (1.6)$$

while the diameter is:

$$d = \frac{|\mathbf{C}_h|}{\pi} = \frac{a\sqrt{u^2 + v^2 + uv}}{\pi}. \quad (1.7)$$

Once the chiral vector is determined, the translational vector  $\mathbf{T}$  can be obtained in the perpendicular direction to the chiral vector, and can also be defined as the unit vector of a one-dimensional carbon nanotube which is parallel to the nanotube axis.  $\mathbf{T}$  shown in the Figure 1.3 is defined as:

$$\mathbf{T} = m\mathbf{a}_1 + n\mathbf{a}_2, \quad (1.8)$$

where  $m$  and  $n$  are integers. Since  $\mathbf{C}_h \cdot \mathbf{T} = 0$ ,  $m$  and  $n$  can be calculated as:

$$m = -\frac{u + 2v}{M}, n = \frac{2u + v}{M} \quad (1.9)$$

where  $M$  is the greatest common divisor of  $u + 2v$  and  $2u + v$ . Hence, the length of the translational vector  $\mathbf{T}$ , *i.e.* the periodicity of nanotube, is:

$$|\mathbf{T}| = \frac{\sqrt{3}a\sqrt{u^2 + v^2 + uv}}{M} = \frac{\sqrt{3}|\mathbf{C}_h|}{M}. \quad (1.10)$$

On the other hand, since a unit cell is defined by the chiral vector  $\mathbf{C}_h$  and the translational vector  $\mathbf{T}$ , the number of carbon atoms  $N_{\text{atom}}$  in a unit cell can be shown as:

$$N_{\text{atom}} = |\mathbf{C}_h \times \mathbf{T}| = \frac{4(u^2 + v^2 + uv)}{M}. \quad (1.11)$$

The angle between the chiral vector  $\mathbf{C}_h$  and the unit vector  $\mathbf{a}_1$  is defined as the chiral angle  $\theta$ , as shown in Figure 1.3. The mathematical expression is given by:

$$\theta = \arccos \frac{\mathbf{C}_h \cdot \mathbf{a}_1}{|\mathbf{C}_h||\mathbf{a}_1|} = \frac{2u + v}{\sqrt{u^2 + v^2 + uv}}. \quad (1.12)$$

As the result of the helical symmetry of graphene sheet, the value of  $\theta$  is usually confined in the range  $0 \leq \theta \leq \frac{\pi}{6}$  when ignoring the handedness. In particular, if the chiral indices of certain carbon nanotubes

satisfy  $u = v$ , which implies  $\theta = \frac{\pi}{6}$ , such nanotubes are called armchair nanotubes; and if  $u > 0, v = 0$ , *i.e.*  $\theta = 0$ , the nanotubes are called zigzag nanotubes; while others are simply called helical/chiral nanotubes. The  $N$ -fold rotational symmetry of a nanotube  $(u, v)$  can be determined easily using the greatest common divisor of the chiral indices  $N = \text{gcd}(u, v)$ .

## 1.4 Energy Dispersion of Single-Walled Carbon Nanotubes

Due to the axial periodicity of a carbon nanotube, the unit cell is defined as the rectangle generated by the chiral vector  $\mathbf{C}_h$  and the translational vector  $\mathbf{T}$ . The number of primitive cells per unit cell  $N$  can be calculated as:

$$N = \frac{|\mathbf{C}_h \times \mathbf{T}|}{|\mathbf{a}_1 \cdot \mathbf{a}_2|} = \frac{2(u^2 + v^2 + uv)}{M}. \quad (1.13)$$

Because there are  $2N$  carbon atoms in each unit cell, the energy bands are consist of  $N$  pairs of  $\pi$  bonding bands and  $\pi^*$  anti-bonding bands.

The reciprocal lattice vectors of a carbon nanotube,  $\mathbf{K}_1$  in the circumferential direction and  $\mathbf{K}_2$  in the axial direction can be obtained from  $\mathbf{R}_i \cdot \mathbf{K}_j = 2\pi\delta_{ij}$ , where  $\mathbf{R}_i$  is the lattice vectors in the real space, *i.e.*  $\mathbf{C}_h$  and  $\mathbf{T}$ . Unlike the case of a graphene sheet, the periodic boundary condition along the circumferential direction quantizes the corresponding wave vector in the  $\mathbf{C}_h$  direction,

$$\Psi_{\mathbf{k}}(\mathbf{r} + \mathbf{C}_h) = e^{i\mathbf{k} \cdot \mathbf{C}_h} \Psi_{\mathbf{k}}(\mathbf{r}) = \Psi_{\mathbf{k}}(\mathbf{r}), \quad (1.14)$$

whereas the wave vector in  $\mathbf{T}$  remains continuous, assuming the length of carbon nanotube is infinite (which is a valid approximation due to the large length/diameter ratio). Therefore, the one-dimensional energy dispersion of a carbon nanotube is  $N$  slices of that of graphene. According to Equation (1.5), the energy dispersion of a SWNT is written as:

$$E_{\mu}(k) = E_{\text{graphene}} \left( k \frac{\mathbf{K}_2}{|\mathbf{K}_2|} + \mu \mathbf{K}_1 \right), \mu = 0, 1, \dots, N-1; -\frac{\pi}{|\mathbf{T}|} < k < \frac{\pi}{|\mathbf{T}|}. \quad (1.15)$$

With Equation (1.15) the detailed band structure of a carbon nanotube  $(u, v)$  can be calculated, as shown in Figure 1.4. Note that, for particular SWNTs  $(u, v)$  satisfying that  $\text{mod}(u - v/3) = 0$ , one of the dispersion curves will just pass through a  $K$  point in the 2D Brillouin zone, where  $\pi$  and  $\pi^*$  energy bands are degenerate by symmetry, therefore the band gap is zero and such SWNTs behave like a metal; while others, where  $\text{mod}(u - v/3) = 1, 2$ , are expected to show semiconducting behavior due to the finite band gaps.



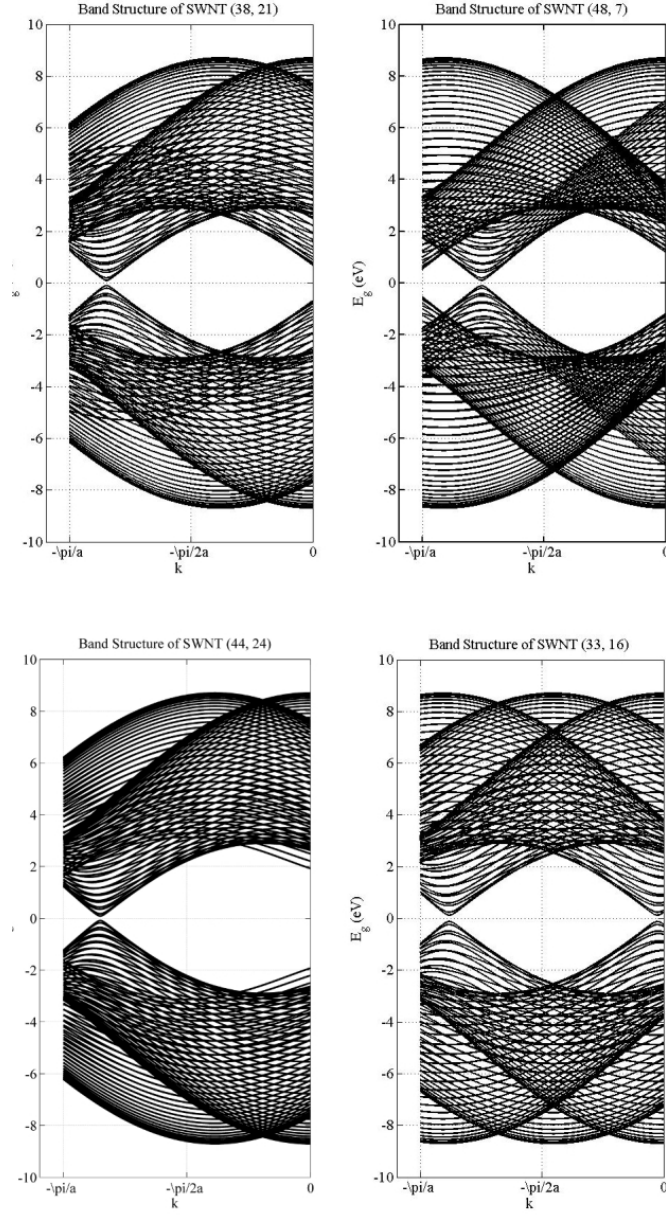


Figure 1.4: Band structure of semiconducting SWNTs. One dimensional energy dispersion relations of SWNTs (38, 21), (48, 7), (44, 24) and (33, 16) are calculated using Equation (1.15). Note that for legibility, not every band is drawn here.

Whether a carbon nanotube is metallic or semiconducting can be determined as followed: Because of the Bloch theorem, the periodic boundary conditions in the circumferential direction of a carbon nanotube impose restrictions that,

$$\Phi_k(\mathbf{r} + \mathbf{C}_h) = e^{i\mathbf{k} \cdot \mathbf{C}_h} \Phi_k(\mathbf{r}) = \Phi_k(\mathbf{r}). \quad (1.16)$$

For any vectors  $\mathbf{k}$  in the vicinity of the Fermi surface, let  $\mathbf{K}_F$  be the Fermi vector, where  $\mathbf{K}_F = \frac{1}{3}(\mathbf{b}_1 - \mathbf{b}_2) = \left(0, \frac{4\pi}{3}\right)$ , which yields  $\mathbf{k} = \mathbf{K}_F + \delta\mathbf{k} = \left(\delta k_x, \frac{4\pi}{3}k_y\right)$ , when  $\mathbf{k}$  is small.

When the chiral indices satisfy  $u - v = 3l$ , where  $l$  is an integer, we have  $e^{i\mathbf{K}_F \cdot \mathbf{C}_h} = 1$ , *i.e.*  $\delta\mathbf{k} \cdot \mathbf{C}_h = 2\pi q$ , with  $q$  being an integer, which restricts the allowed  $\mathbf{k}$  values by the index  $q$ . Therefore the graphene energy dispersion relationship,

$$E(k_x, k_y) = \pm t_0 \sqrt{1 + 4 \cos\left(\frac{\sqrt{3}k_x a}{2}\right) \cos\left(\frac{k_y a}{2}\right) + 4 \cos^2\left(\frac{k_y a}{2}\right)} \quad (1.17)$$

can now be written as

$$E(\mathbf{k} = \mathbf{K}_F + \delta\mathbf{k}) = \pm t_0 \frac{\sqrt{3}}{2} |\delta\mathbf{k}|. \quad (1.18)$$

This linear energy dispersion around the Fermi level implies the existence of metallic state with zero band gap when  $q = 0$  with the Fermi velocity of  $v_F = \frac{\sqrt{3}at_0}{2\hbar}$ .

On the other hand, when the condition of  $u - v = 3l$  is not satisfied, *i.e.*  $u - v = 3l \pm 1$ , we have

$$\delta\mathbf{k} = \frac{2\pi}{|\mathbf{C}_h|} \left(q \pm \frac{1}{3}\right) \kappa_\perp + k_\parallel \kappa_\parallel, \quad (1.19)$$

where  $\kappa_\perp$  and  $\kappa_\parallel$  are the basic vectors along the circumferential and the transnational directions. With similar calculations, the energy dispersion in the vicinity of the Fermi surface is,

$$E_q^\pm(\delta\mathbf{k}) \approx \pm \frac{\sqrt{3}a}{2} t_0 \sqrt{\left(\frac{2\pi}{|\mathbf{C}_h|}\right)^2 \left(q \pm \frac{1}{3}\right)^2 + k_\parallel^2}. \quad (1.20)$$

Now at the Fermi surface, *i.e.*  $k_\parallel = 0$ , the energy difference between the two nearest subbands, which are both defined by  $q = 0$ , can be expressed as,

$$E_{q=0}^+(k_\parallel = 0) - E_{q=0}^-(k_\parallel = 0) = \frac{2\pi at_0}{\sqrt{3}|\mathbf{C}_h|}. \quad (1.21)$$

In other words, the energy band gap in a semiconducting carbon nanotube in the zone-folding approximation can be expressed as

$$E_g^0 = \frac{at_0}{r}, \quad (1.22)$$

where  $r$  is the carbon nanotube radius.

As expected, a very large diameter carbon nanotube can be analyzed as a zero-gap semiconductor similar to a graphene sheet. This inverse linear energy dispersion at the Fermi surface was first discovered by White and Mintmire [16]. However, such model is in the first order approximation and unable to describe the actual energy dispersion for carbon nanotubes dealt as planar sheets while ignoring the curvature effects. Since when wrapping a graphene sheet to a carbon nanotube, the topology will change both the directions and the bond lengths of the basic vectors  $\mathbf{a}_1$  and  $\mathbf{a}_2$ . Furthermore, in the tight binding analysis of graphene, the behaviors of electrons are described using the independent  $\pi$  states. Given that the planar symmetry is broken in a carbon nanotube, the  $\pi$  states are mixed with  $\sigma$  states and the orbitals exhibit both  $sp^2$  and  $sp^3$  characters. As consequences, besides the radius, the band structure of a carbon nanotube also depends on the specific chirality,

$$E_g^1 = \frac{3t_0a_{c-c}^2}{16r^2} \cos 3\theta, \quad (1.23)$$

where  $\theta$  is the chiral angle. The secondary band gap scaled by  $\frac{1}{r^2}$  will become dominant for carbon nanotubes with small diameters, whereas negligible for large ones and particularly armchair carbon nanotubes where the chiral angle is  $30^\circ$ . In this study, most synthesized SWNTs and MWNTs are of diameters around 5 nm, therefore the secondary band gaps in the order of 1 meV are negligible compared with the zone-approximation induced band gaps, which are normally 0.1 - 0.2 eV [17].

## 1.5 Multi-Walled Carbon Nanotubes

A MWNT consists of a nested concentric array of SWNT constituents, separated from one another by approximately 3.4 Å, which is also the interlayer spacing of graphene sheets in graphite. Similar to a SWNT, the individual layers of a MWNT can be entirely defined by chiral indices  $(u, v)$ , and the MWNT is usually represented as  $(u_1, v_1)@ (u_2, v_2)@ \dots @ (u_i, v_i)@ \dots$ , where  $u_i$  and  $v_i$  are the chiral indices of the  $i$ -th shell. MWNTs can be further categorized into double-walled carbon nanotubes (DWNTs), triple-walled carbon nanotubes (TWNTs) and few-walled carbon nanotubes (FWNTs) where the number of shells varies from 3 to 5. The van der Waals interaction between the adjacent tubes is weak, therefore the interlayer spacing is

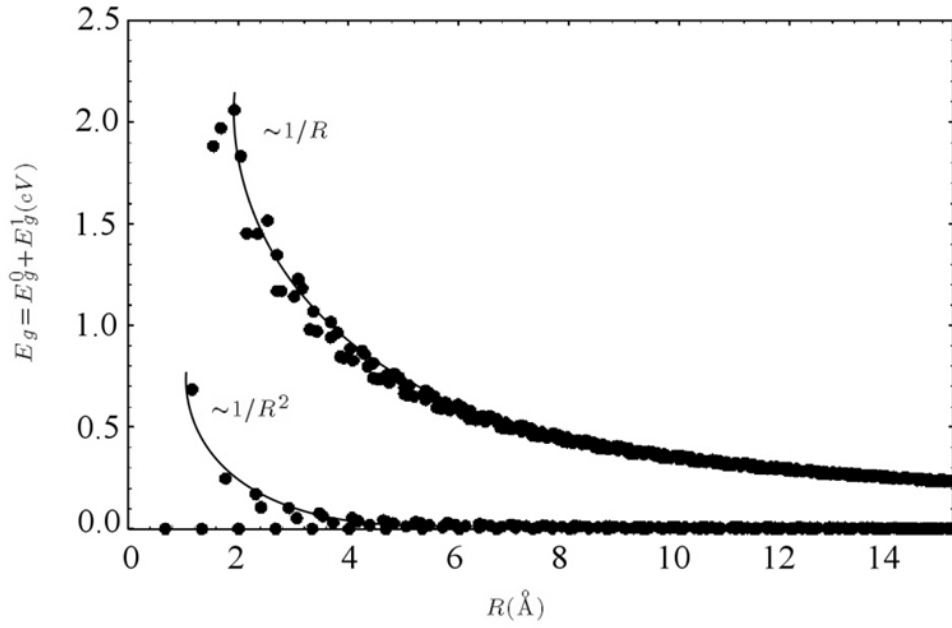


Figure 1.5: Correlation between the band gap of carbon nanotubes and the radii. The band gaps of semi-conducting (top) and metallic (bottom) nanotubes as a function of tube radius. The solid lines are guide to the eye showing that the primary zone-approximation band gap  $E_g^0$  scales a  $1/r$ , and the curvature induced hybridization secondary band gap  $E_g^1$  scales as  $1/r^2$ . Notice  $E_g^1$  is significant only for small metallic tubes and becomes zero for armchair  $(n, n)$  tube.

dominated by the chiral indices  $(u, v)$  of the constituent tubes, and each spacing can be accurately calculated once the structure of a MWNT is known.

Due to the complexity of a multi-walled system and interwall interactions, the band structure of a MWNT cannot be simply treated as the superposition of each individual SWNTs, the symmetry or the commensuration, however, plays a significant role in determining the band structure, as illustrated in Figure 1.6. A MWNT is commensurate if the ratio of the translational vectors  $|\mathbf{T}|$  of two consecutive layers is a rational number, *e.g.* a DWNT  $(5, 5)@(10, 10)$ ; otherwise incommensurate, *e.g.* a DWNT  $(5, 5)@(9, 9)$ . The high symmetry in a commensurate MWNT suggests a periodic system with significant interlayer coupling. Figure 1.6 illustrates the differences in a commensurate DWNT  $(5, 5)@(10, 10)$  induced by symmetry and interlayer interactions. The coupling strength between the nearest-neighboring carbon atoms in incommensurate layers is not translationally invariant along the axial direction, therefore the periodicity is lost and the interlayer coupling is much weaker than in a commensurate case, and in this case the band structure of a MWNT can be approximated as the composition of each constituent SWNTs.

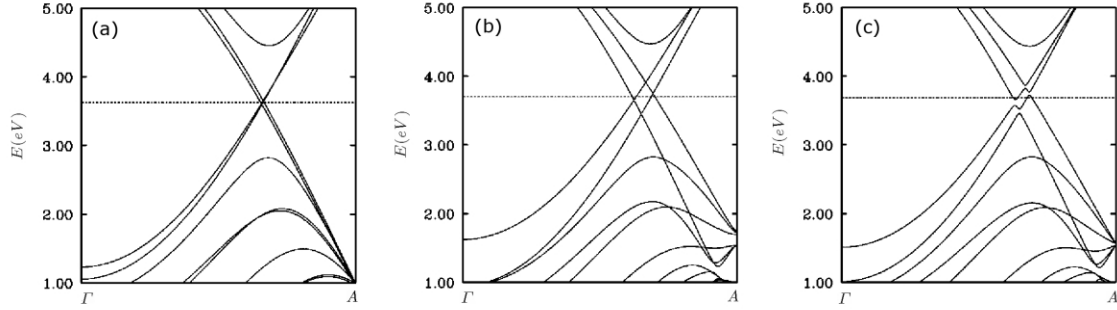


Figure 1.6: Differences of band structure of a commensurate DWNT  $(5, 5)@(10, 10)$  induced by symmetry and interlayer interaction. (a) shows the simple superposition of the band structures of two armchair SWNTs  $(5, 5)$  and  $(10, 10)$ . By introducing interlayer interaction, the band structure shifts a little in (b) while the DWNT remains metallic. However, if the symmetry of such coaxial system is broke by changing the relative angular position between outer and inner shells, a pseudo-gap open as shown in (c).

As a result of the low degree translational symmetry in an incommensurate MWNT, the unit cell is usually very large, which limits the application of the first-principles calculations to commensurate MWNTs with relatively simple structures. Generally, empirical potentials such as the Lennard-Jones and the Brenner-Tersoff potentials are applied to compute the interlayer interaction and the intralayer interaction, respectively. Molecular dynamics calculations have been performed to calculate the interaction potentials, the total energies and the stable state. It has been predicted [18] in theory that the total energy of a MWNT does not depend on the chirality, and the synthesis results of DWNTs with a wide range of chiral angles from  $0^\circ$  to  $60^\circ$  [19, 20] support the theoretical prediction. However, the potential does depend on the relative angular displacement

between the neighboring shells due to the change of symmetry, as shown in Figure 1.6. The dependence of the ground state energy of a DWNT has been formulated with respect to the interlayer spacing and the chiral angle difference [21], and the dependence on chiral angles turns out to be weak.

## 1.6 Mechanical Properties of Carbon Nanotubes

Since the discovery of carbon nanotubes, much attention has been paid to the mechanical properties, especially the elastic response to stress. Using molecular dynamics simulation with Tersoff-Brenner potential for the carbon-carbon interaction, Robertson *et al.* [22] first calculated the Young's modulus of nanotubes as smaller than that of graphene. Lu [23] calculated the Young's modulus for both SWNTs and MWNTs, and claimed that the values are around 1.0 TPa with an empirical force-constant model, which are insensitive to the chirality, the tube size, and the number of walls, and comparable to that of graphene. These results were confirmed in subsequent studies with other approaches including the tight-binding simulation and density-functional calculation [24, 25], the Born's perturbation technique within a lattice-dynamical model [26], as well as a modified Morse potential[27] and MM3 potential [28] .

With the Tersoff-Brenner potential, Yakobson *et al.* [29] and Kudin *et al.* [30] predicted the Young's modulus of 5.5 and 3.86 TPa using continuum elasticity theory. However these values were derived basing on an assumption that the individual wall thickness is of the size of molecular orbital radius. If the inter-wall van der Waals distance is used instead, the Young's modulus is about 1 TPa, which then becomes consistent with other calculations. Table 1.1 summarizes the elastic moduli calculated using various methods. With few exceptions the generally agreed value for the Young's modulus is around 1 TPa.

Compared to the numerous studies on SWNTs, only a few predictions are available for MWNTs due to the complexity of structures. Lu [23] first calculated the Young's and shear moduli of MWNTs as 1.1 and 0.5 TPa using a force-constant model, based on the assumption that all the walls are uniformly loaded. It was also shown that the elastic moduli vary little with the number of walls. Li and Chou [31] used molecular structural mechanics method to obtain similar values. It is generally agreed that the weak inter-wall van de Waals interaction is not sufficient to transfer the mechanical loading from the outer walls to the inner walls. In another analysis of elastic moduli of MWNTs by Shen and Li [32], it was shown that the average Young's and shear moduli are 1.2 and 0.3 TPa, respectively. For torsional strain it was also reported that a critical torsional angle exist beyond which the stiffness of a CNT is significantly reduced because of the torsional buckling [33].

Table 1.1: Values of Young's and shear moduli of carbon nanotubes calculated by various groups with different methods. Young's moduli are on the order of 1 TPa. In Yakobson *et al.*, if the interlayer spacing of 3.4 Å, rather than  $\pi$ -bond length 0.66 Å, is used for van der Waals energy calculation, one obtains the Young's modulus of 1.07 TPa, which is consistent with other calculations.

| Author                            | Year | Young's Modulus (TPa) | Shear Modulus (TPa) | Method             |
|-----------------------------------|------|-----------------------|---------------------|--------------------|
| Robertson <i>et al.</i> [22]      | 1992 | 1.06                  | 0.45                | Tersoff-Brenner    |
| Yakobson <i>et al.</i> [29]       | 1995 | 5.5                   |                     | Tersoff-Brenner    |
| Cornwell and Wille [34]           | 1997 | 1                     |                     | Tersoff-Brenner    |
| Lu [23]                           | 1997 | 0.97                  |                     | Force-constant     |
| Hernandez <i>et al.</i> [24]      | 1998 | 1.24                  |                     | Density Function   |
| Krishnan <i>et al.</i> [35]       | 1998 | 1.3                   | 0.41                | Thermal Vibration  |
| Sanchez-Portal <i>et al.</i> [25] | 1998 | 1.05                  |                     | Density Function   |
| Popov <i>et al.</i> [26]          | 1999 | 1.00                  |                     | Lattice Dynamics   |
| Ozaki <i>et al.</i> [36]          | 2000 | 0.98                  |                     | O(n) Tight binding |
| Van Lier <i>et al.</i> [37]       | 2000 | 1.09                  |                     | Hartree-Fock       |
| Belyschko <i>et al.</i> [27]      | 2002 | 0.94                  | 0.44                | Modified Morse     |
| Li and Chou [31]                  | 2003 | 1.06                  |                     | Energy Approach    |
| Pullen <i>et al.</i> [38]         | 2004 | 1.1                   |                     | GGA                |
| Gupta <i>et al.</i> [39]          | 2005 | 1.2                   | 0.35                | Tersoff-Brenner    |

## BIBLIOGRAPHY

- [1] H. W. Kroto, J. R. Heath, S. C. O'Brien, R. F. Curl, and R. E. Smalley, "C 60: buckminsterfullerene," *Nature*, vol. 318, no. 6042, pp. 162–163, 1985.
- [2] S. Iijima *et al.*, "Helical microtubules of graphitic carbon," *Nature*, vol. 354, no. 6348, pp. 56–58, 1991.
- [3] S. Iijima and T. Ichihashi, "Single-shell carbon nanotubes of 1-nm diameter," *Nature*, vol. 363, no. 6430, pp. 603–605, 1993.
- [4] S. J. Tans, A. R. Verschueren, and C. Dekker, "Room-temperature transistor based on a single carbon nanotube," *Nature*, vol. 393, no. 6680, pp. 49–52, 1998.
- [5] W. A. De Heer, A. Chatelain, and D. Ugarte, "A carbon nanotube field-emission electron source," *Science*, vol. 270, no. 5239, pp. 1179–1180, 1995.
- [6] A. Javey, J. Guo, Q. Wang, M. Lundstrom, and H. Dai, "Ballistic carbon nanotube field-effect transistors," *Nature*, vol. 424, no. 6949, pp. 654–657, 2003.
- [7] S. Frank, P. Poncharal, Z. Wang, and W. A. de Heer, "Carbon nanotube quantum resistors," *Science*, vol. 280, no. 5370, pp. 1744–1746, 1998.
- [8] R. A. Martel, T. Schmidt, H. Shea, T. Hertel, and P. Avouris, "Single-and multi-wall carbon nanotube field-effect transistors," *Applied Physics Letters*, vol. 73, p. 2447, 1998.
- [9] K. Novoselov, A. K. Geim, S. Morozov, D. Jiang, Y. Zhang, S. Dubonos, I. Grigorieva, and A. Firsov, "Electric field effect in atomically thin carbon films," *Science*, vol. 306, no. 5696, pp. 666–669, 2004.
- [10] K. Novoselov, A. K. Geim, S. Morozov, D. Jiang, M. K. I. Grigorieva, S. Dubonos, and A. Firsov, "Two-dimensional gas of massless dirac fermions in graphene," *Nature*, vol. 438, no. 7065, pp. 197–200, 2005.
- [11] Y. Zhang, Y.-W. Tan, H. L. Stormer, and P. Kim, "Experimental observation of the quantum hall effect and berry's phase in graphene," *Nature*, vol. 438, no. 7065, pp. 201–204, 2005.
- [12] A. C. Neto, F. Guinea, N. Peres, K. Novoselov, and A. Geim, "The electronic properties of graphene," *Reviews of Modern Physics*, vol. 81, no. 1, p. 109, 2009.
- [13] P. Wallace, "The band theory of graphite," *Physical Review*, vol. 71, no. 9, p. 622, 1947.
- [14] M. Anantram and F. Leonard, "Physics of carbon nanotube electronic devices," *Reports on Progress in Physics*, vol. 69, no. 3, p. 507, 2006.
- [15] L.-C. Qin, X. Zhao, K. Hirahara, Y. Miyamoto, Y. Ando, and S. Iijima, "Materials science: The smallest carbon nanotube," *Nature*, vol. 408, no. 6808, pp. 50–50, 2000.
- [16] J. Mintmire and C. White, "Universal density of states for carbon nanotubes," *Physical Review Letters*, vol. 81, no. 12, pp. 2506–2509, 1998.
- [17] J.-C. Charlier, X. Blase, and S. Roche, "Electronic and transport properties of nanotubes," *Reviews of Modern Physics*, vol. 79, no. 2, p. 677, 2007.
- [18] A. N. Kolmogorov and V. H. Crespi, "Smoothest bearings: interlayer sliding in multiwalled carbon nanotubes," *Physical Review Letters*, vol. 85, no. 22, pp. 4727–4730, 2000.
- [19] M. Kociak, K. Hirahara, K. Suenaga, and S. Iijima, "How accurate can the determination of chiral indices of carbon nanotubes be?," *The European Physical Journal B-Condensed Matter and Complex Systems*, vol. 32, no. 4, pp. 457–469, 2003.



- [20] A. Hashimoto, K. Suenaga, K. Urita, T. Shimada, T. Sugai, S. Bandow, H. Shinohara, and S. Iijima, "Atomic correlation between adjacent graphene layers in double-wall carbon nanotubes," *Physical Review Letters*, vol. 94, no. 4, p. 045504, 2005.
- [21] L. Bellarosa, E. Bakalis, M. Melle-Franco, and F. Zerbetto, "Interactions in concentric carbon nanotubes: The radius vs the chirality angle contributions," *Nano Letters*, vol. 6, no. 9, pp. 1950–1954, 2006.
- [22] D. Robertson, D. Brenner, and J. Mintmire, "Energetics of nanoscale graphitic tubules," *Physical Review B*, vol. 45, no. 21, p. 12592, 1992.
- [23] J. P. Lu, "Elastic properties of carbon nanotubes and nanoropes," *Physical Review Letters*, vol. 79, no. 7, pp. 1297–1300, 1997.
- [24] E. Hernandez, C. Goze, P. Bernier, and A. Rubio, "Elastic properties of c and b- {x} c- {y} n- {z} composite nanotubes," *Physical Review Letters*, vol. 80, no. 20, pp. 4502–4505, 1998.
- [25] D. Sánchez-Portal, E. Artacho, J. M. Soler, A. Rubio, and P. Ordejón, "Ab initio structural, elastic, and vibrational properties of carbon nanotubes," *Physical Review B*, vol. 59, no. 19, p. 12678, 1999.
- [26] V. Popov, V. Van Doren, and M. Balkanski, "Elastic properties of single-walled carbon nanotubes," *Physical Review B*, vol. 61, no. 4, p. 3078, 2000.
- [27] T. Belytschko, S. Xiao, G. Schatz, and R. Ruoff, "Atomistic simulations of nanotube fracture," *Physical Review B*, vol. 65, no. 23, p. 235430, 2002.
- [28] A. Sears and R. Batra, "Macroscopic properties of carbon nanotubes from molecular-mechanics simulations," *Physical Review B*, vol. 69, no. 23, p. 235406, 2004.
- [29] B. I. Yakobson, C. Brabec, and J. Bernholc, "Nanomechanics of carbon tubes: instabilities beyond linear response," *Physical Review Letters*, vol. 76, no. 14, pp. 2511–2514, 1996.
- [30] K. N. Kudin, G. E. Scuseria, and B. I. Yakobson, "C- {2} f, bn, and c nanoshell elasticity from ab initio computations," *Physical Review B*, vol. 64, no. 23, p. 235406, 2001.
- [31] C. Li and T.-W. Chou, "Elastic moduli of multi-walled carbon nanotubes and the effect of van der waals forces," *Composites Science and Technology*, vol. 63, no. 11, pp. 1517–1524, 2003.
- [32] L. Shen and J. Li, "Transversely isotropic elastic properties of multiwalled carbon nanotubes," *Physical Review B*, vol. 71, no. 3, p. 035412, 2005.
- [33] B.-W. Jeong, J.-K. Lim, and S. B. Sinnott, "Elastic torsional responses of carbon nanotube systems," *Journal of Applied Physics*, vol. 101, no. 8, pp. 084309–084309, 2007.
- [34] C. Cornwell and L. Wille, "Elastic properties of single-walled carbon nanotubes in compression," *Solid State Communications*, vol. 101, no. 8, pp. 555–558, 1997.
- [35] A. Krishnan, E. Dujardin, T. Ebbesen, P. Yianilos, and M. Treacy, "Youngs modulus of single-walled nanotubes," *Physical Review B*, vol. 58, no. 20, p. 14013, 1998.
- [36] T. Ozaki, Y. Iwasa, and T. Mitani, "Stiffness of single-walled carbon nanotubes under large strain," *Physical Review Letters*, vol. 84, no. 8, pp. 1712–1715, 2000.
- [37] G. Van Lier, C. Van Alsenoy, V. Van Doren, and P. Geerlings, "Ab initio study of the elastic properties of single-walled carbon nanotubes and graphene," *Chemical Physics Letters*, vol. 326, no. 1, pp. 181–185, 2000.
- [38] A. Pullen, G. Zhao, D. Bagayoko, and L. Yang, "Structural, elastic, and electronic properties of deformed carbon nanotubes under uniaxial strain," *Physical Review B*, vol. 71, no. 20, p. 205410, 2005.
- [39] S. Gupta, K. Dharamvir, and V. Jindal, "Elastic moduli of single-walled carbon nanotubes and their ropes," *Physical Review B*, vol. 72, no. 16, p. 165428, 2005.

## CHAPTER 2

### Characterization of Carbon Nanotubes

Understanding the atomic structure of carbon nanotubes (CNTs) is essential for further investigation of the physical properties. Various techniques have been applied to characterize the structure, *i.e.* the chiral indices, of CNTs. For example, transmission electron microscopy (TEM), scanning tunneling microscopy (STM), scanning electron microscopy (SEM), atomic force microscope (AFM), X-ray diffraction (XRD), Raman spectroscopy, optical absorption spectroscopy, and nuclear magnetic resonance (NMR) have all been used for the characterization with emphasis on different requirements. Among those techniques, it has been a consensus that TEM is the most accurate and powerful one for characterizing CNT structure. Meanwhile, other techniques are also widely used despite their intrinsic limitations.

#### 2.1 Scanning Tunneling Microscopy and Other Techniques

A scanning tunneling microscope (STM) is an instrument based on the concept of quantum tunneling, which provides a high resolution up to 1 Å. When the metal probe of a STM is brought to the vicinity of sample surface, a bias voltage is applied between the probe and the surface which induces a tunneling current. The magnitude of this current depends on the geometry of the probe as well as local density of states (DoS) of the surface. Therefore, through monitoring the tunneling current, the DoS can be derived and the surface morphology is obtained. Both the atomic structure and the electronic properties of SWNTs have been experimentally measured using STM [1, 2, 3], as shown in Figure 2.1.

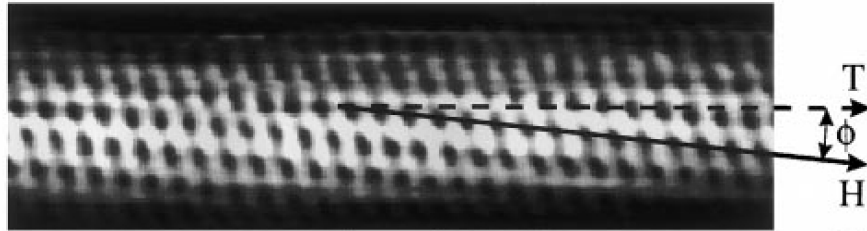


Figure 2.1: Atomically resolved STM image of an individual SWNT.  $\mathbf{T}$ ,  $\mathbf{H}$ , and  $\Psi$  are translational vector, zigzag direction and chiral angle, respectively. The lattice of black dots represents the centers of the hexagons [1].

Despite the high resolution of a STM, the structural deformation [4, 5] caused by the interaction between a CNT and the substrate induces considerable errors in STM measurement. Besides, the interlayer interaction shadows most information of the inner tubes in a MWNT. Thus, STM technique is unable to detect the complete atomic structure of a MWNT [6]. Giusca *et al.* [7] demonstrated that the chirality of the inner shell in a DWNT can be obtained from the STM measurement combined with calculated local DoS. However, the method works only in certain combinations of inner and outer shells and thus can not be universally applied to all MWNTs.

As a successor of STM, an atomic force microscopy (AFM) shares the similar mechanism except using a cantilever with a sharp tip as the probe, which actually in contact with the surface and accurately manipulated with piezoelectric element [8]. Although the lateral resolution is in the order of fraction of nanometer, an AFM only allows one to observe the diameter of a CNT instead of the detailed chiral structure.

Raman spectroscopy is another widely used technique for the study of vibrational, rotational, and other low frequency modes in materials. The diameter dependence of vibrational mode frequencies and the electronic structure of CNTs can be studied by Raman spectroscopy. The energy of interband transition can be obtained from resonance Raman scattering (RRS). A plot of transition energies of all chiral structures calculated from tight-binding model should be compared with those obtained from RRS experiments. With the tube diameter, the chiral indices can be determined by a match between theoretical and measured transition energies[9, 10]. However, the signals become very weak and are broadened for SWNT with large diameter and MWNTs. This is because that the curvature of CNT has less influences and the Raman spectra resemble to that of graphene when the diameter is large. Only the diameter information can be obtained using these two techniques, which is usually not enough to identify the chirality of CNTs [11, 12].

SEM images a sample by scanning the surface with a focused beam of electrons and detecting the secondary electrons to obtain the information of surface topography. In the applications to CNTs, SEM is usually used to determine the macroscopic shapes. Although the resolution of SEM is in the order of 2 nm, the accumulation of electrons on the nonconductive substrate causes image artifacts during scanning and imposes difficulties for accurate imaging.

## **2.2 Transmission Electron Microscopy and Nano-Beam Electron Diffraction**

Transmission electron microscopy (TEM) is a microscopy technique whereby a beam of electrons is passing through an ultra thin specimen. Due to the interaction with the specimen atoms, electrons are scattered and form a magnified image on a fluorescent screen or a CCD camera. Thanks to the small de Broglie wavelength of electrons, especially when electrons are accelerated in a strong electric field, a TEM is capable of imaging

at a prominent higher resolution, theoretically smaller than 1 Å, than previous techniques. It is then possible to characterize material structures at the atomic level. However, the imperfection of the magnetic lenses, which are designed to focus fast electrons in desired direction, restricts the highest resolution to about 1 Å [13]. On the other hand, CNTs, especially SWNTs, are quite vulnerable to high energy electrons. As shown by Smith *et al.* [14] that, the threshold voltage of knock-on damage on a SWNT is around 86 keV. Thus in order to preserve CNTs from incomplete structures during the imaging, the energy of electrons is usually limited to 100 keV.

### 2.2.1 Mechanism of Transmission Electron Microscopy

A TEM [15, 16] produces an image based on the following two-step Abbe principle:

- The incident electrons are scattered by the specimen and form a diffraction pattern on the back focal plane of the objective lens;
- The scattered electrons are recombined to form an image on the image plane.

Two imaging mechanisms are usually used: amplitude contrast and phase contrast [17]. In the amplitude contrast mode, the image contrast is the result from the electrons scattered in different angles within a specimen. The areas of the specimen with higher mass or larger Coulomb potential will scatter more electrons toward large angles. If a small aperture is used, most electrons which are scattered in large angles can be excluded except the selected beam inside the aperture. As a result, the areas corresponding to the higher mass or strong atomic potential positions within the specimen will turn dark in the image. On the other hand, image contrast in the phase contrast mode comes from the phase difference of electrons caused by interactions between electrons and the Coulomb potential of the specimen. A large objective aperture is usually used to allow more scattered beams to pass through the objective lens to form an image. It offers a much higher structural resolution and is usually called high resolution TEM compared to the amplitude contrast mode, but it requires that the specimen be thin.

For phase contrast imaging, the interactions between the incident electrons and the specimen are usually weak and theories can be greatly simplified. In the phase-grating approximation, the wave function of the electrons scattered by specimen can be described [18],

$$\Psi_o(x, y) = e^{-i\beta V_p(x, y)}, \quad (2.1)$$

where  $\beta = \frac{\pi}{\lambda U}$  is the relativistic interaction constant with  $U$  being the accelerating voltage applied to the electrons,  $V_p(x, y)$  is the projected Coulomb potential of specimen in a plane perpendicular to the direction of

the incident electron beam and  $\lambda$  is the wave length of the electrons. For a thin specimen constituted of light atoms, the weak phase object approximation can be applied and Equation (2.1) can be simplified to,

$$\Psi_o(x, y) \simeq 1 - i\beta V_p(x, y), \quad (2.2)$$

where the unit 1 represents the transmitted wave which has no interaction with the specimen and the imaginary part corresponds to the scattered waves. The image wave on the image plane is a convolution of the object wave and the contrast transfer function  $T(\mathbf{r})$ :

$$\Psi_i(\mathbf{r}) = \Psi_o(\mathbf{r}) \otimes T(\mathbf{r}), \quad (2.3)$$

where  $\otimes$  is the convolution operator. The convolution operation of two functions can be expressed as the product of their corresponding Fourier transforms in reciprocal space:

$$\hat{\Psi}_i(\mathbf{q}) = \hat{\Psi}_o(\mathbf{q}) \cdot \hat{T}(\mathbf{q}). \quad (2.4)$$

The contrast transfer function in a TEM includes the information of aperture function, spherical aberration and imperfection of focusing of the objective lens and is given by:

$$T(\mathbf{q}) = a(\mathbf{q})e^{2i\pi\chi(\mathbf{q})}, \quad (2.5)$$

where  $a(\mathbf{q})$  is the aperture function of the objective lens and

$$\chi(\mathbf{q}) = \frac{1}{4}C_s\lambda q^4 + \frac{1}{2}\Delta f q^2, \quad (2.6)$$

where  $C_s$  and  $\Delta f$  are the spherical aberration coefficient and defocus of the objective lens, respectively. Equation (2.2) can be arranged as:

$$\Psi_i(x, y) = 1 + \beta V_p(x, y) \otimes \Re[T(x, y)] - i\beta V_p(x, y) \otimes \Im[T(x, y)], \quad (2.7)$$

where  $\Re[T(x, y)]$  and  $\Im[T(x, y)]$  are the real and imaginary part of  $T(x, y)$ , respectively. In the weak phase object approximation, where  $\beta V_p \ll 1$ , the image intensity can be further simplified as:

$$I(x, y) = |\Psi_i(x, y)|^2 \simeq 1 + 2\beta V_p(x, y) \otimes \Im[T(x, y)]. \quad (2.8)$$

### 2.2.2 Imaging of Carbon Nanotubes in the Real Space with TEM

Due to the low atomic number of carbon, it is valid to apply the weak phase object approximation to interpret the TEM images of the structures [19]. Theoretically, a high resolution of 2 Å can be reached using a TEM with a field emission electron gun, while the quality and the resolution of imaging are limited by thermal and mechanical vibrations, stage drift and instability of the magnetic lenses.

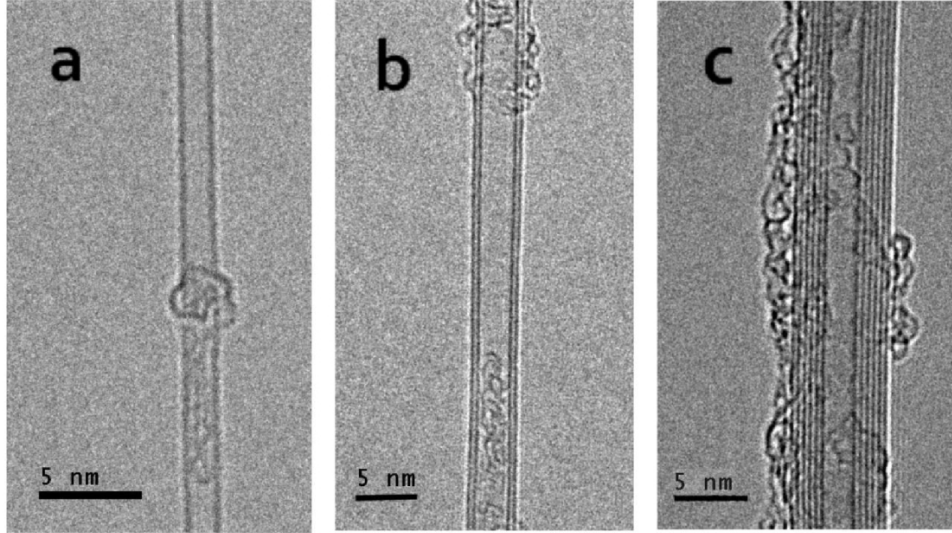


Figure 2.2: TEM images of CNTs. (a) a SWNT, (b) a DWNT and (c) a six-walled CNT. Pictures were captured with JOEL 2010F at 80 kV.

When imaging a SWNT in the real space [20], due to the scattering of electrons at carbon atoms, the tube walls spread out as paired dark lines. Even in the best scenario, a simple measurement of the distance between a pair of walls, corresponding to the tube diameter, is subject to systematic and substantial deviations from the true value due to the inevitable Fresnel fringes arising at the edges of the nanotubes. The diameter measurement is definitely 0.1 nm smaller than the true value provided certain experimental condition. In the case of a MWNT, it is more complicated to measure the diameters of the constituent tubes because of the more intense interference of Fresnel fringes. Hence, the interlayer spacing tends to appear brighter due to the interference, and the interlayer distance is likely to be overestimated [21].

### 2.2.3 Theory of Electron Diffraction of Carbon Nanotubes

In the reciprocal space, the diffraction pattern of a CNT unveils much more information about the chiral structure, which is obscured in the real space. First thoroughly formulated by Qin in 1994 [22] and Lucas *et al.*

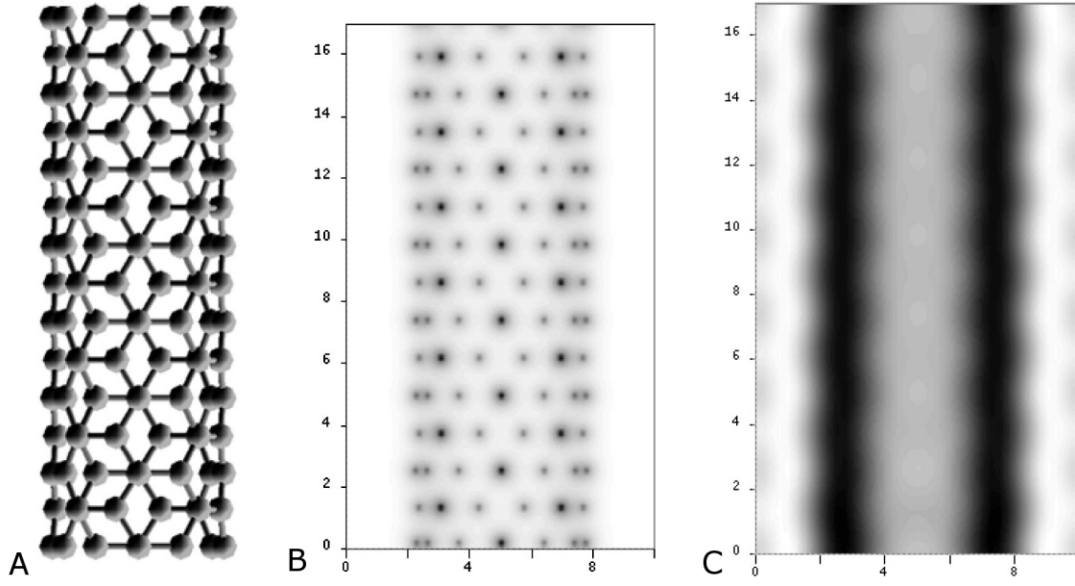


Figure 2.3: Simulated high resolution image of a (4,4) SWNT: (A) Atomic model and (B) corresponding projected potential along the incident electron beam direction for a (4,4) SWNT. The simulation in TEM is shown in (C), where the two walls appear as the dark lines [21].

in 1996 [23], the CNT electron diffraction theory has proved to be the most powerful method to characterize fine structures of CNTs [24, 25, 26, 27, 28].

The diffraction pattern of a CNT should be based on that of a graphene, which is the six-fold symmetrical honeycomb. However, the periodicity introduced by the circumferential confinement significantly distinguishes the diffraction pattern of a CNT.

The convenience of using cylindrical coordinates  $(r, \phi, z)$  encourages us to express the atomic structure of a CNT  $(u, v)$  as  $v$  pairs of helices parallel to  $\mathbf{a}_1$ . Therefore in a unit cell, there are  $\frac{2(u^2 + v^2 + uv)}{Mv}$  atoms in each helix. We can choose the position of an arbitrary atom as the origin  $(r_0, \phi_0, z_0)$ , then we have,

$$\begin{cases} r = r_0 \\ \phi_j^1 = 2\pi j \frac{a \cos \theta}{|\mathbf{C}_h|}, \\ z_j^1 = -ja \sin \theta. \end{cases} \quad (2.9)$$

Similarly, the ones in the secondary helix are shown as,

$$\begin{cases} r = r_0, \\ \phi_j^2 = 2\pi j \frac{a \cos \theta}{|\mathbf{C}_h|} - 2\pi \frac{a_0 \cos(\frac{\pi}{6} + \theta)}{\sqrt{3}|\mathbf{C}_h|}, \\ z_j^2 = -ja \sin \theta + \frac{a \sin(\frac{\pi}{6} + \theta)}{\sqrt{3}}. \end{cases} \quad (2.10)$$

Note that there are three equivalent representations of helices in a CNT depending on different crystallographic directions,  $\mathbf{a}_1$ ,  $\mathbf{a}_2$  or  $\mathbf{a}_3 = \mathbf{a}_2 - \mathbf{a}_1$ . And the position of atoms can be expressed in similar manners in different representations.

It can be expected that due to the existence of multiple helices and cylindrical confinement, compared with the honeycomb-like diffraction patterns of graphene, the diffraction patterns of a CNT will no longer be single spots but distribute in a manner of Bessel functions.

On the other hand, the periodicities in the real space will also be reflected in the diffraction patterns. If we define the spacing between the neighboring atoms on a helix as  $\Delta$ , the pitch length of a helix as  $C$  and the spacing between unit cells as  $c$ , the corresponding periodicities of  $\frac{1}{\Delta}$ ,  $\frac{1}{c}$  and  $\frac{1}{C}$  should be observed in the diffraction pattern, as illustrated in Figure 2.4.

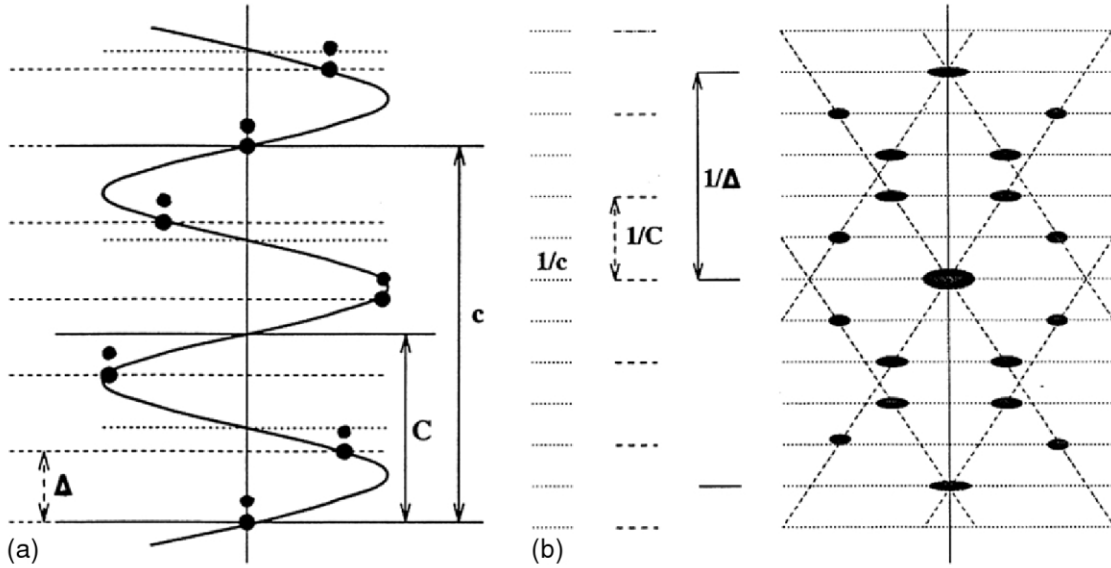


Figure 2.4: Schematic of periodicities in the real space  $c$ ,  $C$  and  $\Delta$  of a CNT with the corresponding diffraction patterns. [27]

The diffraction patterns can also be mathematically determined by solving the Schrödinger equation. When passing through carbon atoms in a CNT, fast electrons are slightly scattered from their incident direction, the scattering amplitude has been detailed and described in the Born approximation,



$$F(\mathbf{q}) = \frac{2\pi me}{h^2} \int U(\mathbf{r}) e^{2i\pi \mathbf{q} \cdot \mathbf{r}} d\mathbf{r}, \quad (2.11)$$

where  $U(\mathbf{r})$  is the Coulomb potential of the scattering atom;  $e$  and  $m$  are the charge and the relativistic mass of electron;  $h$  is Plank's constant and  $\mathbf{q}$  is the scattering vector with the magnitude defined as

$$|\mathbf{q}| = \frac{2 \sin(\Theta/2)}{\lambda}, \quad (2.12)$$

where  $\Theta$  is the total scattering angle and  $\lambda$  is the wave length of the incident electron.

Considering a continuous helix, we can express Equation (2.11) in cylindrical coordinates using Equation (2.9) and Equation (2.10),

$$\begin{aligned} F(R, \Phi, Z) &= \int V(\mathbf{r}) \exp(2\pi i \mathbf{q} \cdot \mathbf{r}) d\mathbf{r} \\ &= \int_{-\infty}^{\infty} \int_0^{2\pi} \int_0^{\infty} V(r, \phi, z) \exp[2\pi i r R \cos(\phi - \Phi)] \exp(2\pi i z Z) r dr d\phi dz, \end{aligned} \quad (2.13)$$

where  $(r, \phi, z)$  and  $(R, \Phi, Z)$  are the cylindrical coordinates in the real space and the reciprocal space, respectively;  $V(r, \phi, z) = \frac{2\pi me}{h^2} U(\mathbf{r})$  is the modified scattering potential. Bessel functions can be defined as,

$$e^{iz \cos \theta} = \sum_{n=-\infty}^{+\infty} J_n(z) \exp \left[ in \left( \theta + \frac{\pi}{2} \right) \right], \quad (2.14)$$

with the property of,

$$J_{-n}(z) = (-1)^n J_n(z). \quad (2.15)$$

Plug the both relationships into Equation (2.13),

$$\begin{aligned} F(R, \Phi, Z) &= \sum_n \int_{-\infty}^{\infty} \int_0^{\infty} V(r, \phi, z) \exp(in\Phi) \\ &\times \left\{ \int_0^{2\pi} \sum_{n=-\infty}^{+\infty} J_n(2\pi r R) \exp \left[ in \left( \Phi - \phi + \frac{\pi}{2} \right) \right] d\phi \right\} \exp(2\pi i z Z) r dr d\phi dz \end{aligned} \quad (2.16)$$

Given the N-fold rotational symmetry of the potential  $V(r, \phi, z)$  and the periodicity  $c$  along the axial direction, the Fourier expansion of the modified scattering potential can be written as,

$$\begin{aligned}
V(r, \phi, z) &= \sum_n V_{nN}(r, z) \exp(-inN\phi) \\
&= \sum_{n=-\infty}^{+\infty} \sum_{l=-\infty}^{+\infty} V_{nl}(r) \exp\left(-in\phi + \frac{2\pi ilz}{c}\right).
\end{aligned} \tag{2.17}$$

By incorporating the z-components into Equation (2.16), the structure factor becomes,

$$\begin{aligned}
F(R, \Phi, l) &= \frac{1}{c} \sum_{n=1}^{\infty} e^{in(\Phi+\pi/2)}, \\
&\times \int_0^c \int_0^{2\pi} \int_0^{\infty} V(r, \phi, z) J_l(2\pi r R) e^{i(-n\phi+2\pi lz/c)} r dr d\phi dz.
\end{aligned} \tag{2.18}$$

Immediately, the constant potential of a continuous helix with a radius of  $r_o$  and a pitch length  $C$  is given as,

$$V(r, \phi, z) = V_o \delta(r - r_o) \delta\left(\frac{2\pi z}{C} - \phi\right). \tag{2.19}$$

Substitute the modified potential into Equation (2.18), the scattering amplitude of one continuous helix is now:

$$F(R, \Phi, l) = r_o V_o J_l(2\pi r_o R) \exp[i(\Phi + \pi/2)l]. \tag{2.20}$$

Given a SWNT with  $j$  atoms on the helix, the structure factor can be given as,

$$F(R, \Phi, l) = \sum_n e^{in(\Phi+\pi/2)} J_n(2\pi r R) \sum_j f_j e^{i(-n\phi_j+2\pi l_j z/c)}. \tag{2.21}$$

where  $f_j$  is the atomic scattering amplitude of the  $j$ -th carbon atom,  $(r, \phi_j, l_j)$  are the cylindrical coordinates, and  $n$  is the integer which is allowed by the selection rule. Note that, the different periodicities of a SWNT in the real space, such as neighboring molecular group spacing  $\Delta$ , helices pitch length  $C$  and periodicity of structure  $c$ , imply repeated diffraction patterns in reciprocal space with periodicities of  $\frac{1}{\Delta}$ ,  $\frac{1}{C}$ , and  $\frac{1}{c}$ , respectively. This gives the selection rule,

$$\frac{l}{c} = \frac{n}{C} + \frac{m}{\Delta}. \tag{2.22}$$

Given a SWNT of  $(u, v)$ , the pitch length is  $C = |\mathbf{C}_h| \tan(\frac{\pi}{3} - \theta)$ , while the neighboring molecular group spacing  $\Delta = a \sin(\frac{\pi}{3} - \theta)$ , and the axial periodicity  $|\mathbf{T}| = \sqrt{3} \frac{|\mathbf{C}_h|}{M}$ , therefore Equation (2.21) can be re-arranged for the exact value of  $l$ .

Meanwhile, by plugging the coordinates of carbon atoms of a SWNT to Equation (2.22), the structure factor of a SWNT  $(u, v)$  can finally be expressed as,

$$F_{uv}(R, \Phi, l) = \sum_{n,m} f \gamma_{uv}(n, m) \chi_{uv}(n, m) J_n(\pi d R) \exp \left[ i n \left( \Phi + \frac{\pi}{2} \right) \right], \quad (2.23)$$

where

$$\chi_{uv}(n, m) = 1 + \exp \left[ 2\pi i \left( -\frac{n + (u + 2v)m}{3v} \right) \right], \quad (2.24)$$

and

$$\gamma_{uv}(n, m) = \begin{cases} v & \text{when } [n + (u + v)m]/v = N \\ 0 & \text{otherwise} \end{cases} \quad (2.25)$$

From the above expressions, the structure factor can be divided into two parts:

1. reflections of graphene lattice,

$$\sum_{n,m} \gamma_{uv}(n, m) \chi_{uv}(n, m). \quad (2.26)$$

2. curvature effects,

$$\sum_{n,m} J_n(\pi d R) \exp \left[ i n \left( \Phi + \frac{\pi}{2} \right) \right]. \quad (2.27)$$

The intensity distribution of diffraction patterns is computed by

$$I_{uv} = |F_{uv}(R, \Phi, l)|^2. \quad (2.28)$$

## 2.2.4 Determination of Chiral Structure of a Carbon Nanotube

Governed by the selection rule Equation (2.22), only  $l = kN$  lines are allowed in the diffraction of a SWNT with the N-fold rotational symmetry. Therefore, the intensities on those lines are described by the Bessel function of certain orders, which provides a convenient approach to determine the chiral indices of a SWNT.

Based on the theory, the diffraction pattern of a SWNT could be simulated, as shown in Figure 2.5. The first three layer lines from the equatorial line are the most significant ones, thus called primary layer lines

labeled as  $l_1, l_2$ , and  $l_3$ . The elongation of the diffraction spots perpendicular to the tubule axis is due to a lack of translational periodicity in this direction. As we can see from the image, the peak of intensity is shifted because of the curvature of the CNT [29].

The intensity distribution on the equatorial layer line is dominated by the 0-th order Bessel function, whereas the allowed values of  $l$  are constrained by the selection rule that,

$$l = n \frac{2u + v}{Mv} + m \frac{2(u^2 + v^2 + uv)}{Mv}, \quad (2.29)$$

where  $n$  and  $m$  are integers. Equation (2.29) gives the lowest order of Bessel function for the principal lines  $l_1, l_2$  and  $l_3$  are  $-v, u$  and  $-(u + v)$ , respectively. Furthermore, each principal line consists of an infinite series of Bessel functions, the orders of which increase in the step of  $\frac{2(u^2 + v^2 + uv)}{M}$ . Since  $\frac{2(u^2 + v^2 + uv)}{M}$  is usually a large number and the magnitudes of the high order Bessel functions are negligible, only the Bessel function of the lowest order is significant. Therefore

$$I(R, \Phi, l_1) \propto |J_v(\pi dR)|^2, \quad (2.30)$$

$$I(R, \Phi, l_2) \propto |J_u(\pi dR)|^2, \quad (2.31)$$

$$I(R, \Phi, l_3) \propto |J_{u+v}(\pi dR)|^2. \quad (2.32)$$

Hence, with the knowledge of the intensity distribution on any two principal layer lines, the chiral indices  $(u, v)$  can be accurately identified. According to the characteristics of the Bessel function  $J_v$ , the ratio of the positions of first two peaks  $\frac{P_2}{P_1}$  in the intensity profile uniquely depends on the order  $v$ , therefore it provides another possibility to determine the chiral indices. While in practice, because of the distraction of inevitable background noises and possible contaminations, it is difficult to accurately locate the position of peaks in the intensity distributions. Whereas the “valleys” on the primary lines, which corresponding to the roots of Bessel function, are much more distinguishable due to the zero intensity. For a certain order Bessel function, the distance between the first pair of roots  $2P_1$  and the interval spacing  $\Delta_{12}$  between the first two roots are also unique [30], as illustrated in Figure 2.6. Hence, both the ratios of  $\frac{P_2}{P_1}$  and  $\frac{P_1}{\Delta_{12}}$  can be used to evaluate the order of Bessel function. The correlation between them can be found in Table 2.1.

Despite of the accuracy of the approach to identify the individual chiral indices of a SWNT, when evaluating the chirality using the experimental diffraction patterns, information is plagued by the low signal/noise ratio, and considerable errors are introduced. Thus another method using spacings between the layer lines is usually applied simultaneously. As illustrated in Figure 2.5, the line spacings  $D_1, D_2$ , and  $D_3$  from the primary layer

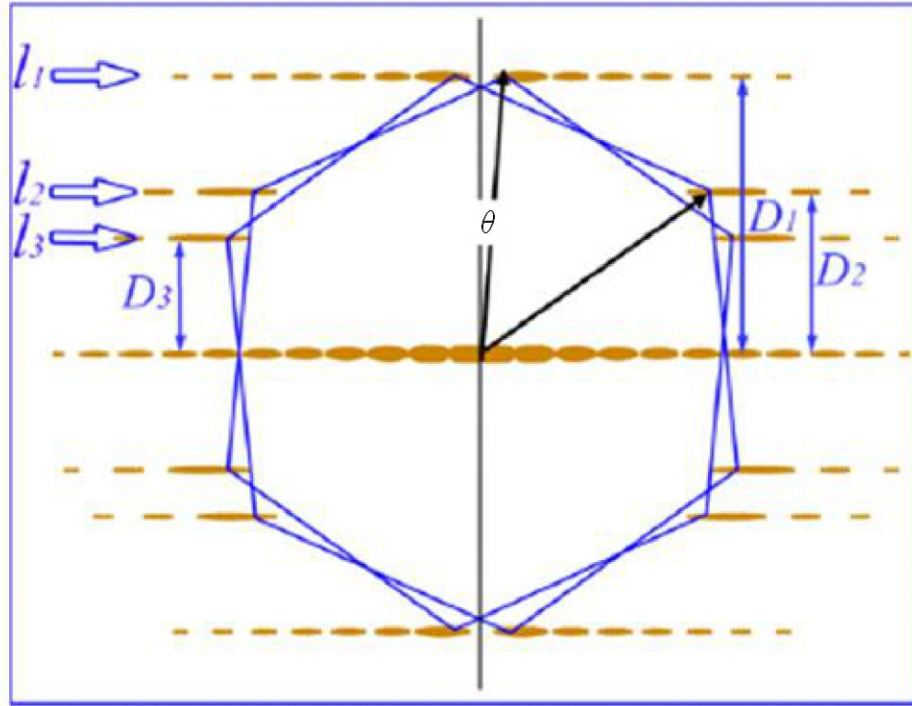


Figure 2.5: Diffraction pattern simulation of an individual SWNT. The two hexagons indicate the primary Bragg reflections from the top and the bottom portion of the carbon nanotube, giving six primary diffraction layer lines on the diffraction pattern, while  $\theta$  shows the distortion of hexagons from the planar diffraction of a graphene caused by the curvature of a SWNT, thus stands for the chiral angle of the SWNT.  $l_1$ ,  $l_2$ , and  $l_3$  are the primary diffraction layers resulting from the Bragg reflections of indices  $(1\ 0)$ ,  $(\bar{1}\ 0)$  and  $(1\ 1)$  directions, whereas  $D_1$ ,  $D_2$ , and  $D_3$  is the spacing between each layer line and the equatorial line [29].

Table 2.1: Characteristic ratio  $P_2/P_1$ ,  $P_1/\Delta_{12}$  for Bessel function of orders from 0 to 50.

| $n$ | $P_1/\Delta_{12}$ | $P_2/P_1$ | $n$ | $P_1/\Delta_{12}$ | $P_2/P_1$ |
|-----|-------------------|-----------|-----|-------------------|-----------|
| 1   | 1.157             | 2.892     | 26  | 11.777            | 1.206     |
| 2   | 1.861             | 2.197     | 27  | 12.096            | 1.201     |
| 3   | 2.485             | 1.904     | 28  | 12.410            | 1.196     |
| 4   | 3.059             | 1.751     | 29  | 12.721            | 1.192     |
| 5   | 3.597             | 1.636     | 30  | 13.028            | 1.188     |
| 6   | 4.107             | 1.565     | 31  | 13.332            | 1.183     |
| 7   | 4.593             | 1.507     | 32  | 13.633            | 1.180     |
| 8   | 5.061             | 1.465     | 33  | 13.931            | 1.176     |
| 9   | 5.512             | 1.428     | 34  | 14.226            | 1.172     |
| 10  | 5.948             | 1.398     | 35  | 14.519            | 1.169     |
| 11  | 6.372             | 1.373     | 36  | 14.808            | 1.166     |
| 12  | 6.784             | 1.350     | 37  | 15.095            | 1.163     |
| 13  | 7.186             | 1.332     | 38  | 15.380            | 1.160     |
| 14  | 7.579             | 1.315     | 39  | 15.662            | 1.157     |
| 15  | 7.963             | 1.301     | 40  | 15.942            | 1.154     |
| 16  | 8.340             | 1.287     | 41  | 16.219            | 1.152     |
| 17  | 8.709             | 1.285     | 42  | 16.495            | 1.149     |
| 18  | 9.072             | 1.266     | 43  | 16.768            | 1.147     |
| 19  | 9.428             | 1.256     | 44  | 17.039            | 1.145     |
| 20  | 9.779             | 1.247     | 45  | 17.308            | 1.142     |
| 21  | 10.124            | 1.239     | 46  | 17.575            | 1.140     |
| 22  | 10.464            | 1.232     | 47  | 17.841            | 1.138     |
| 23  | 10.799            | 1.226     | 48  | 18.104            | 1.136     |
| 24  | 11.129            | 1.218     | 49  | 18.366            | 1.134     |
| 25  | 11.455            | 1.211     | 50  | 18.626            | 1.133     |

lines to the equatorial line can be expressed as

$$D_1 = |\mathbf{b}| \sin\left(\frac{\pi}{2} - \theta\right), \quad (2.33)$$

$$D_2 = |\mathbf{b}| \sin\left(\frac{\pi}{6} + \theta\right), \quad (2.34)$$

$$D_3 = |\mathbf{b}| \sin\left(\frac{\pi}{6} - \theta\right). \quad (2.35)$$

where  $\mathbf{b}$  is the unit vector of the graphene lattice in reciprocal space. Note that, the chiral angle is also expressed in Equation (1.12). The ratio of chiral indices are then deduced as,

$$\frac{v}{u} = \frac{2D_2 - D_1}{2D_1 - D_2}. \quad (2.36)$$

Although instead of the individual chiral indices, only the ratio can be obtained with this method, the independent measurements of  $D_1$ ,  $D_2$ , and  $D_3$  are more discernible and thus provide higher error tolerance. Figure 2.7 shows the simulations of the diffraction patterns of SWNTs (11, 5) and (50, 11), due to the smaller diameter, the peaks on each principle lines of (11, 5) are more spread and easier to locate, whereas the errors when reading the intensity distribution of the larger SWNT (50, 11) are considerable. However, the line spacings between  $D_1$ ,  $D_2$ , and  $D_3$  can always be determined with relatively small errors. Therefore, the method of measuring the spacing of the principal layer lines are preferred and usually combined with the diameter measurement from TEM imaging in the real space to unambiguously determine the chiral structure.

The characterization of chiral structure of a SWNT from the diffraction pattern in practice can be generalized in the following steps:

1. Capture the image of the SWNT in the real space and the diffraction pattern in the reciprocal space at a relative low acceleration voltage;
2. Measure the diameter in the real space image  $d_{\text{real}}$ , note that the deviation from the true value;
3. Locate at least three primary layer lines and therefore at least two line spacings. Plug the spacings into Equation (2.36) to find possible  $v/u$  ratio;
4. Measure the positions of peaks and valleys on at least one discernible primary layer line and look up the order of corresponding Bessel function.
5. Combine the results of  $v/u$  ratio, individual chiral indices and the diameter to determine the most reasonable chiral indices  $(u, v)$  with the least error.

In the case of MWNTs, the diffraction pattern can be considered as the superposition of the diffraction patterns of each shells as individual SWNTs. Provided the layer lines from the component diffraction patterns do not coincide, the similar procedures can be applied. However, provided the existence of two or more commensurate sheels in a MWNT, the corresponding diffraction patterns may overlap. In addition, there is no explicit correspondence between the diameter of each shell and the set of diffraction patterns. In other words, the  $v/u$  ratio calculated from one set of primary layer line might correspond to any shell. Hence extra caution is required for MWNTs diffraction pattern analysis.



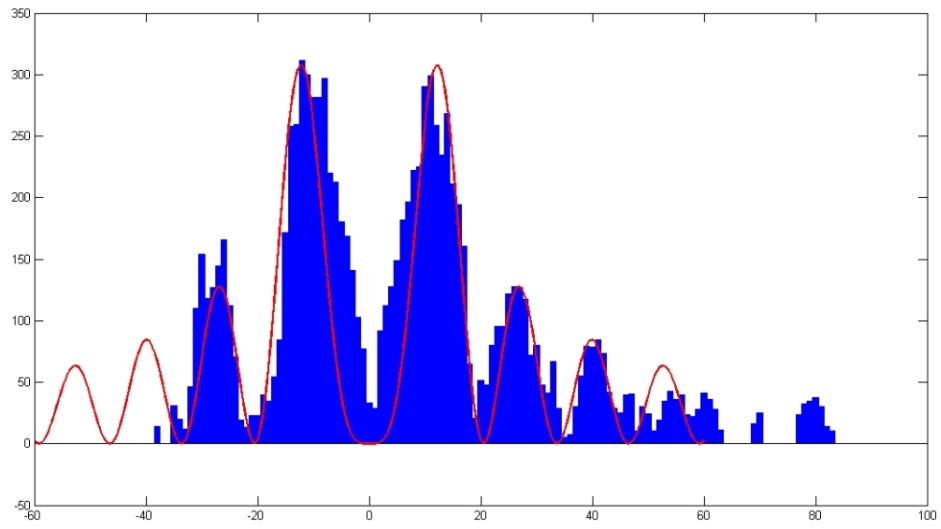


Figure 2.6: Intensity distribution on a principal line and fitted Bessel function. In the intensity distribution, the positions of valleys are more distinguishable than the peaks. Note that, due to the noise extortion, the minima of the intensity profile do not coincide with the minima of the fitted Bessel function.

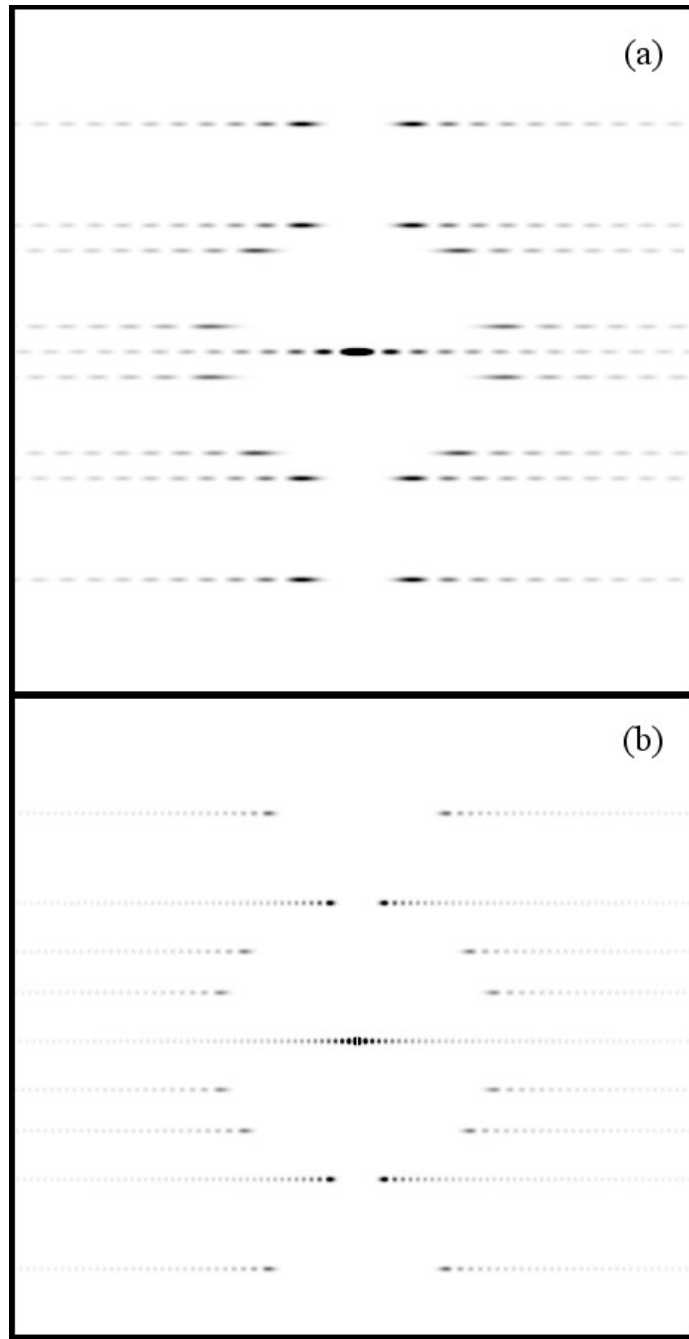


Figure 2.7: Simulated diffraction patterns of SWNTs of different sizes. (a) SWNT (11, 5) of diameter 1.111 nm; (b) SWNT (50, 11) of diameter 4.411 nm. The incident electron beams are normal to the SWNTs.

## BIBLIOGRAPHY

- [1] J. W. Wilder, L. C. Venema, A. G. Rinzler, R. E. Smalley, and C. Dekker, "Electronic structure of atomically resolved carbon nanotubes," *Nature*, vol. 391, no. 6662, pp. 59–62, 1998.
- [2] T. W. Odom, J.-L. Huang, P. Kim, and C. M. Lieber, "Atomic structure and electronic properties of single-walled carbon nanotubes," *Nature*, vol. 391, no. 6662, pp. 62–64, 1998.
- [3] A. Hassanien, M. Tokumoto, Y. Kumazawa, H. Kataura, Y. Maniwa, S. Suzuki, and Y. Achiba, "Atomic structure and electronic properties of single-wall carbon nanotubes probed by scanning tunneling microscope at room temperature," *Applied Physics Letters*, vol. 73, no. 26, pp. 3839–3841, 1998.
- [4] T. Hertel, R. E. Walkup, and P. Avouris, "Deformation of carbon nanotubes by surface van der waals forces," *Physical Review B*, vol. 58, no. 20, p. 13870, 1998.
- [5] E. W. Wong, P. E. Sheehan, and C. M. Lieber, "Nanobeam mechanics: elasticity, strength, and toughness of nanorods and nanotubes," *Science*, vol. 277, no. 5334, pp. 1971–1975, 1997.
- [6] A. Rubio, "Spectroscopic properties and stm images of carbon nanotubes," *Applied Physics A*, vol. 68, no. 3, pp. 275–282, 1999.
- [7] C. E. Giusca, Y. Tison, V. Stolojan, E. Borowiak-Palen, and S. R. P. Silva, "Inner-tube chirality determination for double-walled carbon nanotubes by scanning tunneling microscopy," *Nano Letters*, vol. 7, no. 5, pp. 1232–1239, 2007.
- [8] S. J. Tans, A. R. Verschueren, and C. Dekker, "Room-temperature transistor based on a single carbon nanotube," *Nature*, vol. 393, no. 6680, pp. 49–52, 1998.
- [9] A. Jorio, R. Saito, J. Hafner, C. Lieber, M. Hunter, T. McClure, G. Dresselhaus, and M. Dresselhaus, "Structural (n, m) determination of isolated single-wall carbon nanotubes by resonant raman scattering," *Physical Review Letters*, vol. 86, no. 6, pp. 1118–1121, 2001.
- [10] H. Telg, J. Maultzsch, S. Reich, F. Hennrich, and C. Thomsen, "Chirality distribution and transition energies of carbon nanotubes," *Physical Review Letters*, vol. 93, no. 17, p. 177401, 2004.
- [11] J. Benoit, J. Buisson, O. Chauvet, C. Godon, and S. Lefrant, "Low-frequency raman studies of multiwalled carbon nanotubes: Experiments and theory," *Physical Review B*, vol. 66, no. 7, p. 073417, 2002.
- [12] X. Zhao, Y. Ando, L.-C. Qin, H. Kataura, Y. Maniwa, and R. Saito, "Radial breathing modes of multiwalled carbon nanotubes," *Chemical Physics Letters*, vol. 361, no. 1, pp. 169–174, 2002.
- [13] D. C. Joy and A. D. Romig Jr, *Principles of analytical electron microscopy*. Plenum Publishing Corporation, 1986.
- [14] B. W. Smith and D. E. Luzzi, "Electron irradiation effects in single wall carbon nanotubes," *Journal of Applied Physics*, vol. 90, no. 7, pp. 3509–3515, 2001.
- [15] D. B. Williams and C. B. Carter, *The Transmission Electron Microscope*. Springer, 1996.
- [16] L. Reimer and H. Kohl, *Transmission electron microscopy: physics of image formation*, vol. 36. Springer Verlag, 2008.
- [17] H. Deniz, *Electron diffraction and microscopy study of nanotubes and nanowires*. PhD thesis, University of North Carolina at Chapel Hill, 2007.
- [18] Z. Liu, *Atomic structure determination of carbon nanotubes by electron diffraction*. PhD thesis, University of North Carolina at Chapel Hill, 2005.
- [19] O. Lourie and H. Wagner, "Transmission electron microscopy observations of fracture of single-wall carbon nanotubes under axial tension," *Applied Physics Letters*, vol. 73, no. 24, pp. 3527–3529, 1998.

- [20] N. De Jonge, Y. Lamy, K. Schoots, and T. H. Oosterkamp, "High brightness electron beam from a multi-walled carbon nanotube," *Nature*, vol. 420, no. 6914, pp. 393–395, 2002.
- [21] C. Qin and L.-M. Peng, "Measurement accuracy of the diameter of a carbon nanotube from tem images," *Physical Review B*, vol. 65, no. 15, p. 155431, 2002.
- [22] L.-C. Qin, "Electron diffraction from cylindrical nanotubes," *Journal of Materials Chemistry*, vol. 9, no. 9, p. 2450, 1994.
- [23] A. Lucas, V. Bruyninckx, and P. Lambin, "Calculating the diffraction of electrons or x-rays by carbon nanotubes," *Europhysics Letters*, vol. 35, no. 5, p. 355, 1996.
- [24] J. Zuo, I. Vartanyants, M. Gao, R. Zhang, and L. Nagahara, "Atomic resolution imaging of a carbon nanotube from diffraction intensities," *Science*, vol. 300, no. 5624, pp. 1419–1421, 2003.
- [25] M. Gao, J. Zuo, R. Twesten, I. Petrov, L. Nagahara, and R. Zhang, "Structure determination of individual single-wall carbon nanotubes by nanoarea electron diffraction," *Applied Physics Letters*, vol. 82, no. 16, pp. 2703–2705, 2003.
- [26] S. Amelinckx, A. Lucas, and P. Lambin, "Electron diffraction and microscopy of nanotubes," *Reports on Progress in Physics*, vol. 62, no. 11, p. 1471, 1999.
- [27] L.-C. Qin, "Electron diffraction from carbon nanotubes," *Reports on Progress in Physics*, vol. 69, no. 10, p. 2761, 2006.
- [28] C. Allen, C. Zhang, G. Burnell, A. Brown, J. Robertson, and B. Hickey, "A review of methods for the accurate determination of the chiral indices of carbon nanotubes from electron diffraction patterns," *Carbon*, vol. 49, no. 15, pp. 4961–4971, 2011.
- [29] Z. Liu and L.-C. Qin, "A direct method to determine the chiral indices of carbon nanotubes," *Chemical Physics Letters*, vol. 408, no. 1, pp. 75–79, 2005.
- [30] H. Jiang, D. P. Brown, A. G. Nasibulin, and E. I. Kauppinen, "Robust bessel-function-based method for determination of the (n, m) indices of single-walled carbon nanotubes by electron diffraction," *Physical Review B*, vol. 74, no. 3, p. 035427, 2006.

## **CHAPTER 3**

### **Synthesis of Carbon Nanotubes**

#### **3.1 Introduction**

The synthesis of CNTs has been categorized into physical and chemical methods depending on different procedures to extract carbon atoms from various precursors. Physical methods are the more traditional ones where high energy sources are used, such as arc discharge [1] and laser ablation [2] to extract carbon atoms. Arc-discharge method, in which the first CNT was discovered, employs evaporation of graphite electrodes in electric arcs that involve high temperatures (higher than 3000 °C ) [1]. Although arc-grown CNTs are well crystallized, they are highly impure; about 60 - 70% of the arc-grown product contains metal particles and amorphous carbon. Similarly, Laser-vaporization techniques employ evaporation of high-purity graphite targets by high-power lasers in conjunction with high-temperature furnaces [3]. Although physically grown CNTs have the advantage of better quality, their production yield is relatively low.

On the other hand, chemical approaches rely on the extraction of carbon through catalytic decomposition of precursors using the transition metal nanoparticles. The further categorization of the methods are based on the application of other important aspects of the synthesis process, such as types of precursors and materials of transition metal nanoparticles. Chemical vapor deposition (CVD), incorporating catalyst-assisted thermal decomposition of hydrocarbons, is the most popular method of producing CNTs, where the yield is not high compared to the physical approaches, but the growth process can be well controlled through the nanoparticle catalyst deposited onto the substrate. Other established methods include plastic pyrolysis [4], flame synthesis [5], and liquid hydrocarbon synthesis [6].

#### **3.2 Fundamentals of Chemical Vapor Deposition(CVD)**

Even though the synthesis processes have been studied for decades, the controversies still remain on the synthesis dynamics and mechanisms and no CNT growth mechanism is well established. However, various synthesis techniques with experiment conditions have been reported which all result in the formation of CNTs, the consolidation of observations from multiple authors proposed that all the synthesis methods should be based on a single growth mechanism.

The widely-accepted hypothesis mechanism can be generalized similarly to the diffusion-precipitation mechanism proposed by Baker *et al.* explaining the synthesis of carbon fibers [7, 8], that when in contact with the “hot” metal nanoparticles, a hydrocarbon vapor first decomposes into carbon and hydrogen species; hydrogen gets exhausted and carbon dissolves into the metal. After reaching the carbon-solubility limit in the metal at that temperature, dissolved carbon precipitates out and crystallizes in the form of a cylindrical network having no dangling bonds and hence energetically stable. Hydrocarbon decomposition (being an exothermic process) releases some heat to the metal’s exposed zone, while carbon crystallization (being an endothermic process) absorbs some heat from the metal’s precipitation zone. This precise thermal gradient inside the metal particle keeps the process on, as sketched in Figure 3.1. The catalytic nanoparticle can be located either at the tip or the bottom of a CNT, depending on whether bulk diffusion or surface diffusion is dominant [9], as well as the interaction strength between the catalyst and the substrate.

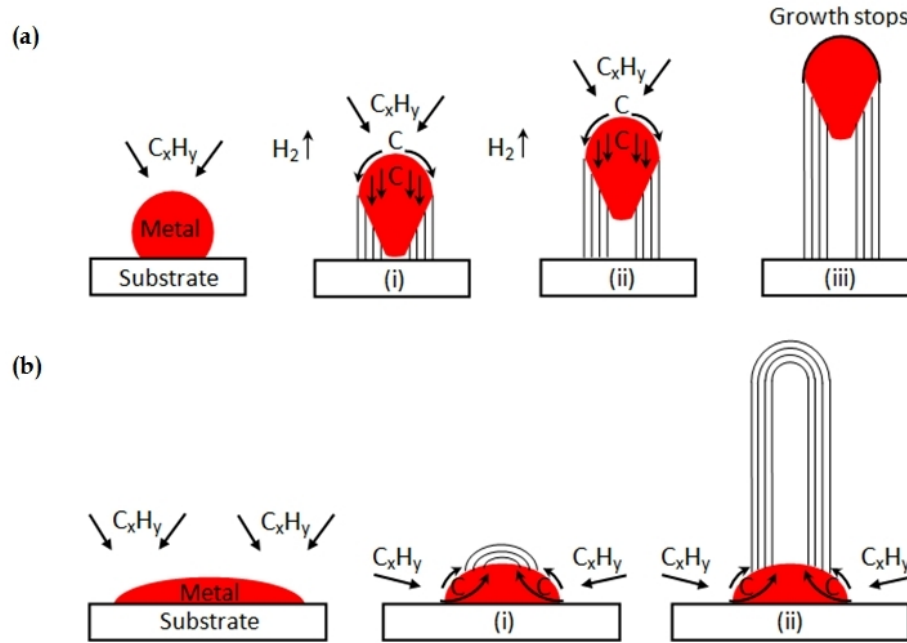


Figure 3.1: Hypothesis for mechanisms of CNT synthesis in CVD. Widely-accepted growth mechanisms for CNTs: (a) tip-growth model, (b) base-growth model.

A typical CVD process consists of placing catalytic nanoparticles (usually supported on a wafer) in a quartz tube inside a furnace which is then heated to the desired growth temperature. Carbon carrier gases are then flowed through the quartz tube for a predetermined period for synthesis. After the growth, the furnace is cooled down and the wafer is inspected for the resultant nanotube growth. This technique was used to grow SWNTs on flat silicon substrates [10]. The process has gained popularity due to the well-separated, long CNTs with few defects and amorphous carbon [11, 12, 13]. The basic setup of a CVD system for CNTs synthesis

is illustrated in Figure 3.2. Before going into the details of this technique it will be helpful to first look into various parameters that define this growth technique.

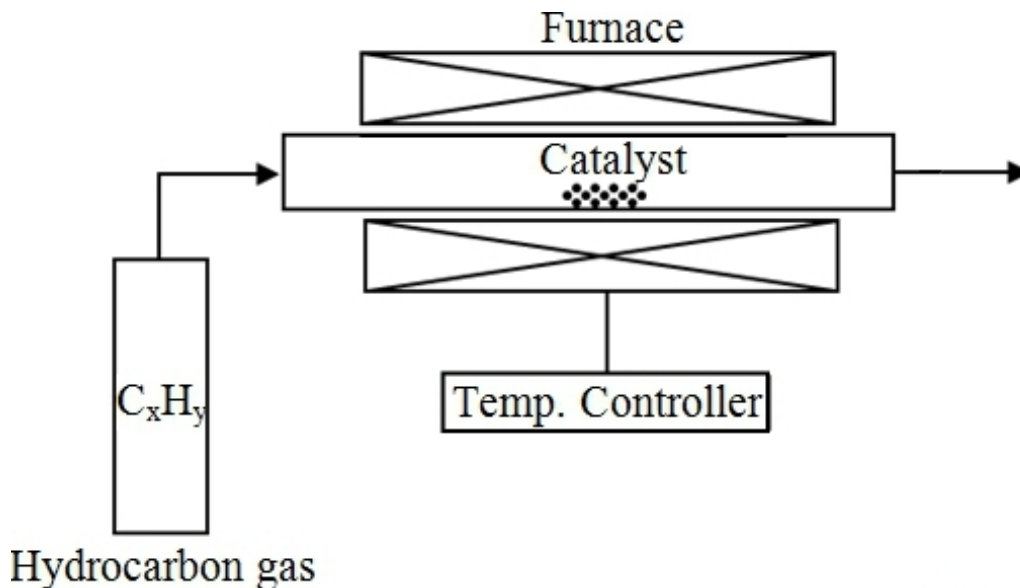


Figure 3.2: Schematic diagram of a CVD setup in its simplest form.

### 3.2.1 Carbon Precursor

A gas phase carbon feedstock provides essential elements in CNT synthesis. Different carbon compounds have been used as precursors, such as carbon monoxide (CO) [14], methane (CH<sub>4</sub>) [15], ethylene (C<sub>2</sub>H<sub>4</sub>) [16], acetylene (C<sub>2</sub>H<sub>2</sub>) [17], benzene (C<sub>6</sub>H<sub>6</sub>) [18], ethanol (C<sub>2</sub>H<sub>5</sub>OH) and methanol (CH<sub>3</sub>OH) [19], where liquid C<sub>2</sub>H<sub>5</sub>OH and CH<sub>3</sub>OH are usually introduced into the system by Ar gas through gas washers. In a typical growth process, carbon precursors are premixed with other gases such as H<sub>2</sub> and Ar to control the reaction rates. Each precursor has a particular decomposition temperature as the synthesis temperature. For example, CH<sub>4</sub> is known to decompose at temperatures higher than 900 °C, whereas C<sub>2</sub>H<sub>5</sub>OH starts decomposing around 800 °C.

Although higher temperatures are required for higher growth rate, excessively high temperatures can initiate self-dissociation of the gases which causes catalyst poisoning. Besides the temperature, the dissociation rate of the precursor can also be controlled by the partial pressures of the gases. For example, CO dissociation rate increases at higher pressure, which results in lower nanotube yield.

Another important parameter associated with the precursor is the feeding rate. At high temperature where the precursor is near self-dissociation, the reaction rate is limited by the precursor feed rate in the system. High feed rates can increase the rate of growth, but it can also result in carbon soot formation and hence catalyst

poisoning. Precursor feed rate is also coupled with the size of catalytic nanoparticles. For example in a study by Cheung *et al.* [20], it is shown that different carbon species can be produced from the same size catalyst nanoparticles but different carrier gas flow rates. At higher flow rates, larger diameter nanoparticles are more populous since the smaller ones will quickly get poisoned.

### 3.2.2 Temperature

The selection of temperature in CVD process is correlated with other parameters. The ideal temperature of CNT synthesis varies from 500 to 1000 °C, and SWNTs tend to be synthesized at higher temperature. Growth temperature is especially important to produce high-quality nanotubes of large diameters [20]. The temperature is a significant factor in CNT synthesis not only of the kinetics during the reaction but also of the conditioning of catalysts prior to the growth. Catalytic nanoparticles are vulnerable to the oxidation under ambient conditions, thus a reduction process at moderate temperature, usually 700 °C, is required to bring the nanoparticles to the unoxidized state [21]. Moreover, ramping rates of temperature also affects CNT synthesis. It has been shown that fast heating in the CVD process produces long and aligned CNTs due to the effect of temperature on the flow conditions near the surface which causes catalyst nanoparticles to leave the substrate and grow long tubes [22]. Also, as the structure of CNTs is more robust to high temperatures, which can be used to remove contaminations such as amorphous carbon in the product. It has been reported by multiple groups that a higher synthesis temperature results in larger diameter CNTs [23, 24].

### 3.2.3 Catalytic Nanoparticles

Transition metal nanoparticles of various sources, such as metal salts and evaporated metal films, have been chosen as catalysts in the CVD process for CNT synthesis, mostly due to their advantages of high carbon solubilities, high carbon diffusion rates, and high melting temperature.

Several approaches have been applied to obtain the nanoparticles, one of the most common methods is to dissolve the metal salt, such as nitrates, sulphates or chlorides, to form a stable nanoparticle complex. A uniform distribution of metal nanoparticles can be also produced by film evaporation with finely controlled annealing treatment [25].

The correlation between the size of catalytic nanoparticles and the diameter of resultant CNTs has proved to be significant [20, 26], as shown in Figure 3.4. Therefore narrowing the catalyst size distribution helps to control the synthesis of CNTs of specific diameter, for example the synthesis of MWNTs requires large size nanoparticles as catalysts.



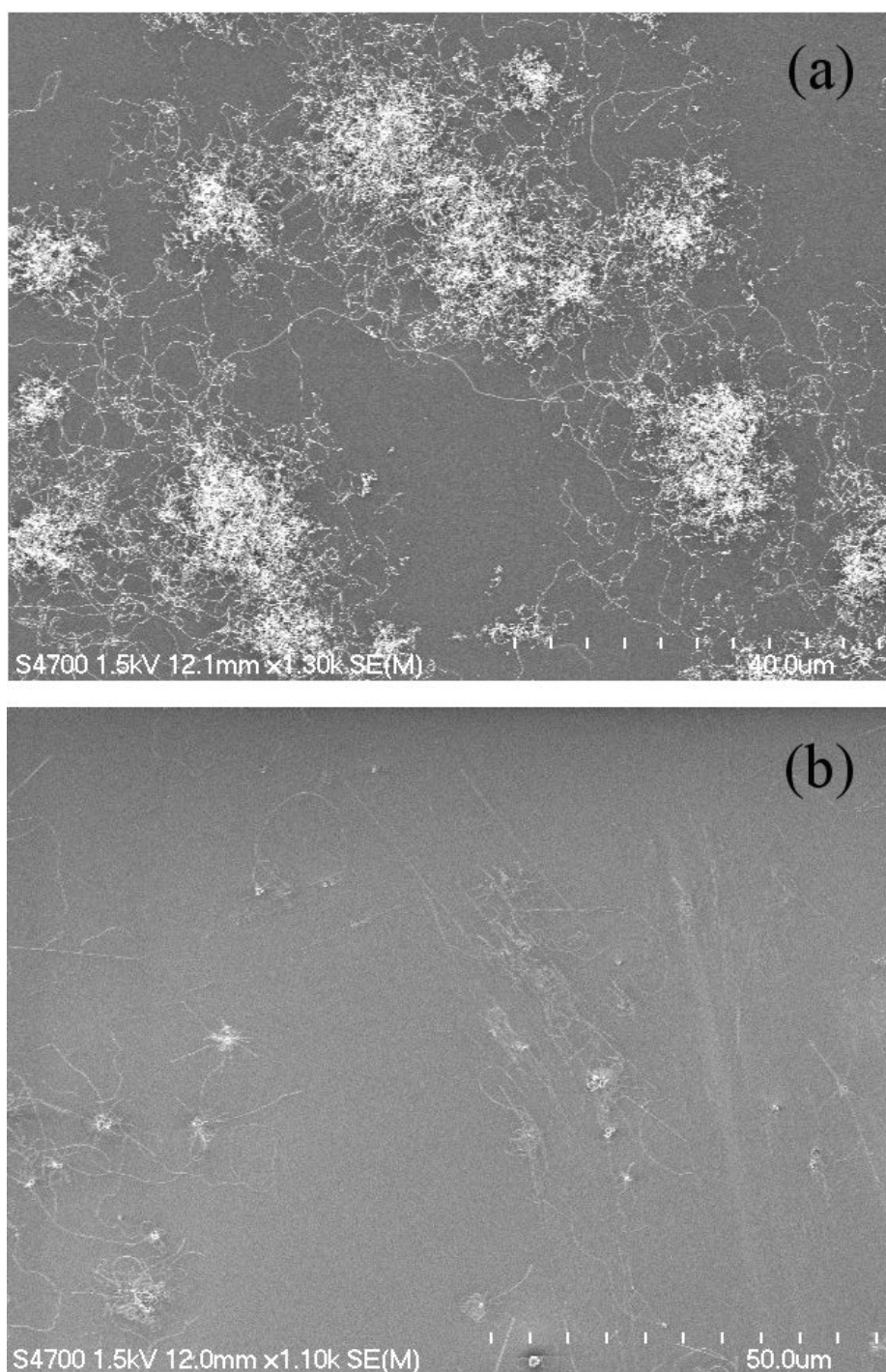


Figure 3.3: Different synthesized CNTs with different growth temperatures. CNTs were grown using the same recipe except for 1100 °C when growing CNTs in (a) and 1000 °C in (b). The difference between the contrast of CNT images indicates different conductances, while the higher temperature tends to produce carbon fibers with high density.

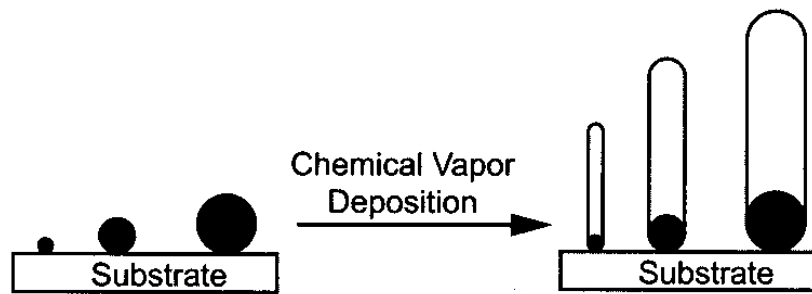


Figure 3.4: Schematic illustration shows the use of different diameter iron nanocluster catalysts for the controlled synthesis of CNTs [21].

The method to disperse the nanoparticles on the growth substrate is important, for the distribution significantly affects the morphology of the synthesis results. Most nanoparticles are suspended in a solvent and tend to clump after drying on the substrate. Several innovative methods have been applied to solve this problem, for example, mixing the nanoparticles with polymers before applying onto the substrates will reduce the surface energy and therefore helps in achieving well-separated particles of uniform size [21].

### 3.2.4 Gas Flow Rates

Gas flow rates in the CVD process is responsible for both carbon dissociation rate during the growth and the length of CNTs. Longer tubes are regularly observed in the periphery of the wafer than the center, while the orientations of CNTs are not always aligned in the gas flow direction. Wavy tubes are the consequences of the unsteady flow near the substrate surface, except in the aligned growth on quartz, where the mechanism is attributed to the crystal steps [27]. One crucial factor of obtaining aligned growth of CNTs has been found as the local thermal oscillations in suspended growth [28]. Various techniques have been applied to stabilize the flow near the surface for better CNTs synthesis, such as decreasing the quartz tube cross section and reducing the flow rate.

## 3.3 CNT Synthesis Experiment

### 3.3.1 Motivation and Objective

Despite of decades of investigations, CNT synthesis process is still riddled with problems about which parameters determine the types of resulting CNTs and how to achieve synthesis reproducibility. One major issue is the lack of thorough characterization techniques to investigate the growth results. Even though AFMs and SEMs have been broadly applied to characterize grown CNTs due to the convenience of direct

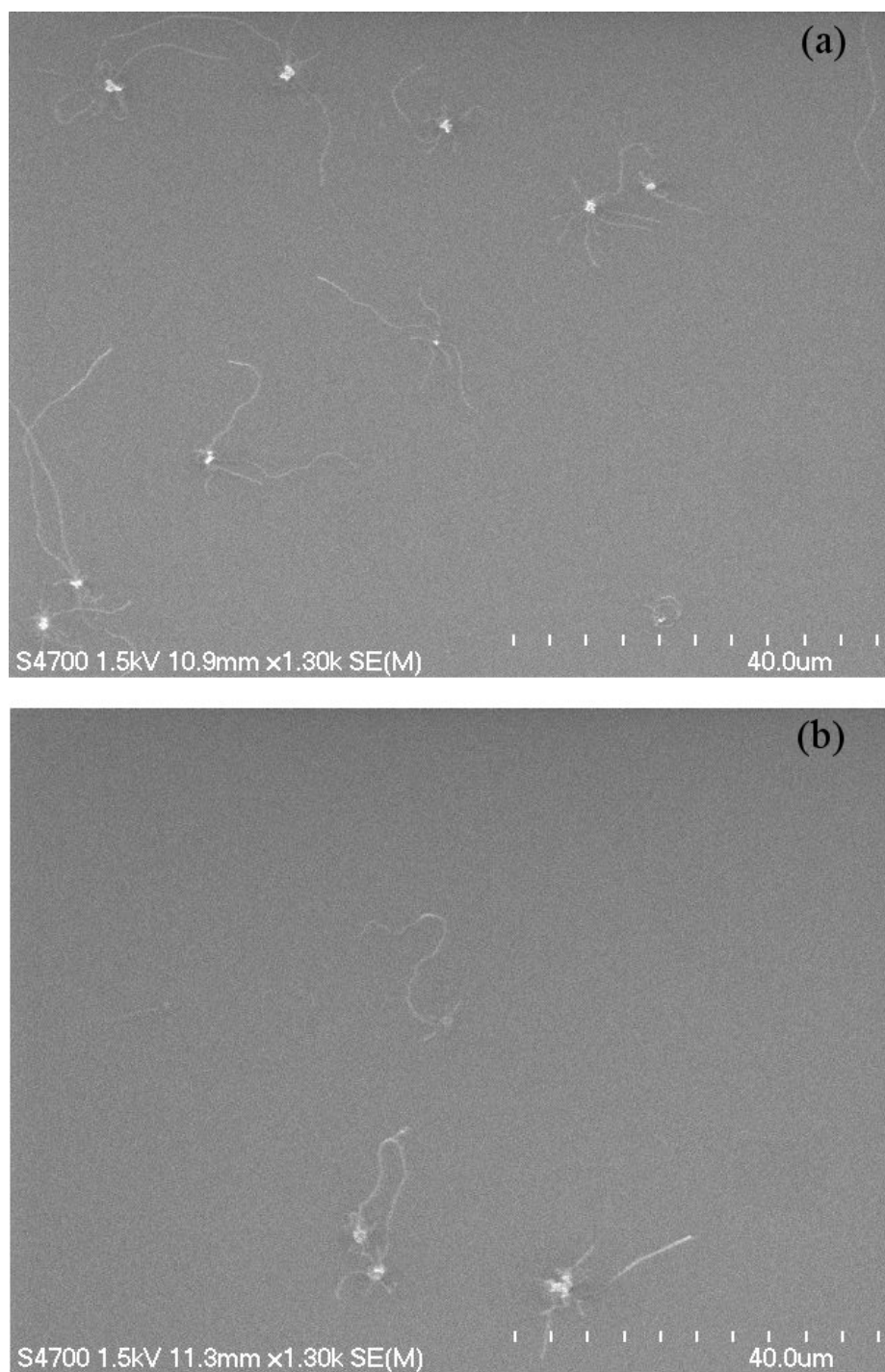


Figure 3.5: Different synthesized CNTs with different gas flow rate. CNTs were grown using the same recipes except of lower flow rate in (a) and higher one in (b). After scrutinizing at various sites on the wafers, SEM images were captured for the typical morphology of CNTs. The orientations of CNTs did not show the preference to the direction of gas flows.

measurements on the substrate without further process, the considerable error margins of diameter measurement as well as the inability to distinguish a SWNT from a MWNT or even a CNT bundle makes those techniques not ideal candidates for detailed investigation. Our project aims to characterize CNTs much more accurately using TEM imaging and electron diffraction on suspended CNTs for the atomic structure. For the purposes of TEM imaging and diffraction pattern, CNTs must be long for multiple imaging and straight to avoid artifacts caused by structural deformation. Also the yield of CNTs can not be too high to avoid excessive CNTs which short the circuits. These prerequisites require corresponding modifications to the original synthesis recipes.

### 3.3.2 Experimental Process

The recipes used in this project for SWNTs, DWNTs and FWNTs synthesis are guided by Dr. Liu's group at Duke University [19, 29, 30, 31].

Different catalytic nanoparticles, mainly iron compounds of  $\text{Fe}(\text{NO}_3)_3$ ,  $\text{FeSi}_2$  and a mixture of  $\text{Mg}(\text{NO}_3)_2$ ,  $(\text{NH}_4)_6\text{Mo}_7\text{O}_{24}$  and  $\text{Co}(\text{NO}_3)_2$ , are used in SWNT, DWNT and FWNT syntheses, respectively. Detailed procedures are described in Appendix A. The catalysts are first dissolved or suspended in methanol, the solution/suspension is then diluted for a lower concentration. The goal is to apply the catalysts onto the substrate without clumping once solvent is evaporated, hence a surfactant polymer is added in the catalyst solution. This polymer can be burned in air before the CNT growth with an extra annealing process. The nanoparticles are then uniformly distributed on the substrate by titrating the appropriate amount of the solution/suspension.

The synthesis of CNTs on quartz wafers, rather than on ordinary  $\text{SiO}_2$  substrates, has proven to be an effective way for long and aligned CNTs growth [27] with the application of various metal catalysts [32], as shown in Figure 3.6. Despite the long and straight CNTs, such approach is not preferred in this project for its high density of grown CNTs, which makes the device fabrication difficult.

As discussed earlier, the size of the nanoparticles affects the diameter of the CNTs significantly, therefore the synthesis of MWNTs, the diameters of which are usually larger than SWNTs, requires larger catalytic nanoparticles. However, one should note that the size of catalytic nanoparticles only defines the maximum diameter, whereas the diameter of one individual resultant CNT can not be pre-determined. So far, no effective approach has been reported to produce a high concentration of a CNT of specific chiral structure. Catalyst size is also an important factor in DWNT synthesis. Since  $\text{FeSi}_2$  catalyst used in the synthesis can't dissolve in methanol, the pulverization of particles is required, as illustrated in Figure 3.7. The ideal size of  $\text{FeSi}_2$  nanoparticles for DWNTs growth is smaller than  $1\ \mu\text{m}$ . Currently, traditional physical grinding is unable to provide a uniform size of nanoparticles, and more studies in future are required.

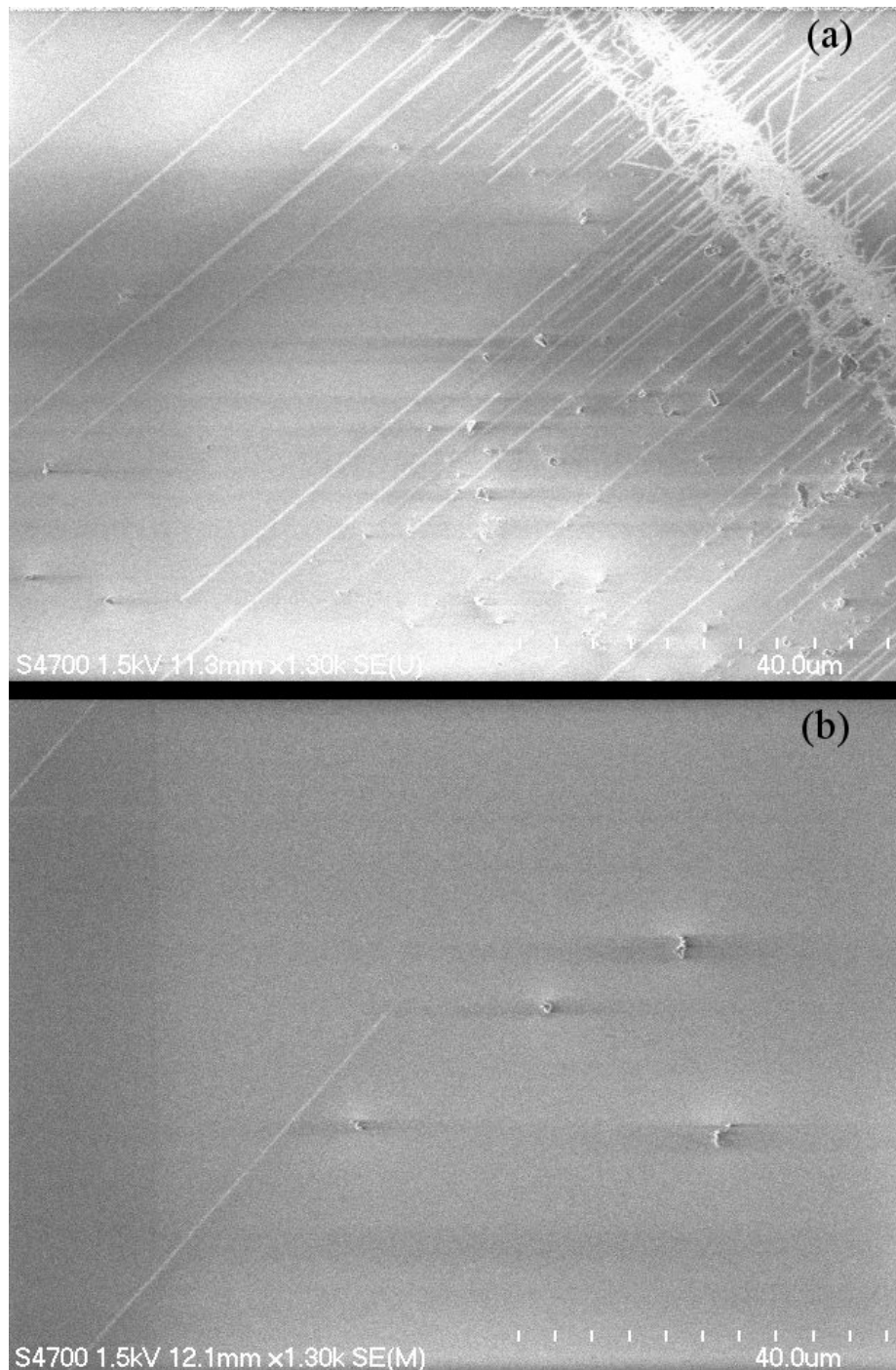


Figure 3.6: Long and aligned CNTs grown on a quartz wafer with (a) high and (b) proper concentrations.

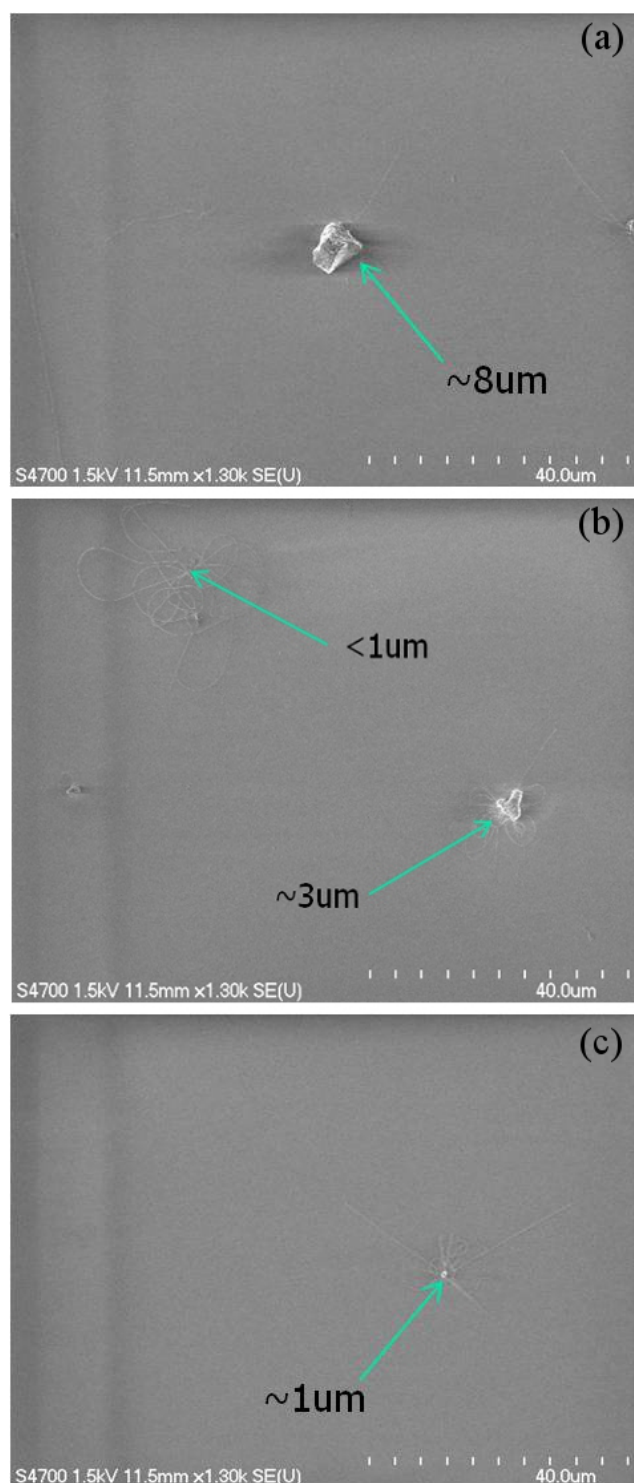


Figure 3.7: Synthesis of DWNTs with different sizes of  $\text{FeSi}_2$  nanoparticles varying from (a) 8  $\mu\text{m}$  to (b,c) less than 1  $\mu\text{m}$ : The SEM images of the synthesis results show that the growth tends to take place at the catalyst islands of size smaller than 1  $\mu\text{m}$ .

Even though it is claimed that low gas flow rate is able to stabilize the flow above the substrate and therefore produce straight and long CNTs, the empirical results in our experiments indicate that the gas flow rate has to be relatively large, and should be tuned for each recipe and CVD system. Moreover, given the enormous amount of CNTs synthesized on the wafer after the growth, the sample size is usually not large enough to accurately determine the distribution of CNTs' lengths and structures.

### 3.3.3 Synthesis Results

Immediately after the synthesis, the substrate is able to be imaged with an SEM for the density and length distribution of CNTs.

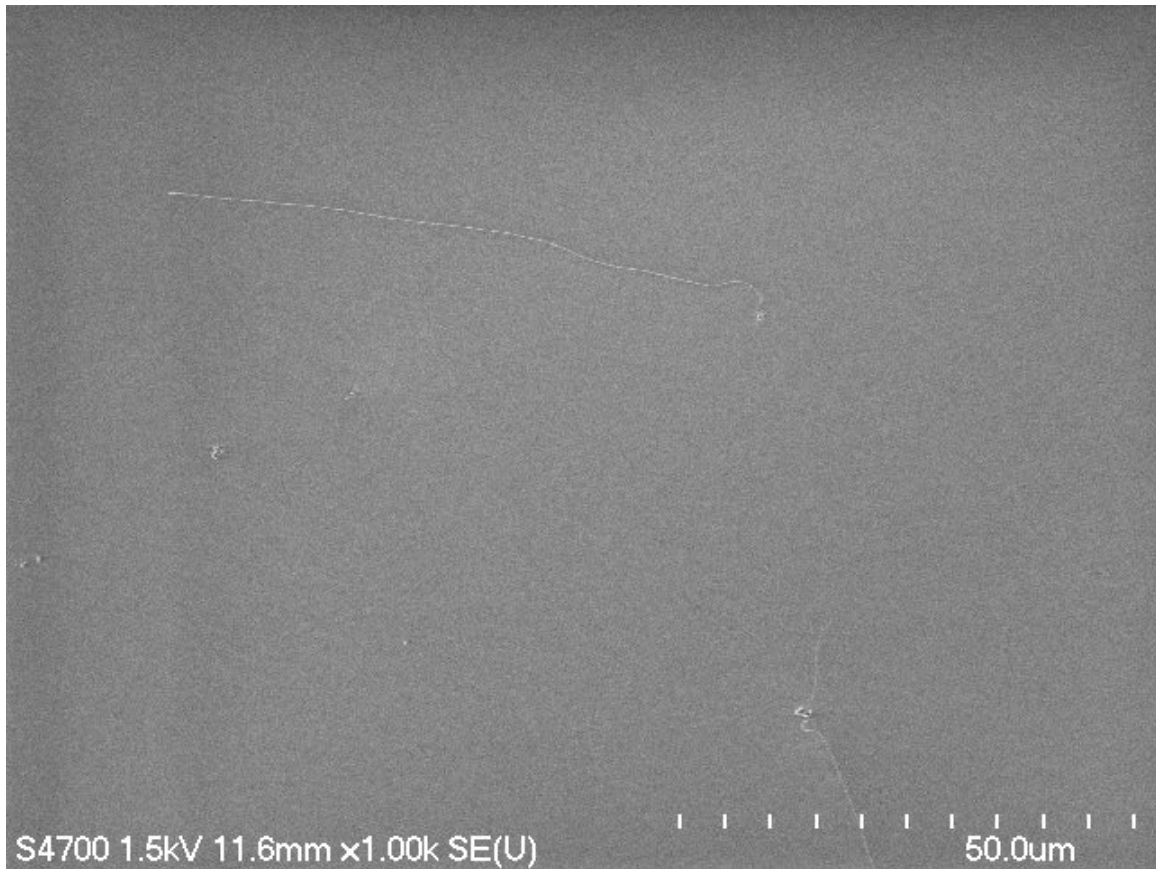


Figure 3.8: SEM image of a substrate with proper distribution of SWNTs.

To further investigate the properties of the synthesized CNTs, the information such as chiralities and diameters can be acquired by imaging the suspended CNTs, which are directly grown on a  $\text{Si}_3\text{N}_4$  grid or a pre-FIB-etched silicon wafer, as shown in Figure 3.9 and Figure 3.10.



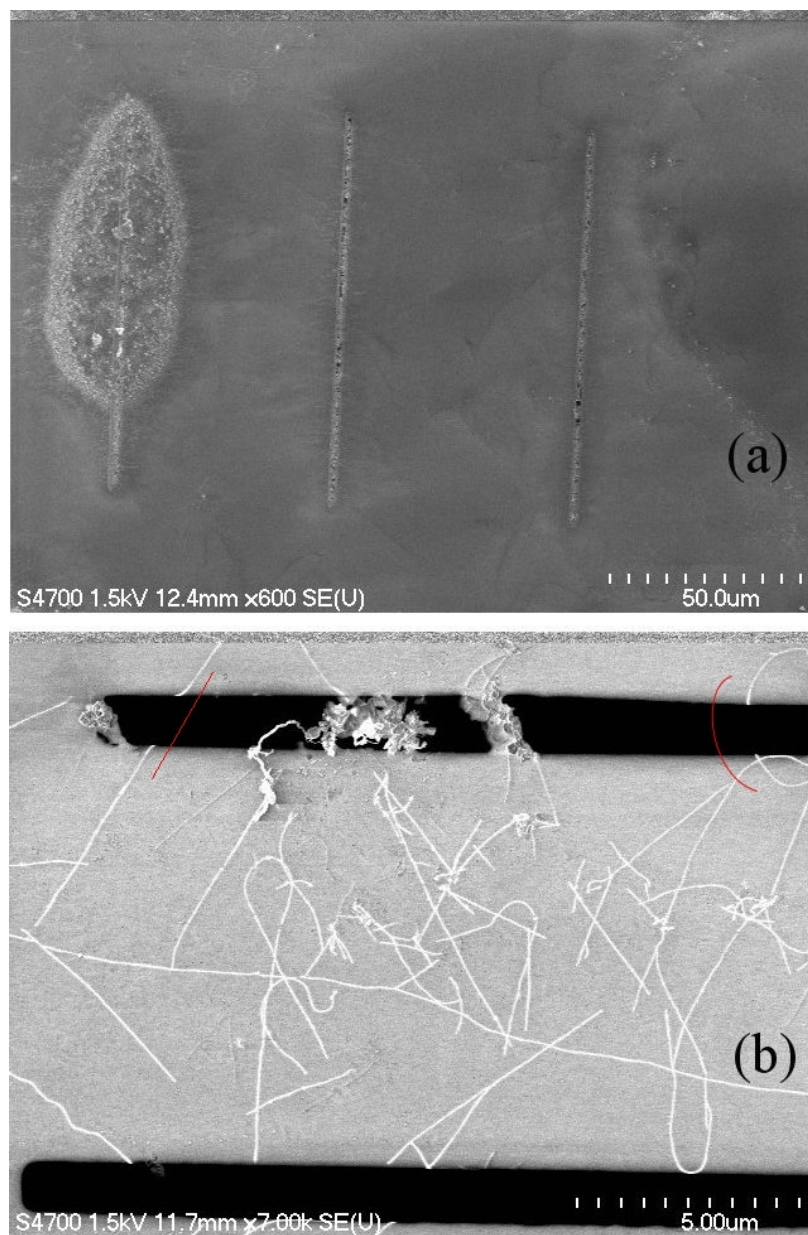


Figure 3.9: Synthesis of CNTs on pre-etched Si/SiO<sub>2</sub> substrates captured with SEM at (a) low and (b) high magnification. Note that, at the high magnification in (b), the suspended part of CNTs are indistinguishable without the substrate.



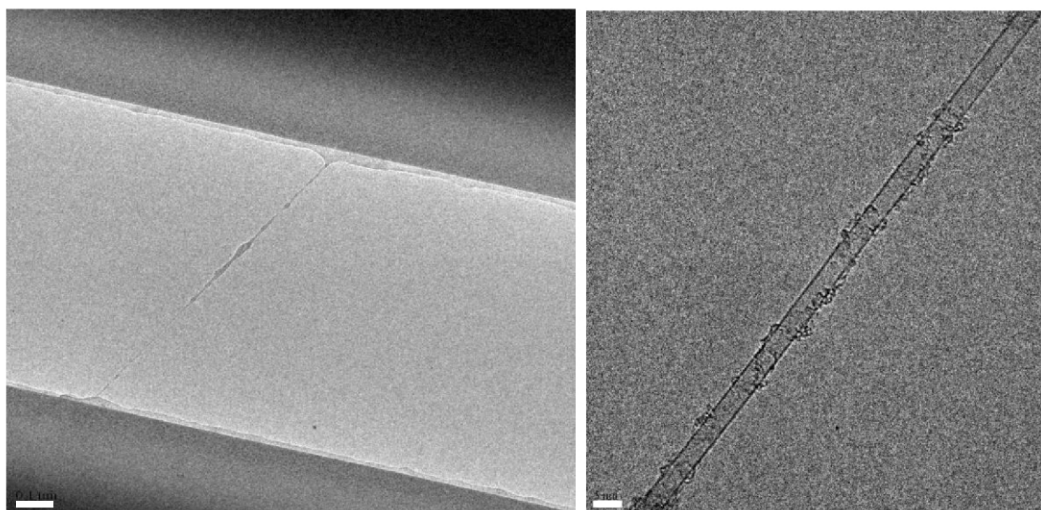


Figure 3.10: Low (left) and high magnifications TEM images of a SWNT grown on a pre-etched substrate with  $\text{Fe}(\text{NO}_3)_3$  catalyst. Scale bars represent  $0.1 \mu\text{m}$  (left) and  $5 \text{ nm}$ , respectively.

## BIBLIOGRAPHY

- [1] S. Iijima *et al.*, “Helical microtubules of graphitic carbon,” *Nature*, vol. 354, no. 6348, pp. 56–58, 1991.
- [2] T. Guo, P. Nikolaev, A. Thess, D. Colbert, and R. Smalley, “Catalytic growth of single-walled nanotubes by laser vaporization,” *Chemical Physics Letters*, vol. 243, no. 1, pp. 49–54, 1995.
- [3] A. Thess, R. Lee, P. Nikolaev, H. Dai, P. Petit, J. Robert, C. Xu, Y. H. Lee, S. G. Kim, A. G. Rinzler, *et al.*, “Crystalline ropes of metallic carbon nanotubes,” *Science-AAAS-Weekly Paper Edition*, vol. 273, no. 5274, pp. 483–487, 1996.
- [4] H. Cheng, F. Li, G. Su, H. Pan, L. He, X. Sun, and M. Dresselhaus, “Large-scale and low-cost synthesis of single-walled carbon nanotubes by the catalytic pyrolysis of hydrocarbons,” *Applied Physics Letters*, vol. 72, no. 25, pp. 3282–3284, 1998.
- [5] L. Yuan, K. Saito, W. Hu, and Z. Chen, “Ethylene flame synthesis of well-aligned multi-walled carbon nanotubes,” *Chemical Physics Letters*, vol. 346, no. 1, pp. 23–28, 2001.
- [6] Y. Zhang, M. Gamo, C. Xiao, and T. Ando, “Liquid phase synthesis of carbon nanotubes,” *Physica B: Condensed Matter*, vol. 323, no. 1, pp. 293–295, 2002.
- [7] R. Baker, P. Harris, R. Thomas, and R. Waite, “Formation of filamentous carbon from iron, cobalt and chromium catalyzed decomposition of acetylene,” *Journal of Catalysis*, vol. 30, no. 1, pp. 86–95, 1973.
- [8] R. Baker, “Catalytic growth of carbon filaments,” *Carbon*, vol. 27, no. 3, pp. 315–323, 1989.
- [9] J. Gavillet, A. Loiseau, C. Journet, F. Willaime, F. Ducastelle, and J.-C. Charlier, “Root-growth mechanism for single-wall carbon nanotubes,” *Physical Review Letters*, vol. 87, no. 27, p. 275504, 2001.
- [10] H. Dai, “Nanotube growth and characterization,” in *Carbon Nanotubes*, pp. 29–53, Springer, 2001.
- [11] A. M. Cassell, J. A. Raymakers, J. Kong, and H. Dai, “Large scale cvd synthesis of single-walled carbon nanotubes,” *The Journal of Physical Chemistry B*, vol. 103, no. 31, pp. 6484–6492, 1999.
- [12] M. Su, B. Zheng, and J. Liu, “A scalable cvd method for the synthesis of single-walled carbon nanotubes with high catalyst productivity,” *Chemical Physics Letters*, vol. 322, no. 5, pp. 321–326, 2000.
- [13] N. R. Franklin and H. Dai, “An enhanced cvd approach to extensive nanotube networks with directionality,” *Advanced Materials*, vol. 12, no. 12, pp. 890–894, 2000.
- [14] B. Zheng, C. Lu, G. Gu, A. Makarovski, G. Finkelstein, and J. Liu, “Efficient cvd growth of single-walled carbon nanotubes on surfaces using carbon monoxide precursor,” *Nano Letters*, vol. 2, no. 8, pp. 895–898, 2002.
- [15] J. Kong, A. M. Cassell, and H. Dai, “Chemical vapor deposition of methane for single-walled carbon nanotubes,” *Chemical Physics Letters*, vol. 292, no. 4, pp. 567–574, 1998.
- [16] K. Hata, D. N. Futaba, K. Mizuno, T. Namai, M. Yumura, and S. Iijima, “Water-assisted highly efficient synthesis of impurity-free single-walled carbon nanotubes,” *Science*, vol. 306, no. 5700, pp. 1362–1364, 2004.
- [17] Z. Ren, Z. Huang, D. Wang, J. Wen, J. Xu, J. Wang, L. Calvet, J. Chen, J. Klemic, and M. Reed, “Growth of a single freestanding multiwall carbon nanotube on each nanonickel dot,” *Applied Physics Letters*, vol. 75, no. 8, pp. 1086–1088, 1999.
- [18] J. Bai and A. Allaoui, “Effect of the length and the aggregate size of mwnts on the improvement efficiency of the mechanical and electrical properties of nanocompositesexperimental investigation,” *Composites Part A: applied science and manufacturing*, vol. 34, no. 8, pp. 689–694, 2003.

- [19] H. Qi, C. Qian, and J. Liu, "Synthesis of high-purity few-walled carbon nanotubes from ethanol/methanol mixture," *Chemistry of Materials*, vol. 18, no. 24, pp. 5691–5695, 2006.
- [20] C. L. Cheung, A. Kurtz, H. Park, and C. M. Lieber, "Diameter-controlled synthesis of carbon nanotubes," *The Journal of Physical Chemistry B*, vol. 106, no. 10, pp. 2429–2433, 2002.
- [21] L. Huang, S. J. Wind, and S. P. O'Brien, "Controlled growth of single-walled carbon nanotubes from an ordered mesoporous silica template," *Nano Letters*, vol. 3, no. 3, pp. 299–303, 2003.
- [22] S. Huang, M. Woodson, R. Smalley, and J. Liu, "Growth mechanism of oriented long single walled carbon nanotubes using fast-heating chemical vapor deposition process," *Nano Letters*, vol. 4, no. 6, pp. 1025–1028, 2004.
- [23] Y. T. Lee, J. Park, Y. S. Choi, H. Ryu, and H. J. Lee, "Temperature-dependent growth of vertically aligned carbon nanotubes in the range 800–1100 c," *The Journal of Physical Chemistry B*, vol. 106, no. 31, pp. 7614–7618, 2002.
- [24] M. Kumar and Y. Ando, "Controlling the diameter distribution of carbon nanotubes grown from camphor on a zeolite support," *Carbon*, vol. 43, no. 3, pp. 533–540, 2005.
- [25] Y. Joon Yoon, J. Cheol Bae, H. Koo Baik, S. Cho, S.-J. Lee, and K. Moon Song, "Growth control of single and multi-walled carbon nanotubes by thin film catalyst," *Chemical Physics Letters*, vol. 366, no. 1, pp. 109–114, 2002.
- [26] O. Nerushev, S. Dittmar, R.-E. Morjan, F. Rohmund, and E. Campbell, "Particle size dependence and model for iron-catalyzed growth of carbon nanotubes by thermal chemical vapor deposition," *Journal of Applied Physics*, vol. 93, no. 7, pp. 4185–4190, 2003.
- [27] L. Ding, D. Yuan, and J. Liu, "Growth of high-density parallel arrays of long single-walled carbon nanotubes on quartz substrates," *Journal of the American Chemical Society*, vol. 130, no. 16, pp. 5428–5429, 2008.
- [28] M. S. Marcus, J. M. Simmons, S. E. Baker, R. J. Hamers, and M. A. Eriksson, "Predicting the results of chemical vapor deposition growth of suspended carbon nanotubes," *Nano Letters*, vol. 9, no. 5, pp. 1806–1811, 2009.
- [29] Q. Fu, S. Huang, and J. Liu, "Chemical vapor depositions of single-walled carbon nanotubes catalyzed by uniform fe<sub>2</sub>o<sub>3</sub> nanoclusters synthesized using diblock copolymer micelles," *The Journal of Physical Chemistry B*, vol. 108, no. 20, pp. 6124–6129, 2004.
- [30] L. Ding, W. Zhou, T. P. McNicholas, J. Wang, H. Chu, Y. Li, and J. Liu, "Direct observation of the strong interaction between carbon nanotubes and quartz substrate," *Nano Research*, vol. 2, no. 11, pp. 903–910, 2009.
- [31] H. Qi, C. Qian, and J. Liu, "Synthesis of uniform double-walled carbon nanotubes using iron disilicide as catalyst," *Nano Letters*, vol. 7, no. 8, pp. 2417–2421, 2007.
- [32] D. Yuan, L. Ding, H. Chu, Y. Feng, T. P. McNicholas, and J. Liu, "Horizontally aligned single-walled carbon nanotube on quartz from a large variety of metal catalysts," *Nano Letters*, vol. 8, no. 8, pp. 2576–2579, 2008.

## CHAPTER 4

### Nano-Electromechanical Device Based on a Suspended CNT

#### 4.1 Introduction

CNTs have been the perfect material candidates for nano-electromechanical system due to the incredible strength and the tiny size. In order to measure its physical properties, experiments have been conducted with various designs and fabrication techniques.

One of the first experiments was designed to investigate the mechanical resonance of a single arc-produced and clamped MWNT with *in situ* TEM measurement and the resonant frequency in the order of 1 MHz was observed within an induced electric field [1]. Such single clamped device is easier to build in experiments, however the configuration is not suitable to measure the structure of CNTs or any electric response to the resonance.

Therefore, NEMS devices based on double clamped CNTs have been proposed. The first successful configuration used a suspended CNT anchored by the source and drain electrodes on each end [2, 3, 4], where the trench beneath the CNT was etched prior to the CNT synthesis at selective catalyst sites [5], then an AFM tip was used to push directly or indirectly on the CNT to cause stresses, and the electric conductance of CNT responding to the bending was simultaneously measured, as illustrated in Figure 4.1.

This NEMS configuration allows one to fabricate a microscopical mechanical oscillator [6], where the electrical resonance of CNTs due to different capacitance was detected. The high resonant frequency and small mass of this oscillator systems makes it an ideal candidate for sensitive mass detection. Several groups used CNT electromechanical oscillators to detect the absorption of individual atoms and their masses [7, 8].

However, the synthesis of CNTs over an open trench requires precise parameters of the CVD process, which results in a low yield and the conditions in different systems vary significantly. Accordingly, different fabrication techniques have been developed to circumvent the difficulty for a suspended CNT NEMS device.

One of the alternative approaches is based on the work done by Walters *et al.* [9], where CNTs were synthesized on the wafer first and then the substrate beneath the CNTs was targeted and removed with lithography and etching techniques, respectively. This approach also provides opportunities to fabricate more complex NEMS devices, such a nano-pendulum where a paddle was deposited onto a CNT which was later

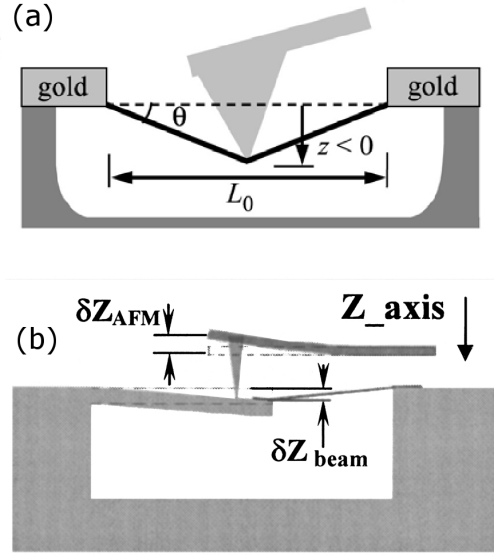


Figure 4.1: Experiment geometry for applying strain and gate voltage with an AFM tip, and measuring conductance with contacts. (a) Direct [4] and (b) indirect [3] push on CNT.

suspended [10] and can be driven by an external electric field or an AFM tip [11]. Several studies have been done with this approach to investigate the behaviors of CNTs under torsional strain [12, 13, 14, 15, 16]. Our project follows this work to design and fabricate an NEMS device based on a suspended CNT for simultaneous torsional strain and electron diffraction measurement, which will be discussed in the following sections.

## 4.2 Device Fabrication

### 4.2.1 Basic Configuration

Inspired by the previous work [9, 11, 13], devices incorporating an individual SWNT, DWNT or FWNT have the same fundamental architecture: one part of the CNT should be unsupported from the substrate while bears a relative small metal paddle, the motion of which in the electric field caused by a side gate electrode will apply a torsional stress directly onto the CNT; the suspended CNT allows the free rotation as well as the imaging with a TEM. While beyond the paddle part, the CNT is anchored by electrodes for electrical measurement; another trench between the electrodes should be etched away to suspend an untwisted CNT to determine the initial structure, as illustrated in Figure 4.3. A detailed procedure of the fabrication is given in Appendix B.

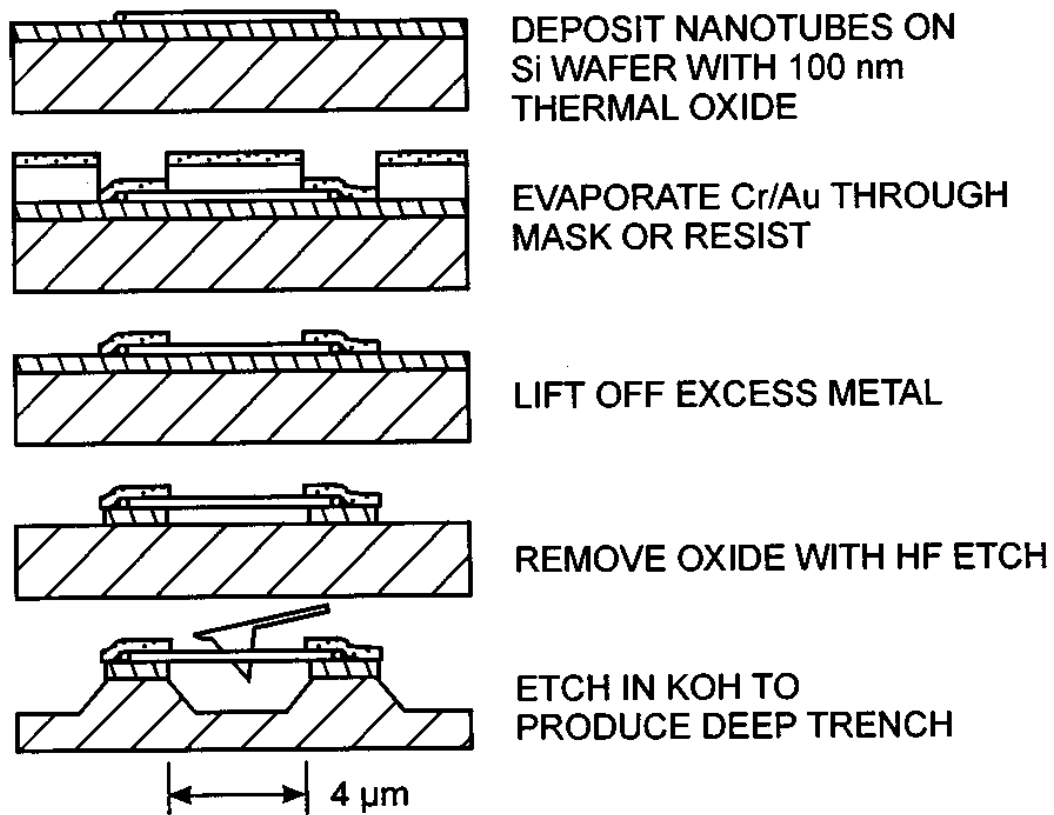


Figure 4.2: Schematic illustration of the fabrication processes of suspended CNT NEMS [9].

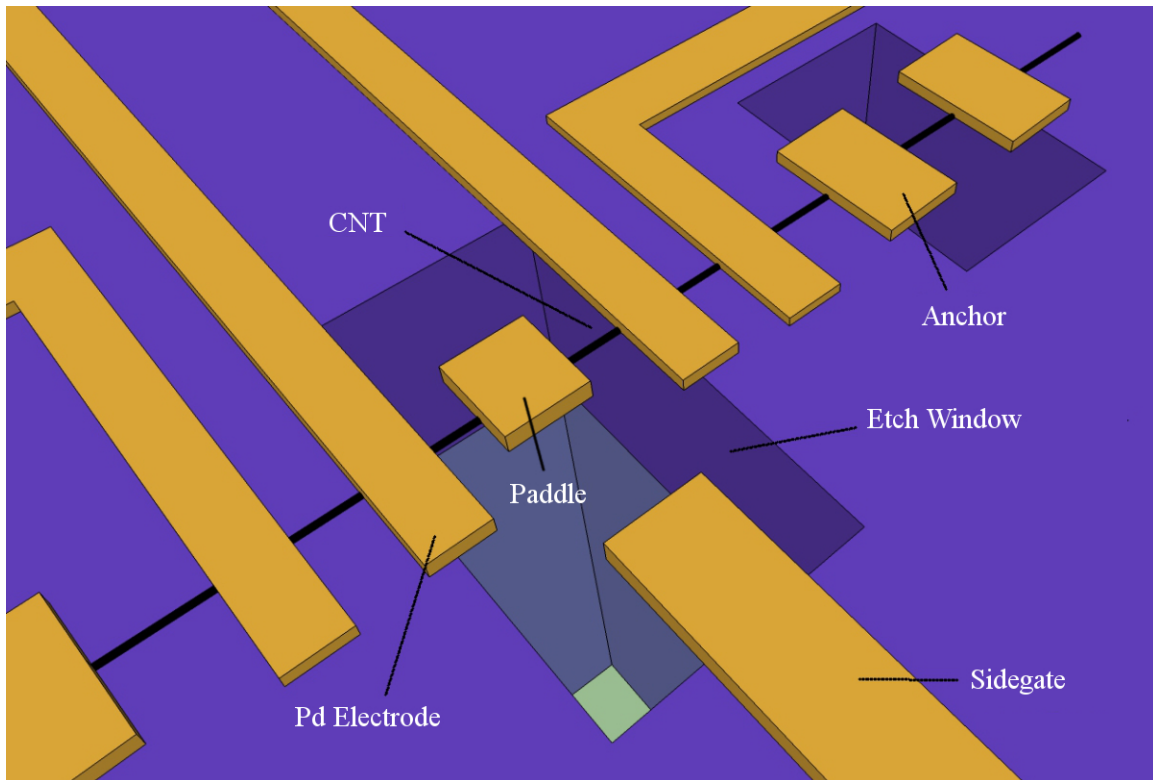


Figure 4.3: Schematic of the suspended CNT NEMS device ready for *in situ* TEM imaging. A suspended CNT is anchored by source and drain electrodes and bearing a metal paddle, the substrate beneath which is removed for TEM imaging.

### 4.2.2 Back Etching

Unlike other NEMS devices where only parts of the substrate beneath the CNT were etched, the purpose of TEM imaging requires an open window beneath the CNT. Due to the common thickness of silicon wafer is in the order of micron, it is necessary to prepare a pre-etched substrate at the beginning of device fabrication.

The wafer substrate chosen for device fabrication is 500  $\mu\text{m}$  Si wafer coated with 300 nm  $\text{Si}_3\text{N}_4$  films on both sides. Photolithography is conducted with a mask to pattern 1 mm  $\times$  1 mm windows on the back side followed by Deep Reactive Ion Etching (DRIE) to remove the  $\text{Si}_3\text{N}_4$  membrane in those windows. The next layer of Si is then etched away with KOH, given the etching rate of  $\text{Si}_3\text{N}_4$  in KOH is much slower than that of Si, the remain  $\text{Si}_3\text{N}_4$  outside the windows protect the beneath Si from excess etching, whereas KOH is an anisotropic Si etchant and etches Si(100) with an angle of  $54.74^\circ$  from the plane at an etching rate approximate 1  $\mu\text{m}$  per minute. Therefore, when the etching depth reaches 400  $\mu\text{m}$ , the size of window shrinks to 0.8 mm  $\times$  0.8 mm. The remained Si membrane supports the top  $\text{Si}_3\text{N}_4$  membrane during future sonication. As the etching of Si in KOH may take several hours, the top  $\text{Si}_3\text{N}_4$  membrane is inevitably etched as well. Hence any existing defects will be significantly magnified afterwards, which results in pin holes in micron that will severely damage the integrity of the circuits. Therefore, additional layers of  $\text{Si}_3\text{N}_4$  and  $\text{SiO}_2$  are required to be deposited on the top after all the etching processes to cover possible pin holes. The processes are shown in Figure 4.4.

### 4.2.3 Fabrication of Circuit and Paddle

CNTs of different structure in proper density can be grown on the pre-etched substrate with the approaches described in Chapter 3. Eight macroscopic electrodes are first deposited with Electron Beam Lithography (EBL) onto the top of substrate within a 80  $\mu\text{m}$   $\times$  80  $\mu\text{m}$  sample area right above the pre-etched 0.8 mm  $\times$  0.8 mm window, as shown in Figure 4.6 and Figure 4.5.

The widths of electrodes in the pattern vary from 1 mm, large enough to be measured with contact pins, to 4  $\mu\text{m}$ , comparable to the length of CNTs. The electrodes consist of a bi-layer metal film of Cr/Au where Cr works as an adhesive layer to the substrate while Au provides good conductance with CNTs. Any CNTs connecting two electrodes are then broken by a large current to prevent short-circuits, as illustrated in Figure 4.7 (the maximum voltage applied between electrodes is limited to 100 mV to prevent the electrodes from melting).

Narrower leads are then deposited to connect the macroscopic electrodes to the CNT with another EBL. A double-layer poly-methyl methacrylate(PMMA) photoresist is spin-coated for a liftoff of thick metal. Figure 4.8 illustrates the liftoff process using double-layer PMMA. Higher-molecular weight PMMA is



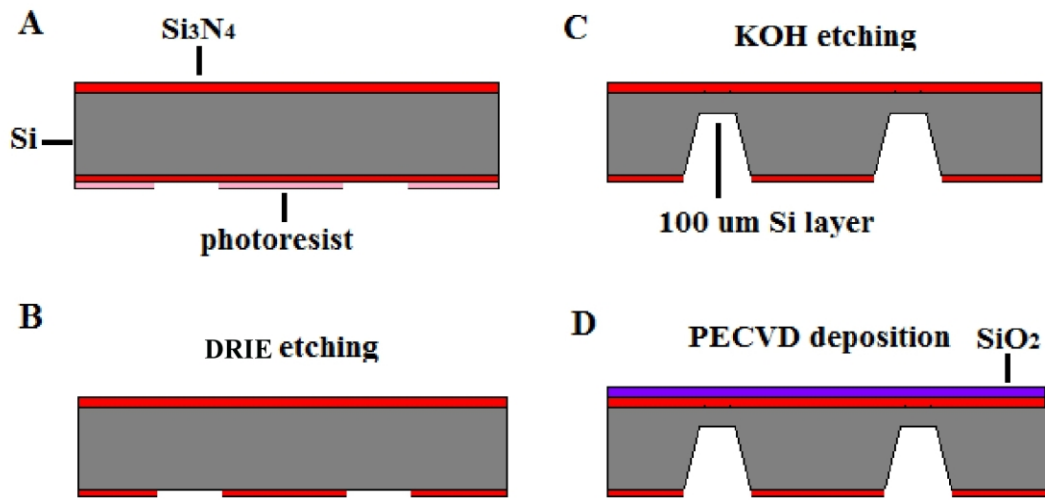


Figure 4.4: Schematic of back etching processes for device fabrication. (A) Photolithography is performed on the backside of the wafer. The photoresist protects the covered area from DRIE etching. (B) DRIE etching is applied to etch the silicon nitride without the protection of photoresist. (C) The sample is dipped in 15% KOH solution for silicon etching. Etching is stopped when the etching depth reaches 400  $\mu\text{m}$ . 100  $\mu\text{m}$   $\text{Si}$  layer is left as a support for the  $\text{Si}_3\text{N}_4$  layer. (D) A 40 nm silicon nitride film and 300 nm  $\text{SiO}_2$  film are deposited onto the top surface of the wafer by PECVD.

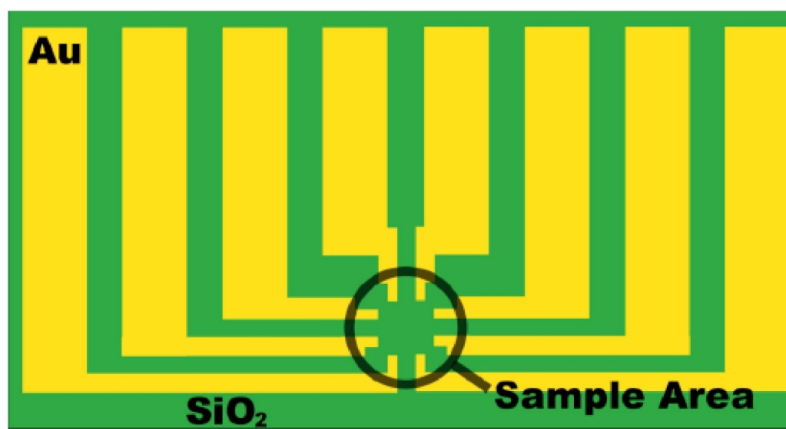


Figure 4.5: Schematic of the macroscopic electrodes deposited onto a wafer by photolithography. The schematic is not drawn to scale for illustration purpose [17].

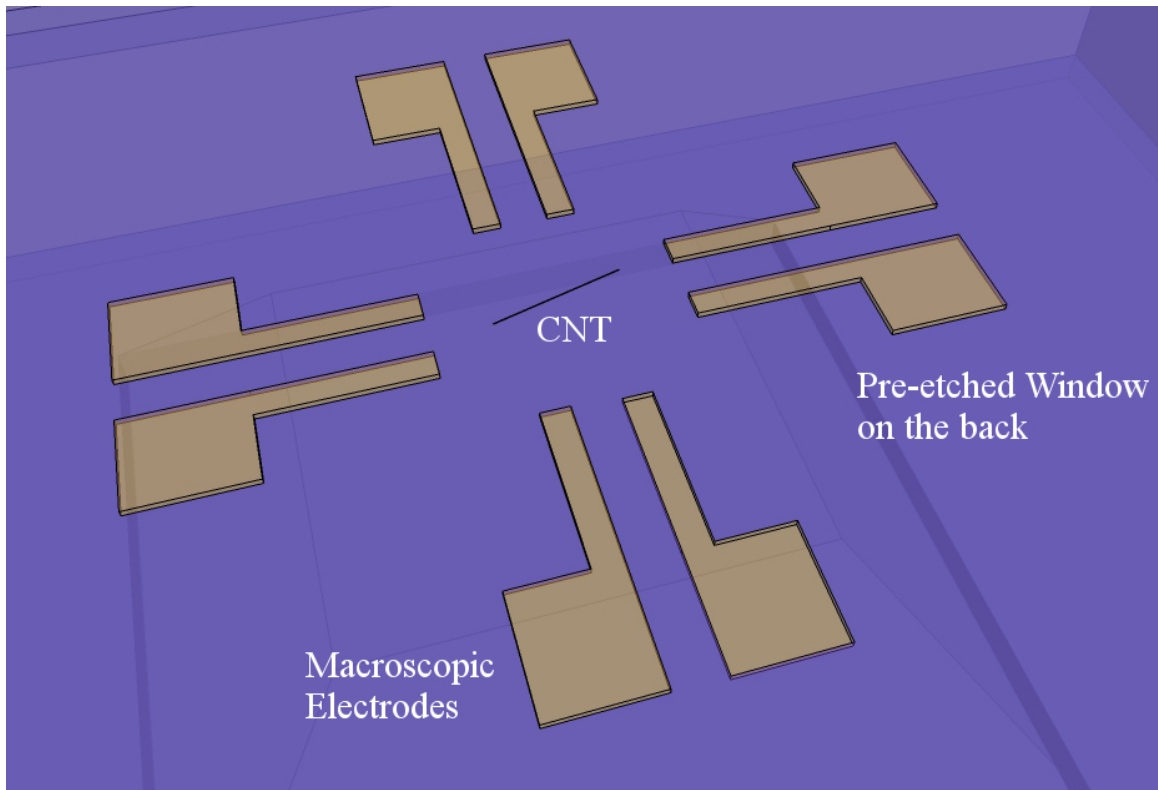


Figure 4.6: Schematic of the alignment of electrodes to the window on the back. Note that the schematic is not drawn to the scale since the top of window is about 100 times larger than the sample area.

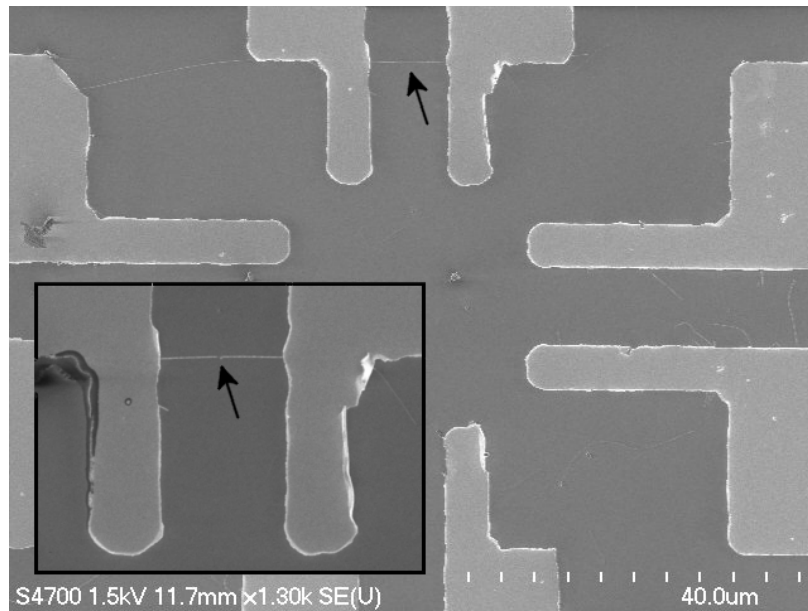


Figure 4.7: Comparison of a CNT connecting two electrodes before and after burn out (inset). A portion of CNT was evaporated (indicated by the arrow) by the heat caused by high current.

deposited over a lower-molecular-weight PMMA layer. After development, the lower-molecular-weight layer gives a larger aperture to form significant undercut to avoid the over exfoliation of metal due to the ductility. Given in direct contact with CNTs, Pd is chosen for the leads due to the negligible Schottky barriers between Pd and CNTs resulting in near-ohmic electrical contacts [18, 19, 20].

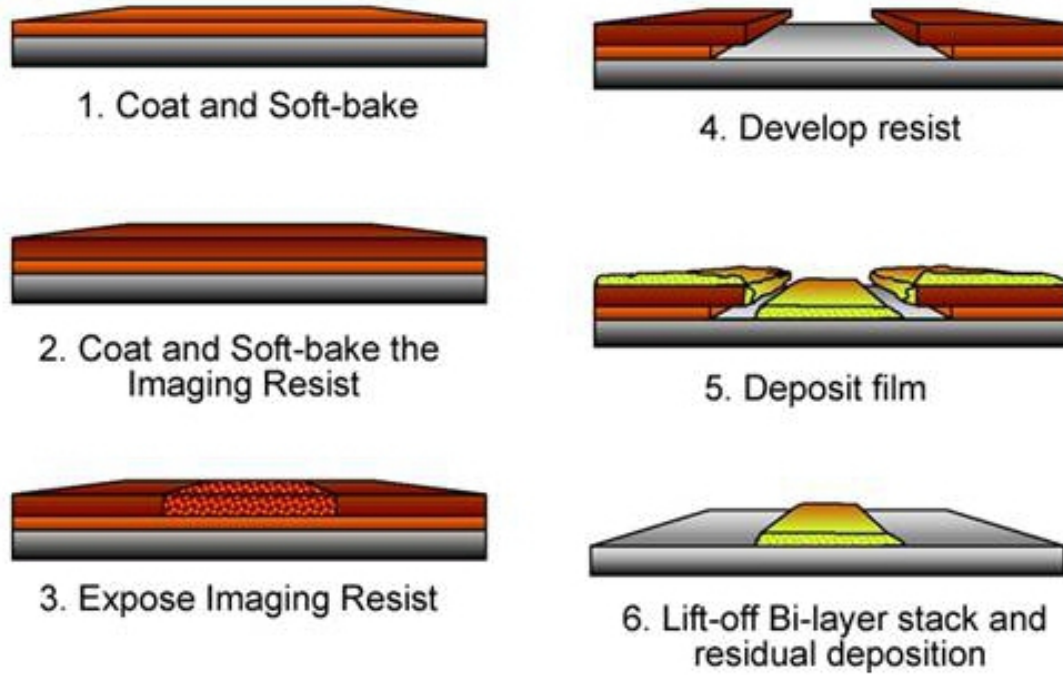


Figure 4.8: Schematic of EBL liftoff process using double-layer PMMA.

Spatial resolution of e-beam exposure is set by the distribution width of secondary electrons, which is the combination of secondary electron generation and their straggling range in resist. The secondary electron generation by back-scattered electrons is negligible since it is distributed over a range of about  $5 \mu\text{m}$  with very small intensity. The range of secondary electron generation by the forward-scattered electrons can be approximately calculated by the following equation,

$$B = 625 \left( \frac{Z}{E_0} \right) t^{3/2} \frac{\rho^{1/2}}{A} \quad (4.1)$$

where  $B$  is the increase in the diameter of the beam at the bottom of the resist,  $Z$ ,  $A$ ,  $\rho$  and  $t$  are the atomic number, atomic weight, density and thickness of the resist, respectively, and  $E_0$  is the electron beam energy. For our process, the incident beam spread at the resist-substrate interface is about  $4.5 \text{ nm}$ . The straggling range of secondary electrons is about  $2-3 \text{ nm}$ , therefore the best estimation of EBL resolution is about  $7 \text{ nm}$ .

However, due to the inaccurate alignment and the mechanical drift of SEM, the experimental resolution is usually much larger than this value, around 100 nm.

To align the patterns better in the EBL process, two kinds of alignment markers are applied. The corners of the macroscopic electrodes are first used for coarse alignment, and the fine alignment is based on four fiducials deposited on the wafer, which improves the accuracy from 2  $\mu\text{m}$  to 200 nm. The experimental EBL process can be accomplished in two approaches as shown in Figure 4.9(a) and Figure 4.9(b). Figure 4.9(a) illustrates the first approach that the fiducials and most of the larger patterns are first deposited after the coarse alignment, and the fine alignment to the fiducials allows the accurately locating the finer structures. However due to the accumulation of drift during two EBL steps, the relative positions between the paddle and the leads could be different from the design. To overcome the difficulty, Figure 4.9(b) illustrates a better method that only the fiducials are deposited first and then all the patterns according to the existing fiducials. Although this approach is still subject to possible drift, the deposition of patterns within one single EBL assures the proper relative positions. Moreover, given the drift in the exposure is unidirectional with a fixed speed, the patterns are sequenced in proper order, while the positions of the patterns in the rear of queue are adjusted accordingly to compensate the drift, as shown in Figure 4.10.

With the target CNTs connected to the electrodes via Pd leads, the device is ready for electrical measurements. Note that given only eight macroscopic electrodes available in one device, four-probe measurement may not be always applicable in every device.

#### 4.2.4 Suspending Nanotube

Wet etching with HNA (hydrofluoric/nitric/acetic acid) on the back, Focused Ion Beam (FIB) on the back, another wet etching with Buffered Hydrofluoric acid (BHF) within the windows patterned with EBL on the front followed by Critical Point Drying (CPD) are applied sequentially to remove the remaining Si,  $\text{Si}_3\text{N}_4$  and  $\text{SiO}_2$  substrates beneath the CNTs. At last, the sample is dried with CPD to protect the CNTs from breaking due to the surface tension. Figure 4.11 shows an SEM image of a sample after Si and  $\text{Si}_3\text{N}_4$  windows were etched away, where the CNTs are supported by a thin membrane of  $\text{SiO}_2$ . The hollow crossing and square in the center are perforated with FIB for the alignment and the test measurement of substrate thickness. Also note that BHF etching of  $\text{SiO}_2$  membrane should be confined inside the FIB-etched windows. Since over-etching will result in the exfoliation of Pd leads and poor electrical contacts. Figure 4.12 illustrates suspended CNTs after the BHF etching.

The ultimate structure of the NEMS device is schematized in Figure 4.13 with the corresponding TEM image in Figure 4.14, where one CNT attached with a metal paddle is completely suspended from the substrate.

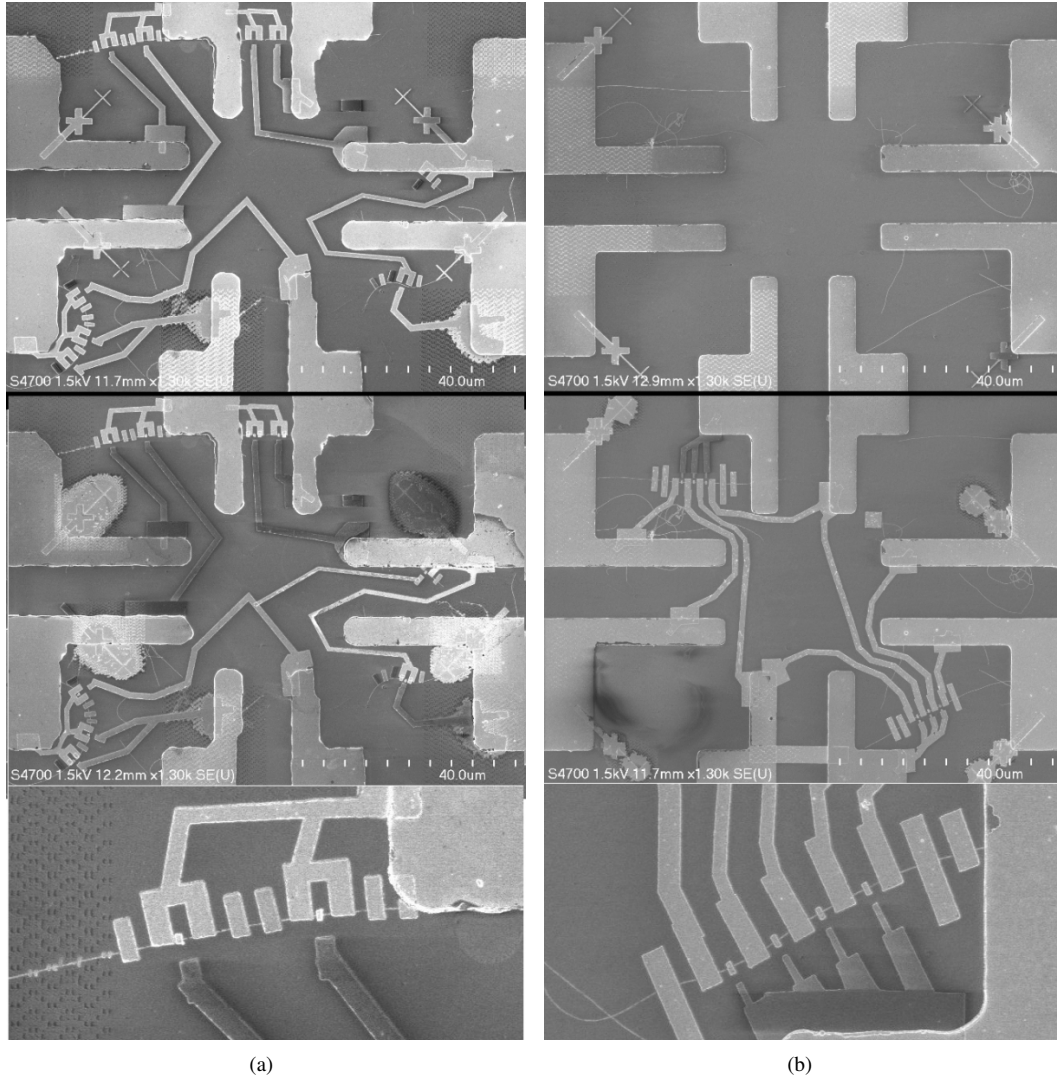


Figure 4.9: Comparison of two EBL processes with the original and the modified (right) sequences of fiducials and patterns. The leads and the paddles in the top figure were deposited by two EBLs, which are subject to the drift and misalignment.

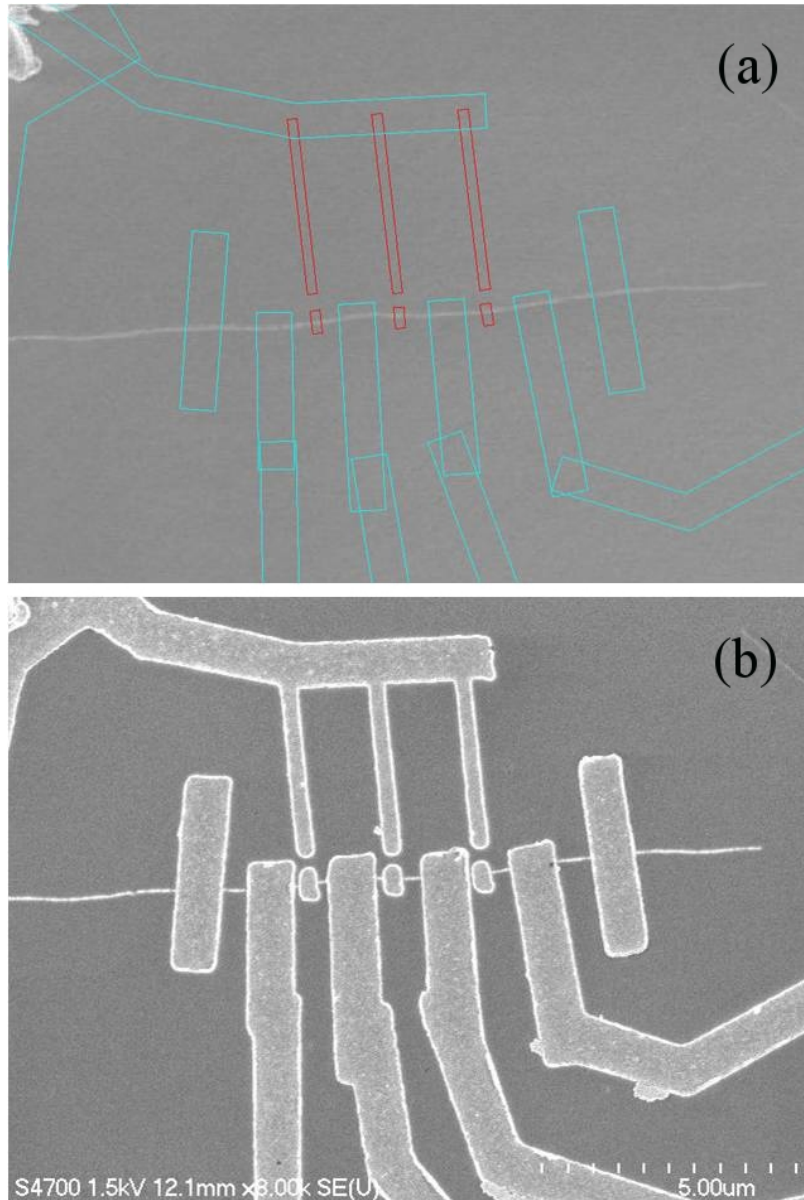


Figure 4.10: Comparison of (a) schematic of EBL design pattern and (b) the actual result. Note that, all the green patterns were first exposed and then the red ones, while the latter is subject to the drift of electron beam to the left. Moreover, the resultant patterns are always larger than the design due to the diffraction of electron beam.

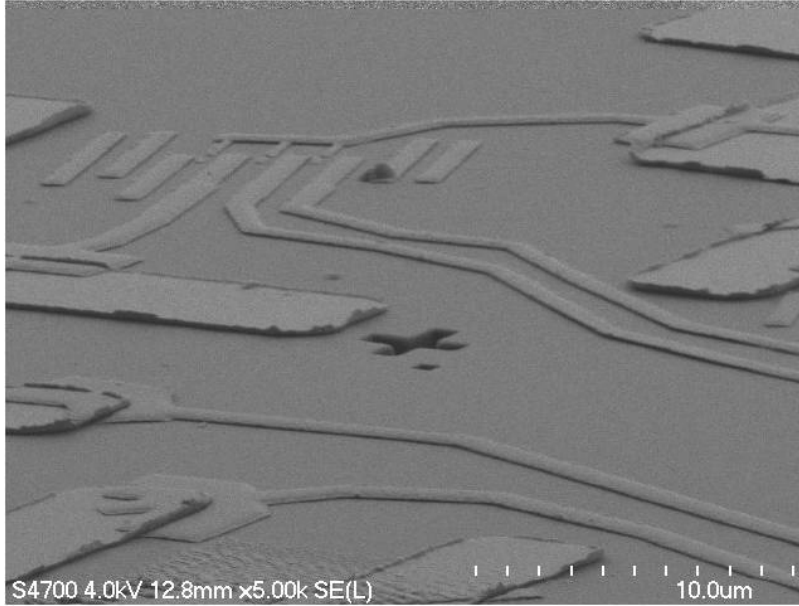


Figure 4.11: A SEM image of a device after Si and Si<sub>3</sub>N<sub>4</sub> windows beneath the paddles were removed with FIB.

### 4.3 Customized NEMS Specimen Holder for *in situ* TEM

In order to carry out the *in situ* electromechanical test in a TEM, a special specimen holder is required. Because the functional part of the experimental setup must fit within the limited volume available in the TEM, the thickness is one of the most stringent dimensional constraints, which is controlled by the gap between the pole pieces of the objective lens. This constraint becomes stricter as the resolution increases since higher resolution usually means a smaller gap.

TEM specimen holders testing CNTs have been designed and engineered for various purposes, from the less sophisticated thermal resonance [21], to the more complicated TEM/STM [22] or TEM/AFM [23]. Based on the experiences of the precursors of the NEMS systems for mechanical testing, a specific TEM specimen holder has been designed which allows measurement of strain by TEM observations and electric responses on CNTs. The complete setup for *in situ* TEM testing using this NEMS device is shown in Figure 4.15.

The specimen holder is made up with 4 major parts: shaft, device stage, head and tail feedthroughs. The aluminum shaft is designed according to the factory made JEOL 2010F holder, also with two grooves on the shaft body for o-rings to seal the vacuum. Feedthroughs at the two ends are designed for wire connections to 8 pins on the samples and are set to the shaft by vacuum glue. While the tail feedthrough is commercially available, the head feedthrough is self designed because of the small size and the irregularity of pin hole positions. Anode oxidation is applied on the head feedthrough to provide an insulating layer from the pin leads.



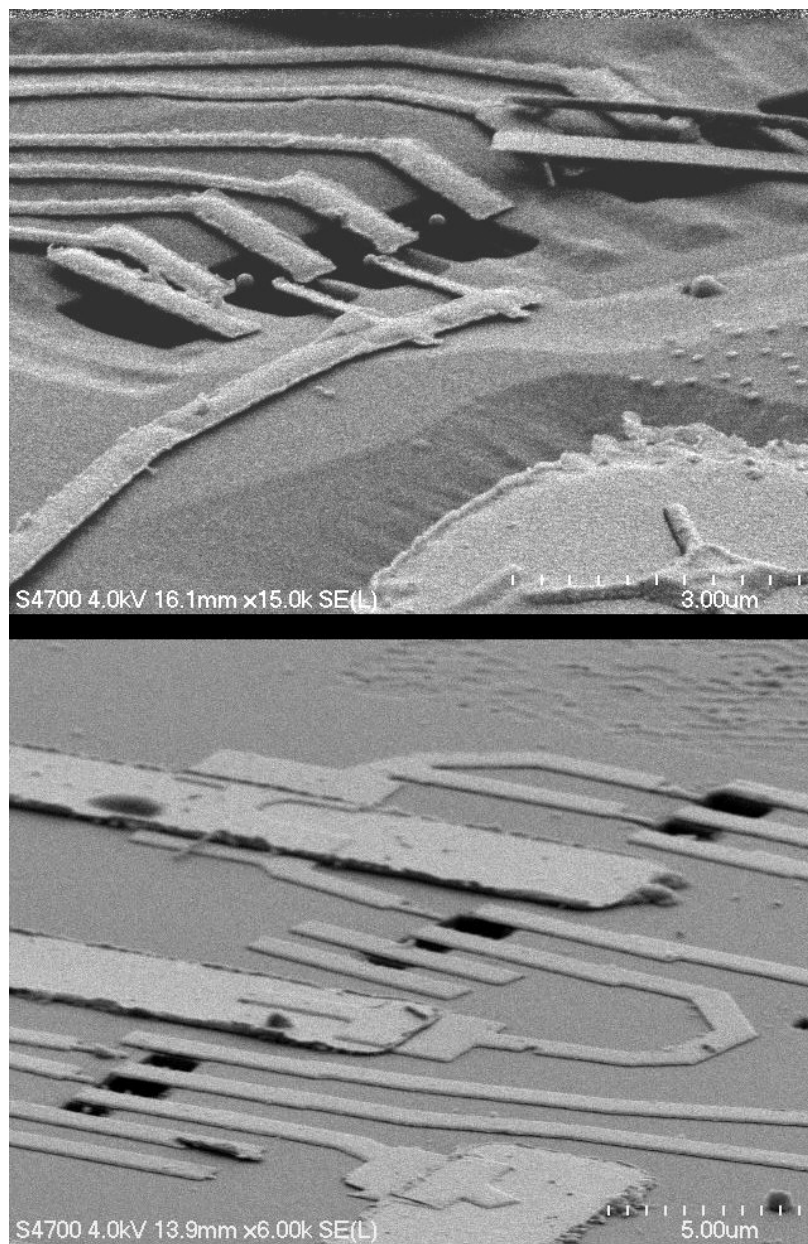


Figure 4.12: SEM images of a sample after CNTs are suspended from the substrate. Note that the top one is over-etched so that the Pd leads are undercut and even peeled off from the substrate.



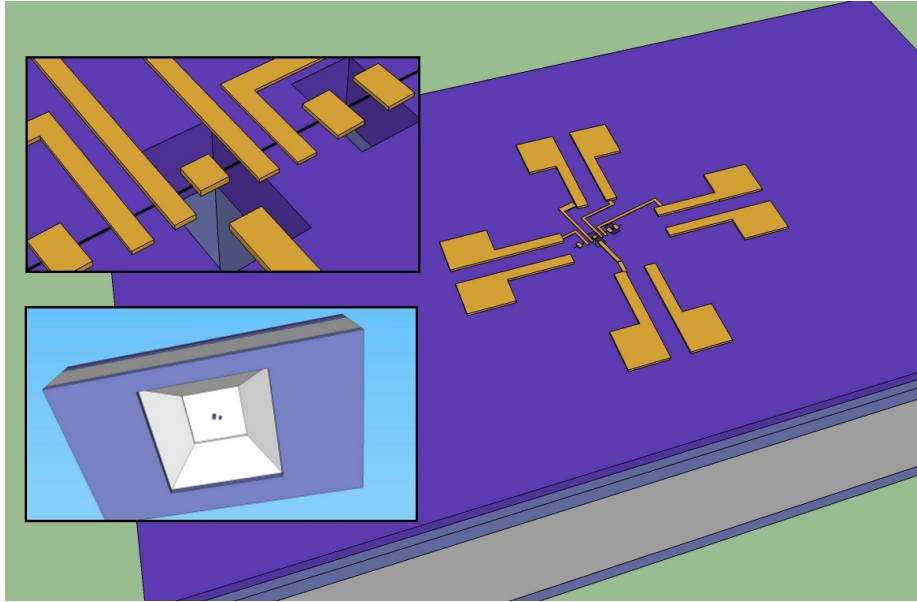


Figure 4.13: Schematic of the final structure of the NEMS device. The insets show the zoomed in view of the playground and the back view of the sample.

The pins going out of the head feedthrough are connected to the leads on the grooves of the sample stage, which are made from phosphor bronze due to the high elasticity and low Hooke constant. Another insulated aluminum pad is screwed to clamp the specimen with the stage. When the specimen is clamped and pushed onto the leads, the bent ends create good contacts between the leads and the electrodes.

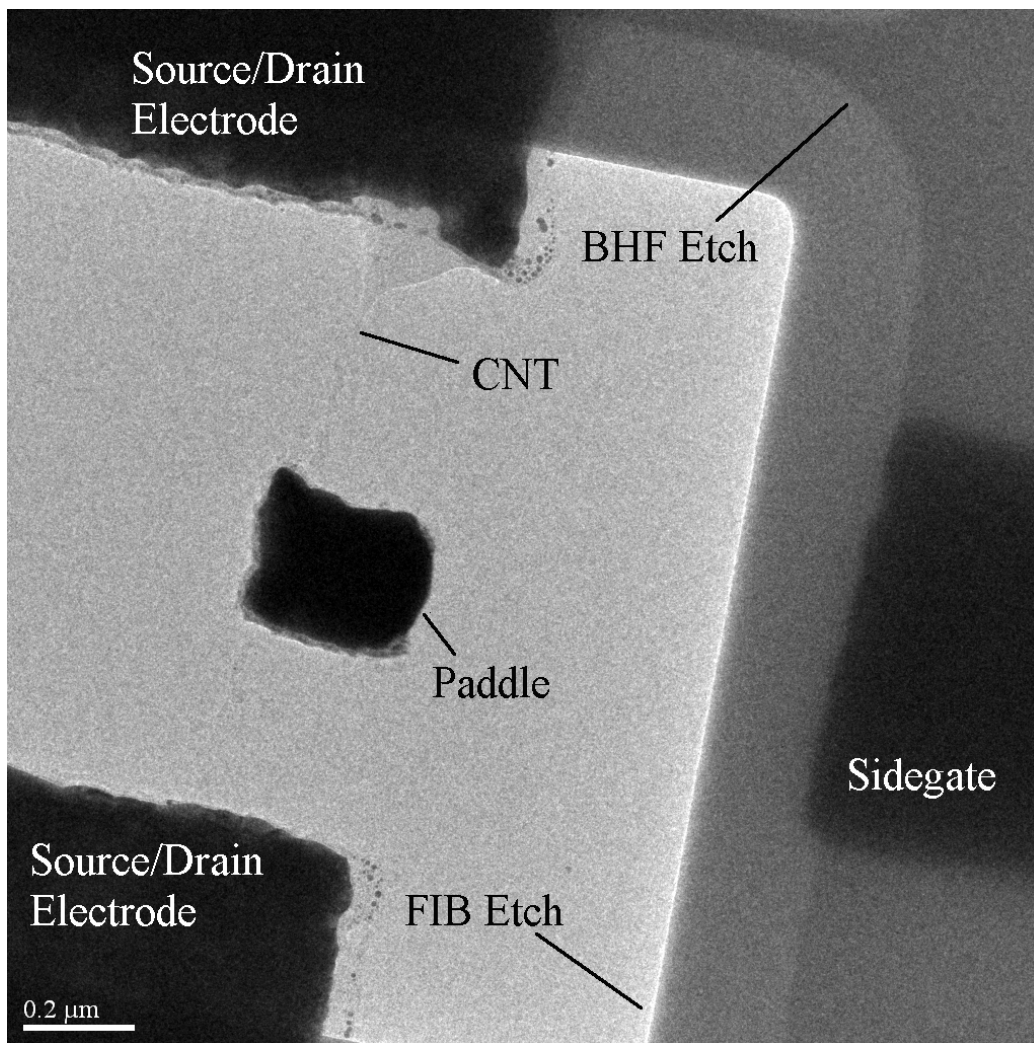


Figure 4.14: A TEM image of the NEMS device. The paddle can be driven by the electric field induced by the sidegate. Two windows etched by FIB and BHF are overlapped but with different sizes.

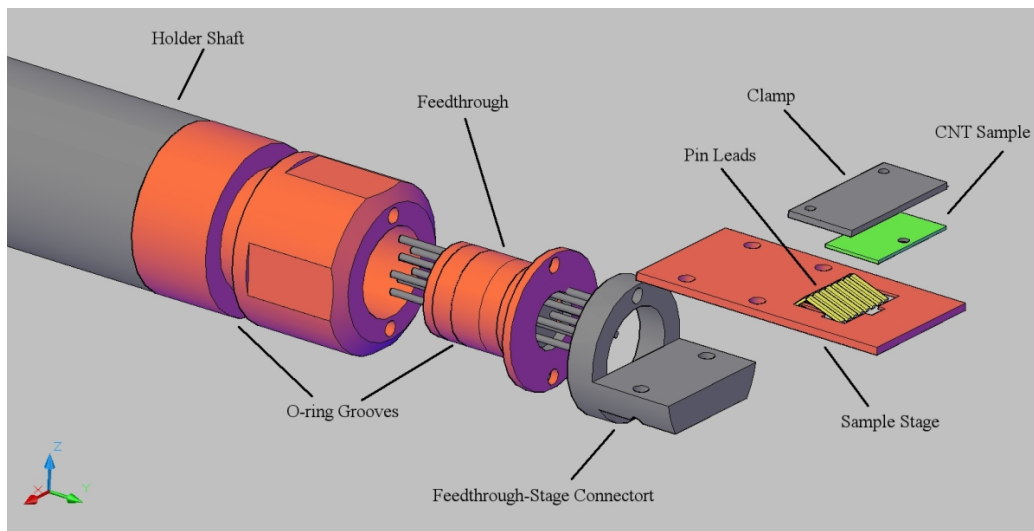


Figure 4.15: Schematic of the TEM specimen holder for *in situ* NEMS experiment. CNT sample is fixed facing downward by the aluminum clamp and the sample stage, where the phosphor bronze pin leads are in good contact with the electrodes on the sample. The hole on the stage are aligned with the playground of the sample so that during TEM imaging the electron beam directly hits on the CNT. The pin leads are wired to the feedthrough which then go through the holder shaft.

## BIBLIOGRAPHY

- [1] P. Poncharal, Z. Wang, D. Ugarte, and W. A. de Heer, “Electrostatic deflections and electromechanical resonances of carbon nanotubes,” *Science*, vol. 283, no. 5407, pp. 1513–1516, 1999.
- [2] T. W. Tombler, C. Zhou, L. Alexseyev, J. Kong, H. Dai, L. Liu, C. Jayanthi, M. Tang, and S.-Y. Wu, “Reversible electromechanical characteristics of carbon nanotubes under local-probe manipulation,” *Nature*, vol. 405, no. 6788, pp. 769–772, 2000.
- [3] J. Cao, Q. Wang, and H. Dai, “Electromechanical properties of metallic, quasimetallic, and semiconducting carbon nanotubes under stretching,” *Physical Review Letters*, vol. 90, no. 15, p. 157601, 2003.
- [4] E. Minot, Y. Yaish, V. Sazonova, J.-Y. Park, M. Brink, and P. L. McEuen, “Tuning carbon nanotube band gaps with strain,” *Physical Review Letters*, vol. 90, no. 15, p. 156401, 2003.
- [5] N. R. Franklin, Q. Wang, T. W. Tombler, A. Javey, M. Shim, and H. Dai, “Integration of suspended carbon nanotube arrays into electronic devices and electromechanical systems,” *Applied Physics Letters*, vol. 81, no. 5, pp. 913–915, 2002.
- [6] V. Sazonova, Y. Yaish, H. Üstünel, D. Roundy, T. A. Arias, and P. L. McEuen, “A tunable carbon nanotube electromechanical oscillator,” *Nature*, vol. 431, no. 7006, pp. 284–287, 2004.
- [7] H.-Y. Chiu, P. Hung, H. W. C. Postma, and M. Bockrath, “Atomic-scale mass sensing using carbon nanotube resonators,” *Nano Letters*, vol. 8, no. 12, pp. 4342–4346, 2008.
- [8] K. Jensen, K. Kim, and A. Zettl, “An atomic-resolution nanomechanical mass sensor,” *Nature Nanotechnology*, vol. 3, no. 9, pp. 533–537, 2008.
- [9] D. Walters, L. Ericson, M. Casavant, J. Liu, D. Colbert, K. Smith, and R. Smalley, “Elastic strain of freely suspended single-wall carbon nanotube ropes,” *Applied Physics Letters*, vol. 74, no. 25, pp. 3803–3805, 1999.
- [10] P. Williams, S. Papadakis, A. Patel, M. Falvo, S. Washburn, and R. Superfine, “Fabrication of nanometer-scale mechanical devices incorporating individual multiwalled carbon nanotubes as torsional springs,” *Applied Physics Letters*, vol. 82, no. 5, pp. 805–807, 2003.
- [11] P. Williams, S. Papadakis, A. Patel, M. Falvo, S. Washburn, and R. Superfine, “Torsional response and stiffening of individual multiwalled carbon nanotubes,” *Physical Review Letters*, vol. 89, no. 25, p. 255502, 2002.
- [12] T. Cohen-Karni, L. Segev, O. Srur-Lavi, S. R. Cohen, and E. Joselevich, “Torsional electromechanical quantum oscillations in carbon nanotubes,” *Nature Nanotechnology*, vol. 1, no. 1, pp. 36–41, 2006.
- [13] A. Hall, L. An, J. Liu, L. Vicci, M. Falvo, R. Superfine, and S. Washburn, “Experimental measurement of single-wall carbon nanotube torsional properties,” *Physical Review Letters*, vol. 96, no. 25, p. 256102, 2006.
- [14] A. R. Hall, M. R. Falvo, R. Superfine, and S. Washburn, “Electromechanical response of single-walled carbon nanotubes to torsional strain in a self-contained device,” *Nature Nanotechnology*, vol. 2, no. 7, pp. 413–416, 2007.
- [15] K. Nagapriya, S. Berber, T. Cohen-Karni, L. Segev, O. Srur-Lavi, D. Tománek, and E. Joselevich, “Origin of torsion-induced conductance oscillations in carbon nanotubes,” *Physical Review B*, vol. 78, no. 16, p. 165417, 2008.
- [16] A. R. Hall, M. R. Falvo, R. Superfine, and S. Washburn, “A self-sensing nanomechanical resonator built on a single-walled carbon nanotube,” *Nano Letters*, vol. 8, no. 11, pp. 3746–3749, 2008.

- [17] A. R. Hall, *Material and device investigations on a carbon nanotube-based torsional nanoelectromechanical system*. PhD thesis, University of North Carolina at Chapel Hill, 2007.
- [18] D. Mann, A. Javey, J. Kong, Q. Wang, and H. Dai, "Ballistic transport in metallic nanotubes with reliable pd ohmic contacts," *Nano Letters*, vol. 3, no. 11, pp. 1541–1544, 2003.
- [19] A. Javey, J. Guo, Q. Wang, M. Lundstrom, and H. Dai, "Ballistic carbon nanotube field-effect transistors," *Nature*, vol. 424, no. 6949, pp. 654–657, 2003.
- [20] W. Kim, A. Javey, R. Tu, J. Cao, Q. Wang, and H. Dai, "Electrical contacts to carbon nanotubes down to 1 nm in diameter," *Applied Physics Letters*, vol. 87, p. 173101, 2005.
- [21] Z. Wang, P. Poncharal, and W. De Heer, "Measuring physical and mechanical properties of individual carbon nanotubes by in situ tem," *Journal of Physics and Chemistry of Solids*, vol. 61, no. 7, pp. 1025–1030, 2000.
- [22] K. Svensson, Y. Jompol, H. Olin, and E. Olsson, "Compact design of a transmission electron microscope-scanning tunneling microscope holder with three-dimensional coarse motion," *Review of Scientific Instruments*, vol. 74, no. 11, pp. 4945–4947, 2003.
- [23] A. Nafari, D. Karlen, C. Rusu, K. Svensson, H. Olin, and P. Enoksson, "Mems sensor for in situ tem atomic force microscopy," *Journal of Microelectromechanical Systems*, vol. 17, no. 2, p. 328, 2008.

## CHAPTER 5

### Electron Transport in Carbon Nanotubes of Known Chirality

#### 5.1 Introduction

CNTs are the perfect platforms to investigate 1-D conductors because of the large length-to-diameter ratio as well as the atomic uniformity. A CNT can be either metallic or semiconducting depending upon the structure described by the chiral indices  $(u, v)$ . In Chapter 1 we have already shown the band structure of a CNT using the zone-folding approximation  $E_g^0$  and the second order modification due to the curvature  $E_g^1$ , that

$$E_g^0 = \frac{at_0}{r}, \quad (5.1)$$

$$E_g^1 = \frac{3t_0a_{c-c}^2}{16r^2} \cos 3\theta, \quad (5.2)$$

which suggest that the band structure of a CNT of large diameter is determined by its radius, especially the armchair SWNTs with chiral angle of  $30^\circ$ , where the secondary band gap scaled by  $\frac{1}{r^2}$  becomes dominant for small CNTs. In this study the diameters of CNTs are around 5 nm, therefore the secondary band gaps in the order of 1 meV are negligible compared with the zone-approximation induced band gaps, which are normally 0.1 - 0.2 eV [1].

Coherent quantum transport in CNT systems can be studied via either the Kubo-Greenwood or the Landauer-Büttiker formalism. The Kubo-Greenwood approach can be used to evaluate the conduction within the linear response regime and gives access to the fundamental transport length scales, such as the elastic mean free path  $L_m$  and the coherence length  $L_\phi$ . While  $L_m$  is due to the elastic backscattering driven by the static perturbations such as defects and impurities;  $L_\phi$  describes the scale beyond which localization effects are suppressed because of the decoherence, such as electron-electron or electron-photon couplings.

Electron transport regimes in a CNT of length  $L$  can be distinguished on the basis of the above lengths:

Ballistic Transport Regime:  $L < L_m$

In a quasi-1D system, the conductance can be described with the Landauer formula  $G(E) = \frac{2e^2}{h} N \cdot T(E)$ , where  $G_0 = \frac{2e^2}{h}$  is the quantum conductance in one subband contributed from two electrons

spinning up and down.  $N$  is the number of subbands participating in electron transport, for a metallic CNT it is conventionally assumed that  $N = 2$  for two subbands near the Fermi level, where the energy difference between the Fermi surface and the next two subbands is much larger;  $T(E)$  is the transmission probability of electrons at the Fermi level.

According to the Landauer-Büttiker Equation, in the ideal case of a ballistic conductor with perfect contacts, *i.e.* the contact with electrodes is completely transparent with no back reflection, the transmission probability  $T$  is unity and the conductance of the system is  $G = N \cdot G_0$  for  $N$  conducting subbands and is independent of the length  $L$ .

Diffusive Transport Regime:  $L > L_m$

In this scenario, backscattering has significant impact on electron transport, a CNT will act as a normal metallic wire according to the Ohm's Law, where the resistance is length dependent. Because of the relatively small mean free path  $L_m$ , at least one collision will happen during the transport, therefore the CNT can be understood as a conductor consisting of several quantum dots, which share ballistic transport properties and are separated by the elastic collisions with phonons, electrons or defects. Assuming the transmission probability of the  $l$ -th channel is  $T_l$ , where  $0 < T_l < 1$ , each of the channels contributes to the total conductance, that  $G = N \cdot G_0 \sum_l T_l$ . The resistance hence can be expressed as

$$R = \frac{1}{G} = \frac{1}{NG_0} + \frac{1}{NG_0} \frac{L}{L_m} + R_{\text{contact}}.$$

Scatterings in the subbands of a metallic CNT, where two subbands cross at the Fermi level, and a semiconducting CNT, where they are separated by a gap  $E_g$ , are different. The backscattering in a semiconducting CNT is allowed because the subbands are mixed with  $\pi$  and  $\pi^*$  characters, whereas is forbidden in a metallic one where the character is either pure bonding or pure antibonding. Hence, it is expected that the scattering in a metallic CNT is much smaller than a doped or thermal excited semiconducting CNT.

Contact resistance is of great importance in transport measurement. When connecting materials of different work functions, the induced charge transfer and the equilibrium electric field will bend the energy bands and cause a barrier for the electron flow, namely Schottky Barrier. Schottky Barriers are universal in electric experiments on CNTs, as it was difficult to select a metal of proper work function as the contact electrode so that Schottky Barrier is a minimum.

Various experiments have been conducted to investigate the transport properties of SWNTs and MWNTs. That SWNTs are ballistic under most conditions have been generally accepted [2, 3, 4, 5]. Ballistic conduction was observed at 10 K in SWNTs from quantum oscillations in a Fabry-Perrot experiment, although low resistance of 7 k $\Omega$  in a SWNT at room temperature suggested low scattering. However, the controversy is still heated of whether MWNTs behave as ballistic [6, 7, 8, 9] or diffusive [10, 11].

Furthermore, though it is believed that the weak interaction between different shells is able to open a pseudo-gap in a high symmetric configuration, given most of MWNTs synthesized and observed in experiments are incommensurate, the impact of the interaction is negligible. Therefore a MWNT is usually considered as decoupled SWNTs, where only the outermost shell contributes to the transport property [12].

Up to date, not many experiments have been conducted to reveal both the chirality and the transport property of a CNT. Unlike other approaches to characterize CNTs, such as optical spectroscopy, atomic force microscopy and etc. [13, 14], the analysis of nano-beam electron diffraction (NBED) [15, 16, 17, 18] is one of the most accurate and reliable methods to identify the atomic structure of a CNT, for it interprets more information in reciprocal space, especially the structures of inner tubes in a MWNT [19]. Combined with HRTEM imaging, NBED allows the determination of exact chiral indices  $(u, v)$  of each shell. However, both HRTEM imaging and NBED require the observed specimen to be electron transparent, which has been usually achieved by manipulating a single CNT on a TEM grid and results in a primitive structure but a low yield rate [9, 20, 21, 22].

In this work, we report on a sophisticated technique of the fabrication of CNT based Nanoelectromechanical systems, with which the electron transport property, the chirality of an individual CNT and the correlation between the both are explored. The experimental results are compared to the theoretical prediction, and the transport mechanism is discussed based on the characteristics of CNTs.

## 5.2 Experimental Results

NEMS devices with SWNTs, DWNTs, and FWNTs are fabricated with the method discussed in the previous chapters. As a compromise of the resolution due to the high energy electrons, both real space images and NBED patterns were acquired using JEOL TEM 2010F operated at a low accelerating voltage of 80 kV for SWNT devices, which is below the threshold energy for knock-on damage to an isolated SWNT [24], and 120 kV for the other MWNT devices, presuming that MWNTs are more robust than SWNTs. With the analysis of the NBED patterns, the chiral indices were able to be determined, so were the diameters according to the HRTEM measurements. The final state of the device configuration is schematized in Figure 5.1.

More than 300 NEMS devices have been fabricated with average 2 CNTs on each device, and two thirds of which the resistance of the CNT was determined in the order of  $k\Omega$  with a linear relationship in  $I - V$  characteristics indicating good contact between Pd electrodes and CNTs. However, only about a dozen have survived the complete device fabrication processes with intact suspended CNTs for TEM investigation. Table 5.1 lists all survived CNTs with their identified chiral indices  $(u, v)$ , the lengths  $L$ , the diameters  $d$ ,



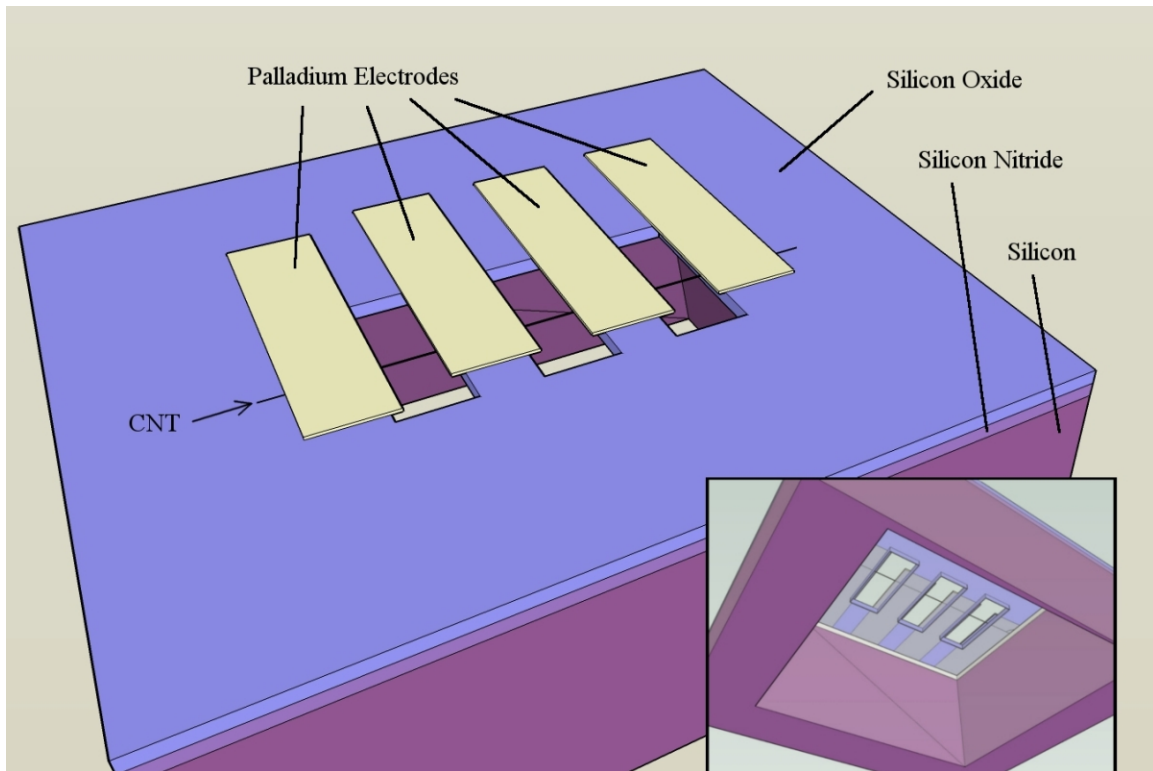


Figure 5.1: Three dimensional schematic of a 4-probe CNT device ready for HRTEM imaging and NBED. The Pd electrodes shown were deposited using EBL and thermal evaporation with width around  $1\ \mu\text{m}$ . The inset shows the upward view of the device. The huge window on Si layer was etched using KOH while  $\text{SiO}_2$  and  $\text{Si}_3\text{N}_4$  were etched using HF and FIB for small windows, respectively, the size of the small windows is usually  $1\ \mu\text{m} \times 3\ \mu\text{m}$ .

the measured resistances  $R$  and the calculated band gap  $E_g = E_g^0 + E_g^1$ , as shown in Equation (5.1) and Equation (5.2).

### 5.2.1 Determination of Chirality

The determination of chirality was guided by the approaches described in Section 2.2.4. After capturing the NBED pattern of a certain CNT, the positions of the first order primary layer lines  $L_1, L_2, L_3$  as well as one of the second order  $L_4$ , which usually has better contrast than  $L_2$  and  $L_3$  and thus more recognizable, can be located. Therefore, with at least two line spacings, the ratio between chiral indices  $\frac{v}{u}$  is given as:

$$\frac{v}{u} = \frac{2D_2 - D_1}{2D_1 - D_2}. \quad (5.3)$$

Moreover, the intensity distribution of  $L_1$  can be used to obtain the chiral index  $v$  by determining the order of the corresponding Bessel function that  $I(R, \Phi, l_1) \propto |J_v(\pi d R)|^2$ , while the signal/noise ratios of the other principal layer lines are lower due to the lower contrast and the contamination of amorphous carbon caused by excessive exposure to electrons. With the chiral indices  $(u, v)$ , the predicted diameter of the shell  $d = \frac{a\sqrt{u^2 + v^2 + uv}}{\pi}$  can be computed and compared to the corresponding measurement from the HRTEM imaging.

Figure 5.2 illustrates the NBED patterns and the HRTEM images of a SWNT. The diameter from the HRTEM images was determined as  $4.1 \pm 0.3$  nm, while the spacings in the NBED patterns was measured and listed in Table 5.2. We measured the distances from three sets of the clearest principal lines  $L_1, L_2$  and  $L_4$  to the equatorial line, which gave an averaged ratio  $\frac{v}{u} = 0.5560 \pm 0.003$ . The results of diameter and the indices ratio, several possible chiralities are listed in Table 5.3. Furthermore, the ratio of  $\frac{P_2}{P_1}$  on the principal lines  $L_1$  and  $L_4$  were measured to be 1.242 and 1.526, respectively, whereas it is unable to identify  $P_1/\Delta_{12}$  due to the large noise in the NBED pattern. The corresponding orders of the Bessel functions were unambiguously determined as  $v = 21$  and  $u - v = 7$  according to Table 2.1. Therefore, the chirality of this SWNT were identified as  $(38, 21)$ , which is semiconducting with a chiral angle of  $20.56^\circ$ . A comparison between the simulated diffraction pattern of a  $(38, 21)$  SWNT and the actual NBED result is shown in Figure 5.3.

Note that, prior to the suspension, the CNTs were all horizontally aligned on the substrates. Due to the large Young's moduli, the anchored CNTs remained straight during the NBED imaging and the angles between the incident electron beam and the CNTs were approximately  $90^\circ$ . Therefore no tilting modification to the NBED analysis is required [15, 25, 26]. This will be further discussed in the following chapter.

The NBED patterns of a MWNT can be understood as the superposition of the NBED patterns of each shell, especially for incommensurate MWNTs, where the principal layer lines of different shells do not

Table 5.1: Summary of physical properties of CNTs, where  $L$  and  $R$  are measured CNT conducting length and the corresponding resistance with low DC bias.  $(u, v)$  and  $d$  are the chiral indices and the diameter of a CNT which are determined from the NBED patterns,  $E_g$  is the band gap calculated based on zone-folding approximation plus the modification due to the curvature effect. S or M indicates whether the SWNT is semiconducting or metallic.

|    |      | $(u, v)$ | $L(\mu\text{m})$ | $d(\text{nm})$ | $E_g(\text{eV})$ | M/S | $R(\text{k}\Omega)$ |
|----|------|----------|------------------|----------------|------------------|-----|---------------------|
| 1  | SWNT | (46,16)  | 0.90             | 4.37           | 0.001            | M   | 56                  |
| 2  | SWNT | (40,7)   | 0.57             | 3.44           | 0.001            | M   | 25                  |
| 3  | SWNT | (22,13)  | 0.60             | 2.40           | 0.006            | M   | 30                  |
| 4  | SWNT | (44,24)  | 0.70             | 4.68           | 0.147            | S   | 86                  |
| 5  | SWNT | (48,7)   | 0.61             | 4.06           | 0.169            | S   | 85                  |
| 6  | SWNT | (38,21)  | 0.62             | 4.06           | 0.170            | S   | 80                  |
| 7  | SWNT | (85,10)  | 0.58             | 7.08           | 0.000            | M   | 45                  |
| 8  | SWNT | (33,16)  | 0.62             | 3.39           | 0.204            | S   | 156                 |
| 9  | DWNT | (27,22)  | 0.63             | 3.33           | 0.208            | S   | 223                 |
|    |      | (30,7)   |                  | 2.67           | 0.258            | S   |                     |
| 10 | DWNT | (38,6)   | 0.65             | 3.24           | 0.212            | S   | 240                 |
|    |      | (19,19)  |                  | 2.58           | 0.005            | M   |                     |
| 11 | DWNT | (48,21)  | 0.63             | 4.80           | 0.001            | M   | 48                  |
|    |      | (43,15)  |                  | 4.09           | 0.168            | S   |                     |
| 12 | DWNT | (40,12)  | 0.62             | 3.69           | 0.186            | S   | 90                  |
|    |      | (28,15)  |                  | 2.96           | 0.234            | S   |                     |
| 13 | DWNT | (54,11)  | 0.53             | 4.72           | 0.145            | S   | 60                  |
|    |      | (47,8)   |                  | 4.03           | 0.001            | M   |                     |
| 14 | DWNT | (49,18)  | 0.62             | 4.71           | 0.146            | S   | 76                  |
|    |      | (36,14)  |                  | 3.50           | 0.197            | S   |                     |
| 15 | TWNT | (53,7)   | 0.58             | 4.45           | 0.154            | S   | 80                  |
|    |      | (42,8)   |                  | 3.64           | 0.188            | S   |                     |
|    |      | (28,11)  |                  | 2.73           | 0.253            | S   |                     |
| 16 | TWNT | (47,13)  | 0.71             | 4.28           | 0.160            | S   | 114                 |
|    |      | (32,20)  |                  | 3.56           | 0.003            | M   |                     |
|    |      | (29,22)  |                  | 3.47           | 0.199            | S   |                     |
| 17 | QWNT | (61,17)  | 0.59             | 5.57           | 0.123            | S   | 65                  |
|    |      | (40,28)  |                  | 4.64           | 0.002            | M   |                     |
|    |      | (35,22)  |                  | 3.90           | 0.177            | S   |                     |
|    |      | (21,21)  |                  | 2.99           | 0.004            | M   |                     |

Table 5.2: NBED pattern calculations for SWNT (38, 21).  $D_1$ ,  $D_2$  and  $D_4$  are the averaged spacings between each principal layer line and the equatorial line.  $(v/u)_1$  and  $(v/u)_2$  are calculated using  $D_1$ ,  $D_2$  and  $D_1$ ,  $D_4$ , respectively.

| $D_1$ | $D_2$ | $D_4$ | $(v/u)_1$ | $(v/u)_2$ |
|-------|-------|-------|-----------|-----------|
| 405   | 337   | 739.4 | 0.5687    | 0.5547    |

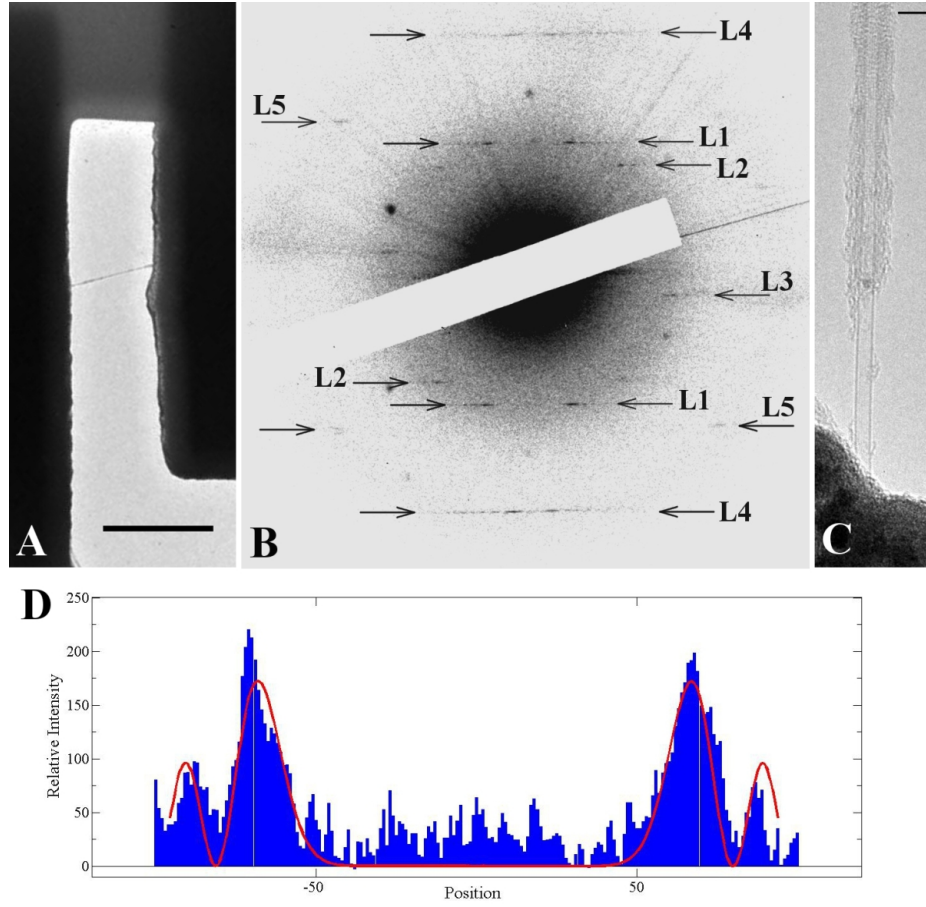


Figure 5.2: Illustration of the diffraction analysis of a SWNT. High and low magnifications TEM images are shown in (A) and (C) with scale bars of 1  $\mu\text{m}$  and 10 nm, respectively. (B) Inverted diffraction pattern of the SWNT with its first order principal layer lines  $L_1$ ,  $L_2$  and  $L_3$  and the second order ones  $L_4$  and  $L_5$ , from which the chirality of the SWNT is derived as (38, 21). (D) The relative intensity distribution along the layer line  $L_1$ , where the red line is the fitted Bessel function of order 21.

Table 5.3: Possible combinations for the NBED result of SWNT (38, 21).

| $u$       | $v$       | $v/u$         | $d(\text{nm})$ |
|-----------|-----------|---------------|----------------|
| 29        | 16        | 0.5517        | 3.10           |
| 34        | 19        | 0.5588        | 3.64           |
| <b>38</b> | <b>21</b> | <b>0.5526</b> | <b>4.06</b>    |
| 43        | 24        | 0.5581        | 4.61           |
| 47        | 26        | 0.5532        | 5.02           |

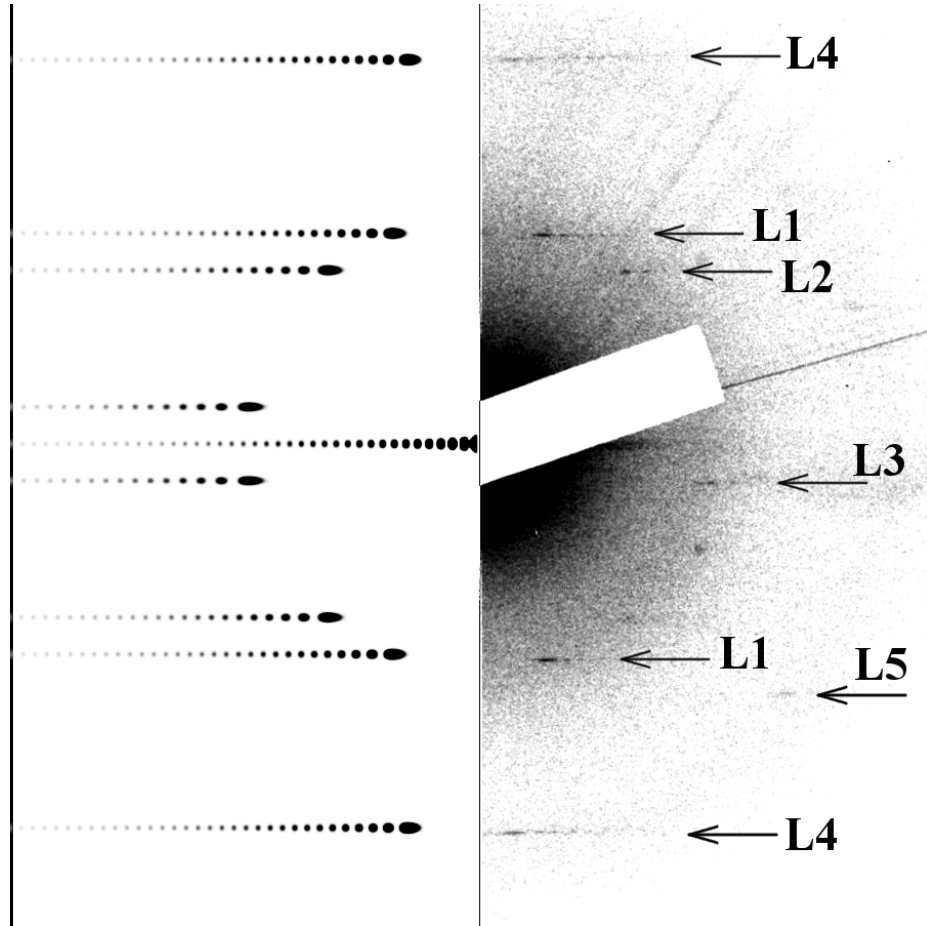


Figure 5.3: Comparison between the simulated diffraction pattern (left) and the NBED result of SWNT (38, 21). Note that only the first order layer lines along with  $L_4$  are included in the simulation.

overlap because of the low rotational symmetry. Hence the similar approach for a SWNT can be also applied. Nevertheless, since the diameter of each shell measured in real space is not always reliable due to the electron interference [27], there is no significant correlation between one set of NBED patterns in reciprocal space and one specific shell of the MWNT. Therefore, instead of using the diameters measured in HRTEM to determine each chiral indices as in the case of SWNTs, we prefer the order of Bessel function according to the intensity distribution on each principal layer lines, as long as the signal/noise ratio is high enough to distinguish the peaks and valleys on principal layer lines.

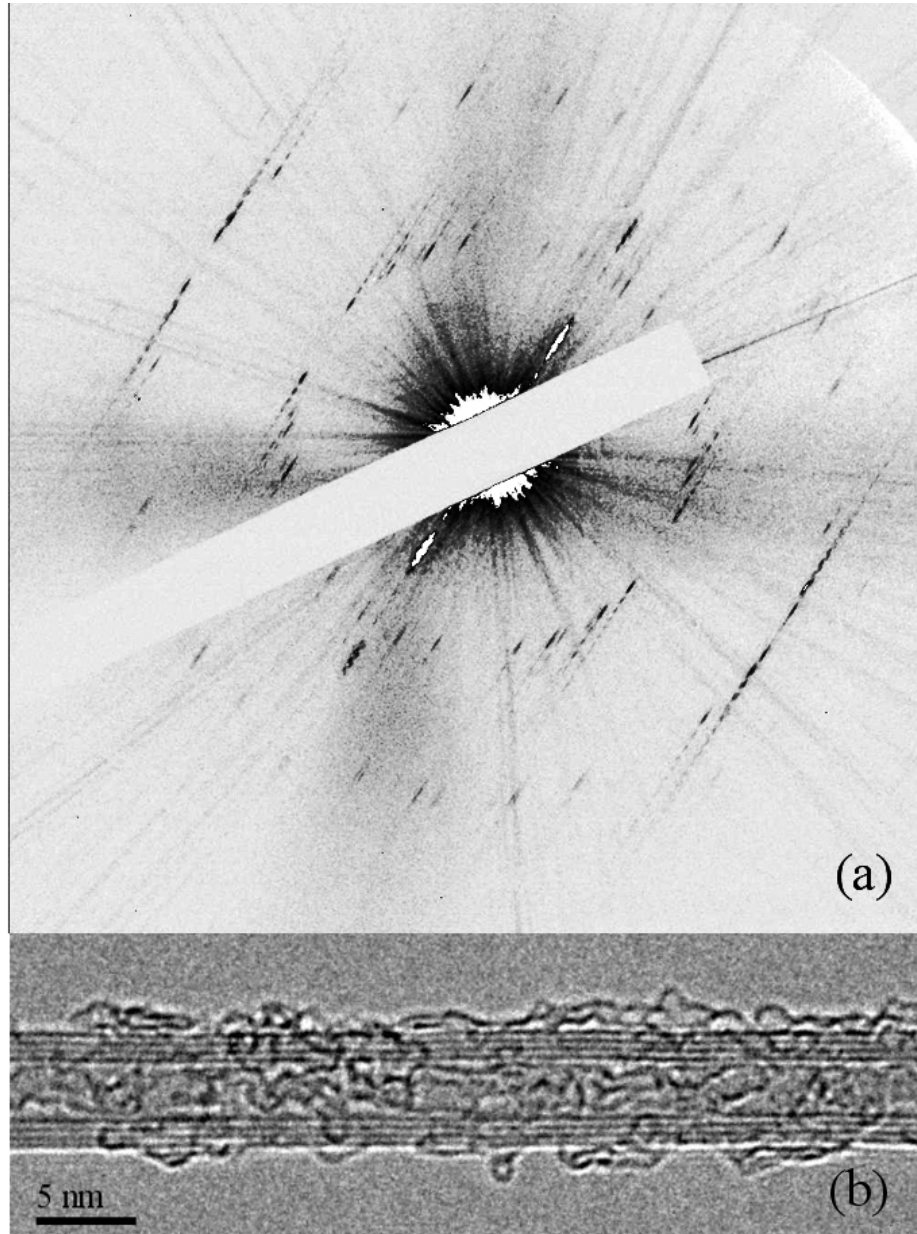


Figure 5.4: (a) NBED pattern of a QWNT consists of first two order principal layer lines with distinguishable intensity distributions. (b) HRTEM image of the CNT confirms the existence of four walls.

Figure 5.4 shows the NBED pattern and the HRTEM image of a quadruple walled carbon nanotube (QWNT). The diameter of each shell, 5.66 nm, 4.66 nm, 4.06 nm, and 3.25 nm, was estimated from the HRTEM image with an uncertainty of  $\pm 0.1$  nm due to the resolution limits. The principal layer lines, especially  $L_2$  and  $L_3$ , the brightness and the contrast of which are usually low, of individual shells can be better sorted and located using fitted hexagons of a constant radius, which equals to the distance from the center to the brightest peak on the principal lines, as illustrated in Figure 5.5. Different colors were assigned to distinguish the NBED patterns of different shells. The cyan hexagon was first identified once the cyan  $L_1$  was located. The fact that only three  $L_1$  lines were distinguishable implied the superposition of two  $L_1$ s of red and yellow. While the last pink hexagon was attributed to an armchair shell, because  $L_1$  and  $L_2$  overlapped and  $L_3$  was on the equatorial line. Because only  $L_4$ s were recognizable, the hexagon fitting to the second order principle layer lines was not feasible. The line spacings and the calculated chiral index ratios are listed in Table 5.4.

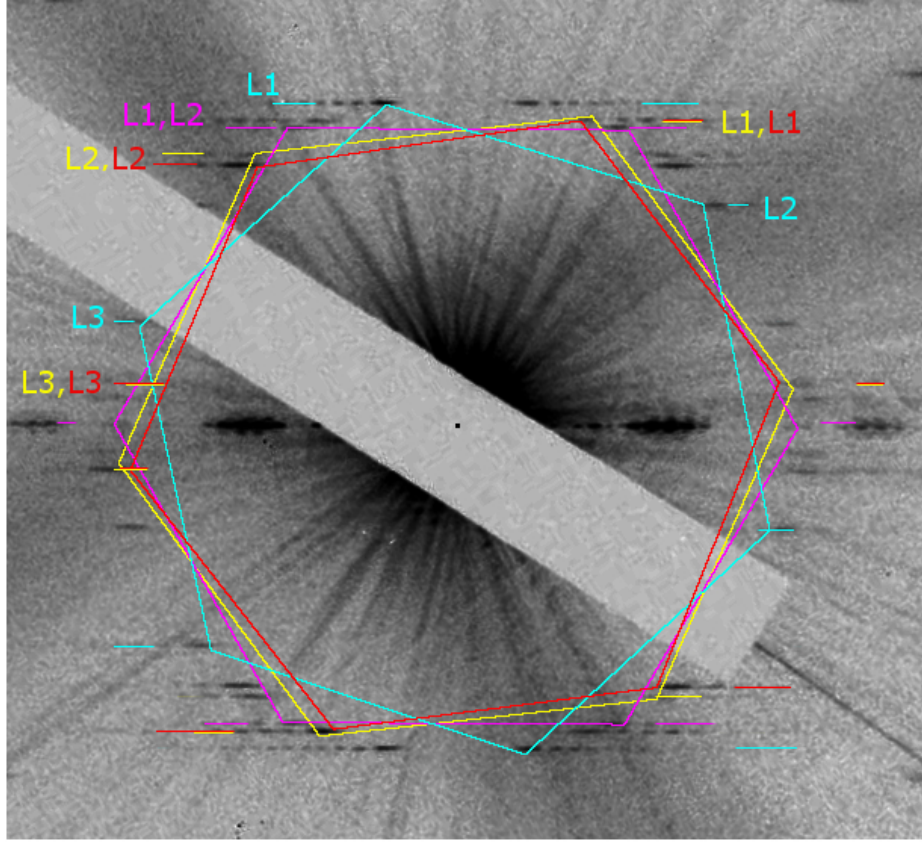


Figure 5.5: NBED pattern of a QWNT with fitted hexagons. Each color represents the NBED pattern of each individual shell.

The intensity distribution on the cyan  $L_1$  indicated the possible values of  $v_{\text{cyan}}$  as 16 or 17, while the  $L_2$ s of the yellow and red hexagons implied  $u_{\text{yellow}} = 40$ , or 41 and  $u_{\text{red}} = 35$ , or 36, and we have  $v_{\text{pink}} = 19$ , 20, or 21

Table 5.4: Determination of the chiral indices ratios  $\frac{v}{u}$  using the interlayer line spacings  $D_1$  and  $D_2$  of each shell in the QWNT.

|        | $D_1$ | $D_2$ | $v/u$  |
|--------|-------|-------|--------|
| cyan   | 426   | 290   | 0.2740 |
| yellow | 403   | 360   | 0.7108 |
| red    | 403   | 347   | 0.6340 |
| pink   | 293   | 293   | 1.0000 |

from the pink  $L_1$ . Apply the restrictions, the selections of the chiral indices  $(u, v)$  were narrowed down, as shown in Table 5.5 and Table 5.6, where the bold rows are the preferred selections.

Therefore, with the  $v/u$  ratio of each shell and the possible order numbers of the principal layer lines, the most plausible combination of the chiral structures of this QWNT is identified as  $(61, 17)@(40, 28)@(35, 22)@(21, 21)$  for the least error. Figure 5.6 compares the experimental NBED pattern to the simulated result. Coincidentally, the NBED patterns of each shell are aligned in the same sequence as the order of in real space, *i.e.*  $L_1$  of the outermost shell is furthest away from the center. The chiral indices of the rest MWNTs were determined using the same approach and summarized in Table 5.1.



Table 5.5: Possible values of  $v/u$  of two shells labeled as cyan and yellow in the NBED pattern of the QWNT. The bold rows are the preferred values according to the intensity distribution of the principal layer lines.  $\delta(v/u)$  is the relative error from the value  $\frac{v}{u} = \frac{2D_2 - D_2}{2D_1 - D_2}$  in the NBED patterns.

|        | $u$       | $v$       | $v/u$         | $\delta(v/u)$ | $d(\text{nm})$ |
|--------|-----------|-----------|---------------|---------------|----------------|
| cyan   | 53        | 15        | 0.2830        | 3.28%         | 4.85           |
|        | 54        | 15        | 0.2778        | 1.37%         | 4.92           |
|        | 55        | 15        | 0.2727        | -0.47%        | 5.00           |
|        | 56        | 15        | 0.2679        | -2.25%        | 5.08           |
|        | <b>56</b> | <b>16</b> | <b>0.2857</b> | <b>4.27%</b>  | <b>5.13</b>    |
|        | <b>57</b> | <b>16</b> | <b>0.2807</b> | <b>2.44%</b>  | <b>5.21</b>    |
|        | <b>58</b> | <b>16</b> | <b>0.2759</b> | <b>0.67%</b>  | <b>5.28</b>    |
|        | <b>59</b> | <b>16</b> | <b>0.2712</b> | <b>-1.03%</b> | <b>5.36</b>    |
|        | <b>60</b> | <b>16</b> | <b>0.2667</b> | <b>-2.68%</b> | <b>5.44</b>    |
|        | <b>60</b> | <b>17</b> | <b>0.2833</b> | <b>3.40%</b>  | <b>5.49</b>    |
|        | <b>61</b> | <b>17</b> | <b>0.2787</b> | <b>1.70%</b>  | <b>5.57</b>    |
|        | <b>62</b> | <b>17</b> | <b>0.2742</b> | <b>0.06%</b>  | <b>5.64</b>    |
|        | <b>63</b> | <b>17</b> | <b>0.2698</b> | <b>-1.53%</b> | <b>5.72</b>    |
|        | <b>64</b> | <b>17</b> | <b>0.2656</b> | <b>-3.06%</b> | <b>5.80</b>    |
|        | 64        | 18        | 0.2813        | 2.64%         | 5.85           |
|        | 65        | 18        | 0.2769        | 1.06%         | 5.92           |
|        | 66        | 18        | 0.2727        | -0.47%        | 6.00           |
| yellow | 39        | 27        | 0.69231       | -2.60%        | 4.50           |
|        | 39        | 28        | 0.7179        | 1.01%         | 4.57           |
|        | 39        | 29        | 0.7435        | 4.62%         | 4.63           |
|        | <b>40</b> | <b>27</b> | <b>0.6750</b> | <b>-5.03%</b> | <b>4.57</b>    |
|        | <b>40</b> | <b>28</b> | <b>0.7000</b> | <b>-1.51%</b> | <b>4.64</b>    |
|        | <b>40</b> | <b>29</b> | <b>0.7250</b> | <b>2.00%</b>  | <b>4.70</b>    |
|        | <b>40</b> | <b>30</b> | <b>0.7500</b> | <b>5.52%</b>  | <b>4.77</b>    |
|        | <b>41</b> | <b>28</b> | <b>0.6829</b> | <b>-3.92%</b> | <b>4.71</b>    |
|        | <b>41</b> | <b>29</b> | <b>0.7073</b> | <b>-0.48%</b> | <b>4.77</b>    |
|        | 41        | 30        | 0.7317        | 2.95%         | 4.84           |
|        | 42        | 29        | 0.6904        | -2.85%        | 4.84           |
|        | 42        | 30        | 0.7142        | 0.50%         | 4.91           |
|        | 42        | 31        | 0.7381        | 3.85%         | 4.97           |

Table 5.6: Possible values of  $v/u$  of two shells labeled as pink and red in the NBED pattern of the QWNT. The bold rows are the preferred values according to the intensity distribution of the principle lines.  $\delta(v/u)$  is the relative error from the value  $\frac{v}{u} = \frac{2D_2 - D_2}{2D_1 - D_2}$  in the NBED pattern.

|      | $u$       | $v$       | $v/u$         | $\delta(v/u)$ | $d(\text{nm})$ |
|------|-----------|-----------|---------------|---------------|----------------|
| pink | 18        | 18        | 1.000         | 0%            | 2.44           |
|      | <b>19</b> | <b>19</b> | <b>1.000</b>  | <b>0%</b>     | <b>2.58</b>    |
|      | <b>20</b> | <b>20</b> | <b>1.000</b>  | <b>0%</b>     | <b>2.71</b>    |
|      | <b>21</b> | <b>21</b> | <b>1.000</b>  | <b>0%</b>     | <b>2.85</b>    |
|      | 22        | 22        | 1.000         | 0%            | 2.99           |
|      | 23        | 23        | 1.000         | 0%            | 3.12           |
|      | 24        | 24        | 1.000         | 0%            | 3.26           |
| red  | 34        | 20        | 0.5882        | -7.22%        | 3.70           |
|      | 34        | 21        | 0.6176        | -2.58%        | 3.77           |
|      | 34        | 22        | 0.6471        | 2.06%         | 3.83           |
|      | 34        | 23        | 0.6765        | 6.70%         | 3.89           |
|      | <b>35</b> | <b>20</b> | <b>0.5714</b> | <b>-9.87%</b> | <b>3.78</b>    |
|      | <b>35</b> | <b>21</b> | <b>0.6000</b> | <b>-5.36%</b> | <b>3.84</b>    |
|      | <b>35</b> | <b>22</b> | <b>0.6286</b> | <b>-0.85%</b> | <b>3.90</b>    |
|      | <b>35</b> | <b>23</b> | <b>0.6571</b> | <b>3.65%</b>  | <b>3.96</b>    |
|      | <b>35</b> | <b>24</b> | <b>0.6857</b> | <b>8.16%</b>  | <b>4.03</b>    |
|      | <b>36</b> | <b>21</b> | <b>0.5833</b> | <b>-7.99%</b> | <b>3.91</b>    |
|      | <b>36</b> | <b>22</b> | <b>0.6111</b> | <b>-3.61%</b> | <b>3.97</b>    |
|      | <b>36</b> | <b>23</b> | <b>0.6389</b> | <b>0.77%</b>  | <b>4.04</b>    |
|      | <b>36</b> | <b>24</b> | <b>0.6667</b> | <b>5.15%</b>  | <b>4.10</b>    |
|      | <b>36</b> | <b>25</b> | <b>0.6944</b> | <b>9.54%</b>  | <b>4.16</b>    |
|      | 37        | 22        | 0.5946        | -6.21%        | 4.05           |
|      | 37        | 23        | 0.6216        | -1.95%        | 4.11           |
|      | 37        | 24        | 0.6486        | 2.31%         | 4.17           |
|      | 37        | 25        | 0.6757        | 6.58%         | 4.23           |

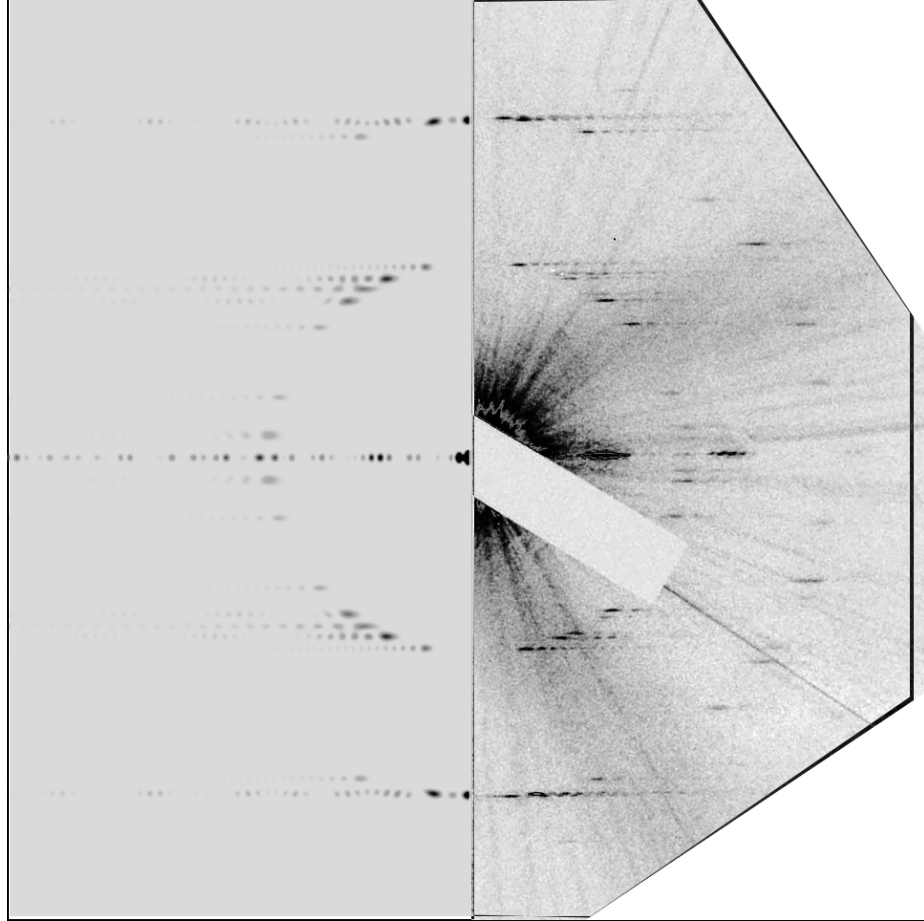


Figure 5.6: Comparison between the simulated diffraction pattern (Left) and the NBED result of the QWNT  $(61, 7)@(40, 28)@(35, 22)@(21, 21)$ . In the simulated pattern, only  $L_1, L_2, L_3$  and  $L_4$  are shown. Both pictures are inverted in contrast.

### 5.2.2 Transport Measurement

The  $I - V$  characteristic of each CNT was measured at room temperature after an annealing process in  $H_2$  flow to improve the contact of Pd electrodes with the CNT [4]. The linear  $I - V$  curves of CNT at low bias of less than 5 mV indicate a transparent ohmic contact with the electrodes, which is as expected due to the high work function of Pd and low Schottky barrier.

Figure 5.7 shows the typical  $I - V$  characteristics of both metallic and semiconducting SWNTs, with the average resistances of 30 k $\Omega$  and 150 k $\Omega$ , respectively. The transport measurements agreed with the classification using the chiral indices  $|u - v| = 3p + q$ , where  $p$  is a integer and  $q = \pm 1$  for semiconducting SWNTs and  $p = 0$  for metallic ones.

Although 3-4 Pd leads were deposited on the CNT, the quality of the contact was not consistent, while it only allowed 4-probe measurement on certain devices. Resistance measurements of most devices included the contributions from the contact. Also, based on the chiralities determined using diffraction analysis, several MWNTs consist of a metallic SWNT as one of the inner shells and a semiconducting outermost shell. However, the total resistances of these MWNTs are much larger than the common resistances of metallic SWNTs, which indicates that the outermost shell that is in intimate contact with the electrodes is dominant in the transport measurement. Therefore the MWNTs can be expected to behave as SWNTs of the same chirality as their outermost shells, which is in consistent with the previous experiments [20, 28] and predictions [29].

It is necessary to determine which transport regime CNTs belong to in our measurement prior to further discussions of the transport properties. Figure 5.8 shows a typical dependence of the measured resistance of a SWNT  $R$  from the  $I - V$  characteristics upon the corresponding separations of the electrodes  $l$ , which suggests the contact resistance of 20 - 30 k $\Omega$  and the 1D resistivities  $\rho = \frac{dR}{dl}$  of approximately 4.5 k $\Omega/\mu\text{m}$ . Hence, the mean free path for of the system is calculated as  $L_m \approx 2\mu\text{m}$  [30]. For similar behaviors have been observed on various CNTs, it is valid to assume that the transport of CNTs is ballistic since the conducting length  $L$  is about 0.1  $\mu\text{m}$  and smaller than  $L_m$ .

For more understanding of the transport phenomenon, it is helpful to evaluate the mean free path of electrons. The analytic prediction of the elastic mean free path  $L_e$  is expressed as [31, 32, 33],

$$L_e = \frac{18\pi t_0^2}{\sqrt{3}W^2}d, \quad (5.4)$$

where  $W = 0.2t_0$  is the variation range of the on-site perturbing potential,  $d$  is the diameter of the CNT. Apply this relationship to our devices of diameter ranging from 3 to 7 nm, the elastic mean free path is found around 2 to 5  $\mu\text{m}$ .

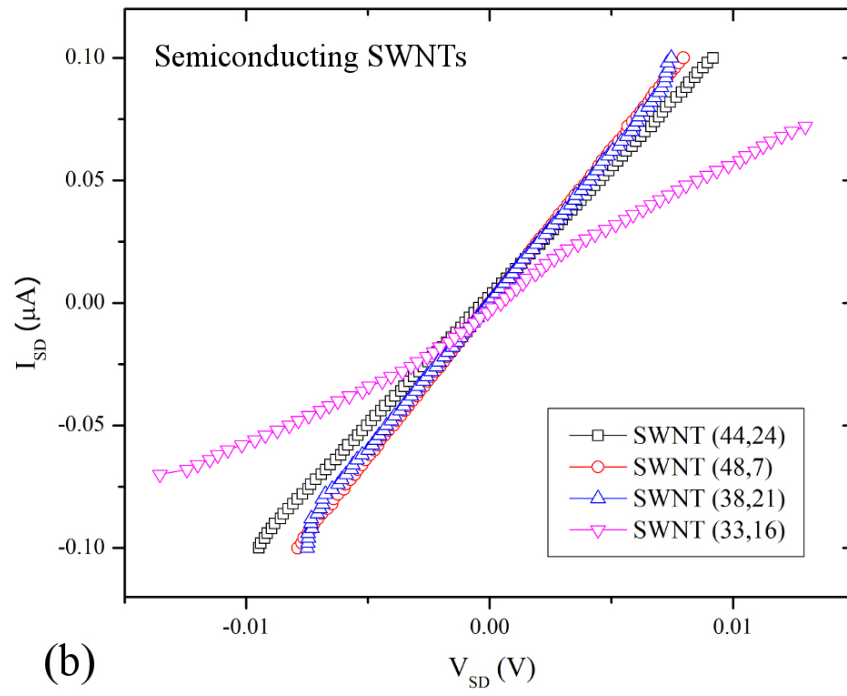
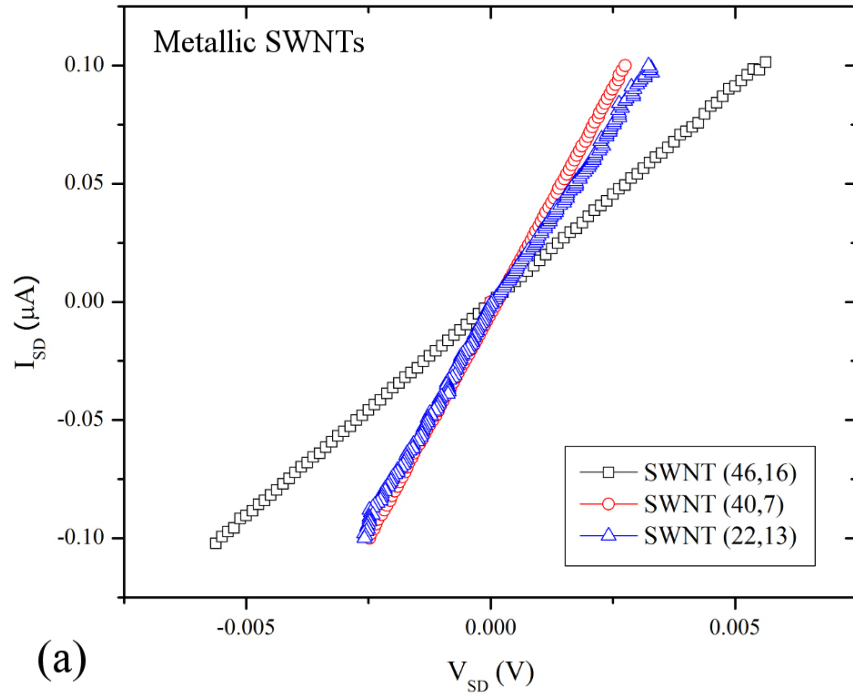


Figure 5.7: Typical linear characteristics of source/drain current  $I_{SD}$  versus voltage  $V_{SD}$  in (a) metallic and (b) semiconducting SWNT devices.

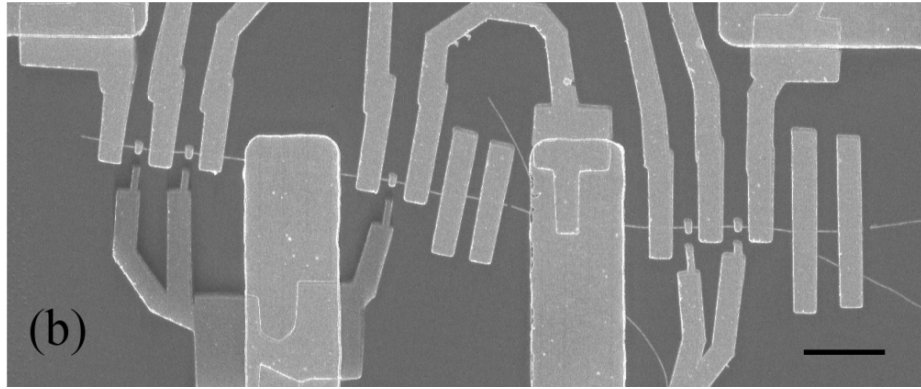
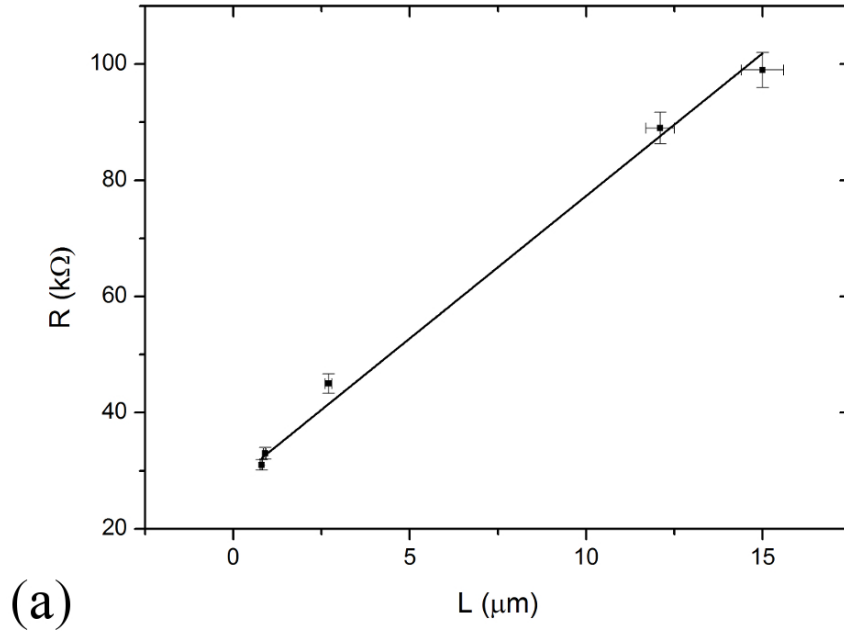


Figure 5.8: (a) Low bias resistance  $R = \frac{dV}{dI}$  near zero bias as a function of conducting length  $L$  of the SWNT shown in (b). Scale bar in (b) represents  $4 \mu\text{m}$ .

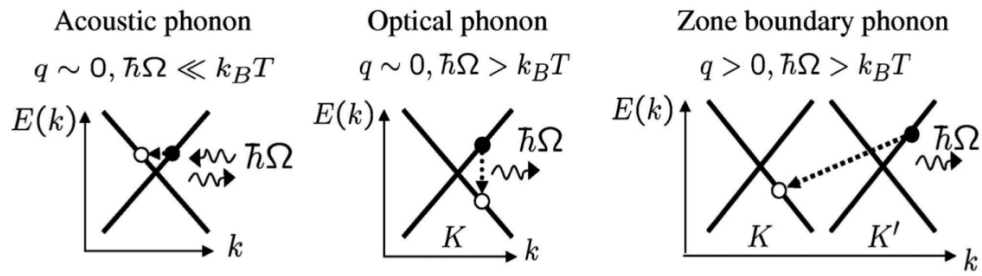


Figure 5.9: Schematic representation of the main phonon contributions to backscattering [1].

Moreover, the inelastic interaction between electrons and phonons significantly reduces the electron conductance, as illustrated in Figure 5.9. While at room temperature with low bias, only the acoustic mode is prominent in electron scattering and the mean free path is denoted as  $L_{ie}$ . A crude estimation has also been proposed in theory for the scattering rates by Park *et al.* [34],

$$\frac{1}{\tau} \approx \frac{4\pi}{\hbar} D^2 \left( \frac{\kappa T}{2\rho v_s^2} \right) \frac{1}{\hbar v_F} \quad \text{when } \hbar\Omega_q \ll \kappa T, \quad (5.5)$$

where  $v_s$  is the acoustic phonon velocity,  $D$  is the deformation potential,  $\hbar\Omega_q$  is the energy of the phonon, and  $\rho$  is the CNT mass density. The inelastic acoustic scattering time is found to be  $\tau \approx 3 \times 10^{12}$  for a SWNT of diameter 1.8 nm, with a subsequent inelastic free mean path of  $L_{ie} = 2.4\mu m$ .

Both the elastic  $L_e$  and the inelastic mean free path  $L_{ie}$  are supposed to be larger than the experimental value of the average mean free path  $L_m \approx 2\mu m$ , because both affect the transport properties of CNTs, therefore the experimental result is consistent with the theory.

### 5.2.3 Bandgaps of CNTs

Once the chiral structures are identified, the explicit band structures can be depicted following the zone-approximation in Equation (1.20), while the modification due to the curvature  $E_g^1$  is much smaller than  $E_g^0$ , thus negligible during the plotting.

Figure 5.10 and Figure 5.11 illustrate the 1D band structures of several metallic and semiconducting SWNTs in the first Brillouin zone (BZ). Previous theoretical studies concentrated on the predictions of SWNTs with simple structures, such as armchair and zigzag ones. For example, there is only one Dirac point at the Fermi surface for any metallic zigzag  $(3n, 0)$  or armchair  $(n, n)$  SWNT, therefore, at least two subbands participate in the transport given no doping or thermal excitation.

However, SWNTs of these particular structures are rare, among 17 CNTs devices in our experiment, there is no zigzag or armchair CNT except one shell in a QWNT is armchair, while most of the CNTs are chiral. Figure 5.10 shows the band structures of three metallic SWNTs from the experimental results including the one with the largest diameter  $(85, 10)$  and the one with the smallest diameter  $(40, 7)$ . Each of the band structures has at least 10 Dirac points at the Fermi surface within the first BZ, which suggests of more than 20 channels contributing to the conductance of corresponding CNT. The band structures of semiconducting SWNTs are also shown in Figure 5.11. Given the diameters  $d$  of CNTs are relatively large, the band gaps proportional to  $\frac{1}{d}$  are around 0.2 - 0.3 eV and are ten times larger than the thermal energy at room temperature  $kT \approx 0.026$  eV, therefore thermal excitation must be taken into account when analyzing the transport property.

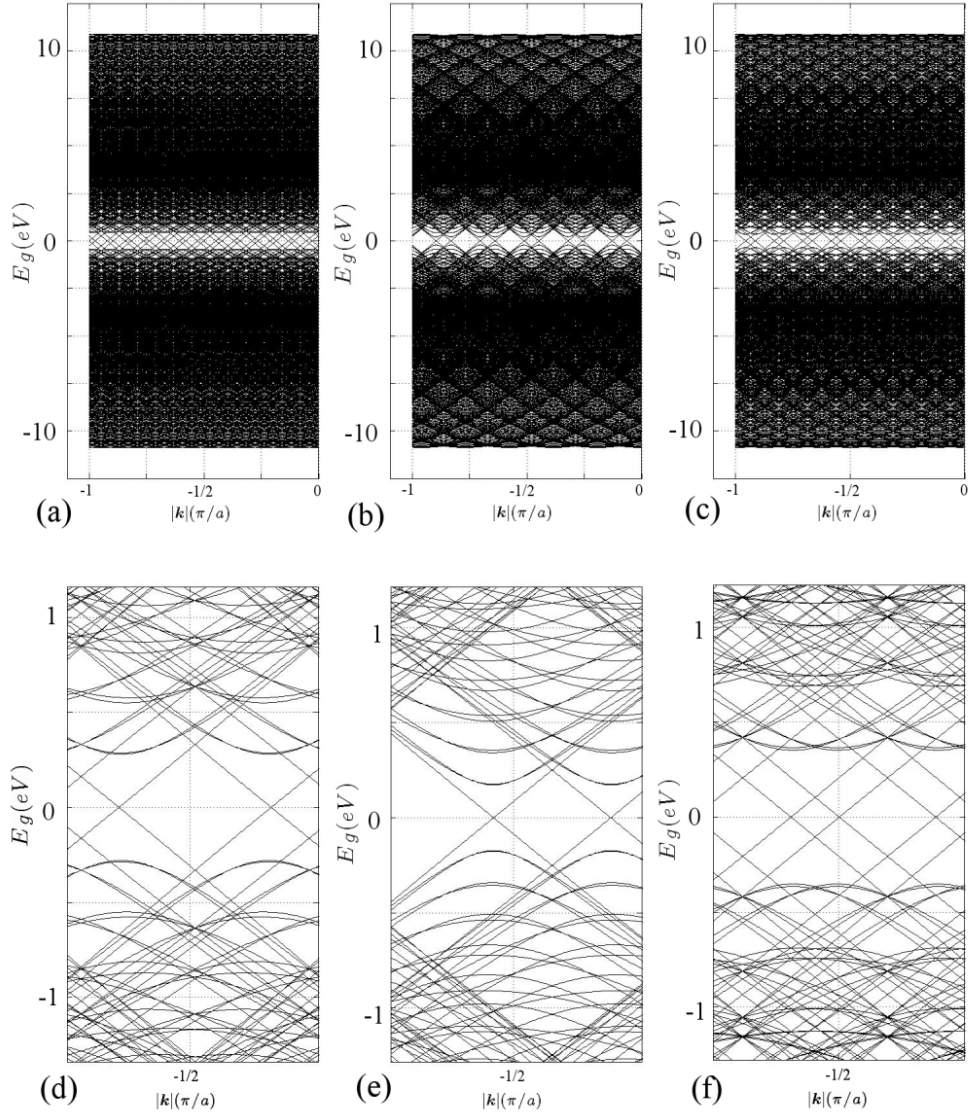


Figure 5.10: Depiction of the energy dispersion of the metallic SWNTs in the first Brillouin zone and in the vicinity of the Fermi surface. There are 26, 10, and 16 Dirac points in (a) SWNT (40, 7), (b) (85, 10), and (c) (46, 16) with the corresponding band structures (d,e,f) in the neighborhood of VHS points.



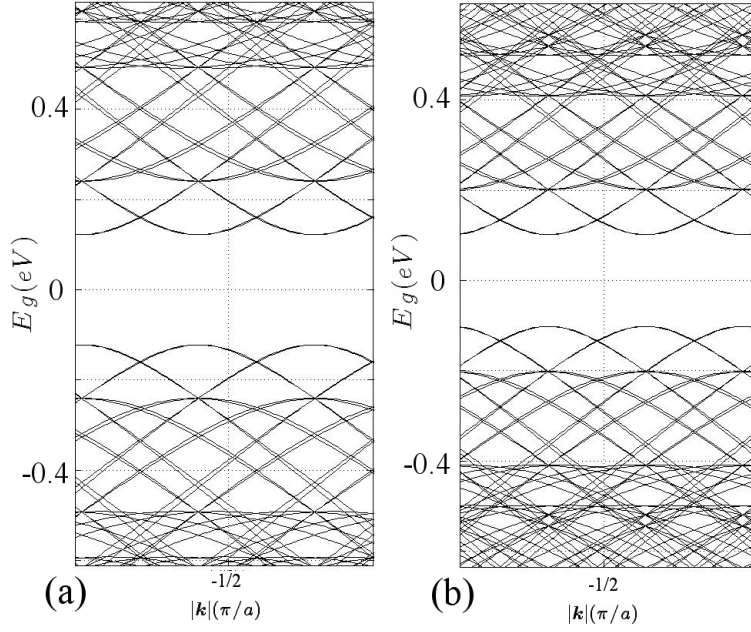


Figure 5.11: Depiction of the energy dispersion of the semiconducting SWNTs in the vicinity of the Fermi surface. The band structures of (a) SWNT (33, 15) and (b) (38, 21) indicate the band gaps of around 0.2 eV around the Fermi surface, which are in accordance with Equation (5.1). Two neighboring tips in the valence band are separated by small amount.

Moreover, provided adequate energy to excite electrons to overcome the band gap, multiple conduction bands in the vicinity of the Dirac points will also become available.

Given the thermal excitation and the multiple conducting subbands, the low bias resistance of the CNT device can be derived from Landauer-Büttiker formula as [35],

$$R = R_c + R_0 + \frac{1}{|t|^2} \frac{h}{4e^2} \frac{1}{N} \left[ 1 + \exp\left(\frac{E_g}{2kT}\right) \right], \quad (5.6)$$

where  $R_c$  is the contact resistance between the Pd electrodes and CNTs,  $R_0$  is quantum limit 6.5 k $\Omega$  for a metallic SWNT and zero for semiconducting ones,  $N$  is the number of subbands participating in the transport and the average number is approximately  $N \approx 16$  as discussed above. The plot fits best (Figure 5.12) with the contact resistance  $R_c = 30$  k $\Omega$ , consistent with the direct measurement in previous experimental results, and the transmission probability  $|t_0|^2 = 0.19$ , which is consistent with the results in other reports [36, 37].

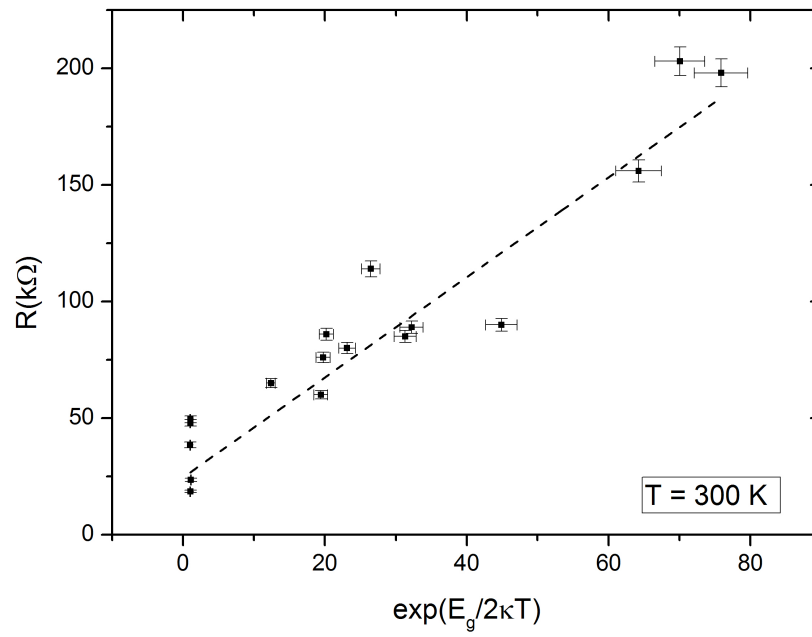


Figure 5.12: The dependence of the measured resistance  $R$  on the band gap  $E_g$  in the ballistic limit at room temperature  $T = 300K$ .

## BIBLIOGRAPHY

- [1] J.-C. Charlier, X. Blase, and S. Roche, “Electronic and transport properties of nanotubes,” *Reviews of Modern Physics*, vol. 79, no. 2, p. 677, 2007.
- [2] J. Kong, E. Yenilmez, T. W. Tombler, W. Kim, H. Dai, R. B. Laughlin, L. Liu, C. Jayanthi, and S. Wu, “Quantum interference and ballistic transmission in nanotube electron waveguides,” *Physical Review Letters*, vol. 87, no. 10, p. 106801, 2001.
- [3] W. Liang, M. Bockrath, D. Bozovic, J. H. Hafner, M. Tinkham, and H. Park, “Fabry-perot interference in a nanotube electron waveguide,” *Nature*, vol. 411, no. 6838, pp. 665–669, 2001.
- [4] A. Javey, J. Guo, Q. Wang, M. Lundstrom, and H. Dai, “Ballistic carbon nanotube field-effect transistors,” *Nature*, vol. 424, no. 6949, pp. 654–657, 2003.
- [5] A. Javey, J. Guo, M. Paulsson, Q. Wang, D. Mann, M. Lundstrom, and H. Dai, “High-field quasiballistic transport in short carbon nanotubes,” *Physical Review Letters*, vol. 92, no. 10, p. 106804, 2004.
- [6] C. Berger, Y. Yi, Z. Wang, and W. De Heer, “Multiwalled carbon nanotubes are ballistic conductors at room temperature,” *Applied Physics A*, vol. 74, no. 3, pp. 363–365, 2002.
- [7] A. Urbina, I. Echeverria, A. Pérez-Garrido, A. Díaz-Sánchez, and J. Abellan, “Quantum conductance steps in solutions of multiwalled carbon nanotubes,” *Physical Review Letters*, vol. 90, no. 10, p. 106603, 2003.
- [8] H. Li, W. Lu, J. Li, X. Bai, and C. Gu, “Multichannel ballistic transport in multiwall carbon nanotubes,” *Physical Review Letters*, vol. 95, no. 8, p. 086601, 2005.
- [9] J. Cao, J. Cao, and H. Dai, “Electron transport in very clean, as-grown suspended carbon nanotubes,” *Nature Materials*, vol. 4, no. 10, pp. 745–749, 2005.
- [10] L. Langer, V. Bayot, E. Grivei, J.-P. Issi, J. Heremans, C. Olk, L. Stockman, C. Van Haesendonck, and Y. Bruynseraede, “Quantum transport in a multiwalled carbon nanotube,” *Physical Review Letters*, vol. 76, no. 3, pp. 479–482, 1996.
- [11] P. G. Collins, M. S. Arnold, and P. Avouris, “Engineering carbon nanotubes and nanotube circuits using electrical breakdown,” *Science*, vol. 292, no. 5517, pp. 706–709, 2001.
- [12] S. Wang and M. Grifoni, “Helicity and electron-correlation effects on transport properties of double-walled carbon nanotubes,” *Physical Review Letters*, vol. 95, no. 26, p. 266802, 2005.
- [13] T. W. Odom, J.-L. Huang, P. Kim, and C. M. Lieber, “Atomic structure and electronic properties of single-walled carbon nanotubes,” *Nature*, vol. 391, no. 6662, pp. 62–64, 1998.
- [14] A. Jorio, R. Saito, J. Hafner, C. Lieber, M. Hunter, T. McClure, G. Dresselhaus, and M. Dresselhaus, “Structural (n, m) determination of isolated single-wall carbon nanotubes by resonant raman scattering,” *Physical Review Letters*, vol. 86, no. 6, pp. 1118–1121, 2001.
- [15] M. Gao, J. Zuo, R. Twisten, I. Petrov, L. Nagahara, and R. Zhang, “Structure determination of individual single-wall carbon nanotubes by nanoarea electron diffraction,” *Applied Physics Letters*, vol. 82, no. 16, pp. 2703–2705, 2003.
- [16] L.-C. Qin, “Electron diffraction from carbon nanotubes,” *Reports on Progress in Physics*, vol. 69, no. 10, p. 2761, 2006.
- [17] K. Hirahara, K. Inose, and Y. Nakayama, “Determination of the chiralities of isolated carbon nanotubes during superplastic elongation process,” *Applied Physics letters*, vol. 97, p. 051905, 2010.

- [18] L. Lin, T. Cui, L.-C. Qin, and S. Washburn, "Direct measurement of the friction between and shear moduli of shells of carbon nanotubes," *Physical Review Letters*, vol. 107, no. 20, p. 206101, 2011.
- [19] Z. Liu, Q. Zhang, and L.-C. Qin, "Accurate determination of atomic structure of multiwalled carbon nanotubes by nondestructive nanobeam electron diffraction," *Applied Physics Letters*, vol. 86, no. 19, pp. 191903–191903, 2005.
- [20] M. Kociak, K. Suenaga, K. Hirahara, Y. Saito, T. Nakahira, and S. Iijima, "Linking chiral indices and transport properties of double-walled carbon nanotubes," *Physical Review Letters*, vol. 89, no. 15, p. 155501, 2002.
- [21] T. Kim, G. Kim, W. I. Choi, Y.-K. Kwon, and J.-M. Zuo, "Electrical transport in small bundles of single-walled carbon nanotubes: Intertube interaction and effects of tube deformation," *Applied Physics Letters*, vol. 96, no. 17, pp. 173107–173107, 2010.
- [22] C. Allen, M. Elkin, G. Burnell, B. Hickey, C. Zhang, S. Hofmann, and J. Robertson, "Transport measurements on carbon nanotubes structurally characterized by electron diffraction," *Physical Review B*, vol. 84, no. 11, p. 115444, 2011.
- [23] D. Mann, A. Javey, J. Kong, Q. Wang, and H. Dai, "Ballistic transport in metallic nanotubes with reliable pd ohmic contacts," *Nano Letters*, vol. 3, no. 11, pp. 1541–1544, 2003.
- [24] B. W. Smith and D. E. Luzzi, "Electron irradiation effects in single wall carbon nanotubes," *Journal of Applied Physics*, vol. 90, no. 7, pp. 3509–3515, 2001.
- [25] K. Hirahara, M. Kociak, S. Bandow, T. Nakahira, K. Itoh, Y. Saito, and S. Iijima, "Chirality correlation in double-wall carbon nanotubes as studied by electron diffraction," *Physical Review B*, vol. 73, no. 19, p. 195420, 2006.
- [26] Z. Liu and L.-C. Qin, "Symmetry of electron diffraction from single-walled carbon nanotubes," *Chemical Physics Letters*, vol. 400, no. 4, pp. 430–435, 2004.
- [27] C. Qin and L.-M. Peng, "Measurement accuracy of the diameter of a carbon nanotube from tem images," *Physical Review B*, vol. 65, no. 15, p. 155431, 2002.
- [28] K. Liu, W. Wang, Z. Xu, X. Bai, E. Wang, Y. Yao, J. Zhang, and Z. Liu, "Chirality-dependent transport properties of double-walled nanotubes measured in situ on their field-effect transistors," *Journal of the American Chemical Society*, vol. 131, no. 1, pp. 62–63, 2008.
- [29] Q. Yan, J. Wu, G. Zhou, W. Duan, and B.-L. Gu, "Ab initio study of transport properties of multiwalled carbon nanotubes," *Physical Review B*, vol. 72, no. 15, p. 155425, 2005.
- [30] S. Datta, *Electronic transport in mesoscopic systems*. Cambridge university press, 1997.
- [31] J. Mintmire and C. White, "Universal density of states for carbon nanotubes," *Physical Review Letters*, vol. 81, no. 12, pp. 2506–2509, 1998.
- [32] S. Roche, G. Dresselhaus, M. Dresselhaus, and R. Saito, "Aharonov-bohm spectral features and coherence lengths in carbon nanotubes," *Physical Review B*, vol. 62, no. 23, p. 16092, 2000.
- [33] F. Triozon, S. Roche, A. Rubio, and D. Mayou, "Electrical transport in carbon nanotubes: Role of disorder and helical symmetries," *Physical Review B*, vol. 69, no. 12, pp. 121410–R, 2004.
- [34] J.-Y. Park, S. Rosenblatt, Y. Yaish, V. Sazonova, H. Üstünel, S. Braig, T. Arias, P. W. Brouwer, and P. L. McEuen, "Electron-phonon scattering in metallic single-walled carbon nanotubes," *Nano Letters*, vol. 4, no. 3, pp. 517–520, 2004.
- [35] J. Cao, Q. Wang, and H. Dai, "Electromechanical properties of metallic, quasimetallic, and semiconducting carbon nanotubes under stretching," *Physical Review Letters*, vol. 90, no. 15, p. 157601, 2003.

- [36] E. Minot, Y. Yaish, V. Sazonova, J.-Y. Park, M. Brink, and P. L. McEuen, “Tuning carbon nanotube band gaps with strain,” *Physical Review Letters*, vol. 90, no. 15, p. 156401, 2003.
- [37] A. R. Hall, M. R. Falvo, R. Superfine, and S. Washburn, “Electromechanical response of single-walled carbon nanotubes to torsional strain in a self-contained device,” *Nature Nanotechnology*, vol. 2, no. 7, pp. 413–416, 2007.

## CHAPTER 6

### Nano-Tribology in MWNT NEMS Devices

#### 6.1 Introduction to the Torsional Experiment on CNTs

Although widely applied and continuously studied, friction has been a phenomenon that is not well understood. Until recently, friction has been directly measured for the very first time by manipulating an individual atom and a molecule on a surface with high resolution STM/AFM techniques [1, 2]. On the other hand, the discovery of CNTs, especially MWNTs, provides an ideal platform to investigate friction in the mesoscopic scale due to the weak interlayer interactions between shells in MWNTs. Multiple theoretical studies have been conducted to predict the properties of friction [3, 4]. Friction could be determined indirectly based on the heat dissipation to the bath, and explicit results were obtained for (9,9)@(14,14) and (9,9)@(22,4) DWNTs, where the intralayer and the interlayer interactions were calculated using Tersoff-Brenner potential and van der Waals potential, respectively, with the average of  $1.07 \times 10^{-4}$  nN per atom and  $1.20 \times 10^{-4}$  nN per atom.

Experimental measurements using MWNTs have been reported mostly for the sliding friction in a telescoping motion between neighboring layers [5, 6]. An arc-discharge grown nanotube was glued onto the tip of a sample manipulator in a TEM. Outer layers of the nanotube were removed by electrical breakdown and the exposed core was spot welded to the tip of an AFM as shown in Figure 6.1. When the AFM tip was pulled along the tubule axis, the telescopic motion between the neighboring layers with the least surface resistance would occur via a self-selecting process. Interlayer friction was estimated to be less than  $1.4 \times 10^{-6}$  nN per atom with the AFM signal. However, the measurement gave only the minimum estimation of the interlayer friction since the telescopic motion prejudicially slides between the layers with the least friction. The interlayer force among other layers remained unclear. Furthermore, the contact area was constantly shrinking during the telescoping motion and this could also affect the measurement of the interlayer force.

Meanwhile, rotating friction is expected to be measured using a torsional NEMS device based on a CNT. This setup, however, was first designed to measure the shear modulus of a MWNT [7, 8, 9] or a SWNT [10, 11]. The device was fabricated on a Si/SiO<sub>2</sub> substrate which was later etched away for a suspended CNT. The paddle attached to the CNT was driven by an external electric field on an AFM tip to apply a torque  $\tau$  on the CNT. The motion of the paddle was observed with an SEM to determine the twist angle  $\theta$  and the geometry of

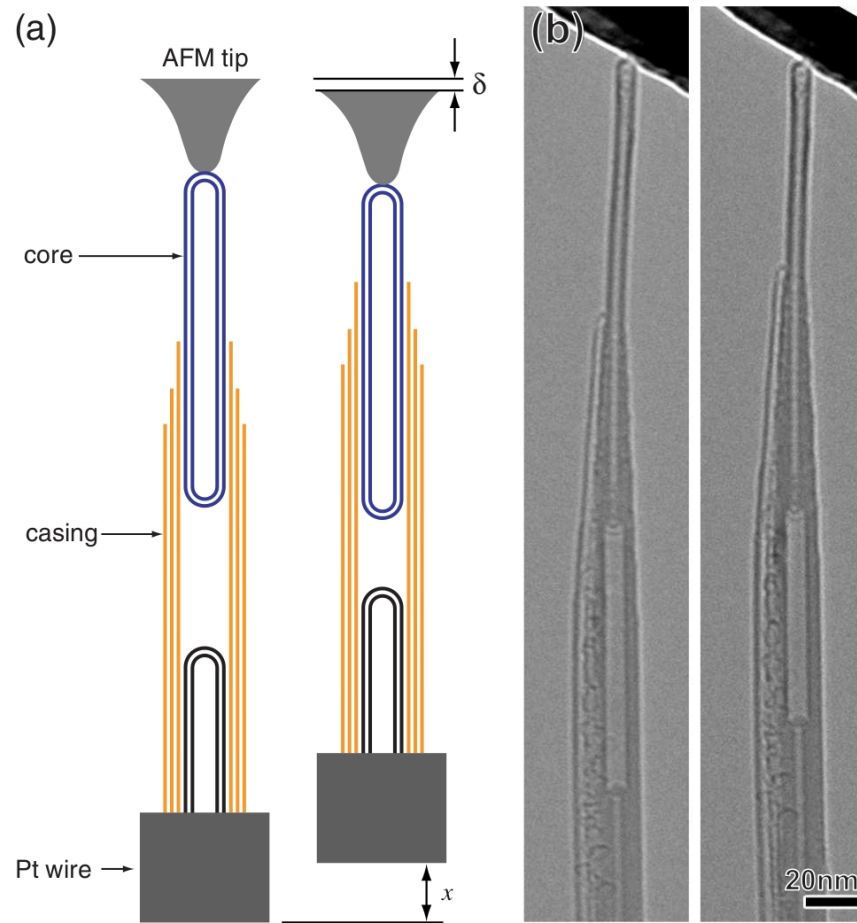


Figure 6.1: Schematic and TEM images of a telescoping MWNT.(a) Schematic drawing of measurement setup. The protruding core of an MWNT is connected to an AFM tip. The outer casing is mechanically connected on the other end to a Pt wire, attached onto a sample manipulator which is used to induce telescoping motion. (b) TEM images of a telescoping MWNT [6].

the device. The shear modulus of the CNT  $G$  was found using the solid model where the CNT was considered as a solid cylinder with

$$G = \frac{\tau l_1 l_2}{r^3 t \pi \theta (l_1 + l_2)}. \quad (6.1)$$

Given the geometry of the device, Finite Element (FE) analysis can be performed to compute the charge density  $\sigma$  on the paddle surface, thus the external torque exerted on the CNT from the paddle can be calculated as a surface integral,

$$\tau = \frac{1}{\epsilon_0} \int_S \sigma^2 \mathbf{r} \times \hat{n} dA, \quad (6.2)$$

where  $\epsilon_0$  is the vacuum permittivity,  $\mathbf{r}$  is the distance of infinitesimal area  $dA$  from the rotation axis of the CNT, and  $\hat{n}$  is the local unit normal vector. The shear modulus computed using this method was 0.5 TPa, which agreed with the theoretical predictions [12].

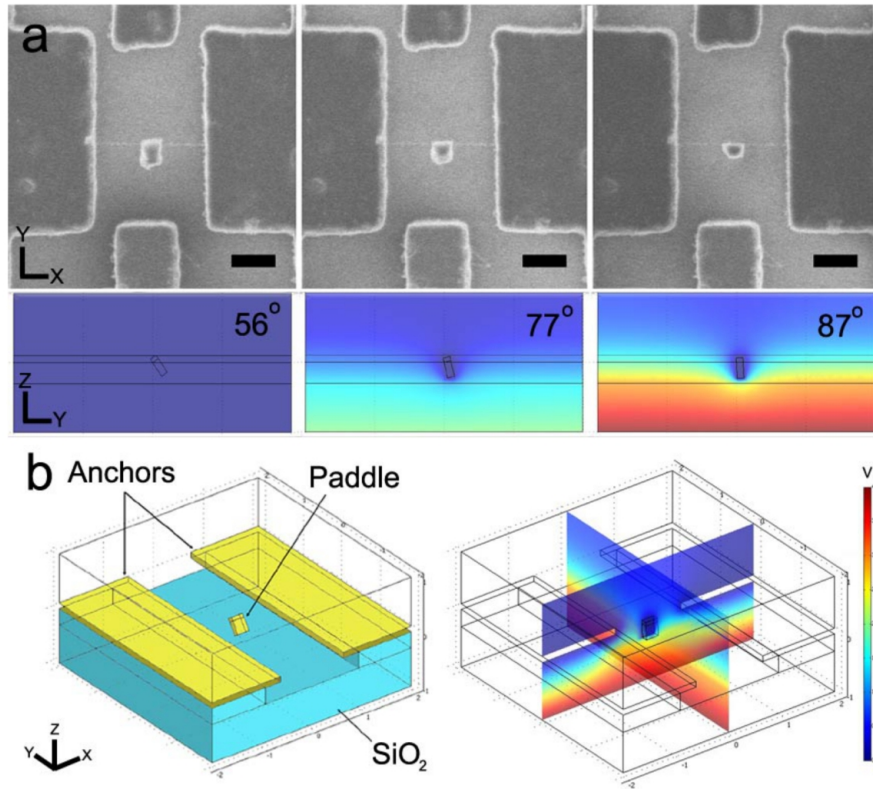


Figure 6.2: Sequential SEM images of a device applied with different voltage. Below each image is the FE calculated electric field potential (in the direction of the SWNT axis) of the device at each bias [11].



## 6.2 Electric Responses of Twisted CNTs

Due to the torsional strain, the effective chiral angle of the CNT changes. For the electric properties near the Fermi level are sensitive to the chirality, a strong electromechanical response of a twisted CNT is expected. There have been numerous theoretical studies on the variation of band gap caused by the mechanical deformation: The uniaxial strain was first studied. Heyd *et al.* [13] investigated the effect of uniaxial stress on electronic density of state using a semi-empirical tight-binding method and found a linear dependence of band gap on stress for zigzag tubes. Kane and Mele [14] predicted the opening of a band gap in armchair tubes under torsion. It was also shown that under either uniaxial or torsional strain, the variation of band gap in a zigzag/armchair tube is the largest, and independent of the diameter. With a tight binding model an analytic expression of band gap change experiencing small strain was derived as [15, 16]

$$\Delta E_g = \text{sgn}(2p + 1)3t_0[(1 + \mu)\sigma \cos 3\theta + \gamma \sin 3\theta], \quad (6.3)$$

where  $\mu$  is the Poisson ratio,  $\sigma$  and  $\gamma$  are the uniaxial and the torsional strains, respectively,  $\theta$  is the chiral angle, and  $p = \text{mod}(u - v, 3)$  determines whether the strain will increase or decrease the band gap. The equation implies that the band gap of a zigzag tubes ( $\theta = 0$ ) is insensitive to the torsional strain, while for an armchair tube ( $\theta = \frac{\pi}{6}$ ) the gap is insensitive to the uniaxial strain, as also shown in Figure 6.3. The change of band gap under strain implies possible metal-insulator transitions for all nanotubes. The linear dependence of band gap on strain is due to the fact that the energy dispersion of graphene near the Fermi level is linear. Because the responses of energy levels to strain vary for different subbands, when a certain strain applied, the energy levels of subbands approach and overlap, thus band gap as function of torsional strain exhibits periodic behavior for large strains [17]. This oscillation of the band gap which further leads to the periodic metal-semiconducting transitions has been observed in experiments and proved in theory as well [18, 19, 20, 21].

Because the interaction between shells is weak, the variation of band gap in a MWNT can be understood in terms of independent shells as individual SWNTs. However, for a commensurate DWNT the presence of inter-wall interactions may produce pseudogaps near the Fermi level due to the high order symmetry [22, 23, 24, 25], which implies the dependence on the commensuration. However, in the general cases of incommensurate MWNTs, the inter-wall couplings hardly change the band gap and have negligible impacts on the electric properties [26, 27].

Assume that a CNT of finite length is connected with metallic probes in perfect ohmic contacts, the conduction is length independent and only determined by the number of available quantum channels, where the quantum conductance per channel gives  $G_0 = \frac{2e^2}{h}$ . For a single SWNT there are two energy subbands

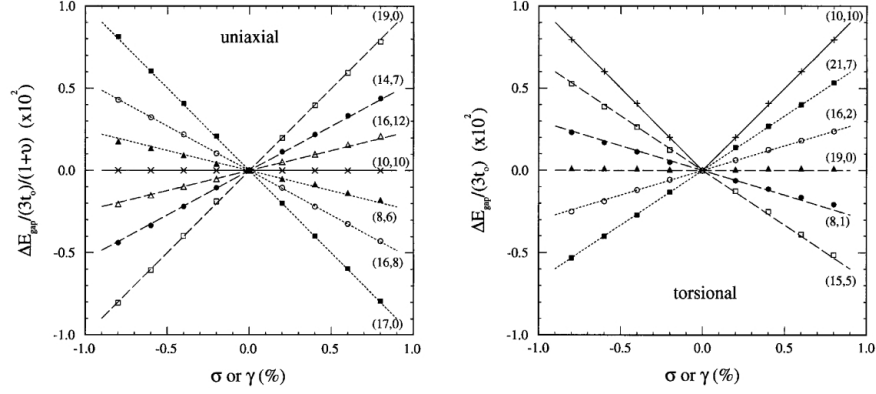


Figure 6.3: Band gap variations of SWNTs under uniaxial and torsional strains. Notice the linearity and the dependence on the chiral indices [16].

across the Fermi level when there is no excitation, thus metallic SWNTs have the quantum limit resistance of  $R_0 = \frac{1}{2G_0} = 6.5 \text{ k}\Omega$  in the ballistic limit [28]. For a semiconducting SWNT, the conductance at low temperature is determined by the thermal excitation of carriers [29], consequently the low-bias resistance of a semiconducting SWNT can be expressed as [30, 31, 32]

$$R = R_c + \frac{1}{N|t|^2} \frac{R_0}{2} \left[ 1 + \exp \left( \frac{E_g + \Delta E_g}{2\kappa T} \right) \right]. \quad (6.4)$$

In most experiments, a torsional strain on a suspended CNT was applied via a metal paddle, which can be manipulated by an external electric field [7, 11, 32] or by an AFM cantilever [30, 31, 33, 34]. With both ends securely anchored, the paddle-attached CNT undergoes a torsional strain as well. Under the torsion both halves of the CNT are twisted by the same amount in the opposite directions  $\phi$  and  $-\phi$ , thus the change to the band gap on either side is different. The total resistance is then given by

$$R(\phi) = R_c + \frac{1}{N|t|^2} \frac{R_0}{2} \left[ \exp \left( \frac{E_g + \Delta E_g(+\phi)}{2\kappa T} + \frac{E_g + \Delta E_g(-\phi)}{2\kappa T} \right) + 2 \right]. \quad (6.5)$$

In the case of a metallic SWNT device, identical band gaps are open on both sides, while the total resistance always increases. However, for a semiconducting SWNT device, the band gap of either segment can increase or decrease depending on its chirality, as shown in Equation (6.3). The net effect on the total resistance is therefore more complex.

For MWNT devices, if there are strong electric couplings between the shells, which suggests that all the tubes have similar symmetries, the conductance consists of the contributions from each shell. However, experimental results have already suggested that a MWNT is usually incommensurate, which therefore keeps the current flows in individual shells effectively insulated. Because the contact with external electrode is only

through the outermost shell, the decoupling prevents the inner shells contributing to the total conductance [35, 36]. Thus, the electromechanical response of an incommensurate MWNT undergoing a torsional strain is expected to be similar to that of the outermost shell as a SWNT.

### 6.3 Chiral Structures of Inner Tubes in a MWNT

One significant drawback in the previous torsional experiments is that a deformed MWNT was treated as a solid model in analyses, rather than a coaxial multi-shell structure, which reflects the actual configuration. The reason is due to the inability to investigate the structure deformation of the inner shells using previous characterization techniques.

Instead, NBED has been proven as a powerful technique to determine the chiral structure, especially in a multiwalled system, as demonstrated in Chapter 5. In general, once the NBED pattern of a MWNT is acquired, the chiral indices of each shell  $(u, v)$  can be calculated using the line spacings  $D_1$  and  $D_2$  between the principal layer lines  $L_1$  and  $L_2$  and the equatorial line by  $\frac{v}{u} = \frac{2D_2 - D_1}{2D_1 - D_2}$  and using the order of the Bessel function on each layer line by locating the maximum and minimum intensity positions [37, 38].

The deformation of a CNT under a torsional strain can be understood that one end of the CNT is twisted about the tube axis whereas the other is fixed. If assuming the cross-section of a twisted CNT remains circular during the deformation, the twisted CNT is equivalent as sheared graphene, where the lattice is uniformly deformed, as illustrated in Figure 6.4.

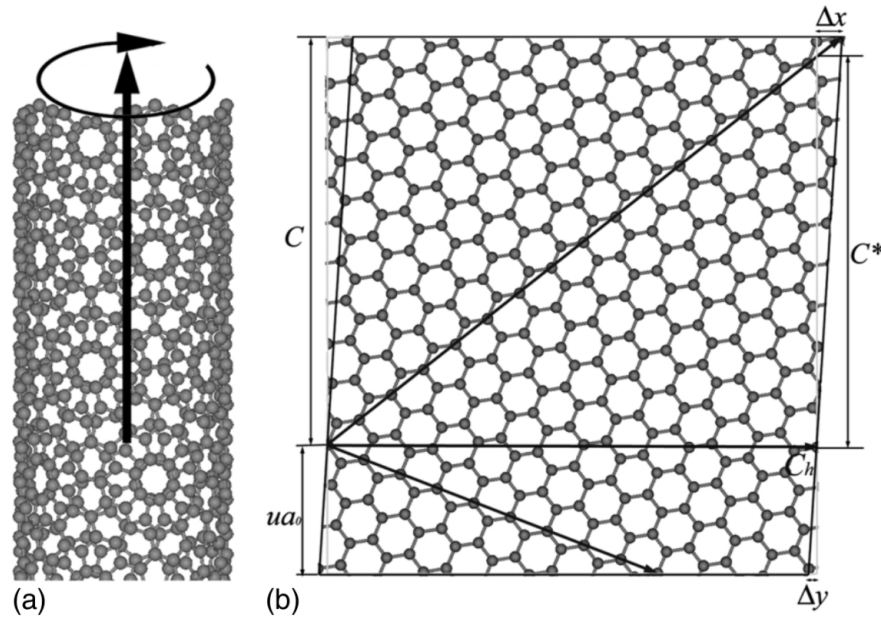


Figure 6.4: (a) Single-walled carbon nanotube (22,2) being twisted clockwise about its axis; (b) Atomic positions of the twisted nanotube in radial projection [39].

Based the analysis similar to Chapter 2, when a CNT of chiral indices  $(u, v)$  is twisted by an angle per unit length of  $\Delta\vartheta$ , the cylindrical coordinates of the atoms on the  $j$ -th pair of helices in the deformed CNT can be expressed as,

$$\begin{cases} r = r_0, \\ \phi_j^1 = \frac{2\pi ja_0}{|\mathbf{C}_h|} \left( \cos \alpha - \frac{\sin \alpha}{\tan(\pi/3 - \alpha)} \frac{\Delta\vartheta}{2\pi} \right), \\ z_j^1 = -ja_0 \sin \alpha. \end{cases} \quad (6.6)$$

and

$$\begin{cases} r = r_0, \\ \phi_j^1 = \frac{2\pi ja_0}{|\mathbf{C}_h|} \left( \cos \alpha - \frac{\sin \alpha}{\tan(\pi/3 - \alpha)} \frac{\Delta\vartheta}{2\pi} \right) - \frac{2\pi a_0}{\sqrt{3}|\mathbf{C}_h|} \cos(\frac{\pi}{6} + \alpha), \\ z_j^1 = -ja_0 \sin \alpha + \frac{a_0}{\sqrt{3}} \sin(\frac{\pi}{6} + \alpha). \end{cases} \quad (6.7)$$

As a result of deformed structure, the NBED pattern of a twisted CNT is different from the untwisted one. The twisting angle  $\Delta\vartheta$  can be expressed in term of the chiral indices  $(u, v)$  and the layer line spacing  $D_1$  and  $D_2$  [39],

$$\frac{\Delta\vartheta}{2\pi} = \frac{(2u + v)/(u + 2v) - D_1/D_2}{D_1/D_2 + v/u}. \quad (6.8)$$

Therefore, the principal layer line spacings  $D_1$  and  $D_2$  in the NBED pattern would either increase or decrease depending on the handedness of the chiral structure, as simulated in Figure 6.5. When a SWNT (22,2) is twisted counterclockwise, opposite to its handedness, the SWNT becomes *less* chiral, therefore the two separated hexagons tend to move closer with larger  $D_1$  and approaching  $L_2$  and  $L_3$ . Hence, not only the twist angle, but also the handedness of this SWNT can be determined from the NBED pattern.

## 6.4 Experimental Results

Using the NBED, the structure deformations of SWNT, DWNT and TWNT under torsional strains were identified. The TEM images and the NBED patterns were first locally acquired at one part of a suspended CNT with no paddle attached in order to determine the chiral indices  $(u, v)$ . The device geometry, *i.e.* the size of the paddle and the length of the suspended CNT, was also measured in the TEM images.

Then the deflections of the paddle driven by the external electric fields at various sidegate voltages were monitored in real time TEM. By examining the projection areas, the deflect angles of the paddle were computed.

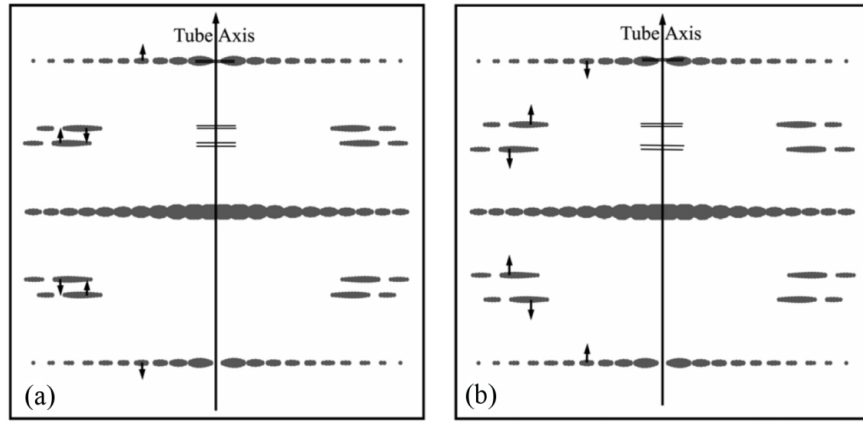


Figure 6.5: (a) Calculated electron diffraction pattern of carbon nanotube (22,2) twisted counterclockwise by  $\Delta\vartheta = -1.20^\circ/\text{nm}$ . (b) The same CNT twisted clockwise  $\Delta\vartheta = +1.20^\circ/\text{nm}$ . The arrows indicate the direction of shifts of the principal layer lines relative to the untwisted structure [39].

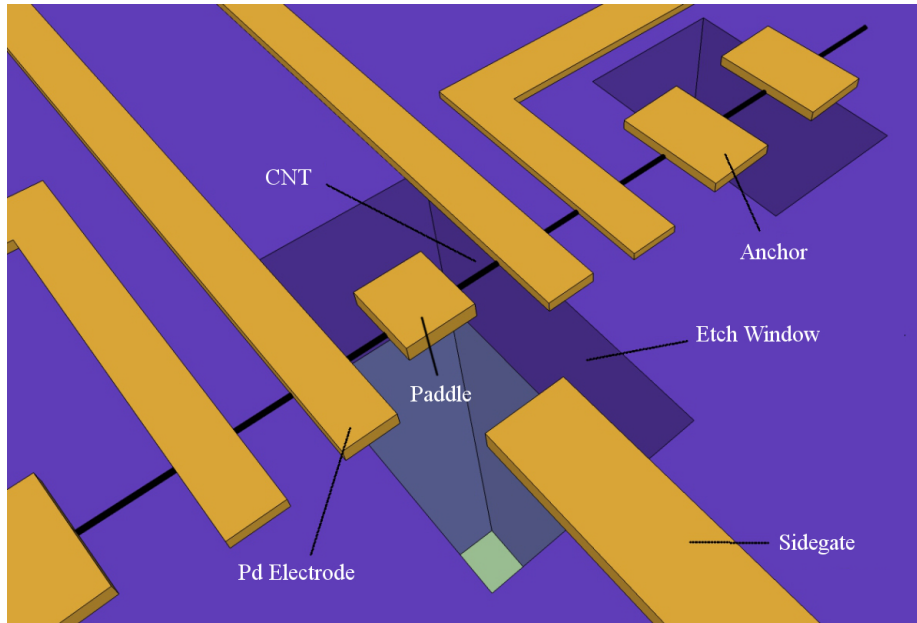


Figure 6.6: Schematic of the device which is ready for electric actuation and *in situ* electron imaging and electron diffraction analysis.

Since the paddle was deposited on the CNT and stayed in secure contact with the CNT, it is expected that both the paddle and the outermost wall were twisted by the same amount. Diffraction patterns of the suspended CNT were taken on both sides of the paddle at each twist angle.

Prior to the analysis of the NBED patterns of the twisted CNT, one should note that the suspended CNT was no longer perpendicular to the incident electron beam, for the electrostatic force that applied on the paddle induced a vertical displacement, as illustrated in Figure 6.7.

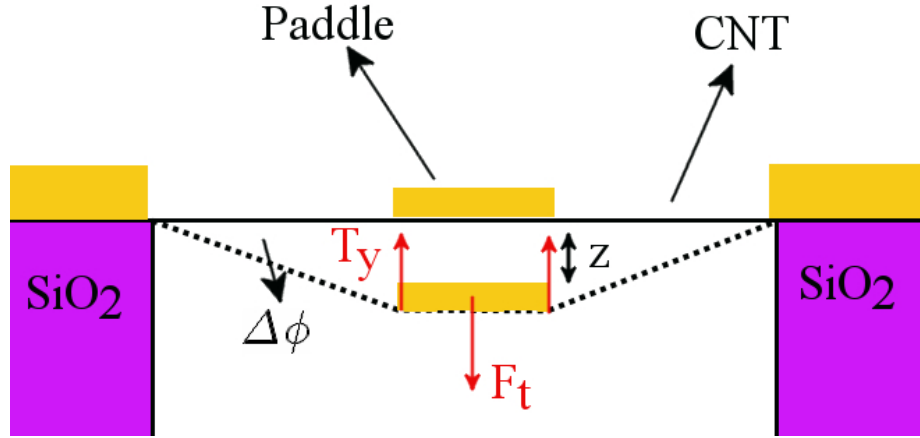


Figure 6.7: Schematic of the device subject to the uniaxial strain caused by electrostatic force  $F_t$ , which is countered by the normal component of the tension  $T_y$  and induces a vertical displacement  $z$  and an angle  $\Delta\phi$  from the horizontal position.

When a uniaxial strain  $\sigma$  is applied on the CNTs, where each suspended segment is stretched down by  $\Delta\phi$  from the horizontal position. The deflection force due to the static charge on the paddle  $F_t$ , which is in the magnitude of 10 nN and can be calculated from the FE simulated value of the electrostatic torque applied on the paddle, is countered by the normal components of the tension force  $T_y = (YA\sigma) \cdot 2 \sin \Delta\phi$ , where  $Y = 1$  TPa is the Young's modulus of CNT [31] and  $A = 2r \cdot dr$  is the cross-section area of the wall. When the uniaxial strain is small, we have

$$\cos \Delta\phi = \frac{1}{1 + \sigma}, \quad (6.9)$$

and,

$$\sigma = \frac{1}{2} \left( \frac{F_t}{YA} \right)^{2/3}. \quad (6.10)$$

The uniaxial strain  $\sigma$  is calculated less than 0.01 with the maximum of the induced angle  $\Delta\phi \sim 5^\circ$ . Therefore the alteration due to this uniaxial deformation on the NBED pattern is negligible [40], otherwise a modification of the NBED analysis towards the tilting effect is required.

Figure 6.8 shows TEM images and NBED patterns of a DWNT device. The deflections were calculated as  $90^\circ$ ,  $117^\circ$  and  $147^\circ$  under DC biases 0 V, 40 V and 60 V applied to the side gate in Figure 6.8 (B)-(D). Once the DC bias was turned off, the return of paddle to the initial position suggests that the observed strain is due to the applied electrostatic torque. The deflection angle of the paddle, which equals to the twist angle of the outermost shell, is measured from the change in the projected length of the paddle. In order to determine the chiral indices, the non-paddle part of the DWNT was imaged for the NBED pattern (Figure 6.8 (E)). The auxiliary hexagons helps to locate the principal layer lines for each of the two shells [41], and the chiral indices were identified as  $(56, 2)@(37, 18)$  with diameters of 4.467 nm and 3.805 nm. From the measurements of  $\frac{D_1}{D_2}$  in Figure 6.8 (F)-(H) at each deflection, the twist angles  $\Delta\vartheta$  of both shells can be calculated with an uncertainty of  $\pm 0.02^\circ/\text{nm}$ , which is from both the pixel resolution limit of the NBED images and the thermal excitation on the outermost shell. The twist angle calculated from the NBED pattern agrees with the result from the TEM imaging. The results are summarized in Table 6.1, with the information of other DWNT device listed below.

Table 6.1: NBED pattern analysis of the twisted DWNT  $(56, 2)@(37, 18)$  with diameters of 4.467 nm and 3.805 nm.

| Sidegate | $L(\text{nm})$ | Shell | $D_1/D_2$ | $\Delta\vartheta(^\circ/\text{nm})$ | $\Delta\theta(^\circ)$ | $\Delta\theta_{TEM}(^\circ)$ |
|----------|----------------|-------|-----------|-------------------------------------|------------------------|------------------------------|
| 0V       | 600            | Outer | 1.950     | 0.16                                | 96                     | 90                           |
|          |                | Inner | 1.263     | 0.01                                | 6                      |                              |
| 40V      | 200            | Outer | N/A       | N/A                                 | N/A                    | 117                          |
|          |                | Inner | 1.241     | 0.07                                | 14                     |                              |
| 60V      | 600            | Outer | 1.981     | 0.25                                | 150                    | 147                          |
|          |                | Inner | 1.272     | 0.04                                | 24                     |                              |
| 60V      | 200            | Outer | 1.698     | 0.73                                | 146                    | 147                          |
|          |                | Inner | 1.236     | 0.09                                | 18                     |                              |

Table 6.2: NBED pattern analysis of the twisted DWNT  $(5, 65)@(24, 44)$  with diameters of 4.467 nm and 3.805 nm.

| Sidegate | $L(\text{nm})$ | Shell | $D_1/D_2$ | $\Delta\vartheta(^\circ/\text{nm})$ | $\Delta\theta(^\circ)$ | $\Delta\theta_{TEM}(^\circ)$ |
|----------|----------------|-------|-----------|-------------------------------------|------------------------|------------------------------|
| 0V       | 560            | Outer | 1.758     | 0.14                                | 78.5                   | 66                           |
|          |                | Inner | 1.214     | 0.02                                | 11.2                   |                              |
| 0V       | 190            | Outer | 1.926     | 0.40                                | 76                     | 66                           |
|          |                | Inner | 1.243     | 0.08                                | 15.2                   |                              |
| 15V      | 560            | Outer | 1.780     | 0.07                                | 39.2                   | 55                           |
|          |                | Inner | 1.215     | 0.01                                | 5.6                    |                              |
| 35V      | 560            | Outer | 1.791     | 0.03                                | 16.8                   | N/A                          |
|          |                | Inner | 1.221     | 0.00                                | 0                      |                              |

The torsional strain of the TWNT device was also measured using the same approach and the complexity of the NBED pattern of a TWNT makes the analysis more challenging. Figure 6.11 shows a comparison between the NBED patterns. The left half was cropped from the NBED pattern of a non-paddle segment to

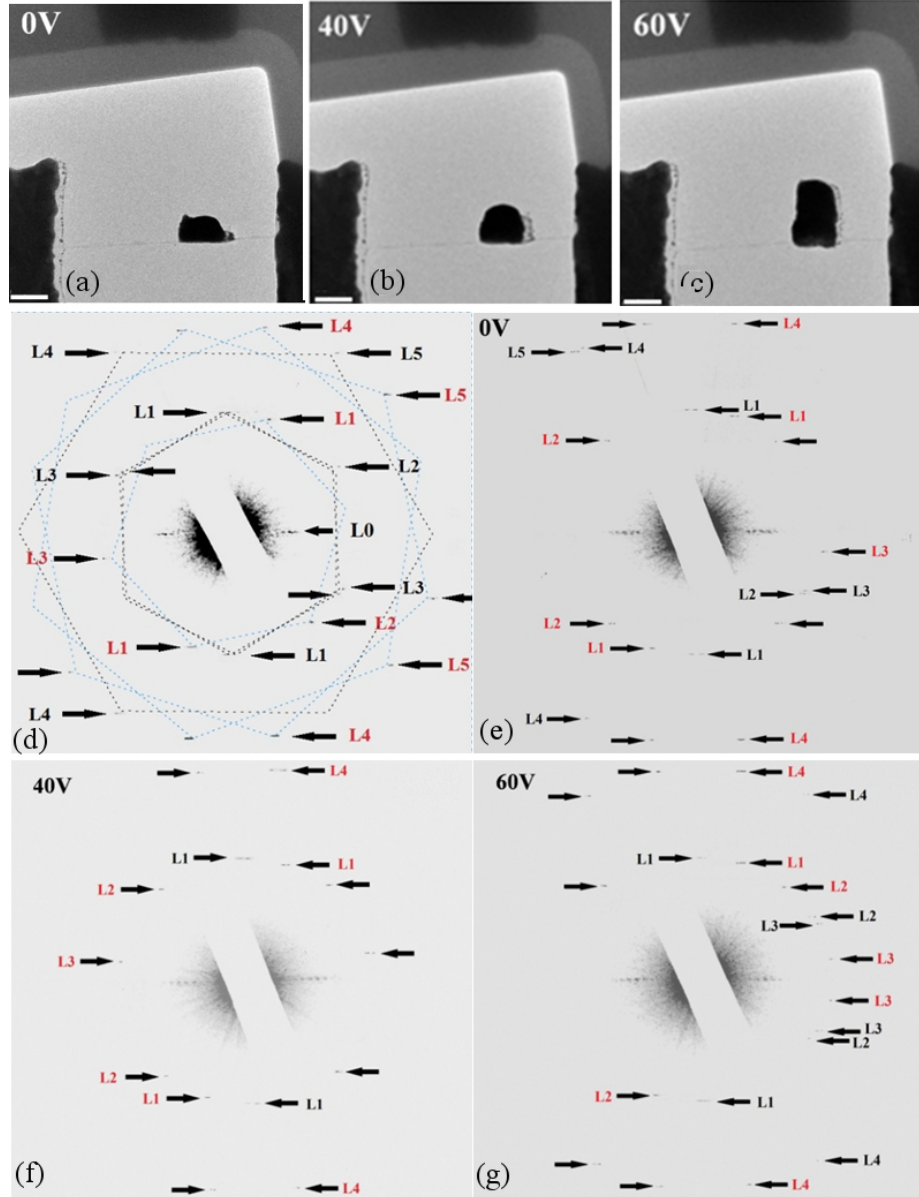


Figure 6.8: TEM images and electron diffraction patterns of the suspended DWNT  $(56, 2)@(37, 18)$ . The diffraction patterns are false-colored and marked by arrows. (a, b, c) TEM images of paddled device as it is actuated. Scale bar: 200 nm. (d) Electron diffraction pattern of the DWNT taken from untwisted segment. The black letters and red letters indicate the diffraction layer lines of the outer shell and the inner shell, respectively. (e, f, g) Electron diffraction patterns of the DWNT when the paddle is twisted under bias voltages of 0, 40, and 60 V [42].



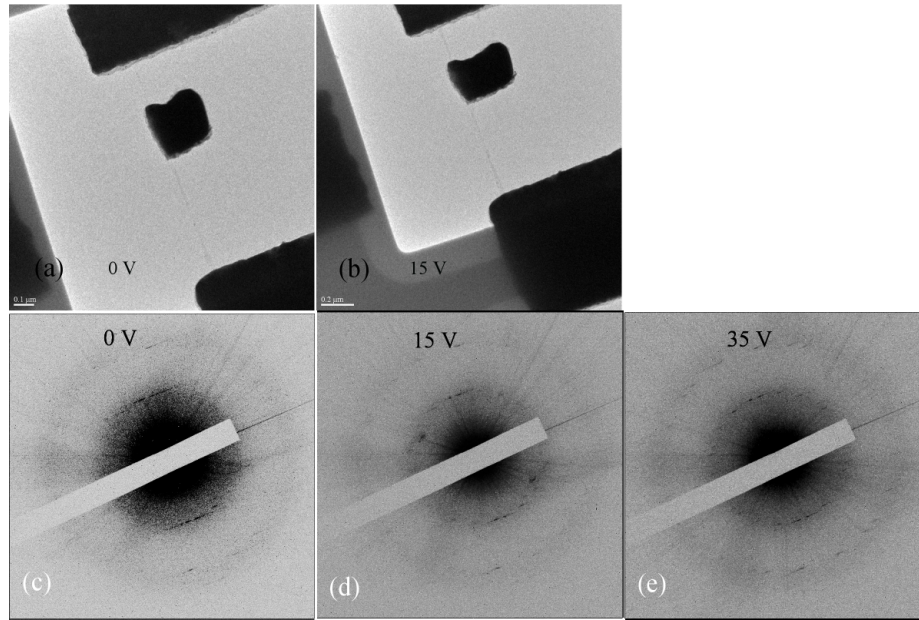


Figure 6.9: TEM images and electron diffraction patterns of the suspended DWNT (65, 5)@(24, 44). The diffraction patterns are false-colored and marked by arrows. (a, b) TEM images of paddled device as it is actuated. Scale bar: 200 nm. (c, d, e) Electron diffraction patterns of the DWNT when the paddle is twisted under bias voltages of 0, 15, and 35 V.

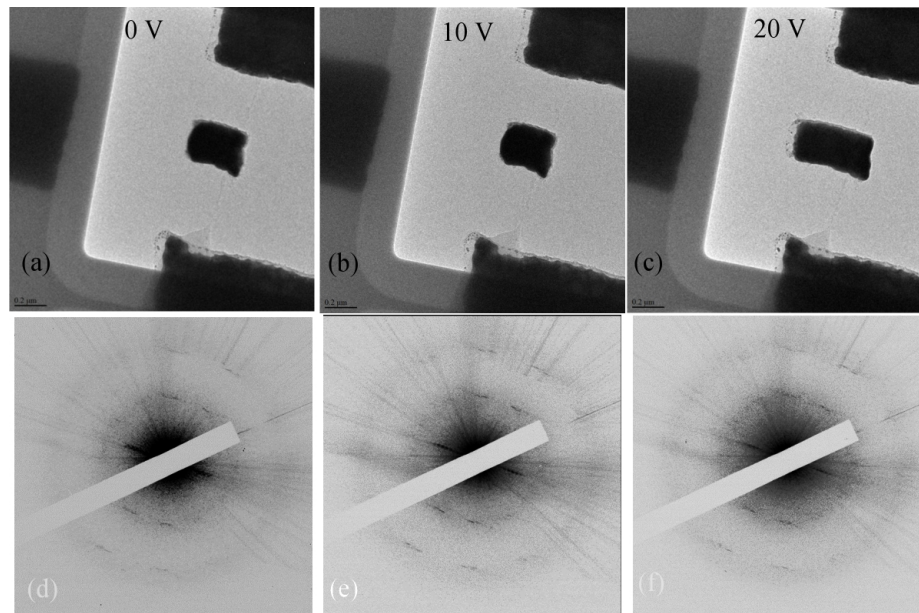


Figure 6.10: TEM images and NBED patterns of the suspended DWNT (49, 18)@(38, 16). The NBED patterns are false-colored and marked by arrows. (a, b, c) TEM images of paddled device as it is actuated. Scale bar: 200 nm. (d, e, f) Electron diffraction patterns of the DWNT when the paddle is twisted under bias voltages of 0, 10, and 20 V.

Table 6.3: NBED pattern analysis of the twisted DWNT (49, 18)@(38, 16) with diameters of 4.705 nm and 3.500 nm.

| Sidegate | $L(\text{nm})$ | Shell | $D1/D2$ | $\Delta\vartheta(^{\circ}/\text{nm})$ | $\Delta\theta(^{\circ})$ | $\Delta\theta_{TEM(^{\circ})}$ |
|----------|----------------|-------|---------|---------------------------------------|--------------------------|--------------------------------|
| 0V       | 490            | Outer | 1.179   | 0.12                                  | 57                       | 56                             |
|          |                | Inner | 1.293   | 0.03                                  | 13                       |                                |
| 0V       | 370            | Outer | 1.661   | -0.15                                 | -54                      | 56                             |
|          |                | Inner | 1.387   | -0.05                                 | -18                      |                                |
| 10V      | 490            | Outer | 1.207   | 0.10                                  | 50                       | 48                             |
|          |                | Inner | 1.327   | 0.01                                  | 6                        |                                |
| 20V      | 490            | Outer | 1.348   | 0.01                                  | 3                        | 5                              |
|          |                | Inner | 1.344   | 0.00                                  | 0                        |                                |

determine the chiral indices as (53, 7)@(42, 8)@(28, 11) with shells labeled as pink, cyan and red, respectively. The corresponding auxiliary hexagons were drawn to distinguish the principle layer lines. The NBED pattern of a paddle segment at 0 V DC bias is shown on the right. Note that, the TWNT had already been twisted by  $63^{\circ}$  prior to applying any DC bias. The alterations of each layer lines can be recognized while the low signal/noise ratio introduced considerable uncertainties when determining  $\frac{D_1}{D_2}$ . Moreover, as all  $L_2$ s were moving away from  $L_3$ s when the paddle was being deflected counterclockwise, all three shells of the TWNT are left-handed.

Table 6.4: NBED pattern analysis of the twisted TWNT (7, 53)@(8, 42)@(11, 28) with diameters of 4.45 nm, 3.64nm and 2.70 nm

| Sidegate | $L(\text{nm})$ | Shell | $D1/D2$ | $\Delta\vartheta(^{\circ}/\text{nm})$ | $\Delta\theta(^{\circ})$ | $\Delta\theta_{TEM(^{\circ})}$ |
|----------|----------------|-------|---------|---------------------------------------|--------------------------|--------------------------------|
| 0v       | 580            | Outer | 1.478   | 0.13                                  | 75.4                     | 63                             |
|          |                | Mid   | 1.502   | 0.05                                  | 29                       |                                |
|          |                | Inner | 1.306   | 0.02                                  | 11.6                     |                                |
| 0v       | 230            | Outer | 2.292   | -0.25                                 | -57.5                    | 63                             |
|          |                | Mid   | 1.762   | -0.09                                 | -20.7                    |                                |
|          |                | Inner | 1.375   | -0.02                                 | -4.6                     |                                |
| 15v      | 580            | Outer | 1.507   | 0.11                                  | 63.8                     | 60                             |
|          |                | Mid   | 1.518   | 0.04                                  | 23.2                     |                                |
|          |                | Inner | 1.306   | 0.02                                  | 11.6                     |                                |
| 30v      | 580            | Outer | 1.507   | 0.11                                  | 63.8                     | 59                             |
|          |                | Mid   | 1.518   | 0.04                                  | 23.2                     |                                |
|          |                | Inner | 1.306   | 0.02                                  | 11.6                     |                                |
| 45v      | 580            | Outer | 1.552   | 0.08                                  | 46.4                     | 50                             |
|          |                | Mid   | 1.551   | 0.02                                  | 11.6                     |                                |
|          |                | Inner | N/A     | N/A                                   | N/A                      |                                |

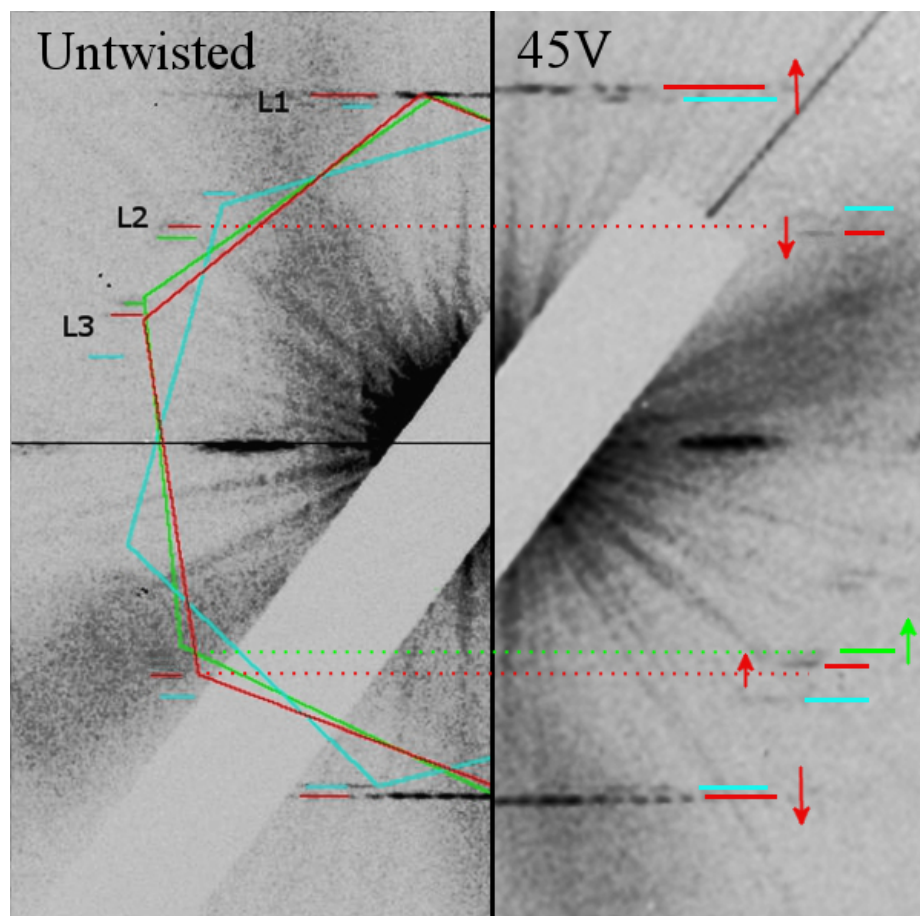


Figure 6.11: Comparison between the NBED pattern of the TWNT  $(53, 7)@(42, 8)@(28, 11)$  before (left) and after the twist.

## 6.5 Results and Discussion

Based on the information shown in the previous Tables, we concluded that the twist angles of the outermost shells match the deflect angles of the paddles within the uncertainties. More importantly, the agreement assures the validity of the NBED analyses, and therefore confirms the measurements on the torsional movement of the inner shells by diffraction patterns. Moreover, the consistency of the NBED patterns at various sites proves that the torsion strain of the outermost shell is uniformly distributed along the CNT. The discrepancy in the measurements of the angles might be attributed to the paddle vibrations caused by the charged electrons during the long exposure to the electron beam.

The multiwalled structure in DWNTs and TWNTs provides an opportunity to investigate the interlayer coupling between the shells, as we have observed that the inner shell was twisted by the torsional strain as well. It is valid to conclude that the inner shell should be driven by the interlayer friction force. Figure 6.12 shows the correlations between the twist angle of inner and outer walls of all MWNT devices. The linearity indicates that the inner shells strain in proportion to the outer shell by a smaller amount, and the zero y-intercept implies that the torsional response is instantaneous without stiction. We attributed the variety in the responses to the different interlayer spacings of MWNTs, therefore different van der Waals interactions. Note that one of the DWNT (49, 18)@(38, 16) has a large interlayer spacing of 0.60 nm, much bigger than the value of graphene sheet 0.35 nm. However, the ratio between the twist angles of both shells  $\frac{\Delta\theta_o}{\Delta\theta_i}$  does not show a significant dependence on the interlayer spacing  $\Delta d$ , as shown in Figure 6.13. Because large diameter CNTs are prone to uniaxial deformations caused by electron beam or contamination, the calculated interlayer spacing from the chiral indices may vary from the actual value.

Before we turn to the investigation of the shear modulus and the friction analysis in MWNT devices, it is worthwhile to review the physics model for the paddle-attached suspended CNT structure. Figure 6.14 schematically illustrates the configuration where a suspended CNT is separated into three segments of lengths  $l_1$ ,  $w$  and  $l_2$ , respectively. The widths of the paddles were designed as 200 nm with small fabrication fluctuations, while the lengths of the suspended CNTs were 800 - 1000 nm. When the paddle was deflected by an angle  $\Delta\theta$ , every part of the outermost shell in the paddle segment was uniformly twisted by the same angle. With some calculations assuming two shells as hollow cylinders with a constant coupling, it can be shown that the twist angle of the inner shell in the paddle segment was also uniform. Therefore, the angular displacements of two shells were identical in the paddle segment. Hence, the strain energy is only induced in the non-paddle segments that undergo shear strains. Also, due to the different structure deformations, the van der Waals energy in each segment should be calculated individually.

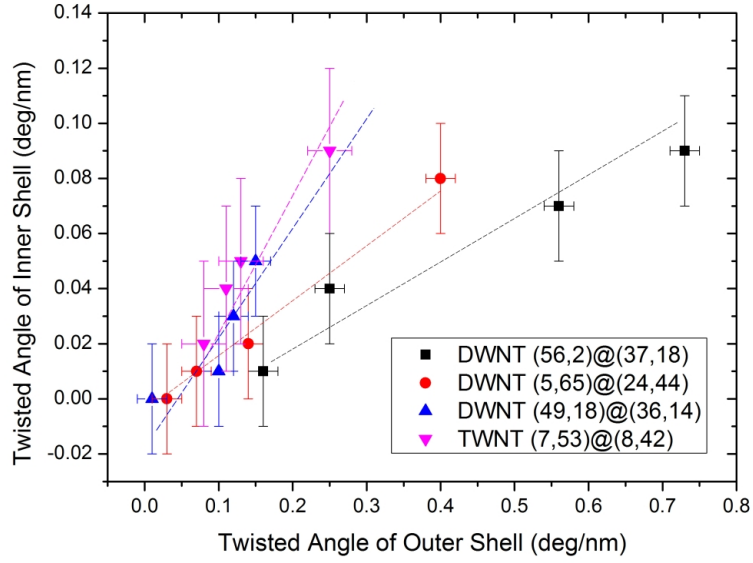


Figure 6.12: The inner shells torsional response to the twist of the outer shell of the four MWNT devices measured. Dashed lines are the corresponding fits. Note that since the twist angle of the innermost shell in the TWNT can not be precisely determined, only the correlation between the outer and the middle shells was drawn.

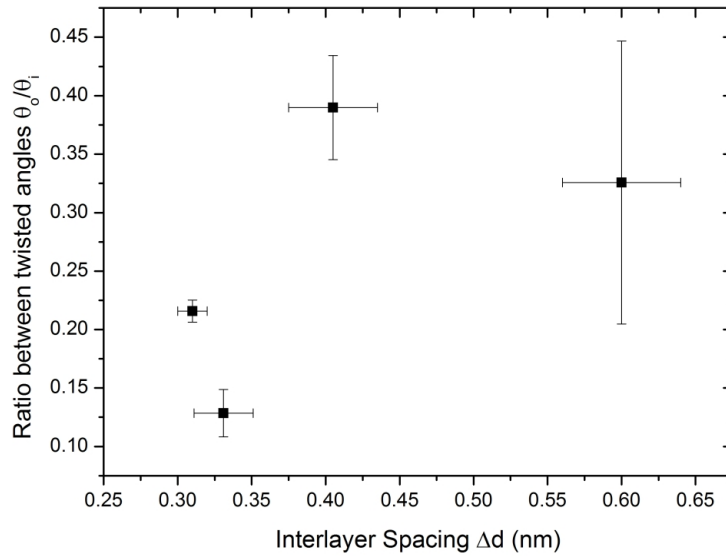


Figure 6.13: The plot of the ratio of the twist angles in the outer and inner shells  $\frac{\theta_o}{\theta_i}$  v.s. the corresponding interlayer spacing  $\Delta d$ .

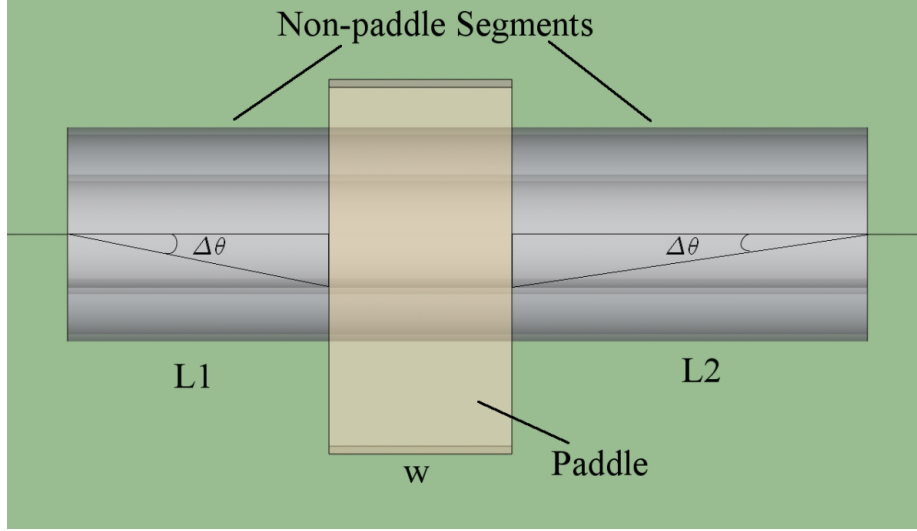


Figure 6.14: Schematic illustration of the suspended CNT device, which is separated into three segments with lengths of  $l_1$ ,  $l_2$  and  $w$ . The paddle is deflected by  $\Delta\theta$ .

Given adequate information of the structure, a MWNT can be considered as a combination of several hollow cylinders with various thicknesses instead of a solid cylinder. The outermost shell of a MWNT is subject to torques from the paddle, which equals to the external electrostatic torque, and from the coupling between the nearest neighboring shell. Likewise, the coupling twists other inner shells, and as the only tangential force, the interlayer friction contributes to the coupling. Therefore we have the torques exerted on the  $i$ -th shell from two neighboring shells as  $\tau_{ij} = f_{ij} \cdot r_i$ , where  $f_{ij}$  is the corresponding friction.

When every shell of a MWNT is in equilibrium, the shear modulus  $G$  is,

$$G = \sum_i \tau_i \frac{1}{2\pi r^3 \Delta\theta t} \left( \frac{l_1 l_2}{l_1 + l_2} \right) = \sum_i f_i \frac{1}{2\pi r^2 \Delta\theta t} \left( \frac{l_1 l_2}{l_1 + l_2} \right), \quad (6.11)$$

where  $\tau_i$  is the  $i$ -th torque applied on the shell;  $r$  is the radius and  $t$  is the thickness of the shell, which can be calculated using the chiral indices and  $t$  is either assumed as 0.34 nm or the average interlayer spacing, which causes less than 5% error in the results. During the calculation, we first assumed that the friction in the paddle part is trivial as more symmetry of system can be preserved by the uniform relative rotation of two shells under the strain. The results of the shear moduli of outer and inner shells  $G_o, G_i$  and the static frictions  $f_s$  are summarized in Table 6.5. Note that the measurement results were not sufficient to determine the torsional properties of the DWNT (6, 65)@(24, 44) and the TWNT.

While the shear moduli were in agreement with the previous predictions and experiments, the smaller static friction in the DWNT (49, 18)@(38, 16) with larger interlayer spacing than the DWNT (56, 2)@(37, 18) implies that the friction depends upon the interlayer coupling. As discussed previously [4, 43], the bearing

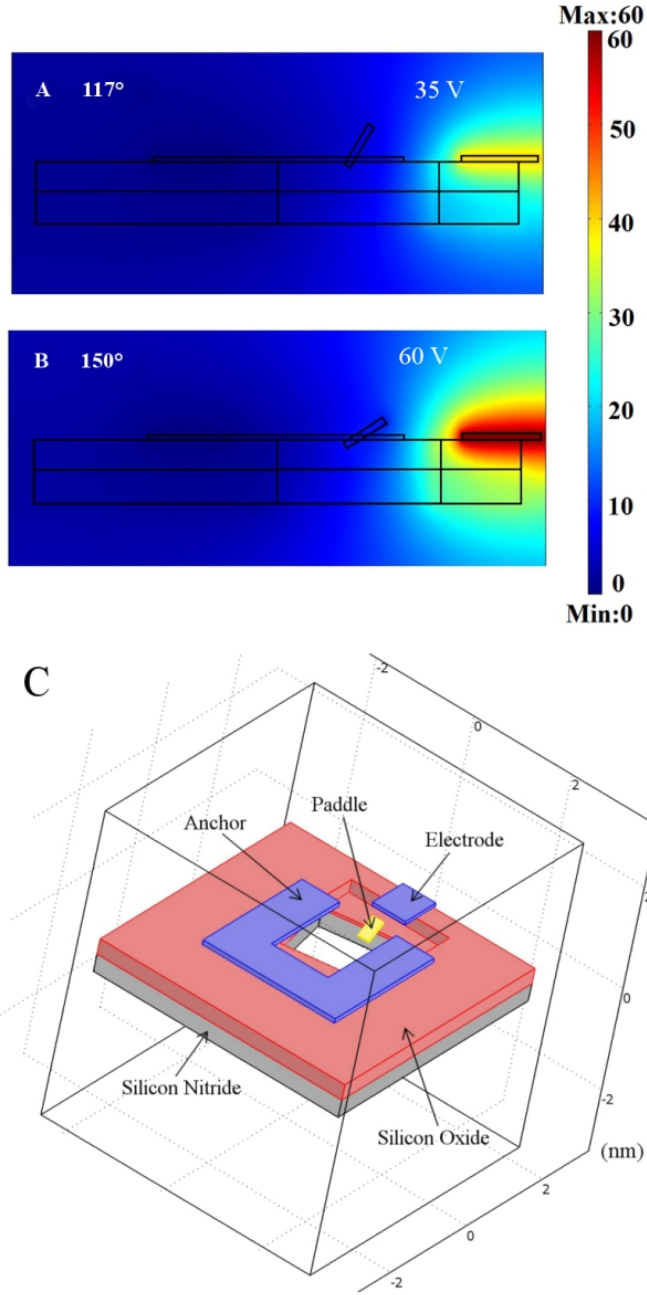


Figure 6.15: The schematic device model and the voltage distribution in FE analysis. (A,B) illustrate the voltage distribution in the space when the DC biases are 60 and 35 V and the paddle is deflected by 117 ° and 150 ° from the initial position. (C) The electrodes and the paddle are all metal with different voltages, while the substrate is composed by  $\text{SiO}_2$  and  $\text{Si}_3\text{N}_4$ . The FE result is simulated using COMSOL [42].

Table 6.5: Summary of the calculated shear moduli and frictions in two DWNT devices.

|                   | $G_o(\text{TPa})$ | $G_i(\text{TPa})$ | Static Friction $f_s (\times 10^{-6} \text{ nN/atom})$ |                     |
|-------------------|-------------------|-------------------|--|---------------------|
| (56, 2)@(37, 18)  | $0.48 \pm 0.01$   | $0.42 \pm 0.04$   | $6.8 \pm 4.0$ (40V)                                    | $9.8 \pm 5.2$ (60V) |
| (49, 18)@(38, 16) | $0.50 \pm 0.02$   | $0.43 \pm 0.05$   | $3.2 \pm 1.8$ (10V)                                    | $4.6 \pm 2.4$ (20V) |

friction in the paddle segment of the CNT was predicted in the magnitude of  $10^{-18}$  N/atom or even less, therefore negligible compared to the frictions of nN/atom in the non-paddle segments.

According to Equation (6.6) and Equation (6.7), once the twist angle of the CNT is known, the explicit atomic structure can be depicted by the coordinates of each carbon atoms, therefore the standard Lennard-Jones potential is able to be used to compute the interlayer van der Waals potential energy [44],

$$\Delta E_{vdw} = 4\epsilon \sum_{i=1}^{N_i} \sum_{j=1}^{N_o} \left[ \left( \frac{\sigma}{r_{ij}} \right)^{12} - \left( \frac{\sigma}{r_{ij}} \right)^6 \right], \quad (6.12)$$

where an atom in the inner and outer shell is denoted by  $i$  and  $j$ ,  $N_i$  and  $N_o$  are the total number atoms of the inner and outer shells,  $r_{ij}$  is the distance between the  $i$ -th atom in the inner shell and the  $j$ -th atom in the outer shell.  $\epsilon = 3.622 \text{ eV/atom}$  and  $\sigma = 0.385 \text{ nm}$  are used. We found that only the contributions from the 300 nearest atoms are significant, therefore the upper cutoff is set. Note that, the changes of van der Waals energy  $\Delta E_{vdw}$  are different in the paddle and the non-paddle segments, and should be calculated separately. Figure 6.16 shows the simulated van der Waals energy of a twisted 100 nm long DWNT (10, 10)@(5, 5). The black solid line represents  $\Delta E_{vdw}$  due to the uniform tangential displacement in the paddle segment. The periodicity of the interlayer potentials agrees reasonably well with the theoretical prediction, for the DWNT (10, 10)@(5, 5) should have a 10-fold rotational symmetry. We define the interlayer rotational corrugation as the maximal variation in the interlayer potential energy as the inner shell rotates around the outer, which is around 0.1 meV/atom in this DWNT. The dashed line is the  $\Delta E_{vdw}$  of the non-paddle segments during the twisting, assuming the twist angle of the inner shell is always 20% of the outer shell. The  $\Delta E_{vdw}$  increases linearly with the twist angle, while the total energy change in a rotation cycle is half of the corrugation in the paddle segment.

On the other hand, every MWNT device in our study is incommensurate with much lower rotational symmetry. Therefore, hardly any atom is in-registry during the twisting, and the energy corrugation was much flatter. For example, Figure 6.17 shows another simulation result of van der Waals interlayer energy in an incommensurate DWNT (11, 10)@(6, 5), where the energy of the paddle segment oscillates during the twisting with a relative flat corrugation of 0.05 meV/atom, and the interlayer energy in the non-paddle segments changes at a rate of 0.005 meV per rotation cycle. The simulation results are in good agreement with the theoretical expectations, because when the structure of a MWNT becomes more complex and more “incommensurate”, each shell can be considered as a solid tube in the continuum model because of the broken symmetry, as a consequence the interlayer energy subject to the torsional strain is a constant.



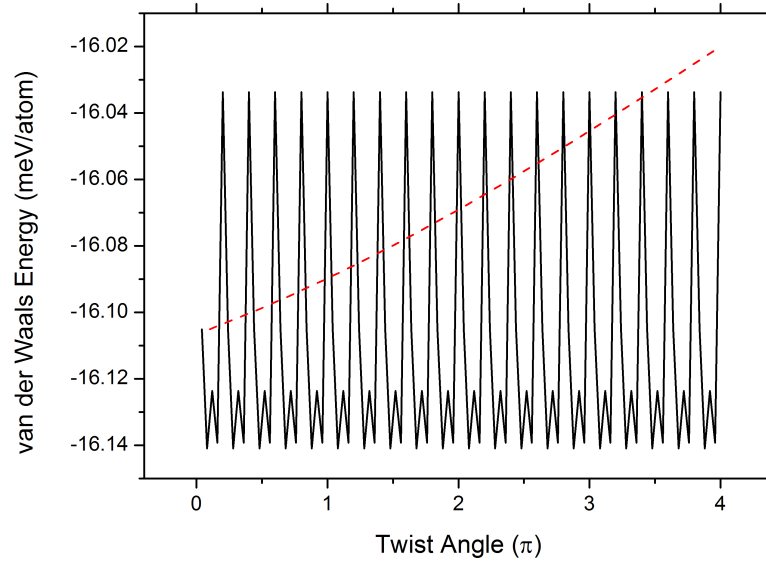


Figure 6.16: Simulated results of the interlayer energy  $(10, 10)@(5, 5)$  in two models. The solid line is the paddle segment while the dashed line is the non-paddle segment.

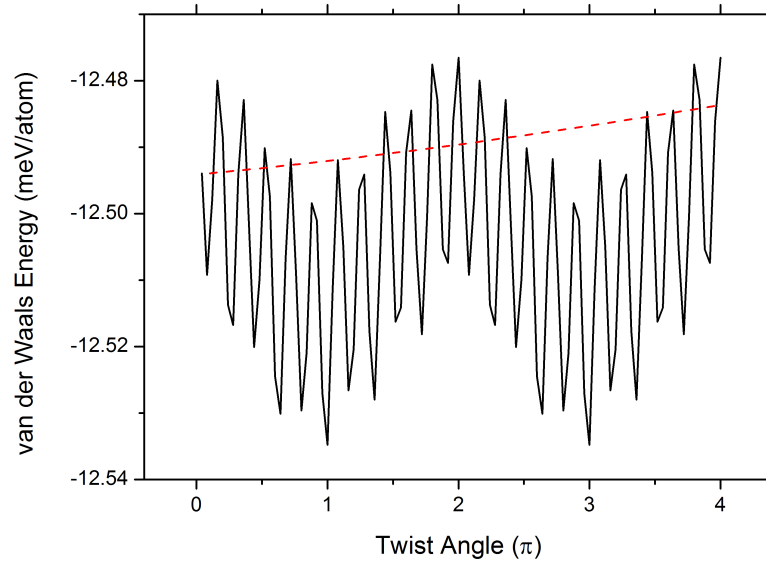


Figure 6.17: Simulated results of the interlayer energy  $(11, 10)@(6, 5)$  in two models. The solid line is the paddle segment while the dashed line is the non-paddle segment.

The intralayer interaction can be described by the Tersoff-Brenner potential [45], which interprets the bonding structure and properties of carbon materials. However, for the shear modulus has already been accurately identified, we computed the change of intralayer energy in a neat approach using the strain energy,

$$\Delta E_s = G\pi \frac{(r_o^4 - r_i^4)(\theta_f^2 - \theta_i^2)}{4(l_1 + l_2)}, \quad (6.13)$$

where  $\theta_f$  and  $\theta_i$  are the final the initial twist angles,  $r_o$  and  $r_i$  are the radii of the outer and the inner shell, respectively. Again, the MWNT in the paddle segment only undergoes a uniform angular displacement, and therefore the strain energy barely changes during the twisting.

When the outer shell is rotated with respect to the inner one, energy conservation requires that the external work done ( $W_e$ ) by the paddle, *i.e.* the electrostatic work done on the paddle by the electric field caused by DC bias, be equal to the changes in the intralayer  $\Delta E_s$  and the interlayer  $\Delta E_{vdw}$  plus the heat ( $W_f$ ) generated by friction. Thus, the average kinetic friction is  $f_k = \frac{4W_f}{\Delta\theta r}$ . Once the  $W_e$  is determined with FE analysis,  $f_k$  in DWNT (56, 2)@(37, 18) and DWNT (49, 18)@(38, 16) can be calculated as  $(2.6 \pm 1.0) \times 10^{-6}$  nN/atom and  $1.8 \pm 1.0 \times 10^{-6}$  nN/atom, respectively. The kinetic frictions are larger than the upper-limit value of kinetic friction measured in a telescoping motion in a MWNT [6].

Moreover, the interlayer van der Waals forces on both shells behave as normal forces and can be calculated using the simulation results for  $f_{vdw} = -\frac{\partial E_{vdw}}{\partial r}$ , as  $8.8 \times 10^{-2}$  and  $5.9 \times 10^{-3}$  nN/atom, respectively. Hence, the kinetic friction coefficients in DWNT (56, 2)@(37, 18) and DWNT (49, 18)@(38, 16) are determined as  $(1.8 \pm 0.7) \times 10^{-5}$  and  $(3.1 \pm 1.7) \times 10^{-4}$ .

Electromechanical experiments were also performed on DWNT (49, 18)@(38, 16) and TWNT (7, 53)@(8, 42)@(11, 28) to measure the changes of the transport property during the twisting. The resistances after etching  $R_0$  were measured as 2.5 M $\Omega$  and 30 M $\Omega$  with low DC bias, compared to the values prior to etching of 76 k $\Omega$  and 80 k $\Omega$ , respectively. The huge increases of the resistances are attributed to the undercut of the contact electrodes during the etching processes. Since only the outermost shell in a MWNT contributes to the overall electron transport property, we only considered the electromechanical response of the outermost shell. We observed the correlation between the resistance and the torsional strain  $\gamma = \frac{d}{l} \Delta\theta$  at room temperature as

$$R(\gamma) = R_c + \frac{1}{G_0 N |t|^2} \left[ 1 + \exp \left( \frac{E_g + 3t_0 \gamma \text{sgn}(2p+1) \sin 3\alpha}{2\kappa T} \right) \right]. \quad (6.14)$$

For both the outermost shells (49,18) in DWNT and (7,53) in TWNT device,  $p = 1$ , therefore we expect that the resistances increase with increasing strains, which agrees with the experimental measurements, as shown in Figure 6.18.

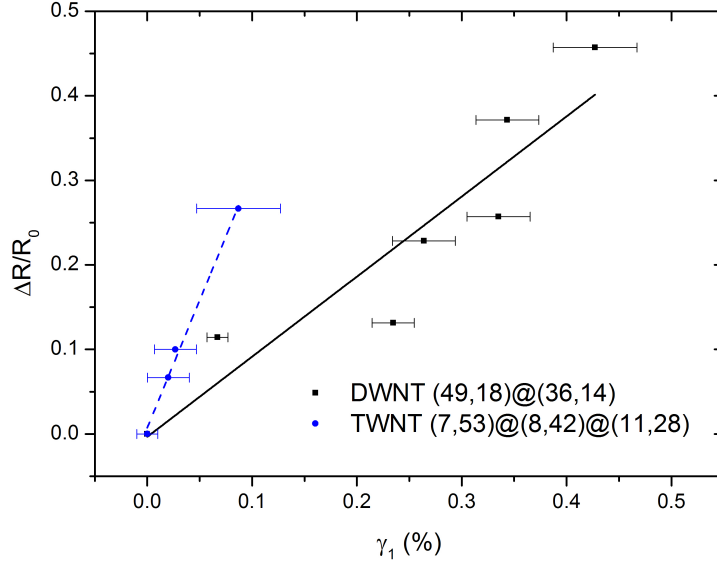


Figure 6.18: Characterization of DWNT (49, 18)@(38, 16) and TWNT (7, 53)@(8, 42)@(11, 28) transport properties under torsional strain on one side of the paddle (490 nm and 580 nm). The solid and dashed lines are the respective fits using the chiral indices of the outermost shells.

The total resistance of the system consists of the resistances from both sides  $l_1, l_2$  of the CNT and the contact resistance  $R_c$ , combining all the above equations, the change of the total resistance at room temperature is

$$\frac{\Delta R}{R_i} = \frac{R_c + R_1(\gamma_1) + R_2(-\gamma_2)}{R_c + R_1(\gamma = 0) + R_2(\gamma = 0)} - 1, \quad (6.15)$$

where  $R_i$  is the total resistance prior to the torsional strain,  $\gamma_2 = \frac{l_1}{l_2}\gamma_1$ , and when  $\gamma \ll 1$ , this ratio is proportional to the strain on one side  $\gamma_1$ . As the contact resistances prior to the etching were in the order of  $k\Omega$ , we consider the change in resistance after the etching as the new contact resistance. The electromechanical effects can be observed at room temperature because the maximum band gap change induced by the torsional strain is comparable to the thermal energy  $kT = 0.0256$  eV, and hence significantly changes the statistics. We then fit for the number of subbands in conductance  $N$  while taking the transmission probability  $|t|^2 = 0.2$  from the results shown in Chapter 5 and the band gap  $E_g$  as the calculated results in Table 5.1. The results of  $N = 14, 18$  in the DWNT and TWNT devices, respectively, indicate that, due to the small band gaps of the large MWNTs, carriers are thermally excited to the conducting bands and the number of subbands are involved in the conductance, which is consistent with the results discussed in Chapter 5.

## BIBLIOGRAPHY

- [1] M. Ternes, C. P. Lutz, C. F. Hirjibehedin, F. J. Giessibl, and A. J. Heinrich, “The force needed to move an atom on a surface,” *Science*, vol. 319, no. 5866, pp. 1066–1069, 2008.
- [2] B. Wolter, Y. Yoshida, A. Kubetzka, S.-W. Hla, K. von Bergmann, and R. Wiesendanger, “Spin friction observed on the atomic scale,” *Physical Review Letters*, vol. 109, no. 11, p. 116102, 2012.
- [3] A. N. Kolmogorov and V. H. Crespi, “Smoothest bearings: interlayer sliding in multiwalled carbon nanotubes,” *Physical Review Letters*, vol. 85, no. 22, pp. 4727–4730, 2000.
- [4] S. Zhang, W. K. Liu, and R. S. Ruoff, “Atomistic simulations of double-walled carbon nanotubes (dwcnts) as rotational bearings,” *Nano Letters*, vol. 4, no. 2, pp. 293–297, 2004.
- [5] J. Cumings and A. Zettl, “Low-friction nanoscale linear bearing realized from multiwall carbon nanotubes,” *Science*, vol. 289, no. 5479, pp. 602–604, 2000.
- [6] A. Kis, K. Jensen, S. Aloni, W. Mickelson, and A. Zettl, “Interlayer forces and ultralow sliding friction in multiwalled carbon nanotubes,” *Physical Review Letters*, vol. 97, no. 2, p. 025501, 2006.
- [7] P. Williams, S. Papadakis, A. Patel, M. Falvo, S. Washburn, and R. Superfine, “Torsional response and stiffening of individual multiwalled carbon nanotubes,” *Physical Review Letters*, vol. 89, no. 25, p. 255502, 2002.
- [8] P. Williams, S. Papadakis, A. Patel, M. Falvo, S. Washburn, and R. Superfine, “Fabrication of nanometer-scale mechanical devices incorporating individual multiwalled carbon nanotubes as torsional springs,” *Applied Physics Letters*, vol. 82, no. 5, pp. 805–807, 2003.
- [9] S. Papadakis, A. Hall, P. Williams, L. Vicci, M. Falvo, R. Superfine, and S. Washburn, “Resonant oscillators with carbon-nanotube torsion springs,” *Physical Review Letters*, vol. 93, no. 14, p. 146101, 2004.
- [10] J. C. Meyer, M. Paillet, and S. Roth, “Single-molecule torsional pendulum,” *Science*, vol. 309, no. 5740, pp. 1539–1541, 2005.
- [11] A. Hall, L. An, J. Liu, L. Vicci, M. Falvo, R. Superfine, and S. Washburn, “Experimental measurement of single-wall carbon nanotube torsional properties,” *Physical Review Letters*, vol. 96, no. 25, p. 256102, 2006.
- [12] J. P. Lu, “Elastic properties of carbon nanotubes and nanoropes,” *Physical Review Letters*, vol. 79, no. 7, pp. 1297–1300, 1997.
- [13] R. Heyd, A. Charlier, and E. McRae, “Uniaxial-stress effects on the electronic properties of carbon nanotubes,” *Physical Review B*, vol. 55, no. 11, p. 6820, 1997.
- [14] C. L. Kane and E. Mele, “Size, shape, and low energy electronic structure of carbon nanotubes,” *Physical Review Letters*, vol. 78, no. 10, pp. 1932–1935, 1997.
- [15] L. Yang, M. Anantram, J. Han, and J. Lu, “Band-gap change of carbon nanotubes: Effect of small uniaxial and torsional strain,” *Physical Review B*, vol. 60, no. 19, p. 13874, 1999.
- [16] L. Yang and J. Han, “Electronic structure of deformed carbon nanotubes,” *Physical Review Letters*, vol. 85, no. 1, pp. 154–157, 2000.
- [17] T. Cohen-Karni, L. Segev, O. Srur-Lavi, S. R. Cohen, and E. Joselevich, “Torsional electromechanical quantum oscillations in carbon nanotubes,” *Nature Nanotechnology*, vol. 1, no. 1, pp. 36–41, 2006.
- [18] C.-J. Park, Y.-H. Kim, and K. Chang, “Band-gap modification by radial deformation in carbon nanotubes,” *Physical Review B*, vol. 60, no. 15, p. 10656, 1999.

- [19] A. Charlier, E. McRae, R. Heyd, and M.-F. Charlier, “Metal–semiconductor transitions under uniaxial stress for single- and double-walled carbon nanotubes,” *Journal of Physics and Chemistry of Solids*, vol. 62, no. 3, pp. 439–444, 2001.
- [20] F. Bogar, J. Mintmire, F. Bartha, T. Mező, and C. Van Alsenoy, “Density-functional study of the mechanical and electronic properties of narrow carbon nanotubes under axial stress,” *Physical Review B*, vol. 72, no. 8, p. 085452, 2005.
- [21] H. Mehrez, A. Svizhenko, M. Anantram, M. Elstner, and T. Frauenheim, “Analysis of band-gap formation in squashed armchair carbon nanotubes,” *Physical Review B*, vol. 71, no. 15, p. 155421, 2005.
- [22] R. Saito, M. Fujita, G. Dresselhaus, and M. Dresselhaus, “Electronic structure of chiral graphene tubules,” *Applied Physics Letters*, vol. 60, p. 2204, 1992.
- [23] R. Saito, G. Dresselhaus, and M. Dresselhaus, “Electronic structure of double-layer graphene tubules,” *Journal of Applied Physics*, vol. 73, no. 2, pp. 494–500, 1993.
- [24] P. Lambin, L. Philippe, J. Charlier, and J. Michenaud, “Electronic band structure of multilayered carbon tubules,” *Computational Materials Science*, vol. 2, no. 2, pp. 350–356, 1994.
- [25] Y.-K. Kwon and D. Tománek, “Electronic and structural properties of multiwall carbon nanotubes,” *Physical Review B*, vol. 58, no. 24, pp. R16001–R16004, 1998.
- [26] Y.-G. Yoon, P. Delaney, and S. G. Louie, “Quantum conductance of multiwall carbon nanotubes,” *Physical Review B*, vol. 66, no. 7, p. 073407, 2002.
- [27] S. Uryu and T. Ando, “Electronic intertube transfer in double-wall carbon nanotubes,” *Physical Review B*, vol. 72, no. 24, p. 245403, 2005.
- [28] L. Chico, V. H. Crespi, L. X. Benedict, S. G. Louie, and M. L. Cohen, “Pure carbon nanoscale devices: Nanotube heterojunctions,” *Physical Review Letters*, vol. 76, no. 6, pp. 971–974, 1996.
- [29] C. Zhou, J. Kong, and H. Dai, “Intrinsic electrical properties of individual single-walled carbon nanotubes with small band gaps,” *Physical Review Letters*, vol. 84, no. 24, pp. 5604–5607, 2000.
- [30] J. Cao, Q. Wang, and H. Dai, “Electromechanical properties of metallic, quasimetallic, and semiconducting carbon nanotubes under stretching,” *Physical Review Letters*, vol. 90, no. 15, p. 157601, 2003.
- [31] E. Minot, Y. Yaish, V. Sazonova, J.-Y. Park, M. Brink, and P. L. McEuen, “Tuning carbon nanotube band gaps with strain,” *Physical Review Letters*, vol. 90, no. 15, p. 156401, 2003.
- [32] A. R. Hall, M. R. Falvo, R. Superfine, and S. Washburn, “Electromechanical response of single-walled carbon nanotubes to torsional strain in a self-contained device,” *Nature Nanotechnology*, vol. 2, no. 7, pp. 413–416, 2007.
- [33] T. W. Tombler, C. Zhou, L. Alexseyev, J. Kong, H. Dai, L. Liu, C. Jayanthi, M. Tang, and S.-Y. Wu, “Reversible electromechanical characteristics of carbon nanotubes under local-probe manipulation,” *Nature*, vol. 405, no. 6788, pp. 769–772, 2000.
- [34] C. Stampfer, A. Jungen, R. Linderman, D. Obergfell, S. Roth, and C. Hierold, “Nano-electromechanical displacement sensing based on single-walled carbon nanotubes,” *Nano Letters*, vol. 6, no. 7, pp. 1449–1453, 2006.
- [35] S. Frank, P. Poncharal, Z. Wang, and W. A. de Heer, “Carbon nanotube quantum resistors,” *Science*, vol. 280, no. 5370, pp. 1744–1746, 1998.
- [36] S. Wang and M. Grifoni, “Helicity and electron-correlation effects on transport properties of double-walled carbon nanotubes,” *Physical Review Letters*, vol. 95, no. 26, p. 266802, 2005.

- [37] Z. Liu, Q. Zhang, and L.-C. Qin, "Accurate determination of atomic structure of multiwalled carbon nanotubes by nondestructive nanobeam electron diffraction," *Applied Physics Letters*, vol. 86, no. 19, pp. 191903–191903, 2005.
- [38] L.-C. Qin, "Electron diffraction from carbon nanotubes," *Reports on Progress in Physics*, vol. 69, no. 10, p. 2761, 2006.
- [39] Z. Liu and L.-C. Qin, "A practical approach to determine the handedness of chiral carbon nanotubes by electron diffraction," *Chemical Physics Letters*, vol. 405, no. 4, pp. 265–269, 2005.
- [40] Z. Liu and L.-C. Qin, "Symmetry of electron diffraction from single-walled carbon nanotubes," *Chemical Physics Letters*, vol. 400, no. 4, pp. 430–435, 2004.
- [41] H. Deniz, A. Derbakova, and L.-C. Qin, "A systematic procedure for determining the chiral indices of multi-walled carbon nanotubes using electron diffraction—each and every shell," *Ultramicroscopy*, vol. 111, no. 1, pp. 66–72, 2010.
- [42] L. Lin, T. Cui, L.-C. Qin, and S. Washburn, "Direct measurement of the friction between and shear moduli of shells of carbon nanotubes," *Physical Review Letters*, vol. 107, no. 20, p. 206101, 2011.
- [43] A. Buldum and J. Lu, "Atomic scale sliding and rolling of carbon nanotubes," *Physical Review Letters*, vol. 83, no. 24, pp. 5050–5053, 1999.
- [44] Q. Zheng, J. Z. Liu, and Q. Jiang, "Excess van der waals interaction energy of a multiwalled carbon nanotube with an extruded core and the induced core oscillation," *Physical Review B*, vol. 65, no. 24, p. 245409, 2002.
- [45] D. Brenner, "Empirical potential for hydrocarbons for use in simulating the chemical vapor deposition of diamond films," *Physical Review B*, vol. 42, no. 15, p. 9458, 1990.

## CHAPTER 7

### Summary

This dissertation provides a comprehensive approach to investigate *in situ* electromechanical manipulation and to measure the corresponding response of a single carbon nanotube with the known atomic structure.

While the nanobeam electron diffraction is superior to other characterization techniques because of its unique capability to identify the chiral structure of a carbon nanotube, especially of a multiwalled carbon nanotube, the diffraction requires the carbon nanotube to be suspended from the substrate during the observation. To overcome this challenge, a customized device fabrication process was designed and developed.

The nano-electromechanical device was based on a single carbon nanotube synthesized with chemical vapor deposition, where various recipes were developed and modified for an appropriate the distribution of carbon nanotubes. The synthesis of carbon nanotubes was sensitive to various growth parameters such as temperature, gas flow rate and catalyst size. The catalyst solution density had a particularly significant effect for the synthesis of low-density carbon nanotubes in the magnitude of  $10^{-8}$  per  $m^2$ . Also, the structures of resultants, *i.e.* SWNTs, DWNTs, or FWNTs, proved to be correlated with the material of catalytic particles.

We developed a fabrication process consisting of photolithography, electron beam lithography and etching techniques for a “nano-pendulum” device, where a multiwalled carbon nanotube attached with a metal paddle was suspended from the substrate with both ends anchored by metal electrodes. The electrostatic field from the side gate drove the paddle, and hence exerted a torsional strain to the carbon nanotube. While the carbon nanotube was under strain, electron diffraction was performed on the suspended part to determine both the chiral structure and the twist angle of each shell.

The transparent contact between the palladium electrodes and the carbon nanotube allowed reliable measurements of the resistances under low DC bias. Since the conducting length of the carbon nanotube is less than the corresponding mean free path, it was concluded that the transport was in the ballistic regime. Given the chiral indices, the band gaps were calculated using the zone approximation with the second order modification due to the curvature effect. The Landauer-Büttiker formula then allowed us to determine the correlation between the chiral structure and the resistance at room temperature by taking account of the thermal excitation. The results suggested that only the outermost shell in a multiwalled carbon nanotube contributed

to the transport properties. Because of the shrinking of band gaps in carbon nanotubes with large diameters, more than two subbands participated in the conduction.

Investigation of the electromechanical responses of multiwalled carbon nanotubes were conducted. Twist angle of each shell in a multiwalled carbon nanotube under a torsional strain was measured. Due to the interlayer coupling, the inner shell strains in proportion to the outer shell but by a smaller amount (20% or less) without stiction. The shear modulus of each shell was calculated to be around 0.4 - 0.5 TPa, which agreed with the theoretical predictions, with the static frictions in the order of  $10^{-6}$  nN/atom. A physical model was established to calculate the van der Waals interlayer interaction energy, while the intralayer strain energy of each shell was estimated using the shear modulus. As a result of energy conservation, the average kinetic friction was derived and slightly smaller than the static friction.

Finally, the torsional electromechanical responses of carbon nanotubes with known chiral structures were observed by monitoring the resistance changes under torsional strains at room temperature. The knowledge of chiral indices correlated the torsional strain with the resistance alteration, and the fitted results indicated the possibility of thermal excitation and more participating subbands, which was in good agreement with the previous conclusions.



## **APPENDIX A**

### **CNTs syntheses with Chemical Vapor Deposition**

This chapter of the appendix details the step-by-step instruction of SWNT, DWNT and FWNT synthesis. Unless indicated, the recipes are performed on silicon wafers coated with a 200 nm SiO<sub>2</sub> film. The system holds constant pressure of 15 - 18 psi. Note that all the parameters listed here are highly sensitive to different apparatuses.

#### **A.1 SWNT synthesis**

1. Solvent clean silicon wafer substrate with Acetone/Methanol followed by UV/Plasma clean.
2. Solve 5 mg Fe(NO<sub>3</sub>)<sub>3</sub> in 50 ml IPA and dilute the solution to 1:10000.
3. Disperse the solution onto the entire wafer surface. Air-dry it slowly in a covered petri dish.
4. Load the wafer into tube furnace.
5. Purge the tube with Argon and Hydrogen at 500 sccm and 200 sccm for 15 min at room temperature.
6. Raise the temperature to 922 C at the ramping rate of 60 C/min.
7. Turn off Argon, increase Hydrogen flow rate to 500 sccm introduce Methane and Ethylene at 1500 sccm and 30 sccm, respectively, for 10 min growth.
8. Turn off Methane and Ethylene. Cool down the furnace to room temperature with Hydrogen on.
9. Turn off Hydrogen and unload the wafer.

#### **A.2 DWNT synthesis**

1. Solvent clean silicon wafer substrate with Acetone/Methanol followed by UV/Plasma clean.
2. Grind down FeSi<sub>2</sub> pellets and suspend 0.12 mg fine powder of FeSi<sub>2</sub> into 40 ml Ethanol. Dilute the suspension to 1:10000.
3. Disperse the sonicated suspension onto the wafer surface. Air-dry it slowly in a covered petri dish.

4. Load the wafer into tube furnace.
5. Bake the wafer in the air at 900 C for 10 min.
6. Purge the tube with Argon at 500 sccm for 15 min at 900 C.
7. Raise the temperature to 922 C.
8. Turn off Argon, introduce Hydrogen, Methane and Ethylene at 500 sccm, 1500 sccm and 30 sccm, respectively, for 10 min growth.
9. Turn off Methane and Ethylene. Cool down the furnace to room temperature with Hydrogen on.
10. Turn off Hydrogen and unload the wafer.

### **A.3 FWNT synthesis**

1. Solvent clean silicon wafer substrate with Acetone/Methanol followed by UV/Plasma clean.
2. 5 mg Catalyst(prepared in Dr. Liu's group at Duke University) is suspended into 50 ml Methanol. The suspension is then diluted to 1:20.
3. Disperse the sonicated suspension onto the wafer surface. Air-dry it slowly in a covered petri dish.
4. Load the wafer into tube furnace.
5. Purge the tube with Hydrogen and Argon at 200 sccm and 1000 sccm while increase the furnace temperature to 1000 C at the ramping rate of 60 C/min.
6. Turn off Argon. Introduce a mixture Ethanol/Methanol of 1:1 to the system by passing another stream of Argon at 500 sccm through a bubbler for 20 min growth.
7. Turn off Argon. Cool down the furnace to room temperature with Hydrogen on.
8. Turn off Hydrogen and unload the wafer.

### **A.4 Aligned SWNT synthesis on quartz wafer**

1. Load the wafer into tube furnace.
2. Bake the sample in the air at 785 C for 10 min. Then let the furnace cool down to room temperature.
3. Purge the tube with Hydrogen at 200 sccm for 10 min.

4. Raise the furnace temperature to 785 C at the ramping rate of 60 C/min. Reduce the sample with Hydrogen for 10 min.
5. Raise the temperature to 922 C. Introduce Methanol/Ethanol by passing two streams of Argon at 1000/500 sccm through bubblers for 10 min growth.
6. Turn off Argon. Cool down the furnace to room temperature with Hydrogen on.
7. Turn off Hydrogen and unload the wafer.

## **A.5 CNT transferring**

1. Spin coat the wafer with grown CNTs with 8% 495K PMMA at 2000 rpm for 30 s.
2. Soft bake the substrate on hotplate at 170 °C for 10 min.
3. Soak the PMMA-coated wafer into boiling 1 M/L KOH solution for 10 min. Frequently add DI water to the solution to keep the density.
4. The PMMA film will remove the CNTs from the substrate and be peeled off from the substrate.
5. Soak the PMMA film into DI water and place it onto the destination wafer.
6. Soft bake the substrate on hotplate at 170 °C for 15 min.
7. Solvent clean the wafer with acetone and methanol.

## **APPENDIX B**

### **Instruction of Suspended CNT Device Fabrication**

The following appendix includes a detailed fabrication procedure of the suspended “nano-pendulum” device which is ready for *in situ* TEM imaging and diffraction analysis. This method is mostly based on Dr. Adam Hall’s and Dr. Letian Lin’s instruction in their PhD dissertations. The procedure begins with a commercial Silicon wafer are pre-coated with 300 nm  $\text{Si}_3\text{N}_4$  films on both sides where only one side is polished and then named as “the front side”, followed by a series of photolithography, e-beam lithography and etching, which require the following apparatuses:

- Karl Suss MA6/BA6 Mask Aligner
- Advanced Vacuum Vision 310 Plasma Enhanced Chemical Vapor Deposition System
- Thermionics VE-100 Electron Beam Evaporator
- Alcatel AMS 100 Deep Reactive Ion Etcher
- Hitachi S-4700 Scanning Electron Microscope
- Nano Pattern Generation System (NPGS) Software (by J. C. Nability)
- Balzers Union CPD 020 critical point drying apparatus

#### **B.1 Backside Etching I**

This step is aimed to etch away  $\text{Si}_3\text{N}_4$  membrane and most of Si substrate from the backside using photolithography, DRIE and wet etching. Addition  $\text{Si}_3\text{N}_4$  and  $\text{SiO}_2$  films are deposited with PECVD to covered any possible leakages caused in the previous etching.

##### **B.1.1 Wafer preparation**

1. Soak the wafer into piranha for 10 min to remove any organics. Rinse and nitrogen dry the wafer.
2. Cut the wafer into  $33 \text{ mm} \times 9 \text{ mm}$  rectangle pieces, each of which could contain 6 circuits in a manner of  $3 \times 2$ .

## **B.1.2 Photolithography**

### **B.1.2.1 Standard solvent clean**

1. Soak the wafer in Acetone/Methanol/DI water sequentially for 5 min with ultrasonication.
2. Rinse under free flowing DI water and nitrogen dry.
3. Plasma clean the wafer for 10 min.

### **B.1.2.2 Coating of photoresist**

1. Place the wafer face down onto a spinner chuck by vacuum, completely cover the backside of wafer with photoresist S1813.
2. Spin coat the wafer at 3000 rpm for 60 s. The thickness of the photoresist is proportional to  $w^{-1/2}$ , where  $w$  is the spinner rotational speed in rpm.
3. Soft bake the wafer on hot plate at 115 C for 1 min to densify the resist.

### **B.1.2.3 Alignment, exposure and development**

1. Load the mask and make sure the mask is securely held by the vacuum.
2. Align the wafer to the mask so that the wafer can evenly hold 6 squares of 0.8 mm  $\times$  0.8 mm.
3. Expose at **HARD CONTACT** mode with **GAP** = 100  $\mu$ m and **EXPOSURE TIME** = 10 s.
4. Soak the wafer into MF319 Photoresist Developer for 40 s.
5. Rinse the wafer with DI water and nitrogen dry.
6. Check whether the photolithography patterns is over or under developed with optical microscope.

## **B.1.3 Removal of Si substrate with wet etching**

1. Soak the wafer into 15% KOH solution on sensor-controlled hot plate to make sure the temperature of KOH is constantly 70 C, the etching rate is roughly 1  $\mu$ m per min.
2. Monitor the etching process by the appearance of hydrogen bubbles caused by the reaction.
3. Check the etched depth every 20 min after first 4 hrs with optical microscope. Frequently add DI water to keep the KOH solution density.

4. Cease the etching when the etched depth reaches 400  $\mu\text{m}$ .
5. Rinse the sample with DI water followed by solvent clean.

### B.1.4 Plasma Enhanced Vapor Deposition

1. Condition PECVD by running **RF Etchback** and **Silicon Nitride** recipes for 30 min and 10 min sequentially.
2. Load the pre-etched wafer onto the center of the stage with the polished side facing up.
3. Run **Silicon Nitride** recipe for 3 min to deposit a 20 nm thick  $\text{Si}_3\text{N}_4$  film. (the deposition rate is approximately 7 nm/min)
4. Unload the sample. Condition with **RF Etchback** and **Oxide** recipes for 30 min and 10 min.
5. Load the sample.
6. Run **Oxide** recipe for 8 min to deposit a 200 nm thick  $\text{SiO}_2$  film (the deposition rate is approximately 27 nm/min).

Various CNTs are grown on the front side of the sample using the CVD methods mentioned in Chapter A. An appropriate density is usually 3 CNTs per  $10^4 \mu\text{m}^2$ , while each CNT is 20 - 30  $\mu\text{m}$  long.

## B.2 Circuit Deposition

Due to the resolution limit of photolithography and the yield limit of e-beam lithography, the circuit is deposited in two steps: first, large electrodes as small as 5  $\mu\text{m}$  are metallized in the batch of six identical circuits. Then the wafer is cut into six pieces, on each of which e-beam lithography is performed for channels of 100 nm wide to connect the large electrodes with CNTs. Fiducials are photolithography pattern prior to channels for finer alignment.

### B.2.1 Photolithography for large electrodes

#### B.2.1.1 Standard solvent clean

1. Soak the wafer in Acetone/Methanol/DI water sequentially for 5 min with ultrasonication.
2. Rinse under free flowing DI water and nitrogen dry.
3. Plasma clean the wafer for 10 min.

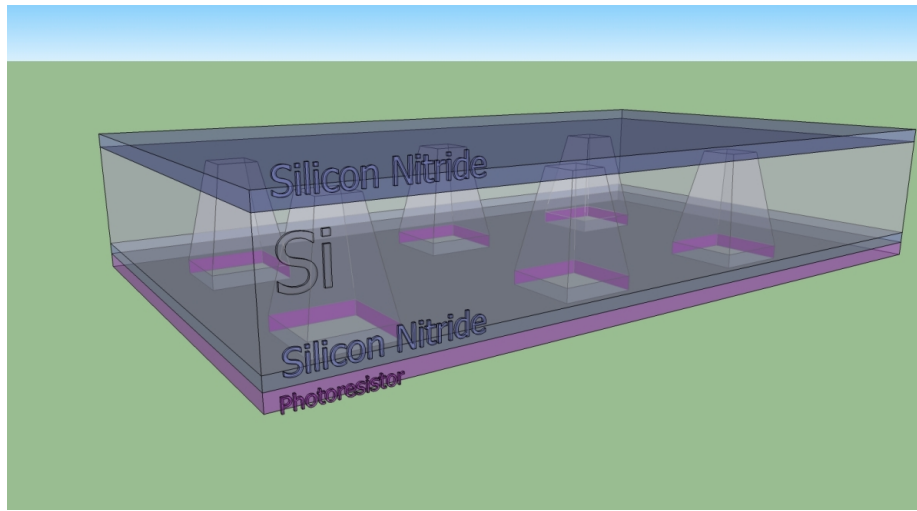


Figure B.1: Six windows of size  $0.4\text{ mm} \times 0.4\text{ mm}$  are etched on the backside of the wafer with DRIE and KOH according to photolithography patterns

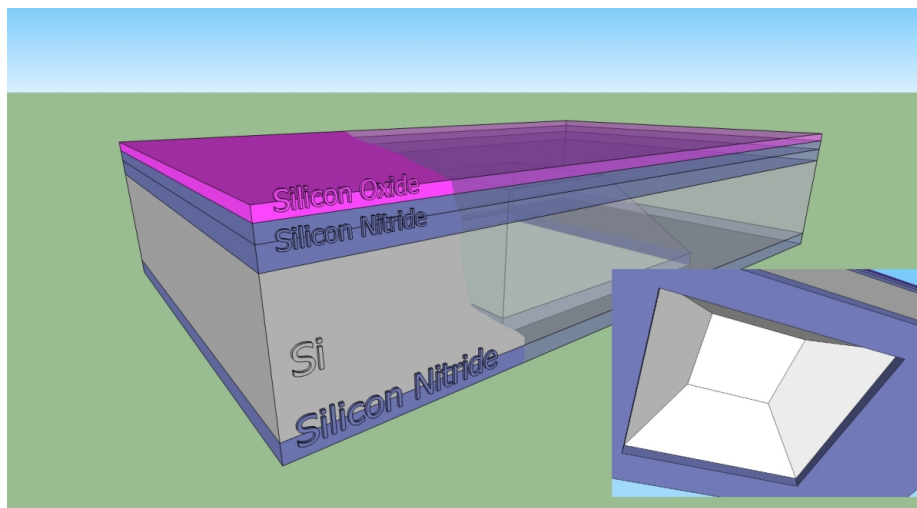


Figure B.2: The  $\text{Si}_3\text{N}_4$  film of 20 nm is deposited to cover any possible cracks in the KOH etching, whereas the  $\text{SiO}_2$  film provides an essential substrate for CNT growth.

### B.2.1.2 Coating of photoresist

1. Place the wafer face down onto a spinner chuck with vacuum, completely cover the wafer with photoresist S1813.
2. Spin coat the wafer at 3000 rpm for 60 s. The thickness of the photoresist is proportional to  $w^{-1/2}$ , where  $w$  is the spinner rotational speed in rpm.
3. Soft bake the wafer on hot plate at 115 C for 1 min to densify the resist.

### B.2.1.3 Alignment, exposure and development

1. Load the mask and make sure the mask is securely held by the vacuum.
2. Place the double sides alignment wafer chunk into the chunk holder.
3. Turn on the backside microscopes by clicking **BSA**.
4. Align the microscope position so that the desired circuit patterns on the mask can be seen through both two backside microscopes.
5. Lock the backside microscope position and capture two pictures of both microscopes by clicking **GRAB**. The pictures are permanently shown side by side on the monitor.
6. Load the wafer.
7. Align the wafer to the mask by changing the wafer position so that the two circuit patterns in the capture picture overlap with the 0.4 mm  $\times$  0.4 mm square windows etched on the backside of the wafer, respectively.
8. Expose at **HARD CONTACT** mode with **GAP** = 100  $\mu$ m and **EXPOSURE TIME** = 10 s.
9. Soak the wafer into MF319 Photoresist Developer for 40 s.
10. Rinse the wafer with DI water and nitrogen dry.
11. Check whether the photolithography patterns are over or under developed with optical microscope.

### B.2.1.4 Metallization

1. Vent the chamber, note that it takes more than half an hour to reach the atmosphere pressure.
2. Load the wafer into the e-beam evaporator.



3. Pump the chamber until it reaches  $10^{-6}$  Tor.
  4. Deposit 8 - 10 nm Cr and 50 nm Au films sequentially. Double check the metal selection knob before each run.
  5. Vent the chamber and unload the sample.
  6. Lift off the metal film by soaking the wafer in Acetone for at least 40 min, carefully sonicate the wafer in Acetone for 1 min or less.
  7. Solvent clean the sample and nitrogen dry.
1. Cut the wafer into six individual chips, each of which has a complete circuit. Avoid the silicon debris scratching the chip surface to damage the circuits.
  2. Hook up a chip to the stage connected to a Keithley multimeter.
  3. Set the Keithley as a voltage source and measure the current flow between each adjacent electrodes and with the back gate.
  4. A current reading larger than 10 pA implies possible CNTs connecting the electrodes. Gradually increase the voltage in the step of 10 V until the CNTs are burned when the current drops to couple pA.
  5. The threshold voltage can go up to 100 V in the case of robust CNTs or MWNTs. However, higher voltage is more likely to melt the metal electrodes given any shorts in the substrate.
  6. Capture a high resolution image of the playground area on the chip at the magnification of **1.3k** with SEM at **1.5 kV** and **20 uA**, as shown in Figure B.3

## **B.2.2 E-beam Lithography of fiducials**

### **B.2.2.1 Bi-layer Resist Coating**

1. Solve 495K and 950K poly-(methyl methacrylate)(PMMA) in chlorobenzene, respectively, both for 4 %. Sonicate for 10 min. Prepare the resist solutions 24 hours prior to the usage.
2. Pre bake the sample at 150 C for 30 min.
3. Spin coat 4 % 495K PMMA at 5000 rpm for 40 s, bake on hotplate at 180 C for 5 min.
4. Spin coat 4 % 950K PMMA at 4000 rpm for 40 s, bake on hotplate at 180 C for 5 min.

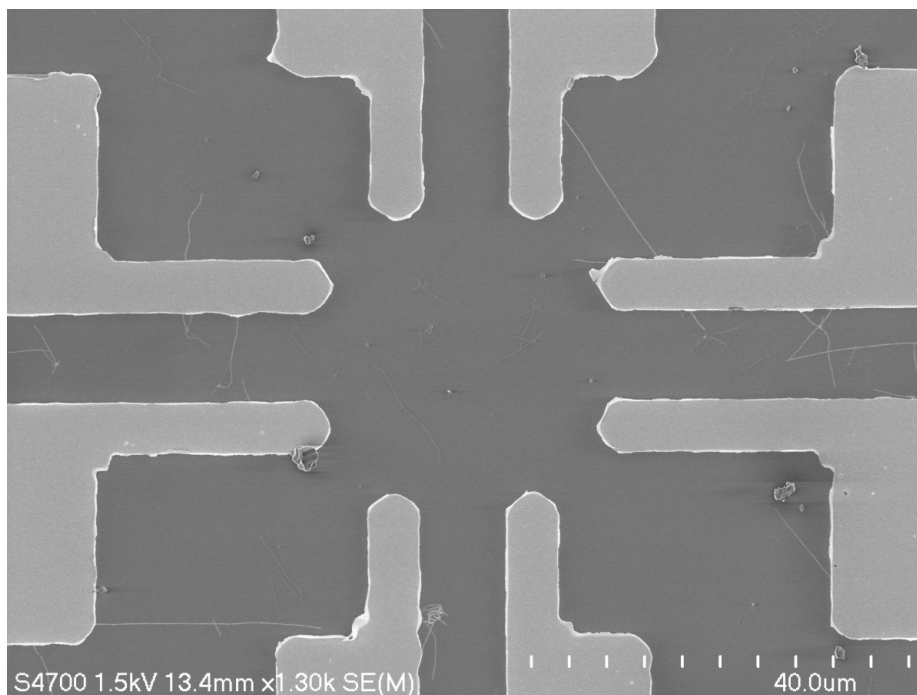


Figure B.3: The playground of the chip after the deposition of large electrodes under SEM

5. Bake the sample in tube furnace in the air at 180 C for 2 hour.
6. Mark a scratch near the playground on the resist without touching any metal to avoid shorts.

#### B.2.2.2 CAD

1. Load the high resolution image in the DesignCAD software.
2. Load coarse alignment pattern, **coarsealign.dc2**, and fiducials patten, **fiducial.dc2**. Note that the patterns are specifically designed for images captured at 1.3k magnification.
3. Scale the image by inputting the length of the SEM scale bar. (shortcut **U**)
4. Center the image.(shotcut **V**)
5. Copy and paste the four fiducials to the image. Adjust the positions of the individual fiducials to avoid overlapping on CNTs. Note that the fiducials can be overlapped with the electrodes.
6. Copy and paste the coarse alignment patterns to the image. Place the crossings right onto any recognizable corner, also avoiding overlapping with CNTs.
7. Delete the background image.

8. **NPGS** → **Save** the fiducials as a file named **F\*\_dev.dc2** and the alignment crossings as **F\*\_aln.dc2**, respectively.

### **B.2.2.3 Run File Set up**

1. In NPGS software, **Project** → **Creat New Project**, add the folder where the .dc2 files are saved.
2. Open **Run File Editor**, set **entities** to 2, the first layer as **alignment** with **F\*\_aln.dc2** and the second as **pattern** with **F\*\_dev.dc2**.
3. In **alignment** tab, set **Magnification = 900**, **Measured Beam Current = 12 pA**, **Line Spacing = 2000 Å**.
4. In **pattern** tab, set **Magnification = 900**, **Measured Beam Current = 12 pA**, **Line Spacing = 300 Å**, **dose = 1.1 nC/cm**.
5. Save the run file as **F\*.rf6** and process the file with SEM off.

### **B.2.2.4 Exposure**

1. Use the sample holder with Faraday hold for e-beam lithography. Short all the electrodes to the stage with copper tapes to avoid static charge accumulation.
2. Set the SEM at **30 kV** and **5 uA**. Connect the cable from the ground to the nano-ampere meter.
3. Quickly find the scratch and Faraday hole, save two positions in the SEM. Now the stage can be moved between two positions with the beam off to avoid over-exposure.
4. Move to the scratch position with the beam off, set **Condense Lens = 1.0**, align the SEM. Then **Condense Lens = 9.0**, do the alignment again.
5. Move to Faraday hole, record the reading  $I_{\text{off}}$  on the ampere meter with the beam off. Turn on the beam, set the magnification to 100k and adjust **Condense Lens** until the reading  $I_{\text{on}}$  satisfying  $I_{\text{on}} - I_{\text{off}} = -12$  pA, as required in the run file.
6. Move back to the scratch with the beam off. Check the alignment.
7. Repeat previous steps until the imaging at the scratch is well aligned and focused while the beam current is 12 pA at Faraday hole.
8. Fast move the stage to the playground from the scratch with the beam on. Center the beam. Set the magnification to the preset value in the run file.

9. Switch from **SEM** to **NPGS**, click **Process file** on the NPGS computer.
10. Align the crossings to the preset corners. Shortcut **A** is to auto adjust of contrast and brightness; **Insert** move to the next scanning window.
11. Turn off the SEM beam when the exposure ends. Switch back to **SEM**.

#### **B.2.2.5 Development**

1. Prepare 20 ml of developer, Methyl isobutyl ketone(MIBK) : IPA = 1 : 3, and adequate IPA.
2. Soak the sample in the developer for 70 s.
3. Rinse the sample with IPA and nitrogen dry.
1. Load the wafer into the e-beam evaporator.
2. Deposit 8 - 10 nm Cr and 80 nm Au films sequentially. Double check the metal selection knob before each run.
3. Lift off the metal film by soaking the wafer in Acetone for at least 1 hour. Don't sonicate the sample unless necessary.
4. Solvent clean the sample and nitrogen dry.

### **B.2.3 E-beam Lithography of channels**

#### **B.2.3.1 Bi-layer Resist Coating**

1. Pre bake the sample at 150 C for 30 min.
2. Spin coat 4 % 495K PMMA at 5000 rpm for 40 s, bake on hotplate at 180 C for 5 min.
3. Spin coat 4 % 950K PMMA at 4000 rpm for 40 s, bake on hotplate at 180 C for 5 min.
4. Bake the sample in tube furnace in the air at 180 C for 2 hour.
5. Mark a scratch near the playground on the resist without touching any metal to avoid shorts.

#### **B.2.3.2 CAD**

1. Capture a high resolution image with SEM at magnification of **1.3k, 1.5 kV** and **20 uA**.
2. Load the high resolution image in the DesignCAD software.

3. Load fine alignment pattern, **finealign.dc2**. Note that the patterns are specifically designed for images captured at 1.3k magnification.
4. Scale the image by inputting the length of the SEM scale bar. (shortcut U)
5. Center the image.(shotcut V)
6. Copy the three-layer crossings in **finealign.dc2** to the image. Align the positions of crossings in each layer to the corresponding markers in the fiducials.
7. Set the width of line as **600 nm**, draw lines to connect the CNTs with the electrodes. Avoid any obtuse angle which NPGS can not handle while drawing. The spacing between the lines should be large than **200 nm** due to inevitable beam drift.
8. Draw anchors and paddles on the CNTs with line widths of **1  $\mu\text{m}$**  and **200  $\mu\text{m}$** , respectively.
9. Delete the background image.
10. **NPGS** → **Save** the patterns as a file named **P\*\_dev.dc2** and the alignment crossings as **P\*\_aln.dc2**, respectively.

### B.2.3.3 Run File Set up

1. In NPGS software, **Project** → **Creat New Project**, add the folder where the .dc2 files are saved.
2. Open **Run File Editor**, set **entities** to 2, the first layer as **alignment** with **P\*\_aln.dc2** and the second as **pattern** with **P\*\_dev.dc2**.
3. The proper magnification should be the biggest possible value in the SEM, usually 900, which is smaller than both magnifications shown in two .dc2 files.
4. In **alignment** tab, set **Magnification = 900**, **Measured Beam Current = 12 pA**, separate layers 7 - 18 to three sets, while **Line Spacing(7-10) = 2000 Å**, **Line Spacing(11-14) = 456 Å**, **Line Spacing(15-18) = 192 Å**.
5. In **pattern** tab, set **Magnification = 900**, **Measured Beam Current = 12 pA**, **Line Spacing = 300 Å**, **dose = 0.9 nC/cm**, the dose value could be as low as 0.6 nC/cm given finer pattern structures.
6. Save the run file as **P\*.rf6** and process the file with SEM off for test. If errors, check the pattern design.

#### B.2.3.4 Exposure

1. Use the sample holder with Faraday hold for e-beam lithography. Short all the electrodes to the stage with copper tapes to avoid static charge accumulation.
2. Set the SEM at **30 kV** and **5 uA**. Connect the cable from the ground to the nano-ampere meter.
3. Quickly find the scratch and Faraday hole, save two positions in the SEM. Now the stage can be moved between two positions with the beam off to avoid over-exposure.
4. Move to the scratch position with the beam off, set **Condense Lens = 1.0**, align the SEM. Then **Condense Lens = 9.0**, do the alignment again.
5. Move to Faraday hole, record the reading  $I_{\text{off}}$  on the ampere meter with the beam off. Turn on the beam, set the magnification to 100k and adjust **Condense Lens** until the reading  $I_{\text{on}}$  satisfying  $I_{\text{on}} - I_{\text{off}} = -12\text{pA}$ , which is required in the run file.
6. Move back to the scratch with the beam off. Check the alignment.
7. Repeat previous steps until the imaging at the scratch is well aligned and focused while the beam current is 12 pA at Faraday hole.
8. Fast move the stage to the playground from the scratch with the beam on. Center the beam. Set the magnification to the preset value in the run file.
9. Switch from **SEM** to **NPGS**, click **Process file** on the NPGS computer.
10. Align the three layer crossings to the responding markers in the fiducials. Shortcut **A** is to auto adjust of contrast and brightness; **Insert** switch between the scanning windows; **Space** proceed to the next layer
11. Turn off the SEM beam when the exposure ends. Switch back to **SEM**.

#### B.2.3.5 Development

1. Soak the sample in the developer(MIBK : IPA = 1 : 3) for 70 s.
2. Rinse the sample with IPA and nitrogen dry.

#### B.2.3.6 Metallization

1. Load the wafer into the e-beam evaporator.
2. Deposit a 80 nm Pd film.

3. Lift off the metal film by soaking the wafer in Acetone for at least 1 hour. Don't sonicate the sample unless necessary.
4. Solvent clean the sample and nitrogen dry.

### **B.3 Backside Etching II**

1. Place a large silicon wafer on hot plate at 60 C in the hood.
2. Cut a 5 mm × 5 mm copper tape. Cover the top half of the front side with the tape to protect the playground from etching.
3. Place the sample face down onto the pre heated wafer.
4. Drip drops of HNA(Hydrofluoric/Nitric/Acetic Acid) with pipette into the Si window on the backside of the sample.
5. Repeat the previous step until all Si are etched away.
6. Rinse the sample with DI water followed by solvent clean. For the remain substrate of Si<sub>3</sub>N<sub>4</sub> and SiO<sub>2</sub> is thin and thus fragile, no sonication is allowed in the following step, and gently dry the sample with nitrogen gun.

### **B.4 FIB Etching**

#### **B.4.1 Front Etching**

1. Short all the electrodes on the sample with a piece of copper tape.
2. Load the sample facing up in the FIB chamber.
3. In the SEM moder Center the sample to a corner of the upper left electrode.
4. Adjust the height while tilting the stage between 0 °, 7 ° and then 0°, 52° to locate the eucentric point.
5. Tilt the stage to 52° and switch to the ion beam mode.
6. Ion etch a 13 μm × 13 μm square in a blank area with etch depth of **550 nm** to etch through the Si<sub>3</sub>N<sub>4</sub> and SiO<sub>2</sub>
7. Tile the sample back to 0° and switch to the SEM mode.

8. Center the stage to the center of the playground, find the new eucentric point.
9. Ion etch a crossing of 700 nm wide and 3  $\mu\text{m}$  long in a blank area with etch depth of **550 nm**.
10. Switch back to the SEM mode and capture a image of the playground at the magnification of 1.3k.
11. Record the relative positions of all desired etchings to the crossing.
12. Unload the sample.

### **B.4.2 Back Etching**

1. Load the sample facing down in the FIB chamber.
2. Locate the crossing in the SEM mode. Find the eucentric point and then switch to the ion beam mode.
3. Etch 0.5  $\mu\text{m}$   $\times$  0.5  $\mu\text{m}$  squares right besides the crossing with different etch depth to find out the thickness of the substrate according to the beam respond curve. Double check the front SEM imaging to make sure there is no metal channel.
4. Locate the desired etching positions relative to the crossing. Draw rectangles at the positions of widths smaller than the spacing between the neighbor electrodes and of length 2  $\mu\text{m}$ .
5. Etch the rectangles with appropriate etch depth, which is 100 nm lower than the substrate thickness, to etch away all  $\text{Si}_3\text{N}_4$  membrane but leave a 100 nm  $\text{SiO}_2$  film to support the CNTs.
6. Unload the sample.
7. Check the etched rectangle positions with optic microscope.

### **B.4.3 E-beam Lithography of windows**

#### **B.4.3.1 Bi-layer Resist Coating**

1. Pre bake the sample at 150 C for 30 min.
2. Spin coat 4 % 950K PMMA at 4000 rpm for 40 s, bake on hotplate at 180 C for 5 min.
3. Bake the sample in tube furnace in the air at 180 C for 2 hour.
4. Mark a scratch near the playground on the resist without touching any metal to avoid shorts.



#### B.4.3.2 CAD

1. Capture a high resolution image with SEM at magnification of **1.3k, 1.5 kV** and **20 uA**.
2. Load the high resolution image in the DesignCAD software.
3. Load fine alignment pattern, **finealign.dc2**. Note that the patterns are specifically designed for images captured at 1.3k magnification.
4. Scale the image by inputting the length of the SEM scale bar. (shortcut U)
5. Center the image.(shotcut V)
6. Copy the three-layer crossings in **finealign.dc2** to the image. Align the positions of crossings in each layer to the corresponding markers in the fiducials.
7. Set the width of line as **200 nm**, draw lines at the corresponding positions of the etched rectangles in the FIB etch step.
8. Delete the background image.
9. **NPGS** → **Save** the patterns as a file named **E\*\_dev.dc2** and the alignment crossings as **E\*\_aln.dc2**, respectively.

#### B.4.3.3 Run File Set up

1. In NPGS software, **Project** → **Creat New Project**, add the folder where the .dc2 files are saved.
2. Open **Run File Editor**, set **entities** to 2, the first layer as **alignment** with **E\*\_aln.dc2** and the second as **pattern** with **E\*\_dev.dc2**.
3. In **alignment** tab, set **Magnification = 900**, **Measured Beam Current = 12 pA**, **Line Spacing = 2000 Å**.
4. In **pattern** tab, set **Magnification = 900**, **Measured Beam Current = 12 pA**, **Line Spacing = 300 Å**, **dose = 1.1 nC/cm**.
5. Save the run file as **E\*.rf6** and process the file with SEM off.

#### B.4.3.4 Exposure

1. Use the sample holder with Faraday hold for e-beam lithography. Short all the electrodes to the stage with copper tapes to avoid static charge accumulation.
2. Set the SEM at **30 kV** and **5 uA**. Connect the cable from the ground to the nano-ampere meter.
3. Quickly find the scratch and Faraday hole, save two positions in the SEM. Now the stage can be moved between two positions with the beam off to avoid over-exposure.
4. Move to the scratch position with the beam off, set **Condense Lens = 1.0**, align the SEM. Then **Condense Lens = 9.0**, do the alignment again.
5. Move to Faraday hole, record the reading  $I_{\text{off}}$  on the ampere meter with the beam off. Turn on the beam, set the magnification to 100k and adjust **Condense Lens** until the reading  $I_{\text{on}}$  satisfying  $I_{\text{on}} - I_{\text{off}} = -12\text{pA}$ , which is required in the run file.
6. Move back to the scratch with the beam off. Check the alignment.
7. Repeat previous steps until the imaging at the scratch is well aligned and focused while the beam current is 12 pA at Faraday hole.
8. Fast move the stage to the playground from the scratch with the beam on. Center the beam. Set the magnification to the preset value in the run file.
9. Switch from **SEM** to **NPGS**, click **Process file** on the NPGS computer.
10. Align the three layer crossings to the responding markers in the fiducials. Shortcut **A** is to auto adjust of contrast and brightness; **Insert** switch between the scanning windows; **Space** proceed to the next layer
11. Turn off the SEM beam when the exposure ends. Switch back to **SEM**.

#### B.4.3.5 Development

1. Soak the sample in the developer(MIBK : IPA = 1 : 3) for 70 s.
2. Rinse the sample with IPA and gently dry the sample with nitrogen gun.
3. Check the position of windows with optical microscope.

#### B.4.4 Buffered hydrofluoric acid etching

1. Place the sample facing up on a Telfon stage in the hood.
2. Drip several drops of 1 : 5 BHF(Buffered Hydro-Fluoric acid) onto the surface of sample. Be careful not to let BHF reach the edges.
3. Wait 0.5 - 1 min for a thorough etch of SiO<sub>2</sub>. Note that the etch rate of BHF on PECVD SiO<sub>2</sub> is roughly 250 nm/min.
4. Carefully transfer the sample into a 100 ml beaker full DI of water to stop etching.
5. Soak the sample in 20 ml Acetone for 1 hr to remove the PMMA. When transferring the sample between DI water and acetone, keep the surface wet with liquid coverage all the time.
6. Transfer the sample to 100 ml Ethanol without taking the sample out of Acetone.
7. Transfer the sample to another 100 ml Ethanol. Repeat to dilute Acetone.

#### B.4.5 Critical Point Dry

1. Fill the chamber with little Ethanol to cover the sample.
2. Place a small glass ring as flow protector in the chamber, and a right-angle ceramic fragment inside the ring.
3. Transfer the sample to the chamber without breaking the surface tension. Place one side of the sample on the ceramic support so that the sample is tilted 45 ° from the chamber bottom. The sample should face down.
4. Close the lid and turn on two tanks of CO<sub>2</sub>. Press **MAINS**.
5. Set the goal temperature to **15 °C**.
6. Once 15 °C, slightly turn on **GAS IN** to slowly fill the chamber with liquid CO<sub>2</sub>.
7. Turn off **GAS IN**, turn on **GAS OUT** and **METERING VALVE** to drain the liquid but not the liquid level drop below the sample.
8. Repeat the fill and drain process for 4 - 5 times until the liquid is clear and all Ethanol is replaced by CO<sub>2</sub>.
9. Turn off all valves.

10. Set the goal temperature to **45 °C**. The transition can be observed when reaching the desired temperature.
11. After transition, completely turn on **METERING VALVE** whereas slightly turn on **GAS OUT** to avoid condensation.
12. Unload the sample when the pressure reaches the atmosphere pressure.

## B.5 Before Starting

1. Check and record the reading of Vacuum Gauges.

$$P_1 \approx 0; 60 \text{ l/s}$$

$$P_2 < 2 \times 10^{-5} \text{ Pa}; 150 \text{ l/s}$$

$$P_4 \approx 1 \times 10^{-6} \text{ Pa}$$

$$P_5 \approx 0$$

2. Check the vacuum monitor on the left bottom of the control desk: lights **V2, V13, V17, V5b, V8 and V21** should be green.
3. Fill the cold finger with liquid nitrogen.
4. Check Condenser Aperture and Objective Aperture are out.
5. Neutralize Stage Position by clicking **EXCHANGE** in the FasTEM computer dialogue and pressing **N** on the left of the screen.
6. Set the desired voltage by selecting **HT** in FasTEM computer .
7. Place the sample facing down onto the sample holder.
8. Unload the sample substitute and load the sample holder following the procedure.
9. Press **V1** on the bottom of the left control panel to open the gun valve.

## B.6 Alignment

1. Insert the largest condenser aperture(110  $\mu\text{m}$ ) in the FasTEM computer.
2. Set the **DV**, Deviation Voltage, to +0 nm on the monitor: adjust **OBJ FOCUS**, OBJective FOCUS, back and forth until **DV** changes from -0 nm to +0 nm. Press **MAG2** to set this point as the optimum focus point.

3. Press **LOW MAG** to switch to the low magnification mode. Center the stage to find a large empty hold on the TEM sample. Press **MAG2** to raise the magnification to 40k.
4. Focus the image using **Z-CONTROL**.

## **B.6.1 Condenser Aperture Alignment**

### **B.6.1.1 Condenser Aperture Centering**

1. Converge the beam with **BRIGHTNESS** to reach crossover. Center crossover with **CONDENSER SHIFT X, Y**.
2. Adjust **BRIGHTNESS** back and forth through crossover.
3. Adjust the aperture position using the FasTEM computer until the beam expands and contracts concentrically.
4. Center crossover. Repeat until the aperture is centered.

### **B.6.1.2 Condenser Lens Astigmatism**

1. Go to crossover. Press **COND STIGMATOR** on the right bottom drawer.
2. Adjust **DEF X, Y** until the beam is circular at magnifications of both 40k and 300k.
3. Center the aperture position.

## **B.6.2 Gun Shift**

1. Switch TEM mode between the largest spot 1-3 and the smallest spot 5-3 using **SPOT SIZE**.
2. Press **GUN** on the right bottom drawer.
3. At TEM 5-3 mode, center crossover by **CONDENSER SHIFT X, Y**; at 1-3 mode, center crossover by **SHIFT X, Y**.
4. Repeat the steps until crossover doesn't shift when changing the mode.

## **B.6.3 Gun Tilt**

1. Leave **GUN** on and TEM mode 1-3.
2. Center crossover with **SHIFT X, Y**.

3. Press **ANODE WOBBLER** and adjust **DEF X, Y** until the beam expands and contracts symmetrically.
4. Repeat the steps until both Gun Shift and Gun Tilt are aligned.

#### **B.6.4 Condenser Deflector Tilt/Pivot Point Balance**

1. Center crossover at 300k. Press **COND DEF ADJ TILT** on the right bottom draw.
2. Toggle **TILT** switch to **X** and adjust **SHIFT X** and **DEF X** to converge the separated central spots.
3. Toggle **TILT** switch to **Y** and adjust **SHIFT Y** and **DEF Y** to converge the separated central spots.
4. Center crossover.

#### **B.6.5 Beam Tilt/Voltage Center**

1. Set the magnification to 300k.
2. Center and focus a recognizable feature.
3. Press **IMAGE WOBBLE X/Y**, the image will stop oscillating and the contrast will reach a minimum when at focus.
4. Expand the beam beyond the large screen edge while maintaining a discernible image.
5. Press **HT**, High Tension wobbler and **BRIGHT TILT**.
6. Adjust **DEF X, Y** until the image is stable.

#### **B.6.6 Intermediate Lens Astigmatism/Caustic Point**

1. Center the beam at 40k. Spread the beam to the maximum by turning **BRIGHTNESS** full clockwise until it beeps.
2. Press **DIFF** on the right top panel to switch to diffraction mode.
3. Set the camera length to 60 cm on the monitor with **SELECTOR**.
4. Press **STIGMATOR INT** on the right bottom drawer. Adjust **DEF X, Y** until the caustic spot is a symmetrical crossing/star.
5. Focus with **DIFF FOCUS** to minimize the caustic spot size while it can still be observed.

### B.6.7 Condenser Deflector Shift

1. In diffraction mode, press **PROJ**, deflector PROJector, on the right bottom drawer.
2. Center the caustic spot with **SHIFT X, Y**.
3. Press **COND DEF ADJ TILT** on the right bottom draw.
4. Toggle **SHIFT** switch to **X** and adjust **SHIFT X** and **DEF X** to converge the separated central spots.
5. Toggle **SHIFT** switch to **Y** and adjust **SHIFT Y** and **DEF Y** to converge the separated central spots.
6. Center the caustic spot with **PROJ** and **SHIFT X, Y**.

### B.6.8 Objective Lens Astigmatism

1. Focus the image with **Z HEIGHT** at 300k while using **IMAGE WOBBLER X/Y** to check.
2. Underfocus or overfocus the image a little with **OBJ FOCUS**.
3. Insert CCD camera, obtain the live image and reduced FFT image of amorphous carbon.
4. Press **STIG OBJ**, OBJtive STIGmatism, adjust **DEF X, Y** until the concentric ellipses in the reduced FFT image become the concentric circles.

## B.7 Nanobeam Diffraction

1. Align the TEM following the previous procedures.
2. Center the screen to an empty area in the vicinity of the specimen.
3. Switch to low magnification by pressing **LOW MAG**. Change the condenser aperture to 3, center the aperture. For small specimens, change the condenser aperture from 3 to 4 and center it.
4. Press **CBD** in the left top panel to switch to CBD(Converging Beam Diffraction) mode. Change the spot size from **1.0 nm - 9** to **0.5 nm - 1** using the **Spot Size** and  $\alpha$  **selector** knobs on the left panel.
5. Center the crossover with **CONDENSER SHIFT X, Y** and with **PROJ** and **SHIFT X, Y** if necessary.
6. Align the voltage center and correct the condenser astigmatism at 300k in CBD mode.
7. Press **DIFF** to go to the diffraction mode and set the camera length as 40 or 30 cm. Center the beam with **PROJ**.

8. Go to CBD mode at 300k. Position the beam at the feature of interest. Wait (normally 10 min) until the beam is stabilized.
9. Go to diffraction mode, focus the beam using **BRIGHTNESS** for the smallest and sharpest beam spot. Center the beam with **PROJ**.
10. Go to CBD mode, align the voltage center and the condenser astigmatism. Focus the beam for the minimum contrast.
11. Go to diffraction mode, lower the beam stopper to block the beam.
12. Capture an image with exposure time of 40 s.

## **B.8 Finishing TEM Session**

1. Set the magnification at 40k by pressing **MAG2**.
2. Center the beam. Spread the beam by turning **BRIGHTNESS** fully clockwise until it beeps.
3. Press **V1** to close the gun valve.
4. Click **EXCHANGE SAMPLE** in the FasTEM computer. Press **N** to neutralize the specimen position.
5. Take off condenser aperture.
6. Remove the sample holder and insert the holder substitute.
7. Set the acceleration voltage to 181 kV.
8. Insert the anti-contamination device into the cold finger and press **ACD HEAT**.